

Cross-anatomical single-cell definition and characterization of human adipose progenitor niche

Présentée le 28 mars 2023

Faculté des sciences de la vie
Unité du Prof. Deplancke
Programme doctoral en biotechnologie et génie biologique

pour l'obtention du grade de Docteur en médecine et ès sciences (MD-PhD)
par

Radiana FERRERO

Acceptée sur proposition du jury

Prof. E. Oricchio, présidente du jury
Prof. B. Deplancke, directeur de thèse
Prof. N. Pitteloud, rapporteuse
Prof. C. R. Kahn, rapporteur
Prof. M. Stoeffel, rapporteur

“To write a thesis is like cooking a rare steak; it takes time to get it done just right and even then, it's better served with a glass of red wine.”

Unknown

"I have not failed. I've just found 10,000 ways that won't work."

Thomas Edison

“The most important thing is if you can find satisfaction in the little advances that you make, either on the problem itself or on your own skills and expertise.”

Bart Deplancke

Acknowledgements

Looking back in time, I was totally unaware of the magnitude of the MD-PhD endeavor when I first got to meet you Bart, I am sure you must have felt it. Nevertheless, from day one you believed in me and gave me the opportunity to embark on this wonderful journey surrounded by the amazing team you carefully put together throughout these years. Thank you for your unwavering support, guidance, and encouragement throughout my doctoral work. You will always be a model to me and I aspire one day to become a caring leading figure like yours.

Thanks to you all, dear colleagues of the Deplancke lab, you are the most brilliant and inspiring people I met so-far. Your work expertise and insights have been invaluable to me and I am grateful for your social commitment that helped preserving my mental health while achieving my academic goals. A special thank goes to the current and past members of the “adipoteam”. Magda, I could not have hoped for a better mentor, you thought me the scientific rigor that was necessary to build solid foundation to my future work and was always supportive on the personal level. I still remember the first scRNA-seq experiment we performed together as an absolute overwhelming experience, luckily, you were there for me until 10.30pm, I could have never achieved anything close to that alone. Pernille, my PhD soul-mate, needless to say that without your bioinformatics “magic” there would have been no doctoral thesis. I have loved working so close to you as I felt accompanied in the PhD process. I will always remember our endless ping pongs on manuscript versions and figures but even more so the endless funny slack conversations (the green and the red apples!) but also the tea times about personal issues. I am sure that not only will you be the perfect mum to Sia, but also a very successful scientist in Copenhagen. Horia, like me you came to the lab from a very different background, and yet look at you, blooming like a bright and independent scientist. Thank you for your positive mind, enthusiasm and for providing me with so much food...! I admire your strong belief in good values and your dedication to make this world a more gender balanced one especially in terms of pharma. The adipoteam is lucky to have you onboard, Marie, Marius and Laurine, for the upcoming scientific and adipogenic challenges, I wish I could stay longer in the lab to see the great discoveries you will make together. Daniel, thanks for your guidance on hASPC culturing and BRB-seq, you paved my way in the lab. Carles, I rarely encountered such a positive-minded and efficient scientist, I would have loved to work under your guidance, thanks for all the feedbacks you provided on the thesis and the manuscript, you are the perfect leader of the new adipo-team. Beyond the adipo-team a special thanks goes to Guido, such an inspiring post-doc, extremely versatile and always keen on helping, it was great culturing all those cells together. Thanks for all your help in reviewing my writing. Benoit too was a great lab-mate, your social emotion struck me and I am glad to be today a friend of yours.

At the crossroad between a colleague and a friend, here you stand, Julie, lab manager and people manager. Not only you enlighten our work environment with your energy, enthusiasm and efficiency but you also put your emotional intelligence at our disposal, cheering us up and pushing us through every single step of our journey in the lab. Who would

have thought that I would have found one of my best friends disguised as a colleague? Thanks for all the support you provided me during the past four years, both technically and emotionally. I look forward to all the good moments we will spend together beyond the every-day lab life. I would also like to thank my friends outside of academia, especially Rodrigue, Yann, Heloise, Claire, Eugenie, Saida, Evelyn, Vanesa, Yoann, Alice, Chiara P, Umberto, Agostino, Adalberto, Chiara S, Alexandre, Rita, for their support, encouragement, and friendship over the years. Your unwavering belief in me and my abilities has been a source of strength and motivation, and I am grateful for your presence in my life.

I am grateful to all the clinician collaborators Dr. Lucie Favre, Dr. Styliani Mantziari, Dr. Tobias Zingg, Professor Nelly Pitteloud, Professor Michel Suter, Professor Maurice Matter. You made the collaboration smooth and stainless. I am also grateful to the members of my dissertation committee, Professor Ronald Kahn, Professor Markus Stoffel, and Professor Nelly Pitteloud, for their insightful feedback, constructive criticism, and helpful suggestions. Your expertise in your respective fields has enriched my work immeasurably, and I am grateful for your time and attention. A special thanks goes to my jury president Professor Elisa Oricchio for her smooth handling and coordination of the oral exam. I would also like to thank the staff and faculty of EPFL and Unil, especially those in the MD-PhD program, Mme Thérèse Liechti and Mme Sandra Roux, for their administrative support and encouragement throughout my doctoral studies. Thanks to Joanna too, your administrative work in the lab is outstanding and it was an honour to have you help me out with all the admin issues. A special thanks goes to Professor Ivan Stamenkovic and Dr. Carlo Fusco respectively my master supervisor and mentor who sowed in me the seed of scientific curiosity.

I must thank my family for their love, support, and encouragement throughout my academic journey. Alessandra and Daniele, my fellow scientific cousins, I am so grateful the Leenaards Foundation made us meet! Having you and Agata in Lausanne makes me feel at home. Giuliana, you are family to me. Thank you for all the support you have always provided Carlo, mum and myself. You were my best friend when I was 10 years old, and you are even more so today. Dad, I know you look upon us from where you are. Thanks for your protection and for having gifted me with life. Carlo, you are the most amazing older brother, dot. I love you from the bottom of my heart, thank you for always have been such a perfect model to me. Mum, if am who I am today it is nothing but thanks to you. You always guided me through my life choices, challenging every single aspect of them in order to open my mind and make me think outside the box. A book would not be enough to let you know how grateful I am for all the life lessons you thought me. I love you.

Not only this MD-PhD journey made me grow into the better person I am today but it also allowed me to meet my better half. Bianca, I love your way of thinking, your sensitivity, your humour and your enthusiasm. Your unwavering belief in me and my abilities has been a constant source of inspiration, and I am grateful for your love and support. I look forward to share my life with you.

Lausanne, the 8th March 2023

Abstract

Adipose tissue is a key metabolic and highly-dynamic organ whose dysregulation may cause clinical conditions of concern such as obesity and lipodystrophy. Its function varies based on the anatomy, in fact, visceral adipose tissue expansion carries a greater risk of life-threatening associated comorbidities than subcutaneous expansion. Among the responsible for adipose tissue plasticity are the adipose-derived stem and progenitor cells (ASPCs) which can commit to form new mature adipocytes even in a post-developmental adult organism. The advent of scRNA-seq techniques allowed to delineate a clear and unbiased picture of the murine ASPC landscape across depots, unraveling subpopulations with distinct functional properties and even non- and anti-adipogenic features, however a similar depth of understanding is still lacking in humans.

This work focuses on defining the human ASPC niche composition and equilibrium across four different depots (Subcutaneous (SC), Omental (OM), Perirenal (PR) and Mesocolic (MC)) and over more than 75 individuals of various BMIs. We took advantage of bulk and scRNA-seq techniques to explore hASPC heterogeneity then functionalize our findings *in vitro* over 30 donors.

We found that two main populations, the highly-proliferative adipose stem cells and highly-adipogenic pre-adipocytes, are ubiquitously present in all analyzed depots but their relative proportions display a depot-specific and BMI-dependent distribution. Despite their omnipresence, these subpopulations still exhibited depot-specific gene expression patterns, likely reflecting distinct AT properties. Five minor subpopulations are also shared across depots and have specific gene expression patterns resembling populations previously described in mice. We further identified two OM-specific mesothelial cell populations, cobblestone in morphology, out of which one highly expresses and secretes IGFBP2 (Insulin-like growth factor binding protein 2). This OM-specific IGFBP2+ population constitutes 2-5% of the non-immune, non-endothelial OM stromal vascular fraction depending on the donor's BMI, appears to transition between mesothelial and mesenchymal cell states and inhibits the adipogenic capacity of hASPCs in a depot-specific manner through IGFBP2 secretion and integrin receptor signaling.

Altogether, our in-depth characterization of hASPC heterogeneity and function not only highlights the cellular uniqueness of different adipose niches but also identifies a new mechanism underlying the limited adipogenic capacity of OM hASPCs by uncovering an OM-specific IGFBP2+ mesothelial-like cell population that negatively regulates hASPC adipogenesis through IGFBP2 signaling. Further dissecting the precise mechanism of negative regulation in adipogenesis may lead to the discovery of new druggable targets to combat excessive adipose tissue expansion.

Keywords

Obesity, adipogenesis, human, adipose stem and progenitor cells, mesothelial cells, mesothelial to mesenchymal transition, anti-adipogenic, omentum, IGFBP2, TM4SF1, MSLN, scRNA-seq

Résumé

Le tissu adipeux est un organe clé et hautement dynamique du métabolique dont la dérégulation entraîne des manifestations cliniques préoccupantes telles que l'obésité et la lipodystrophie. Sa fonction varie en fonction de l'anatomie, en effet, l'expansion du tissu adipeux viscéral comporte un plus grand risque de comorbidités associées potentiellement mortelles que l'expansion du tissu adipeux sous-cutané. Parmi les responsables de la plasticité du tissu adipeux figurent les cellules souches et progénitrices dérivées du tissu adipeux (adipose-derived stem and progenitor cells = ASPC) qui peuvent se différencier en nouveaux adipocytes matures même dans un organisme adulte qui n'est plus en phase de développement. L'avènement des techniques de séquençage du transcriptome de cellule unique (single-cell RNA sequencing = scRNA-seq) ont permis de définir une image claire et non-biaisée de la configuration des ASPC chez la souris dans différents dépôts. Ceci a permis d'identifier des sous-populations ayant des propriétés fonctionnelles distinctes allant jusqu'à des comportements non et anti-adipogéniques. Une telle compréhension de la constellation des ASPCs fait toujours défaut chez l'Homme.

Ce travail se concentre sur la définition de la composition et de l'équilibre de la niche ASPC humaine dans quatre dépôts différents (sous-cutané (SC), omental (OM), périrénal (PR) et mésocolique (MC)) à partir de plus de 75 individus de divers IMC. Nous avons tiré parti d'analyses transcriptomiques pour explorer l'hétérogénéité des ASPC humaines, puis avons fonctionnalisé nos découvertes *in vitro* sur 30 donneurs.

Nous avons établi que deux sous-populations principales, les cellules souches adipeuses hautement prolifératives et les pré-adipocytes hautement adipogéniques, sont omniprésentes à travers tous les dépôts analysés, mais leur abondance relative est spécifique à chaque dépôt et dépend de l'IMC du donneur. Malgré leur omniprésence, ces sous-populations présentaient toujours des profils d'expression génique spécifiques au dépôt, reflétant probablement des propriétés propres à chaque tissu adipeux. Cinq sous-populations mineures sont également réparties entre les dépôts et ont des modèles d'expression génique spécifiques ressemblant à des populations précédemment décrites chez la souris. Nous avons en outre identifié deux populations de cellules mésothéliales qui sont spécifiques à l'OM, rondes de morphologie, dont l'une exprime et sécrète fortement l'IGFBP2 (Insulin-like growth factor binding protein 2). Cette population, *IGFBP2+* et spécifique à l'OM, constitue 2 à 5% de la fraction stromale et vasculaire non-immune et non-endothéliale et corrèle avec l'IMC du donneur. En outre, elle est susceptible de transitionner entre les cellules mésothéliales et mésenchymateuses et capable d'inhiber l'adipogénèse des hASPC d'une manière dépôt-spécifique grâce à la sécrétion d'IGFBP2 lui-même et sa signalisation via le récepteur d'intégrine.

Dans l'ensemble, notre caractérisation approfondie de l'hétérogénéité et de la fonction des ASPC humaines met non seulement en évidence l'unicité cellulaire des différentes niches adipeuses, mais identifie également un nouveau mécanisme sous-jacent à la reluctance adipogénique de ASPC omentales en découvrant une population cellulaire de type mésothélial *IGFBP2+* qui inhibe l'adipogénèse des ASPC humains via la signalisation liée à IGFBP2 lui-même. Disséquer davantage le mécanisme de régulation négative du tissu adipeux peut conduire à la découverte de nouvelles cibles médicamenteuses pour lutter contre l'obésité.

Mots-clés

Obésité, adipogénèse, humain, cellules souches et progénitrices adipeuses, cellules mésothéliales, transition mésothéliale à mésenchymateuse, anti-adipogénique, omentum, IGFBP2, TM4SF1, MSLN, scRNA-seq

Contents

ACKNOWLEDGEMENTS.....	V
ABSTRACT	VI
KEYWORDS	VI
RÉSUMÉ	VII
MOTS-CLÉS.....	VII
CONTENTS.....	VIII
LIST OF FIGURES	XI
LIST OF TABLES	12
LIST OF SUPPLEMENTARY FIGURES.....	13
LIST OF ABBREVIATIONS.....	15
CHAPTER 1 INTRODUCTION	19
1.1 THE RELEVANCE OF STUDYING ADIPOSE TISSUE PLASTICITY.....	20
1.2 CLINICAL PATHOLOGIES OF THE HUMAN ADIPOSE TISSUE	20
1.2.1 The overweight and obesity syndromes	20
Etiology.....	22
Clinics.....	23
Treatments	23
1.2.2 Lipodystrophy.....	25
Clinics.....	26
Treatments	26
1.3 THE BIOLOGY OF THE ADIPOSE TISSUE	27
1.3.1 A common structure different depots and functions.....	28
1.3.2 Anatomy dictates the function of adipose tissue.....	29
1.4 THE ASPC HETEROGENEITY	30
1.4.1 Three Main Subpopulations in White Adipose Tissue.....	30
1.5 THE ADIPOSE STEM CELL POPULATION	34
1.5.1 ASCs in inguinal WAT.....	34
1.5.2 ASCs in epigonadal WAT.....	35

1.6	THE PRE-ADIPOCYTE POPULATION	36
1.6.1	PreAs in inguinal WAT	36
1.6.2	PreAs in epigonadal WAT	36
1.7	THE ADIPOGENESIS REGULATORS POPULATION.....	40
1.7.1	Aregs in iWAT	40
1.7.2	Aregs in Visceral WAT.....	40
1.8	HIERARCHY OF ASPCs	41
1.9	MESOTHELIAL CELLS.....	42
1.10	ASPCs AND OBESITY	43
1.10.1	ASCs and obesity	43
1.10.2	PreAs and obesity.....	43
1.10.3	Aregs and obesity	43
1.11	THE SCOPE OF THIS THESIS.....	45
CHAPTER 2 A HUMAN OMENTUM-SPECIFIC MESOTHELIAL-LIKE STROMAL POPULATION INHIBITS ADIPOGENESIS THROUGH IGFBP2 SECRETION		47
2.1	ABSTRACT	48
2.2	INTRODUCTION	49
2.3	RESULTS.....	50
2.3.1	Human SVF precursor cells exhibit depot-dependent differences in their <i>in vitro</i> adipogenic potential.....	50
2.3.2	Human SVF-adherent cells exhibit transcriptomic differences that reflect their anatomical origin and adipogenic potential	51
2.3.3	scRNA-seq of SVF Lin ⁻ fraction reveals both common and unique subpopulations across the subcutaneous, visceral, mesocolic, and perirenal adipose depots	55
2.3.4	The Lin ⁻ fraction of SVF harbors three main subpopulations with specific functions that are ubiquitous across depots	60
2.3.5	Mesothelial cells inhibit adipogenesis of omental hASPCs	65
2.3.6	IGFBP2+ OM SVF Lin ⁻ cells can be found in situ and appear to transition between mesothelial and mesenchymal cell types	66
2.3.7	IGFBP2+ SVF Lin ⁻ OM cells inhibit adipogenesis through IGFBP2.....	71
2.3.8	IGFBP2-mediated adipogenic inhibition occurs in an IGF-independent manner	72
2.4	CONCLUSION	77
2.5	MATERIALS AND METHODS.....	80
2.6	MISCELLANEOUS	91
2.7	SUPPLEMENTARY FIGURES AND TABLES	92

CHAPTER 3 CONCLUSION AND FUTURE PERSPECTIVES	135
3.1 THE ADIPOSE-TISSUE SVF AND ITS HETEROGENEITY ACROSS SPECIES	136
3.1.1 The ASPC heterogeneity in mouse	136
3.1.2 The ASPC heterogeneity in human.....	138
3.2 MESOTHELIAL CELLS ARE KEY EFFECTORS OF THE STROMAL VASCULAR FRACTION	140
3.3 THE EMERGING CONCEPT OF NEGATIVE REGULATION OF ADIPOGENESIS.....	142
3.3.1 Do Aregs exist in human?	142
3.3.2 Adipogenesis is differentially regulated across anatomic locations.....	143
3.4 UNDERSTANDING THE ADIPOGENIC LINEAGE.....	145
3.4.1 The mesothelium as a possible origin for OM adipocytes	145
3.4.2 Redirecting the adipogenic lineage towards beiging	145
3.5 THE OMENTUM AT AS A HOTSPOT FOR ABDOMINAL CANCER METASTASIS	146
REFERENCES	149
CURRICULUM VITAE	166

List of Figures

Figure 1.1 – Lipodystrophy syndromes overview	27
Figure 1.2 – Integrated scRNA-seq data of SVF isolated from eWAT and iWAT.	33
Figure 1.3 – Integrated scRNA-seq data of SVF isolated from iWAT or from eWAT.	38
Figure 1.4 – Adipose derived stem and progenitor cells: toward a consensus view.....	44
Figure 2.1 – <i>Ex vivo</i> cultures of SVF-adherent cells feature an anatomic footprint in their phenotype and transcriptome.....	53
Figure 2.2 – scRNA-seq reveals common and specific cell populations across adipose depots.	58
Figure 2.3 – The SVF Lin [−] composition differs between subcutaneous, omental, and perirenal adipose tissues, and shared sub-populations from different anatomical locations exhibit consistent but also intrinsic molecular and cellular phenotypes.	64
Figure 2.4 – OM SVF harbors cells and signals that mediate adipogenic inhibition, while IGFBP2 ⁺ cells appear in transition between mesothelial cells and ASPCs.	69
Figure 2.5 – IGFBP2 ⁺ cells secrete IGFBP2 to inhibit adipogenesis of neighboring cells through an IGF-independent, paracrine mechanism.	76
Figure 3.1 – IGFBP2 expression at t0 and t14 across depots.....	144

List of Tables

Table 1.1 – Clinical definition of weight status based on BMI.....	22
Table 1.2 – Risk identification of developping health comorbidities based on combined BMI and waist circumference.....	22
Table 1.3 – Genetic obesity in human	23
Table 1.4 – Anti-Obesity Medications [adapted from	25
Table 1.5 – Methodological differences across scRNA-seq studies.....	32
Table 2.1 – Donors' informations	132
Table 2.2 – Donors' specifications for scRNA-seq.....	133
Table 2.3 – Cohorts specifications	133
Table 2.4 – Antibody specifications for FACS	133
Table 2.5 – Antibody specifications for IHC.....	133

List of Supplementary Figures

Supplementary Figure 2.1.1 – Across depot comparisons of SVF-adherent cells at low passage.	92
Supplementary Figure 2.1.2 – Adipogenic differentiation potential of cell lines is highly variable across individual donors.	94
Supplementary Figure 2.1.3 – The adipogenic potential of SVF-adherent lines from different depots and their correlation with metadata.	96
Supplementary Figure 2.1.4 – Human SVF-adherent cells from different depots differentially upregulate the adipogenesis response upon exposure to an adipogenic cocktail.	97
Supplementary Figure 2.1.5 – SVF-adherent cells from different depots have distinct transcriptomic signatures both when undifferentiated and when differentiated.	99
Supplementary Figure 2.1.6 – The expression of genes related to “inflammatory response” and “vasculature and epithelium development” is enriched in OM adipose depot-derived cells compared to those from other depots.	100
Supplementary Figure 2.2.1 – scRNA-seq reveals common cell populations across adipose depots and donors.	101
Supplementary Figure 2.2.2 – Human ASCs and PreAs feature different signaling pathways.	103
Supplementary Figure 2.2.3 – Several cell populations that were identified in the human SVF Lin ⁻ fraction across adipose depots correspond to cell populations identified in mice.	105
Supplementary Figure 2.2.4 – Metadata of the scRNA-seq atlas of hASPCs and mesothelial cells published by Emont et al.(Emont et al. 2022).	107
Supplementary Figure 2.2.5 – A HHIP ⁺ hASPC population shares key marker genes with the murine Adipogenesis regulators (Aregs).	108
Supplementary Figure 2.2.6 – A population of IFIT ⁺ hASPCs features enriched viral immune response gene expression.	109
Supplementary Figure 2.2.7 – A hASPC population shared across depots is defined by high SFRP2 and SFRP4 expression.	110
Supplementary Figure 2.2.8 – Mesothelial and IGFBP2 ⁺ cell markers are enriched in SVF cells from the OM adipose depot compared to other depots, both pre- and post-adipogenic induction.	111

Supplementary Figure 2.3.1 – The selection of scRNA-seq-inferred surface markers enables the enrichment of main SVF cell populations across all analyzed adipose depots.	113
Supplementary Figure 2.3.2 – Correlation between the FACS-based abundance of the indicated SVF Lin [−] subpopulations shared across depots and physiological data of the donors.	115
Supplementary Figure 2.3.3 – ASCs and PreAs, even if detected across depots, exhibit distinct gene expression profiles.	116
Supplementary Figure 2.4.1 – Known anti-adipogenic markers are overrepresented in OM-specific cell populations that express TM4SF1, and the proportion of TM4SF1 ⁺ cells positively correlates with BMI. Mesothelial and IGFBP2 ⁺ cells also display different morphologies.	117
Supplementary Figure 2.4.2 – Mixing OM SVF with PR SVF does not affect the adipogenic potential of PR cells.	118
Supplementary Figure 2.4.3 – IGFBP2 ⁺ cells exhibit a specific gene expression profile that also shares signatures with both ASPCs and mesothelial cells.	119
Supplementary Figure 2.4.4 – Cells from the sc and snRNAseq atlas of WAT published by Emont and colleagues are predicted as IGFBP2 ⁺ cells.	120
Supplementary Figure 2.4.5 – IGFBP2 ⁺ cells are cells that transition between mesothelial and mesenchymal cell states.	122
Supplementary Figure 2.4.6 – TM4SF1 and MSLN markers allow distinguishing between the two OM-specific subpopulations.	124
Supplementary Figure 2.4.7 – Detection of TM4SF1 ⁺ /MSLN ⁺ and TM4SF1 ⁺ /MSLN [−] cells by in situ immunohistochemistry.	125
Supplementary Figure 2.4.8 – TM4SF1 ⁺ /MSLN [−] cells change morphology upon expansion <i>in vitro</i>	127
Supplementary Figure 2.5.1 – PR SVF-adherent cells are insensitive to the inhibition exerted by IGFBP2-secreting cells in a transwell setting.	128
Supplementary Figure 2.5.2 – Experimental titration of IGFBP2, IGF-I, and IGF-II recombinant proteins to test their effect on adipogenic differentiation.	129
Supplementary Figure 2.5.3 – Treatment with IGFBP2 did not significantly affect the adipogenic differentiation of PR SVF-adherent cells, while treatment with Echistatin increased the accumulation of lipid droplets.	131

List of Abbreviations

APC	Adipose progenitor cells
ASC	Adipose stem cells
ASPC	Adipose stem and progenitor cells
AT	Adipose tissue
ATAC	Assay for Transposase-Accessible Chromatin
ATP	Adenosine triphosphate
BAM	Binary Alignment Map
BAT	Brown adipose tissue
BIOP	Bioimaging and optics facility
BMI	Body mass index
BRB	Bulk RNA barcoding
BSA	Bovine serum albumine
CAC	Complete adipogenic cocktail
CER	Comité éthique pour la recherche
CHUV	Centre hospitalier universitaire vaudois
CP	Committed preadipocytes
Ct	Cycle threshold
CT	Computerized tomography
D	Donor
DE	Differentially expressed
DEG	Differentially expressed gene
DEXA	dual energy X-ray absorptiometry
DMEM	Dulbecco's modified eagle medium
DN	Double negative
DNA	Deoxyribonucleic acid
DP	Double positive
DPBS	Dulbecco phosphate buffered saline
ECM	Extracellular matrix
EDBB	École doctorale biotechnologie et bioingénierie
ELISA	Enzyme-linked immunosorbent assay
EMT	Epithelial to mesenchymal transition
EPFL	École polytechnique fédérale de Lausanne
FACS	Fluorescence activated cell sorting
FBS	Fetal bovine serum
FC	Fold change
FCCF	Flow cytometry core facility
FCF	Flow cytometry facility
FCS	Flow cytometry standard
FDR	False discovery rate

FIP	Fibro-inflammatory progenitors
FMO	Fluorescence minus one
GAM	Generalized additive model
GB	Gallbladder
GECF	Gene expression core facility
GFP	Green fluorescent protein
GLP-1	Glucagon-like peptide-1
GO	Gene ontology
GRC	Genome Reference Consortium
GSEA	Gene set enrichment analysis
HCF	Histology core facility
HDL	High-density lipoprotein
HFD	High fat diet
HIV	Human immunodeficiency virus
HSC	Hematopoietic stem cell
HSD	Honestly significant difference
HSP	Heat shock proteins
IBI	Institute of bioinformatics
IBMX	3-Isobutyl-1-methylxanthine
IGF	Insulin-like growth factor
IGFBP2	Insulin-like growth factor binding protein-2
IHC	Immunohistochemistry
ILC2	type 2 innate lymphoid cells
IMC	Indice de masse corporelle
IP	Interstitial progenitors
KD	Knock-down
KO	Knock-out
LAGB	Adjustable gastric banding
LOESS	Locally estimated scatterplot smoothing
MACS	Magnetic activated cell sorting
MAD	median absolute deviation
MC	Mesocolon
MD	Medical doctor
MEM	Modified eagle medium
MMP	Matrix metalloproteinases
MMT	Mesothelial to mesenchymal transition
MRI	Magnetic resonance imaging
MSLN	Mesothelin
NA	Numerical aperture
NAFLD	non-alcoholic fatty liver disease
NC1	Negative control 1
NGS	Next generation sequencing

NTP	Nucleotides triphosphate
OM	Omenum
OSAS	Obstructive sleep apnea syndrome
P	Passage
PB	Pacific blue
PBS	Phosphate buffered saline
PC	Principal component
PCA	Principal component analysis
PCOS	Polycystic ovary syndrome
PCR	Polymerase chain reaction
PDGF	Platlet-derived growth factor
PDGFR	Platlet-derived growth factor receptor
PFA	Paraformaldehyde
PR	Perirenal
RELM	Regional Earthquake Likelihood Models
RNA	Ribonucleic acid
RT	Real-time
RYGBP	Roux-en-y gastric bypass
SARS	Severe acute respiratory syndrome
SC	Subcutaneous
SCA1	Stem cells antigen-1
SFM	Serum free medium
SFRP	Soluble frizzled-related proteins
SG	Sleeve gastrectomy
SNP	Single nucleotide polymorphism
SV	Science de la vie
SVF	Stromal vascular fraction
t-SNE	t-distributed stochastic neighbor embedding
T2DM	Type 2 diabetes mellitus
T2DM PA	Type 2 diabete mellitus preadipocytes
TGF- β	Transforming growth factor beta
TM4SF1	Transmembrane 4 L Six Family 1
UCP1	Uncoupling protein 1
UMAP	Uniform Manifold Approximation and Projection
UMI	Unique molecular identifier
UNIL	Université de Lausanne
VD	Vaud
VSMP	Vascular smooth muscle progenitor cells
WAT	White adipose tissue
WC	Waist circumference
WHR	Waist to hip ratio
WHtR	Waist-to-height ratio

Chapter 1 | Introduction

Note: This chapter is based on a published review “Toward a Consensus View of Mammalian Adipocyte Stem and Progenitor Cell Heterogeneity” Trends Cell Biol 30, 937–950 (2020).

Authors: Radiana Ferrero*, Pernille Yde Rainer* and Bart Deplancke.

* These authors contributed equally

My contribution: Conceptualized and wrote the manuscript.

1.1 The relevance of studying adipose tissue plasticity

Over thousands of years, humans have evolved leading a lifestyle where, getting food, mainly by hunting and gathering, was nearly as costly in energy as the energy that the food brought back. Throughout ages and civilizations, being overweight has been considered a privileged condition reserved only to the elite who could “afford it”. The recent revolution in human lifestyle as well as the increasing availability and degrading quality of food, have contributed to the dramatic change in the world’s weight distribution landscape. In 2016, more than 25% of the world’s population is overweight or obese¹, regardless of gender, age, or social background². What is alarming about excessive fat accumulation in the human body though is the consequences that it has for the metabolic health of patients.

Insulin resistance followed by type 2 diabetes, dyslipidemia, and high blood pressure together with obesity form the clinical features of the metabolic syndrome which facilitates the insurgence of cardiovascular diseases such as heart or brain stroke, as well as cancer³. Alone, cardiovascular diseases and cancer are the cause of a quarter of the world’s deaths⁴, and with it, obesity is thus one of the most widespread and preventable killers to be on earth. In addition, follow-up of these chronic and complex conditions such as metabolic syndrome, cardiovascular disease, and cancer drains numerous healthcare resources with a consequent negative impact on the financing of healthcare systems⁵. Despite long-term efforts from the scientific community to understand the mechanisms underlying fat accumulation and to develop effective therapies, no treatment is currently available⁶, and exercise and lifestyle change are not always applicable, especially in severely affected patients.

Efficient personalized medicine in the field of fat biology would permit a decrease in the excessive body fat burden both for patients and healthcare systems. If as shortly presented above, excess in adipose tissue mass can be highly detrimental to the human organism, it is not nevertheless a disposable organ as illustrated by the lipotoxic consequences of lipodystrophic conditions⁷. Overall, it is now well appreciated in the scientific community that adipose tissue constitutes a highly dynamic, endocrine-type organ playing an indispensable role in several biological processes including development, immunity, and energy homeostasis.

1.2 Clinical pathologies of the human adipose tissue

1.2.1 The overweight and obesity syndromes

Excess in body fat mass leads first to overweight followed by obesity. In an average men population, fat weight accounts for 15%-20% of the total weight, while for 25-30% of the woman's total weight^{8,9}. To

diagnose overweight and obesity conditions, physicians require reliable and convenient measurements to use on a daily basis.

In clinical practice, the easiest metric to use is the Body Mass Index (BMI [kg/cm²]), defined as the weight of the individual divided by the square of their height. Empirically determined cutoffs define underweight, normoweight, overweight and obesity following the values shown in **Table 1.1**. BMI measurement however misses an important factor in the body weight distribution and can easily be biased by the ratio of “lean mass” = muscles versus “fat mass” = adipose tissue¹⁰. Moreover, it will not account for the anatomic distribution of the adipose mass, and for equal BMIs, a person can have its fat accumulated in the subcutaneous compartment versus the visceral one with the first case having a lower risk for developing obesity-associated comorbidities¹⁰. To partially overcome BMI limitations in discriminating between metabolically unhealthy visceral obesity versus subcutaneous one¹¹ the waist circumference (WC) and the waist-to-hip ratio (WHR) are often used as complementary quick and affordable diagnostic tools, with the WC outperforming the BMI ratio when it comes to predicting intraperitoneal adipose tissue mass, and outperforming WHR when predicting posterior subcutaneous adipose tissue mass¹². Combining BMI and WC measures allows for identifying normal risk, high risk and very high risk for developing associated lethal comorbidities as illustrated in **Table 1.2**. Finally, a recent study underly the importance of keeping waist circumference lower than half your height (Waist-to-height ratio (WHtR) ≤ 0.5) to prevent metabolic risk, out-performing the BMI and WC classification in terms of early detection of increased metabolic risk¹³.

With technological advances, and limited to research purposes for practical reasons, several more sophisticated methods have been used to precisely determine fat mass distribution in health and disease and to scientifically predict morbidity and mortality linked to overweight and obesity. Among those, bioelectric impedance, hydrodensitometry and air displacement plethysmography are non-invasive investigative techniques that rely on differences in conduciveness of hydrophobic adipose tissue and hydrophilic soft tissues¹⁴. The affordability and easy-to-use features of these devices justify their use in big population-based studies. However, the measure of adipose tissue being indirect and based on pre-set equations often calibrated on image-based quantification performed on white men reference population makes them inaccurate when transferred to different populations such as elders, children or women¹⁵. Dual-energy X-ray absorptiometry (DEXA)-scan relies on low-dose radiation exposure and attenuation of the electron beam based on the tissue it encounters in the body¹⁶. Although highly reproducible and relatively easy to perform, the output of the DEXA-scan measure is in two dimensions and thus cannot distinguish visceral fat from subcutaneous fat^{17,18}. Once again, algorithms based on image-based adipose tissue measurements were developed to infer what percentage of the measured adipose mass is visceral¹⁹ and implemented in recent DEXA analysis software, however, the same limitation in transferability across populations described above apply in this case. Finally, image-based methods, such as computerized tomography (CT) and magnetic resonance imaging (MRI),

represent the highly technical albeit reference measuring tools to localize adipose tissue and accurately associate its anatomic distribution to morbidity²⁰.

Table 1.1 – Clinical definition of weight status based on BMI²¹

Weight	BMI (kg/m ²)
Underweight	< 18.5
Severe underweight	< 16.0
Moderate underweight	16.0–16.99
Mild underweight	17.0–18.49
Normal range	18.5–24.99
Overweight	≥ 25
Pre-obese	25.0–29.99
Obese	≥ 30
Obese class I	30–34.99
Obese class II	35–39.99
Obese class III	≥ 40

Table 1.2 – Risk identification of developing health comorbidities based on combined BMI and waist circumference¹³

BMI classification	Waist circumference		
	Low	High	Very high
Normal weight	No increased risk	No increased risk	Increased risk
Overweight (25 to less than 30kg/m ²)	No increased risk	Increased risk	High risk
Obesity I (30 to less than 35kg/m ²)	Increased risk	High risk	Very high risk
Obesity II (35 to less than 40kg/m ²)	Very high risk	Very high risk	Very high risk
Obesity III (40kg/m ² or more)	Very high risk	Very high risk	Very high risk

Waist Circumference: Low (men <94 cm, women <80 cm); High (men 94–102 cm, women 80–88 cm); Very high (men >102 cm, women >88 cm).

Etiology

The number one cause of the onset of overweight and obesity is behavioral. On the one hand, are poor dietary habits such as eating large amounts of processed food and drinking sugary drinks for a daily calorie intake higher than 2000 kcal, on the other hand, reduced physical activity results in reduced energy expenditure greatly contributing to weight gain over time.

Some rare forms of obesity accounting for less than 0.001% of the overall prevalence are driven by monogenic mutations (mainly in the leptin and melanocortin endocrine axis²²) and are at times associated with developmental delay **Table 1.3**, while several clinical syndromes with high familiarity prevalence including Polycystic Ovary Syndrome (PCOS), hypothyroidism and hypogonadism are characterized by early onset and resistant obesity²³.

Importantly, epigenetics seem to play a key role in obesity onset, and obese parents tend to give birth to obesity-predisposed offsprings²⁴. Finally, among iatrogenic causes of weight gain are medications including atypical antipsychotics, anticonvulsants, mood stabilizers, hypoglycemic drugs, glucocorticoids, and antidepressants²⁵.

Table 1.3 – Genetic obesity in human [adapted from Sadaf Farooqi and Stephen O’Rahilly²⁶]

Obesity Associated With Developmental Delay
Prader-Willi Syndrome
Fragile X Syndrome
Bardet-Biedl Syndrome
Borjeson-Forssman-Lehmann Syndrome
Wilson-Turner Syndrome
Albright's Hereditary Osteodystrophy (AHO)
BDNF and TRKB Deficiency
Obesity Without Developmental Delay
Alstrom Syndrome
Ulnar-Mammary Syndrome
Simpson-Golbi-Behmel, Type 2
Congenital Leptin Deficiency
Leptin Receptor Deficiency
POMC Deficiency
Prohormone Convertase 1 Deficiency
Malanocortin 4 Receptor Deficiency

Clinics

In the context of excessive body weight, what is the most concerning are the linked comorbidities. Metabolically, insulin resistance followed by type 2 diabetes typically onset early in the context of obesity, together with dyslipidemia and high blood pressure they constitute the dreadful triad of the metabolic syndrome²⁷. The obstructive sleep apnea syndrome (OSAS) is typically linked to obesity and metabolic syndrome and contributes to an overall increase in the risk for cardiovascular diseases including stroke and heart failure²⁸. In the longer term, the metabolic imbalance also leads to non-alcoholic fatty liver disease and chronic kidney disease²⁹.

The osteoarticular system is also highly challenged by excessive weight. This results in a higher incidence of arthrosis, arthritis and sciatica events among obese patients^{30,31}. Osteo-articular pathogenic conditions also contribute to a vicious circle where pain impedes exercise which in turn worsens the cause of pain.

The onset of several cancers is facilitated by underlying obesity. Among the scientifically demonstrated ones are the esophagus adenocarcinoma, colorectal, pancreas, liver, gallbladder, kidney, thyroid, uterus, breast, ovary and blood (myeloma) cancers^{32,33}. In the attempt to explain such a striking correlation between obesity and cancers, several adipokines have been put forward as critical drivers³⁴.

Finally, not only the body is affected by obesity, but also the mind. Depression and anxiety are typically more prevalent in the obese population than the normoweight population³⁵. If the main explanation stems from the societal look that patients have to carry throughout their life, a physiologically detrimental impact of the high-sugar and high-lipids blood content on the brain is not to be excluded^{36,37}.

Treatments

The first line of management of overweight and obesity syndromes is nutritional and physical education accompanied by motivational support in the context of weight-management programs. With such a

conservative approach physicians can hope to achieve 5%-10% body weight loss which is often sufficient to improve the underlying metabolic dysbalance³⁸. The most challenging aspect of weight loss however is long-term maintenance. Five years after the weight-loss intervention, only 3% of the weight loss is usually retained³⁹.

When weight-management programs fail to significantly reduce the body weight of the patient, and the BMI remains above 30 kg/m², Swiss physicians can count on three anti-obesity medications to achieve a supplementary weight loss of 3 to 12% and improve the overall metabolic health^{40,41} (**Table 1.4**). Pancreatic lipase inhibitors (orlistat) induce malabsorption of free fatty acids and result in a median weight loss of 2.12kg⁴² which is associated with a reduction of both type 2 diabetes mellitus and cardiovascular risk⁴³. The unpleasant side effect of malabsorption often limits the therapy to a couple of years. The agonist of the Glucagon-like peptide-1 (GLP-1) receptor (Liraglutide, Semaglutide) acts as an appetite suppressor and slows the gastrointestinal transit down. The resulting weight loss is an average of 3.2kg⁴⁴ and comes with positive effects on glycemia, blood pressure and cholesterol. Finally, a controverted combined medication (naltrexone/bupropion) analog of the amphetamine was approved by the European Medicine Agency in 2015 and at cost of several side effects such as headache, nausea and constipation has the potential of reducing the patients' weight up to 5%⁴⁵. The American Food and Drug Administration approved in addition to the above-described drugs, several molecules acting on the brain (serotonin and opioid receptors), or physically taking space in the stomach to reduce caloric intake⁴⁶ (**Table 1.4**).

The last bullet clinicians have to improve the metabolic health of morbidly obese patients is bariatric surgery, also known as metabolic surgery. The most common methods of bariatric surgery are adjustable gastric banding (AGB), sleeve gastrectomy (SG) and the Roux-en-y gastric bypass (RYGBP). The rationale stands on the one hand to restrict the stomach volume (AGB, SG and RYGBP), preventing excessive food intake, and/or on the other hand inducing malabsorption (RYGBP). If LAGB has been abandoned based on poor weight-loss outcomes in the long term⁴⁷, LSG and LRYGBP, being both laparoscopic surgeries, are safe and associated with low risks of perioperative complications and minimal mortality (0.1 to 0.2%)⁴⁸. Long-term (> 10 years) follow-up reveals that on average 20-30% of the initial weight is lost without relaps⁴⁹. The weight loss is accompanied by significant improvement, at times complete remission, of several obesity-related comorbidities, coupled with an increase in patients' survival up to 30-40%^{50,51}.

Table 1.4 – Anti-Obesity Medications [adapted from Tchang et al.^{46]}

Name (Trade Names)	Year Approved	Mechanism of Action / Clinical Effect	Average placebo-subtracted weight loss (%) at 14 months	Achieved ≥5% Weight Loss, Intervention vs. placebo (%)	FDA approval	EMA approval
<i>Approved for short-term use (3 months)</i>						
Phentermine (Adipex, Lomaira)	1959	Sympathomimetic / Suppresses appetite	4.4 at 28 weeks	49 vs. 16 at 28 wks	Yes	No
Diethylpropion	1979	Sympathomimetic / Suppresses appetite	6.6 at 6 months	67.6 vs. 25.0	Yes	No
<i>Approved for long-term use</i>						
Orlistat (Alli, Xenical)	1999	Intestinal lipase inhibitor / Reduces fat absorption by up to 30%	3.8	50.5 vs. 30.7	Yes	Yes
Phentermine-topiramate (Qsymia)	2012	Combination sympathomimetic and carbonic anhydrase inhibitor / Decreases appetite and binge eating behaviors	8.6	70 vs. 21	Yes	No
Bupropion-naltrexone (Contrave)	2014	Combination of a dopamine and norepinephrine re-uptake inhibitor and mu-opioid receptor antagonist / Decreases appetite and cravings	4.8	48 vs. 16	Yes	Yes
Liraglutide 3.0mg (Saxenda)	2014	GLP-1 receptor agonist / Decreases appetite, increases fullness, increases satiety	5.4	63.2 vs. 27.1	Yes	Yes
Gelesis100 (Plenity)	2019	Superabsorbent hydrogel particles of a cellulose-citric acid matrix / Increases fullness. Considered a medical device but functions as a medication.	2.0 at 6 months	58.6 vs. 42.2	Yes	No
Setmelanotide (Imcivree)	2020	Melanocortin-4-receptor agonist / Decreases appetite	N.A.	N.A.	Yes	No
Semaglutide 2.4 mg (Wegovy)	2021	GLP-1 receptor agonist / Decreases appetite, increases fullness, increases satiety	12.4	86.4 vs. 31.5	Yes	Yes

1.2.2 Lipodystrophy

Opposite to overweight and obesity are lipodystrophic syndromes, characterized by the inability to generate and maintain functional adipose tissue. Lipodystrophy mainly concerns the subcutaneous adipose tissue and localizes differentially based on the type of syndrome⁷ (**Fig. 1.1**). The condition can be congenital, generalized (autosomal recessive mutation of *AGPAT2*, *BSCL2* and *CAV1* genes) or familial partial (autosomal dominant mutation of *LMNA*, *CIDEA*, *LIPE* or recessive missense mutation of adipogenesis master regulators *PPARG* and *PLIN-1* as well as zinc finger protein *ZMPSTE24*), or acquired, once again generalized, partial or even localized in the case of subcutaneous drug injections (recombinant insulin treatment in the context of diabetes for example)⁵² (**Fig 1.1**). Lipodystrophy can also occur under long-term anti-retroviral therapy in the context of HIV infection⁵³. The prevalence of lipodystrophic syndromes is difficult to estimate but is in the range of extremely rare disorders (1-5 cases per million people)⁵⁴. The progressive loss of mature adipocytes leads to a number of metabolic and endocrinologic impairments including leptin and adiponectin defects as well as lipotoxicity and insulin resistance.

Clinics

The inability to store free fatty acids in mature adipocytes results in diffuse lipotoxicity. Non-specialized organs such as the liver, the pancreas and the heart will buffer the excessive circulating triglycerides at cost of having their function compromised⁵⁵. Physically, patients have cadaveric facies, prominent muscles and veins as well as lytic skeletal changes. The associated hypo-leptinemia induces persistent hunger and voracious appetite. Metabolically, patients suffer from insulin-resistant diabetes mellitus coupled with hyperinsulinemia together with hypertriglyceridemia and low serum HDL levels. With disease progression, NAFLD followed by non-alcoholic steatohepatitis, pancreatitis, hypertrophic cardiomyopathy, nephropathy and organomegaly take over and undermine patients' life expectancy. For the congenital forms of lipodystrophy, the average lifespan is 65 years old⁵⁶, namely 30 years less than a healthy individual.

Treatments

The management of lipodystrophic syndrome is directed to limit the metabolic burden of lipotoxicity. First are dietary and exercise measures to keep a balanced diet and avoid excessive food intake. Leptin analog therapy allows for decreasing the appetite, the serum levels of glycosylated HbA1c and triglycerides within 4 months^{57,58} and is indicated for generalized lipodystrophic syndromes, while it is used off-label for the treatment of partial syndromes as it proved to be less effective in this context⁵⁵.

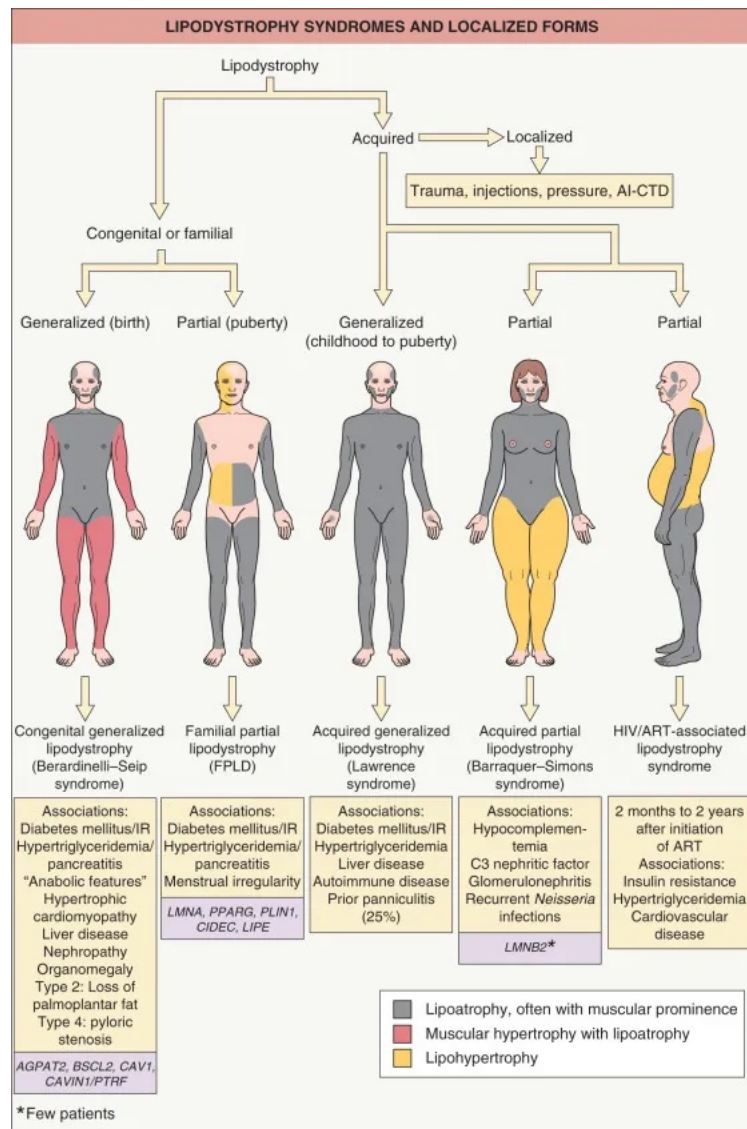


Figure 1.1 – Lipodystrophy syndromes overview [adapted from <https://plasticsurgerykey.com/lipodystrophies-2/>]

1.3 The biology of the adipose tissue

If we want to combat obesity, there is an urgent need to better understand fundamental biologic processes involving adipose tissue (AT) expansion. In this work, I decided to focus on characterizing cells at the very root of the AT expansion, i.e. the stem cells that reside within the AT and are able to regenerate it. In order to be as close as possible to human biology, I decided to work with human samples and explored similarities and differences in the composition of the stem cells across four different anatomic depots. To date, the composition and behavior of the adipose-derived stem and progenitor cells (ASPCs) have mainly been studied in the mouse model while studies including human material have been limited to computational analysis and little to no functionalization of the findings was so far performed^{59–61}. In this section, I will present the state

of the art of ASCs composition and function with a main focus on the murine model starting with a short overview of AT structure, function and anatomy.

1.3.1 A common structure different depots and functions

AT is the main center for long-term energy storage and lipids handling. Its conservation from simple invertebrates such as *D. melanogaster* all the way up to humans underlies its fundamental role for survival. It is defined as a connective tissue that arises from the mesenchymal layer of the embryo⁶² but, contrary to other connective tissues such as bone or cartilage it accounts for higher cellularity and a lower content of the extracellular matrix. Nested in a collagen net, adipocytes are the mature cells residing in the adipose tissue. Their size can vary from as little as 20 μm to 300 μm in diameter⁶³, and although they account for less than 30% of the absolute cell number of the adipose tissue^{64,65} they make up the biggest volume of the tissue and are therefore considered as the principal cell type in the tissue. Their main role is to store free fatty acids in the form of triglycerides, by doing so, they will increase their intracellular volume up to a point that becomes detrimental to the metabolic health of the entire individual. In fact, in the long term, this process, called hypertrophy, can lead to the exhaustion of the adipocyte itself which will start to secrete pro-inflammatory signals, eventually contributing to insulin resistance and metabolic syndrome.

Surrounding and supporting adipocytes stands the stromal vascular fraction (SVF), which not only hosts resident and transient immune cells and endothelial cells along blood vessels but is also the nest for a number of other poorly defined cell types, the so-called adipose-derived stem and progenitor cells (ASCs). ASCs are multipotent stem cells that are able to form a new functional adipose tissue when transplanted in lipodystrophic mice and are able to accumulate intracellular lipid-filled vesicles when cultured *in vitro*^{66–68}. Upon adipose tissue remodeling, ASCs can commit and differentiate into mature adipocytes even in the adult organism. This process is called hyperplasia, and opposite to hypertrophy is associated with good metabolic health as it will allow to store free fatty acids in newly formed small and un-exhausted adipocytes. Hyperplasia likewise hypertrophy will eventually lead to the increase of the volume of the depot upon chronic excessive calory intake.

If the structure is common to all ATs, when it comes to function, it is important to distinguish between depots that store lipids and the ones that burn the lipids to generate heat. As such, three functional types of adipose tissue exist white, brown or beige ATs^{69,70}. Adipocytes of the white adipose tissue typically harbor a unique large lipid vesicle (unilocular) and are specialized in lipids storage. When it comes to brown AT, a vestigial adipose tissue in humans, but an important organ in mice, its main mission is to maintain body temperature homeostasis. It is in fact able to generate heat by highly expressing the uncoupling protein 1 (UCP-1). UCP-1 allows for the dissipation of the energy needed to produce ATP from the electron transport chain in the mitochondria and generate heat. Adipocytes of the brown adipose tissue are typically smaller in size than

the ones from the white adipose tissue and harbor more than one (multilocular) small lipid droplet in their cytoplasm. Finally, beige AT is an in-between and adaptive tissue type that upon external stimulation, develops within white adipose tissue and is able to generate heat. External stimulation is typically cold or adrenergic stimuli that result in the upregulation of the UCP-1 protein expression. Adipocytes of the beige adipose tissue are unilocular and express UCP-1. Whether beige adipocytes arise from an interconversion of white adipocytes or from a differential commitment of ASCs is still a debated concept, but finding means to reprogram white adipose tissue to become thermogenic is a valuable research avenue in the context of improving the metabolic status of obese individuals.

1.3.2 Anatomy dictates the function of adipose tissue

A common way to define AT is based on its anatomy, which has been shown to correlate with metabolic health when overgrown. As such, “metabolically healthy” subcutaneous AT, using hyperplasia as a preferential mean of growth, is conventionally opposed to the “unhealthy” visceral one which typically expands through hypertrophy. However, the terms “visceral” and “subcutaneous” underlie several finer anatomic locations and, with it, potentially finer AT functions. For instance, visceral AT is the perirenal AT, which locates around the kidney and is attracting increasing attention being a site of dormant brown adipogenesis^{71,72}. It’s possible that crosstalk with the kidney itself to undermine kidney function is also an interesting detrimental mechanism linked to perirenal adipose tissue expansion⁷¹. The mediastinal AT situated around the esophagus and the trachea is also considered as a visceral adipose tissue and a potential site for human brown-beige adipogenesis^{73,74}, yet it is but at the same time like the perirenal one is not confined within a mesothelial layer contrary to for example the pericardial, mesenteric or omental ATs, with the latter being considered as the “golden standard” visceral adipose depot¹¹. Pericardial adipose tissue and its anatomically close friend, epicardial adipose tissue are considered pro-inflammatory, proatherogenic, and cardiotoxic in the context of cardiometabolic disease, but also as an important source of energy for the myocardium when energy demand is increased⁷⁵. The mesenteric adipose tissue, a fold connecting the intestine to the abdominal wall, contributes to buffering the intestinal intake in many ways, both as an immune barrier and a lipidic reservoir to prevent lipid hepatotoxicity⁷⁶. Needless to say, that omental adipose tissue has consistently been linked to type 2 diabetes onset, cardiometabolic complications, and an overall proinflammatory status⁷⁷. The same heterogeneity holds between subcutaneous ATs. For example, the abdominal SC AT is slightly different from the gluteal one⁷⁸. So far, most of the functional analyses are restricted to subcutaneous and omentum, often taking advantage of the mouse model for practical reasons, however, evidence points to a regional specialization of every single adipose depot in the adult human body⁷⁹, there is, therefore, need to take these regional differences into account and better functionally characterize all existing adipose tissues.

1.4 The ASPC heterogeneity

In mouse, SCA1 surface protein, encoded by the *Ly6a* gene, is well established as the main marker to enrich ASPCs for a precursor cell population that has enhanced *in vitro* adipogenic capacity⁸⁰. However, not all SCA1+ cells give rise to adipocytes *in vitro*, implying that an even finer granularity of cell states or even cell types exist. Therefore, much effort has been devoted to uncover additional surface markers. For example, mesenchymal markers, such as CD34, CD29, CD24, and platelet-derived growth factor receptor (PDGFR) α/β , were also shown to enrich for adipogenic precursors, or a fraction of them^{81–84}. Our integration confirmed that *Cd34*, *Cd29*, and *Pdgfra* are expressed by virtually all ASPCs, while *Cd24* and *Pdgfrb* exhibit a nonuniform expression, as discussed later (**Fig. 1.2D-E**). However, while SCA1 is widely used for enriching ASPCs in mouse, there is no SCA1 ortholog in human. Consequently, the *in toto* Lin[–] fraction of adipose SVF tends to be considered as the best representation of human ASPCs (hASPCs). Markers, such as *CD29*, *CD34*, *CD13*, *CD44*, *CD73*, *CD90*, *CD142*, *CD9*, *CD10*, and *CD200*^{85,86}, have been used to further enrich for adipogenic cells in human, but there is no consensus yet on the exact molecular signature of hASPCs. Until recently, the identification of these markers was mostly based on flow cytometry and immunohistochemistry using hematopoietic, endothelial, and neural tissues as reference, which tends to introduce marker selection bias. However, over the past few years, the single-cell technology revolution has allowed researchers to delineate ASPCs at an unprecedented resolution (**Fig. 1.2** and **1.3**).

1.4.1 Three Main Subpopulations in White Adipose Tissue

Numerous studies^{59,60,87–91} recently resolved ASPC heterogeneity in mouse subcutaneous (inguinal) white adipose tissue (WAT) and visceral (specifically epigonadal WAT) WAT (iWAT and eWAT, respectively). Despite differences in the utilized methodologies and/or mouse models (**Table 1.5**), all studies in mouse stratified ASPCs into two to three main subpopulations. Qualitative cross-comparison of the population-specific markers supports the notion that these populations are shared between subcutaneous and visceral depots, although intrinsic differences remain that are far from being fully understood. To empirically validate this ASPC classification, we integrated public data sets (highlighted in gray in **Table 1.5**) using the standard integration workflow of Seurat^{92,93}. This large, integrated meta-data set provides a powerful means to explore the observed ASPC landscape across studies in an unbiased fashion. This is because it enables verification of the expression distribution and, thus, the specificity of previously established ASPC markers. In addition, it allows us to computationally explore parallels between the recently published scRNA-seq studies and to support the proposed population nomenclature. Specifically, our analyses revealed that the three populations (Adipose Stem Cells (ASC), Pre-Adipocytes (PreAs), and Adipogenesis regulators (Aregs)) are robust since they: 1) are characterized by specific gene expression signatures; 2) were first independently detected in each of the

utilized data sets; 3) can be projected onto one another upon data integration (**Fig. 1.2 A**, and **Fig. 1.3A,G**); and 4) are consistently clustered in various subclusters upon analysis of the integrated data set (**Fig. 1.2B**, and **Fig. 1.3B,H**). Finally, we were able to confirm that the three populations align with populations published across different studies (**Fig. 1.2C**, and **Fig. 1.3C,D,I,J**). Altogether, the integration shows that ASCs are a distinct population compared with PreAs and Aregs, which are closer in terms of gene expression but still feature distinct transcriptomic profiles. Specific to visceral fat are the mesothelial cells which also populate the Lin[−] fraction of visceral SVF together with ASPCs^{80,88,89,94,95}.

For human, only a couple of scRNA-seq studies have been published^{61,96,97}, and these do not necessarily reach the same conclusions. This renders it difficult to establish a clear picture of hASPC heterogeneity. However, a closer look at the reported findings does suggest that, based on shared gene signatures, at least two ASPC subpopulations are conserved between mouse and human, namely the ASCs and PreAs.

Table 1.5 – Methodological differences across scRNA-seq studies

Study	Model	Technique	Anatomical depot	SVF enriching strategy	Pop. names	Populations markers	Proposed nomenclature	
Schwalie et al.	Adult Mouse	Fluidigm C1	Inguinal*	CD45-/CD31-/Ter119-/CD29+/CD34+/Sca1+	P1	CD55+/IL13RA1+	ASCs	
					P2	VAP1+/ADAM12+	PreAs	
					P3	CD142+/ABCG1+	Aregs	
		10x Genomics	Inguinal*	CD45-/CD31-/Sca1+	G1	Equivalent to P1	ASCs	
					G2	Equivalent to P2	PreAs	
					G3	Equivalent to P3	Aregs	
					G4	Equivalent to P1	ASCs	
Burl et al.	Adult Mouse	10x Genomics	Inguinal*	Whole SVF CTL	ASC1	Unsorted	PreAs	Aregs
				b3AR agonist stim	ASC2	Unsorted	ASCs	
			Epigonadal ^o	Whole SVF CTL	ASC1	Unsorted	PreAs	Aregs
				b3AR agonist stim	ASC2	Unsorted	ASCs	
					Fibro	Unsorted	Mesothelial	
Hepler et al.	Adult Mouse	10x Genomics	Epigonadal ^o	PDGFR β +	APC	LY6C-/CD9-	PreAs	
					FIP	LY6C+	ASCs	
					Meso	LY6C-/CD9+	Mesothelial	
Merrick et al.	Adult Mouse	10x Genomics	Inguinal*	CD45-	IP	DPP4+/CD142-	ASCs	
	Pups Mouse				CP	ICAM1+/CD142-	PreAs	
					CD142+	CD142+	Aregs	
	Human obese	10x Genomics	Abdominal and flank*	CD45-	IP	DPP4+/CD142-	ASCs	
					CP	ICAM1+/CD142-		
Cho et al.	Adult Mouse control & under diet-induced obesity	10x Genomics	Epigonadal ^o	CD45-/CD31-/Ter119-/Sca1+	Cluster 1	CD55 ^{high} CD81 ^{low}	ASCs	
					Cluster 5	CD55 ^{high} CD81 ^{high}	ASCs	
					Cluster 2	CD55 ^{low} CD9 ^{low-mid} CD81 ^{low}	PreAs	Aregs
					Cluster 4	CD55 ^{low} CD9 ^{low-mid} CD81 ^{high}	PreAs	Aregs
					Cluster 6	CD55 ^{low} CD9 ^{high}	PreAs	Aregs
Spallanzani et al.	Adult Mouse	10x Genomics	Epigonadal ^o	CD45-/CD31-/PDGFR α +/Sca1+/PDPN+	VmSC1	PPARG-/THY1-	Mesothelial cells	
					VmSC2	THY1+/CD55+	Adipose stem cells	
					VmSC3	THY1+/CD55-	Aregs	
					VmSC4	PPARG+/THY1-	PreAs	
					VmSC5	PPARG+/THY1+	PreAs	
Vijay et al.	Human obese	10x Genomics	Abdominal*	CD34+	T2D PA	Unsorted		
					Fibro	Unsorted		
					HSC	Unsorted		
			Omental ^o	CD34+	T2D PA	Unsorted		
					Fibro	Unsorted		
					HSC	Unsorted		
					Meso	Unsorted	Mesothelial cells	

Abbreviations: APC, adipose progenitor cells; Aregs, adipogenesis regulators; ASC, adipose stem cells; CP, committed preadipocytes; Fibro, fibroblasts; FIP, fibro inflammatory progenitors; HSC, hematopoietic stem cells; IP, interstitial progenitors; Meso, mesothelial cells; PreA, preadipocytes; T2DM PA, type 2 diabetes-dependent preadipocytes; Gray boxes indicate data sets used in the integration analysis (see Fig. 1.2 and Fig. 1.3) ; Schwalie *et al.*⁸⁷, Burl *et al.*⁸⁸, Hepler *et al.*⁹⁸, Merrick *et al.*⁶⁰, Cho *et al.*⁹⁰, Spallanzani *et al.*⁹⁹, Vijay *et al.*⁹⁴.

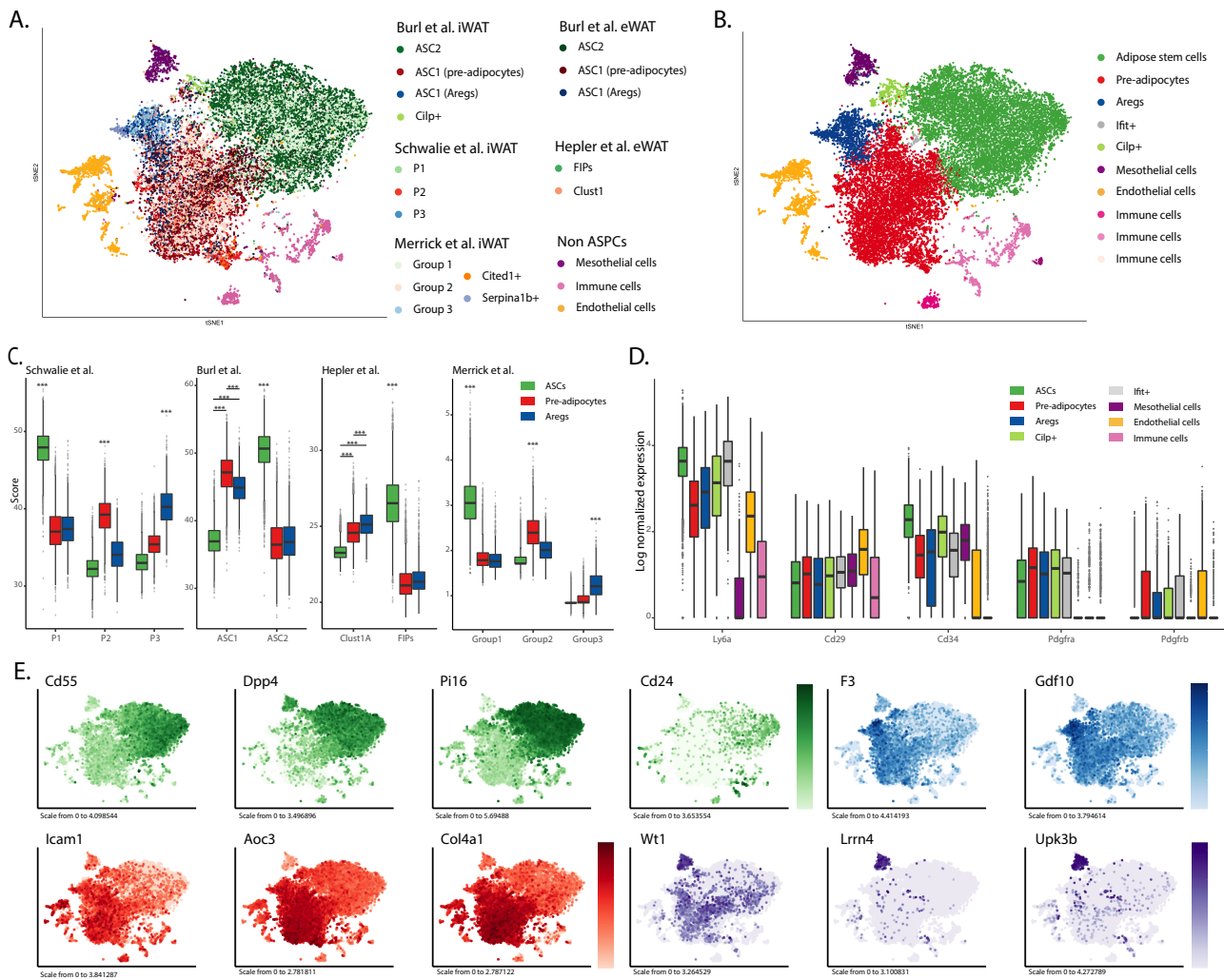


Figure 1.2 – Integrated scRNA-seq data of SVF isolated from eWAT and iWAT.

Publicly available scRNA-seq data of SVF that was isolated from eWAT (6645 cells) ^{100,101} and iWAT (17608 cells) ^{96,100,102} were integrated using the standard workflow of Seurat ^{103,104}.

- t-distributed stochastic neighbor embedding (tSNE) 2D cell map displaying the clustering of each dataset, analyzed individually.
- tSNE 2D cell map colored by cell cluster identification.
- Boxplot showing the distribution of scores of populations defined in different studies across cells. The score is calculated as the sum of scaled integrated expression of the top 100 DE genes of ASPC populations (Schwalie et al. ¹⁰², Burl et al. ¹⁰⁰ (aggregate Mouse eWAT and iWAT), Hepler et al. ¹⁰¹) or of a shorter list of specific markers (Merrick et al. ⁹⁶) since the DE genes were not publicly available (Group1: *Pi16*, *Dpp4*, *Dact2*, *Gpr1*, *Ptgs2*, *Bmp7*, *Wnt2*, *Stmn4*, *Wnt10b*; Group2: *Fabp4*, *Pparg*, *Icam1*, *Cd36*, *Dlk1*, *Gsc*, *Cyp1b1*; Group3: *F3*, *Fmo2*, *Clec11a*).
- Boxplot showing the distribution of log normalized expression of selected markers (Ly6a: Stem cell antigen 1 SCA1).
- tSNE colored by the log normalized expression of selected markers (Aoc3: VAP1; F3: CD142). The colors reflect population specificity (Green: ASCs, Red: PreAs, Blue: Aregs, Purple: Mesothelial cells).

1.5 The Adipose Stem Cell Population

1.5.1 ASCs in inguinal WAT

A first population of ASCs that was uncovered using scRNA-seq (P1 in ⁸⁷, Group1 in ⁶⁰, and ASC2 in ⁸⁸) was most stem-like in nature. This is why we propose to refer to this population as ASCs^{60,87,88} (**Fig. 1.2A-C**). Not only do ASCs express stem-related genes, such as *Ly6a*¹⁰⁵, *Dpp4*^{106–108}, *Cd55*^{109,110}, and Wnt signaling pathway inhibitor *Sfrp4*¹¹¹, but they also lack others (e.g., *F3*, encoding for CD142^{60,87,112,113}) (**Fig. 1.2D-E**), and are also highly proliferative *in vitro*⁶⁰. From a functional perspective, when ASCs [CD142–/DPP4+ (dipeptidyl peptidase 4)] are *in vitro* stimulated with insulin alone, they tend to be refractory to adipogenesis and barely express adipocyte-specific genes⁶⁰. However, when stimulated with a complete adipogenic cocktail (CAC), ASCs (CD142–/DPP4+⁶⁰ or SCA1+/CD55+⁸⁷) exhibit relatively high adipogenic potential, although its extent varied among studies^{60,87}. This suggests that ASCs require key factors to unlock their commitment and differentiation potential and/or that they give rise to distinct cell states with different adipogenic potentials. Thus, ASCs likely represent a pool of mesenchymal stem cells that commit to adipogenesis only when exposed to the right mix of factors (i.e., CAC). In addition, their conserved capacity to form osteoblasts and induce osteoblast-specific markers (*Alpl*, *Bsp*, *Osx*, and *Ocn*) underscores their multipotency⁶⁰.

Altogether, Lin–/SCA1+/CD55+ and Lin–/CD142–/DPP4+ cells, described in two different studies^{60,87}, represent two cell populations with similar molecular and functional properties that are indicative of a stem-like nature. So far, the molecular mechanisms underlying the stemness of ASCs remain poorly understood. However, the known antiadipogenic factor, transforming growth factor (TGF) β ^{70,114}, is able to regulate the identity and function of DPP4+ cells⁶⁰. In fact, treatment with TGF β increased the proliferative capacity of ASCs, inhibited adipocyte formation (even when using a CAC), and upregulated the expression of ASC-specific markers, whereas the inhibition of TGF β signaling had opposite effects. Noteworthy, neither TGF β agonists nor antagonists had any effect on other ASC subpopulations, underscoring the specificity of TGF β signaling to DPP4+ cells. The antiadipogenic Wnt signaling pathway⁷⁰ also appears to have a role in regulating neoadipogenesis. This is because cells tend to maintain their stem state when β -catenin levels exceed those of TCF7L2, whereas the inverse balance induces adipogenesis¹¹⁵. Collectively, these findings point to the involvement of multiple signaling pathways in ASC maintenance, but the exact underlying molecular mechanisms remain poorly understood, including to which extent these pathways crosstalk, what triggers them, and how they influence overall cell state.

In human, even if a first low resolution study reported “homogeneity” amongst hASPCs⁹⁷, it nevertheless showed, similar to mouse, that genes such as *CD55* and *THY1* were not uniformly expressed. Indeed, thereafter, it has been shown that one hASPC subpopulation expresses *DPP4*, *CD55* and *MFAP5* and

transcriptionally resembles mouse ASCs⁹⁶. In addition and again similar to mouse, human ASCs showed full adipogenic potential only when stimulated by a combination of several adipogenic triggers, as opposed to insulin alone⁹⁶. Interestingly, a mesenchymal stem population characterized by *THY1* expression has been described as responsible for adipogenic degeneration of the muscle in individuals suffering from type 2 diabetes¹¹⁶. If this population transcriptomically resembles hASCs remains to be robustly proven.

1.5.2 ASCs in epigonadal WAT

A population with molecular and functional properties similar to ASCs has been uncovered in the scRNA-seq data sets from mouse eWAT (called ASC2⁸⁸ and Clusters 1 and 5⁹⁰) (**Fig. 1.2B-E**, and **Fig. 1.3G-J**). Visceral ASCs (Lin[−]/SCA1⁺/CD55^{high} cells), for instance, showed higher proliferation and lower adipogenic differentiation capacity than the rest of visceral ASPCs⁹⁰. Furthermore, visceral ASCs (Lin[−]/CD142[−]/DPP4⁺ cells) exhibited lower adipogenic potential and responded to TGFβ treatment in a similar fashion as subcutaneous ASCs⁶⁰. Interestingly, the relative abundance of ASCs was lower in eWAT than in iWAT, suggesting that visceral WAT (visWAT) features a smaller early-stem cell pool⁶⁰.

From a mechanistic perspective, the PDGF pathway has a key role in adipose commitment and ASC pool maintenance and has been mostly studied in eWAT^{84,117,118}. PDGF receptors have been linked to stemness maintenance and need to be downregulated to initiate adipogenesis¹¹⁸. It has been suggested that all mature adipocytes in major fat depots derive from *Pdgfra*⁺ cells⁸³ and that the expression of PDGFRα precedes that of PDGFRβ¹¹⁹. It has also been reported that adipocytes emerge from PDGFRβ⁺ preadipocytes in response to a high-fat diet (HFD)⁸⁴. Based on our integration of scRNA-seq data sets, *Pdgfra* is virtually positive in all ASPCs, while *Pdgfrb* is only very lowly expressed by ASCs (compared with the rest of the ASPC pool) (**Fig. 1.2D**, **Fig. 1.3E,K**). These collective observations support the notion that ASCs are the ‘real’ ASCs that give rise to more committed progenitors, which in turn differentiate into adipocytes.

The implication of the PDGF pathway in stemness and adipogenesis prompted the community to specifically characterize the PDGFRβ⁺ progenitor pool using scRNA-seq (Hepler et al. 2018). A PDGFRβ⁺ population that shares many markers with ASCs was identified in such a way (Hepler et al. 2018) (**Fig. 1.3I**). Such cells were termed fibro inflammatory progenitors (FIPs) by the authors and were isolated as PDGFRβ⁺/LY6C⁺ cells. In line with previous observations in ASCs⁶⁰, analysis of the gene expression profile of FIPs revealed an active TGFβ signaling signature, and TGFβ treatment further upregulated FIP-specific markers, especially collagen (hence ‘Fibro’). At the same time, FIPs also exhibited a functional proinflammatory phenotype, expressing several cytokine genes, such as *Il6*, *Cxcl2*, and *Cxcl10*, and showing an ability to activate macrophages *in vitro* (hence ‘Inflammatory’). Finally, it was shown that FIPs are reluctant to undergo adipogenesis depending on

the culturing conditions, which supports the hypothesis that FIPs are similar to ASCs (Hepler et al. 2018). Nevertheless, the authors also revealed that FIPs exert antiadipogenic properties through a yet-to-be determined secreted factor. Thus, even if visceral FIPs share important markers with ASCs (**Fig. 1.2A,C**, and **Fig. 1.3I**), distinct phenotypic characteristics also appear to differentiate them from subcutaneous ASCs, making it difficult to establish a clear and definite analogy. Indeed, subcutaneous ASPCs cannot be stratified based on the markers that were used to sort FIPs since all subcutaneous PDGFR β ⁺ cells are also LY6C⁺. Therefore, FIPs currently constitute a rather mysterious cell population that may reflect an inherent ability of (visceral) ASCs to alter their own cell state and possibly function in response to specific immunological stimuli or physiological conditions

1.6 The Pre-adipocyte Population

1.6.1 PreAs in inguinal WAT

The second and most abundant ASPC population uncovered through scRNA-seq, which we define here as PreAs, features cells that are marked by the expression of *Icam1* and *Aoc3* and several collagen and extracellular matrix remodeling factors (**Fig. 1.2E**, and **Fig. 1.3F**). So far, no study has primarily focused on PreAs. However, the molecular signatures as well as initial, functional characterization all point to a more committed adipogenic state compared with ASCs: first, several genes involved in adipogenesis-related functions, such as *Pparg*, *Fabp4*, *Lpl*, *Plin2*, or *Cd36*, are significantly upregulated in this population (P2 in ⁸⁷, Group 2 in ⁶⁰, and ASC1 in ⁸⁸; **Fig. 1.2E**, and **Fig. 1.3F**); second, PreAs show lower proliferation compared with ASCs⁶⁰, while exhibiting a high adipogenic capacity^{60,87}, even when stimulated by insulin only, as opposed to ASCs. Taken together, Lin[−]/CD142[−]/ICAM1⁺ (intercellular adhesion molecule 1) cells⁶⁰ and Lin[−]/SCA1⁺/VAP1⁺ (vascular adhesion protein 1) cells⁸⁷ appear to constitute similar cell populations that are in a committed adipogenic state. From a mechanistic perspective, PreAs are also the most refractory to the antiadipogenic effect of TGF β ⁶⁰, which further supports the hypothesis that they are lineage-committed ASPCs.

In humans, a population resembling mouse PreAs, defined, among others, by the expression of *ICAM1*, *PPARG* and *GGT5*, was equally identified⁹⁶. Human PreAs seem to behave like mouse PreAs *in vitro*⁹⁶.

1.6.2 PreAs in epigonadal WAT

Burl et al.⁸⁸ identified a population (ASC1) in both visceral and subcutaneous depots that resembles the PreA population (**Fig. 1.2B-E**, and **Fig. 1.3G-J**). In our analysis of this published data set, the fraction identified as ASC1 shares top markers with both PreAs and Aregs (CD142⁺) and could consequently further be stratified (**Fig. 1.2C**, and **Fig. 1.3C,I**). Although the latter study⁸⁸ was largely computational, a parallel study⁹⁸ uncovered

a population defined by Lin[−]/PDGFRβ⁺/LY6C[−]/CD9[−] that, according to our data integration analyses, projects partially to PreAs (and to Aregs) (**Fig. 1.2A,C**, and **Fig. 1.3G,H**). Sorted Lin[−]/PDGFRβ⁺/LY6C[−]/CD9[−] cells exhibited a higher adipogenic potential compared with the Lin[−]/PDGFRβ⁺ total population, in line with the behavior of subcutaneous PreAs. Thus, it is likely that the authors analyzed a subset of PDGFRβ⁺ PreAs that were isolated from visWAT. Another independent study⁹⁰ also revealed a higher adipogenic propensity in three clusters (Clusters 2, 4, and 6) that also project partially to PreAs and Aregs (integration by ⁹⁰).

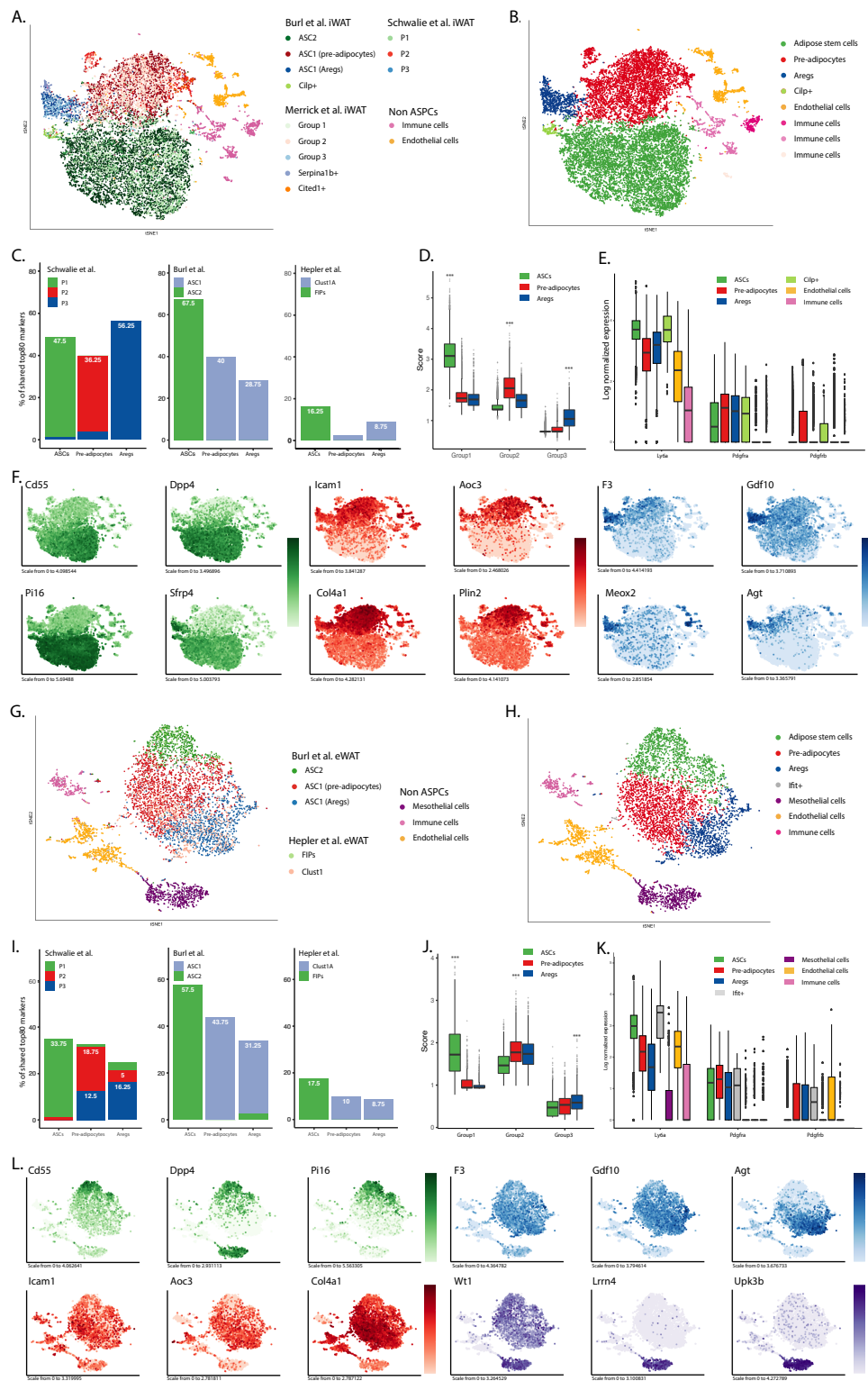


Figure 1.3 – Integrated scRNA-seq data of SVF isolated from iWAT or from eWAT.

Publicly available scRNA-seq data of SVF isolated from iWAT (17608 cells)^{96,100,102} (**panel A-F**) or eWAT (6645 cells)^{100,101} (**panel G-L**) were integrated using the standard workflow of Seurat^{103,104}.

- A. tSNE 2D cell map displaying the clustering of each dataset from iWAT, analyzed individually.
- B. tSNE 2D cell map from iWAT colored by cell cluster identification.
- C. Percentage of the top 100 population markers that overlap with the top 100 population markers of published studies: Schwalie *et al.* (iWAT) ¹⁰², Burl *et al.* ¹⁰⁰ (aggregate Mouse eWAT and iWAT), Hepler *et al.* ¹⁰¹ (eWAT, PDGFRβ+).
- D. Boxplot showing the distribution of scores across cells for the Group1, Group2 and Group3 defined in Merrick *et al.* ⁹⁶. The score is defined as the sum of the scaled integrated expression of a list of specific markers discussed in Merrick *et al.* ⁹⁶ (Group1: *Pi16*, *Dpp4*, *Dact2*, *Gpr1*, *Ptgs2*, *Bmp7*, *Wnt2*, *Stmn4*, *Wnt10b*; Group2: *Fabp4*, *Pparg*, *Icam1*, *Cd36*, *Dlk1*, *Gsc*, *Cyp1b1*; Group3: *F3*, *Fmo2*, *Clec11a*).
- E. Boxplot showing the distribution of log normalized expression of selected markers (*Ly6a*: Stem cell antigen 1 SCA1)
- F. tSNE colored by the log normalized expression of selected markers. (*Aoc3*: VAP1; *F3*: CD142). The colors reflect population specificity (Green: ASCs, Red: PreAs, Blue: Aregs, Purple: Mesothelial cells).
- G. tSNE 2D cell map displaying the clustering of each dataset from eWAT, analyzed individually.
- H. tSNE 2D cell map from eWAT colored by cell cluster identification.
- I. Percentage of the top 100 population markers that overlap with the top 100 population markers of published studies: Burl *et al.* ¹⁰⁰ (eWAT), Hepler *et al.* ¹⁰¹.
- J. Boxplot showing the distribution of scores across cells for the Group1, Group2 and Group3 defined in Merrick *et al.* ⁹⁶. The score is defined as the sum of the scaled integrated expression of a list of specific markers discussed in Merrick *et al.* ⁹⁶ (Group1: *Pi16*, *Dpp4*, *Dact2*, *Gpr1*, *Ptgs2*, *Bmp7*, *Wnt2*, *Stmn4*, *Wnt10b*; Group2: *Fabp4*, *Pparg*, *Icam1*, *Cd36*, *Dlk1*, *Gsc*, *Cyp1b1*; Group3: *F3*, *Fmo2*, *Clec11a*).
- K. Boxplot showing the distribution of log normalized expression of selected markers (*Ly6a*: Stem cell antigen 1 SCA1)
- L. tSNE colored by the log normalized expression of selected markers. (*Aoc3*: VAP1; *F3*: CD142). The colors reflect population specificity (Green: ASCs, Red: PreAs, Blue: Aregs, Purple: Mesothelial cells).

1.7 The Adipogenesis Regulators Population

1.7.1 Aregs in iWAT

A third population, closer in terms of gene expression to PreAs than to ASCs and defined by the expression of *F3* (encoding CD142) (**Fig. 1.2C,E**), was first identified within iWAT of adult mice⁸⁷. Functionally, these cells were not only refractory to adipogenesis *in vitro*, but also had the capacity to inhibit the adipogenic differentiation of the remaining ASCs, both *in vitro* and *in vivo*. Therefore, these cells were termed Aregs by the authors (**Fig. 1.3F**).

Given their distinctive transcriptomic clustering pattern, a second study also focused on CD142+ cells⁶⁰, but, contrary to the first⁸⁷, found CD142+ cells to be fully adipogenic. While there were clear methodological and mouse model differences, the exact reason why CD142+ ASCs behaved differently between the two studies has yet to be resolved. Nevertheless, the overall consensus is that CD142+ ASCs constitute a distinct population of cells featuring a transcriptomic signature that is clearly different from that of ASCs and PreAs (**Fig. 1.2B,C**, and **Fig. 1.3C,F**).

Going beyond adipose tissue, Areg-like cells have been recently identified in muscle¹²⁰, exhibiting molecular and functional (e.g., antiadipogenic) properties that are in line with those reported for subcutaneous Aregs⁸⁷. The authors proposed a mechanistic model that involves the secreted factor GDF10 as one of the main factors responsible for the inhibitory capacity of CD142+ cells, both in mouse and human. Interestingly, dystrophic mice were found to harbor fewer ‘muscle Aregs’ than their wild-type (WT) counterparts, raising the hypothesis that this change in cellular composition explains the increased accumulation of fat cells in dystrophic muscle¹²⁰.

1.7.2 Aregs in Visceral WAT

No scRNA-seq study of visWAT has so far specifically explored the existence of Aregs and, even though they both appear to display an antiadipogenic phenotype, FIPs and Aregs are clearly molecularly distinct (**Fig. 1.2C**)⁸⁹. Even though a higher fraction of CD142+ cells in eWAT compared with iWAT has been reported using flow cytometry⁸⁷, to date, no one has ever sorted and characterized visceral Aregs fully. However, a recent study described an ASC population (Lin[−]/Sca1⁺/PDGFRA⁺/PDPN⁺/THY1⁺/CD55[−] cells) that was transcriptomically similar to Aregs and that exhibited a low adipogenic propensity, even though it was not sorted using the CD142 surface marker itself⁹⁹. In line with this, our integration results revealed a population that express Areg-like markers in eWAT (**Fig. 1.3H,I**). Surprisingly, even though *F3* remains a differentially expressed (DE) gene, it appears not to be the best marker for this population because it lacks specificity (**Fig.**

1.3F versus Fig. 1.3L). Such a broad, diffuse expression pattern could explain the higher CD142+ fraction observed in flow cytometry in visWAT⁸⁷ without necessarily implying a higher proportion of actual Aregs. Nonetheless, using the relative fraction inferred from scRNA-seq data, and keeping in mind possible biases due to cell selection, the proportion of Areg-like marker-expressing cells in the visceral data set remains substantially higher than in the subcutaneous one (23.5% versus 7% when considering only ASPCs). A higher fraction of ASPCs featuring an antiadipogenic character, potentially comprising both ‘visceral Aregs’ and FIPs, would be consistent with the low adipogenic potential of total visceral ASPCs compared with their subcutaneous counterparts, a well-established notion in the field^{121,122}. These observations highlight once again not only the intrinsic similarities, but also differences between the different fat depots, and clearly emphasize the need to better functionalize all ASPC fractions.

And what about Aregs in humans? Markers of mouse Aregs (CD142, CLEC11A and FMO2) appeared broadly expressed across the two main human subpopulations: ASCs and PreAs⁹⁶. We conclude therefore that either orthologous human Aregs do not exist or may not be defined by this set of markers at the transcriptomic level. In accordance, no functional differences were found between sorted human CD142+ and ICAM1+ ASPCs⁹⁶. Nevertheless, when human CD142+ cells were sorted and compared to the corresponding CD142- and Lin- fractions, the same non-adipogenic character observed for mouse Aregs was seen for human CD142+ ASPCs¹⁰². This underscores the general interest in providing a more in-depth molecular and functional characterization of human CD142+ cells.

1.8 Hierarchy of ASPCs

As implied by the names given to the different ASPC subpopulations in this introduction (ASCs, PreAs and Aregs), we propose a hierarchy between ASPCs (see arrows in **Fig. 1.4**). First of all, the expression pattern of *Pdgfra* and *Pdgfrb*, as already detailed above, indicates that the ASCs are the most stem-cell like ASPCs. The higher expression of *Cd24* in ASCs further supports this hypothesis (**Fig. 1.2 E**). Indeed, it has been proposed that CD24+ adipocyte precursors are stem cell-like ASPCs that become further committed by losing CD24 expression¹²³. Recently, this hierarchy has also been suggested *in silico* by applying a pseudotemporal trajectory analysis on scRNA-seq datasets^{96,124}, after which it was validated *in vivo* using fluorescence-based cell tracing⁹⁶. Specifically, when fluorescently-labelled subcutaneous ASCs (DPP4+ cells) were transplanted in a wild type subcutaneous fat pad, these cells acquired PreAs and Aregs markers (ICAM1 and CD142 respectively) within 7 days post-transplantation and a subset of them lost DPP4 expression after 14 days⁹⁶. These findings indicate that ASCs (DPP4+) give rise to both preAs (ICAM1+) and Aregs (CD142+). In contrast, fluorescently-labeled preAs (ICAM1+) and Aregs (CD142+) did not acquire DPP4 expression over time⁹⁶, underscoring the overall unidirectionality of ASC commitment and differentiation. However, PreAs and Aregs may

undergo immunophenotypic interconversion since a subset of mTomato-labeled ICAM1+ and CD142+ cells acquired to a certain extent CD142 and ICAM1 markers respectively⁹⁶. How this interconversion is molecularly encoded, what determines the hierarchical equilibrium, and how different metabolic conditions affect this equilibrium, are important, yet outstanding questions (see section “The ASPCs and Obesity”).

1.9 Mesothelial cells

Mesothelial cells constitute the peritoneum both in mouse and human and belong exclusively to the visceral SVF. Not only do they line the walls of the abdominal cavity, but they are also found in small clusters within the visceral WAT itself, in the form of so-called ‘milky spot’ or ‘fat-associated lymphoid clusters’^{125,126}. *Msln*, *Wt1*, *Lrrn4*, and *Upk3b* are typical mesothelial markers and, *in vitro*, such cells display a characteristic epithelial/cobblestone morphology^{127–129}. Not surprisingly, mesothelial cells were found among visceral ASPCs using scRNA-seq (in mouse^{80,88,95,98}, in human^{59,60,94}) (**Fig. 1.2A, B, E**, and **Fig. 1.3G, H, I**). Thus, one should be aware that, for both human and mouse, cells of the mesothelial lineage exist within the visceral SVF and may cloud functional read-outs. Therefore, we argue that it may be best to sort these cells out before any downstream *in vitro* characterization of ASPCs.

However, what is interesting about mesothelial cells in the context of adipose biology, besides being a heterogeneous population themselves^{80,94,130}, is their role at the crossroads between adipose tissue function and immunity as well as them being hotpots for cancer metastasis^{126,131,132}. When peritonitis occurs, they recruit neutrophils for peritoneal fluid clearance⁸⁰, whereas in physiological conditions, they support the interleukin (IL)-33 driven recruitment and differentiation of type 2 innate lymphoid cells (ILC2s)^{99,133,134}. ILC2 cells secrete type 2 immunomodulatory cytokines¹³⁰, which, together with regulatory T cells and eosinophils, enable the visceral cavity and adipose tissue to remain in a normal, uninfamed state, countering the development of type 2 diabetes¹³⁵. In turn, loss of IL-33 results in weight gain, although the underlying mechanisms, as well as implications of ASPCs in this process remain poorly understood¹³³.

In human, less is known about the interplay between mesothelial, immune, and stromal cells. However, it has been proposed that subclusters of mesothelial cells are implicated in beige adipogenesis based in the fact that these subclusters express a higher proportion of mitochondrial genes than any other ASPC subpopulation and that their relative cell number negatively correlated with glucose fasting levels⁹⁴. Moreover, the beige adipocyte markers *PLA2G2A*¹³⁶ and *SOD2*¹³⁷ were enriched among mesothelial subclusters, but not *MYF5* and *ZIC1*, two brown adipocyte precursors cell markers¹³⁷, providing additional support for the involvement of these human mesothelial cells in beige adipogenesis.

1.10 ASCs and obesity

1.10.1 ASCs and obesity

We currently have a poor understanding of ASC dynamics in obesity, and we know even less about the implication of each subpopulation¹³⁸. Nevertheless, scRNA-seq was performed, for example, on eWAT from both lean and diet-induced obese mice¹³⁹, revealing that obesity redistributes the prevalence of individual ASC subpopulations. In addition, obesity specifically enriches for subgroups of ASCs that exhibit enhanced extracellular matrix and immunomodulatory capacities as well as altered differentiation abilities¹³⁹. In line with this, the frequency of FIPs increased when mice were fed a HFD¹⁰¹, while the DPP4+ stem fraction decreased⁹⁶. Together, these findings suggest that ASCs may play an important immunomodulatory role in WAT, consistent with previous observations¹⁴⁰, and that a diet-induced ASC imbalance toward a FIP-like phenotype may be one of the factors underlying obesity-induced adipose inflammation.

1.10.2 PreAs and obesity

One hypothesis is that intrinsic properties of ASCs could explain the distinct impact of differential anatomical fat deposition during obesity on the development of metabolic disease (reviewed in¹³⁸). In line, subcutaneous ICAM1+ cells have a comparably high adipogenic capacity regardless of whether they are isolated from obese or lean mice, while visceral ICAM1+ cells exhibited a lower adipogenic potential when retrieved from obese mice compared to lean⁹⁶. This observation may explain why hypertrophic WAT expansion is favored over hyperplasia in the abdomen.

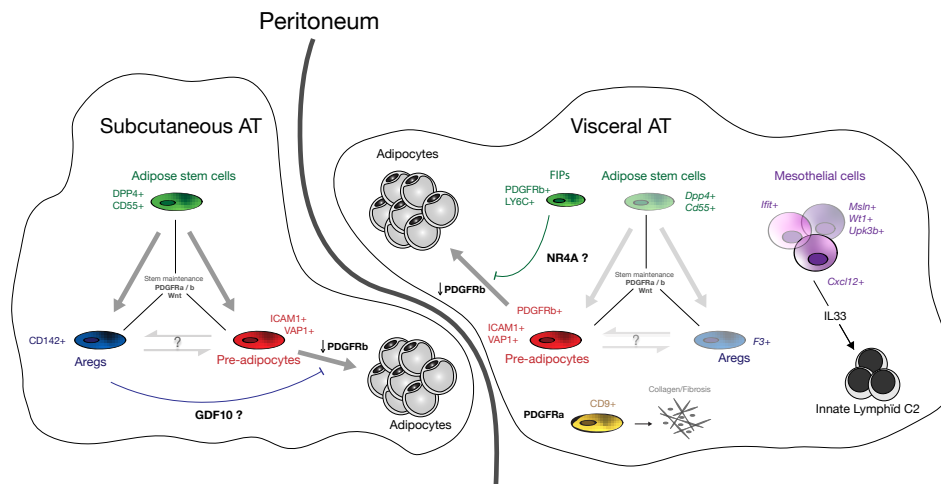
Interestingly, a relative increase in the proportion of human PreAs seems to correlate with insulin resistance and type two diabetes based on a large scRNA-seq dataset from 25 obese patients⁶¹. To our knowledge, this is the first time that a correlation has been found between a metabolic disease phenotype and differential ASC composition in human. Whether this correlation, based on scRNA-seq cell proportions only, reflects causality remains to be established.

1.10.3 Aregs and obesity

The fact that WAT may harbor ASCs such as Aregs or FIPs that could negatively modulate adipocyte formation has triggered a paradigm shift in our understanding of how adipose tissue plasticity could be mediated, pointing to potential novel therapeutic applications. For example, a reduction in adipogenesis-suppressing cells may be one of the mechanisms that lead to fat cell hyperplasia. Inversely, their increase may lead to fat cell hypertrophy due to a suppression of adipocyte formation. Interestingly, it has been proposed that a depletion of ASCs may be responsible for the switch from hyperplasia to hypertrophy in the context of overfeeding^{141,142}. The fact that the abundance of CD142+ cells varies across depots and physiological state

would support this possible shift^{96,102}. Indeed, while the increase of CD142+ cells in obese mice may at first glance seem counterintuitive given their possible anti-adipogenic phenotype, it may instead reflect a defensive strategy aimed at limiting adipose tissue (hyper)expansion. The main drawback of such a mechanism would be a balance favoring hypertrophy over hyperplasia upon excessive weight gain.

A. Mouse



B. Human

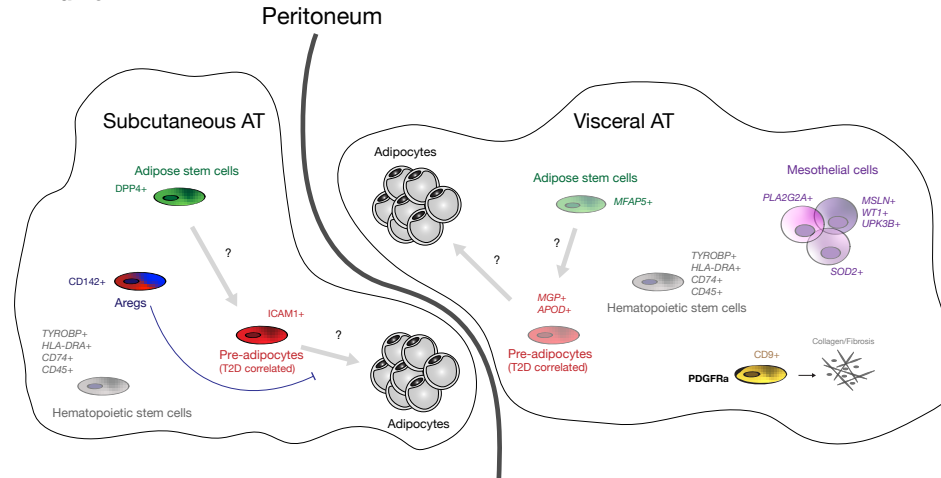


Figure 1.4 – Adipose derived stem and progenitor cells: toward a consensus view.

- A.** Mouse white adipose tissue (WAT)^{96,100–102,139,143}: ASCs give rise to PreAs and Aregs. Aregs exert an inhibitory effect on adipogenesis. Such effect may in part be mediated by GDF10 based on Areg-like cells found in muscle¹²⁰. FIPs, CD9+ and mesothelial cells are exclusively present in visceral WAT. FIPs also exert an inhibitory action on adipogenesis. Mesothelial cells bridge ASCs and immunoregulation. CD9+ cells are profibrotic¹⁴⁴.
- B.** Human WAT^{61,96}: hASCs supposedly give rise to hPreA-like cells. CD9+ cells are profibrotic and, similar to mesothelial cells, exclusively present in visceral WAT. Hematopoietic stem cells are found in human SVF and are marked by CD45⁶¹.

Shadowed sections are based on (sc)RNA-seq analyses only, plain colors mean FACS isolation and characterization.

1.11 The scope of this thesis

This work attempts to redefine in an unbiased and cross-anatomical fashion the cellular composition of human adipose-derived stem and progenitor cells (hASPCs), a cellular compartment within the stroma of adipose tissue responsible for its renewal. We took advantage of cutting-edge single-cell RNA sequencing (scRNA-seq) techniques to identify cells that have common characteristics based on their RNA expression. I then characterized them molecularly and phenotypically with the ultimate goal of understanding why *in vitro* hASPCs isolated from intra-peritoneal depots are strikingly less adipogenic than the ones isolated from extra-peritoneal adipose depots.

At first, I performed scRNA-seq experiments on the non-endothelial, non-immune stromal vascular fraction (SVF) of the adipose tissue from four distinct anatomic origins: subcutaneous, omental, perirenal and mesocolic adipose tissues. This allowed to perform thorough bioinformatics analysis to identify new subpopulation and put them in the context of what was previously described in the literature about human and mouse ASPCs. I then identified surface proteins against which I designed and validated a sorting strategy that allowed to study each subpopulation separately with regard to their relative abundance in the SVF, adipogenic potential and proliferation ability in a systematic way across all adipose depots. Whenever possible I tried to link donor's metadata including age, sex and BMIs to my findings.

At last, I explored the role of omentum-specific mesothelial cells in the context of adipogenesis. I demonstrated that mesothelial cells within the SVF of omental adipose tissue secrete inhibitory cues which are at least partially responsible for the observed low-adipogenic phenotype of intraperitoneal-derived SVF-adherent cells. I further proposed that the observed inhibition signaling originates specifically from mesothelial cells and relies on the IGFBP2 secreted protein which acts through an IGF-independent mechanism. Interfering with this signaling resulted in enhanced adipogenesis by the omentum.

Chapter 2 | A human omentum-specific mesothelial-like stromal population inhibits adipogenesis through IGFBP2 secretion

Note: This chapter is based on a manuscript under submission “A human omentum-specific mesothelial-like stromal population inhibits adipogenesis through IGFBP2 secretion”

Authors: Radiana Ferrero*, Pernille Yde Rainer*, Julie Russeil, Magda Zachara, Joern Pezoldt, Guido van Mierlo, Vincent Gardeux, Wouter Saelens, Daniel Alpern, Lucie Favre, Styliani Mantziari, Tobias Zingg, Nelly Pitteloud, Michel Suter, Maurice Matter, Carles Canto, and Bart Deplancke.

* These authors contributed equally

My contribution: Conceptualized the study and wrote the manuscript. Conducted all experimental procedures and analyzed acquired images, flow cytometric measures, qPCRs, ELISAs and immunohistochemistry.

2.1 Abstract

Adipose tissue (AT) is a key metabolically dynamic organ that tends to have distinct functions dependent on its anatomical location. For example, subcutaneous (SC) AT tends to be more adipogenic compared to visceral AT whose expansion carries a greater risk for obesity-related co-morbidities. While significant progress has been made in mice to understand which cells mediate AT plasticity and how these are distributed across distinct adipose depots, a similar level of understanding is still lacking in humans.

Here, we probed the differentiation capacity of human Adipose-derived Stem and Progenitor cells (hASPCs, defined as Stromal Vascular Fraction (SVF) Lineage (Lin)-negative cells) from four adipose depots (SC, perirenal (PR), omental (OM), and mesocolic (MC)), revealing striking differences in their adipogenic potential. To explore the molecular and cellular origins of these differences, we performed bulk RNA-seq of 20 SC, 8 PR, 19 OM, and 4 MC primary ASPC samples and scRNA-seq of ~34'000 cells from these four depots, followed by functional characterization of the identified cell subpopulations.

On the one hand, these analyses revealed at least two major, ubiquitous hASPC subpopulations, adipose stem cells and pre-adipocytes, with distinct proliferative and adipogenic properties and whose proportions differed in function of adipose depot type and BMI. Moreover, despite their omnipresence, these subpopulations still exhibited depot-specific gene expression patterns, likely reflecting distinct AT properties. On the other, we identified an OM-specific, mesothelial-like stromal population that is defined by high expression of *IGFBP2*, constitutes 2-5% of the OM SVF Lin⁻ fraction depending on the donor's BMI, appears to transition between mesothelial and mesenchymal cell states, and inhibits the adipogenic capacity of hASPCs in a depot-specific manner through IGFBP2 secretion.

Altogether, our in-depth characterization of hASPC heterogeneity and function not only highlights the cellular uniqueness of different adipose niches, it also identifies a new mechanism underlying the limited adipogenic capacity of OM hASPCs by uncovering an OM-specific *IGFBP2*⁺ mesothelial-like cell population that negatively regulates hASPC adipogenesis through IGFBP2 signaling.

Keywords: obesity, adipogenesis, human, adipose stem and progenitor cells, mesothelial cells, mesothelial to mesenchymal transition, anti-adipogenic, omentum, IGFBP2, TM4SF1, MSLN, scRNA-seq

2.2 Introduction

Our understanding of key adipose tissue (AT) phenotypes, such as turnover and expansion dynamics in health and in response to altering metabolic conditions, is still limited, especially when it comes to human AT. This is further exacerbated by the fact that these AT phenotypes vary according to the anatomical location of the respective AT with for example the frequent opposition of the “metabolically healthy” subcutaneous (SC) AT to the “unhealthy” visceral one when overgrown. However, the terms “visceral” and “subcutaneous” underlie several finer anatomic locations and, with it, potentially more fine-grained AT characteristics⁷⁹. For instance, among visceral AT is the perirenal (PR) AT, which locates around the kidney and is attracting increasing attention as being a potential site of dormant brown adipogenesis^{71,72}. Its possible crosstalk with the kidney itself influences renal function and constitutes an independent risk factor for cardiovascular and chronic kidney disease⁷¹. Even if PR AT can be considered as a visceral tissue, it is not confined within a mesothelial layer, contrary to for example the mesenteric (MC) and omental (OM) ATs. The latter tends to be considered the “golden standard” visceral adipose depot and is typically linked to type 2 diabetes onset, cardiometabolic complications, and an overall proinflammatory status^{11,77}. The MC AT, a fold connecting the intestine to the abdominal wall, contributes to buffering the intestinal intake, both as an immune barrier and a lipidic reservoir to prevent lipid hepatotoxicity⁷⁶. It serves as a scaffold to the mesenteric vasculature that nourishes the small and large intestines and, based on its anatomy, can further be stratified in the mesentery and the mesocolon, depending on whether it binds the small or large intestine, respectively.

While it is thus well-accepted that human ATs from distinct anatomical locations are linked to different metabolic risks when overgrown, little is known about what causes these phenotypic differences. One attractive hypothesis is that these differences could at least be partially driven by variation in the cellular composition of the stromal vascular fraction (SVF) across depots and specifically in that of the adipose-derived stem and progenitor cell (ASPC) pool. This hypothesis is supported by i) a recently published comprehensive single cell transcriptomic (scRNA-seq) atlas of whole human AT, as well as previously published studies, revealing the existence of several subpopulations amongst human ASPCs (hASPCs)^{61,96,145}. However, these scRNA-seq studies focused on the two most commonly studied ATs: subcutaneous and omentum. Hence, a more overarching view on similarities and/or differences in hASPC composition beyond the SC and OM depots remains elusive. ii) While still scarce in humans, substantial evidence is mounting that in mice, ASPCs are also highly heterogeneous with the detection of at least three major ASPC subpopulations^{91,96,100,102,143,145–149}. Moreover, extensive downstream validation suggests that these subpopulations exhibit different functional properties with the *Dpp4+* (or *Ly6c+*) cells being labeled as stem cells, the *Icam1+* (or *Aoc3+*) ones as pre-adipocytes and the *F3+* cells as adipogenesis-regulatory cells^{91,96,100,102,143,145–149}. A similar level of phenotypic characterization of hASPC populations is still lacking, likely reflecting the challenge of having access to and/or gathering enough human material to do so. Nevertheless, in one study, efforts were undertaken to functionally characterize

hASPC subpopulations that were similar to the ones found in mice, with the DPP4+ ASCs being highly proliferative and less adipogenic than the ICAM1+ ASCs⁹⁶. Together, these findings suggest that, similar to mouse, hASPCs may not only be highly heterogeneous but also functionally distinct. Yet, to date, no systematic, functional characterization of hASPC heterogeneity and behavior has been performed across several human adipose depots.

Here, we provide a comprehensive overview of gene expression profiles of SVF-adherent cells over 30 human donors in four major human depots: SC, PR, OM, and MC AT, supplemented with scRNA-seq data on ~34,000 non-immune (CD45–) and non-endothelial (CD31–) SVF cells (SVF/Lin–). We consistently detected two main hASPC subpopulations that are common to all depots and addressed similarities but also differences across these depots, as well as in comparison to the most commonly studied mouse ATs. Specifically, we found that pro-adipogenic/developmental genes are enriched in SC, non-adipogenic/inflammatory ones in OM, mitochondrial/thermogenic ones in PR, and protein folding/trafficking in MC. We isolated, quantified, and characterized different cellular subpopulations in SC, OM, and PR depots with regard to their adipogenic potential and proliferation abilities, validating two surface markers, CD26 and VAP-1, that enable the enrichment of highly proliferative and highly adipogenic cells, respectively, across all depots. Finally, we focused on resolving the mechanism underlying the lower adipogenic potential of OM-isolated SVF-adherent cells, compared to SC and PR ones. We identified a new and omentum-specific cell population that is susceptible to undergoing mesothelial-to-mesenchymal transition and negatively impacts the adipogenic potential of OM and SC hASPCs. We further linked the observed adipogenic inhibition to the secretion of IGFBP2, which potentially acts through the $\alpha 5\beta 1$ integrin receptor.

2.3 Results

2.3.1 Human SVF precursor cells exhibit depot-dependent differences in their *in vitro* adipogenic potential

To characterize the function of SVF-adherent cells, including hASPCs, across distinct human adipose depots, we differentiated cell lines from SC (20 donors), PR (8 donors), OM (19 donors), and MC (4 donors) AT (**Table 2.1**). As no consensus exists on the surface markers defining hASPCs and to not bias our strategy towards a potential ASPC (sub)population, we did not implement any enrichment strategy beyond plating SVF cells and culturing SVF-adherent cells, as is commonly done in the field. Once confluent, these distinct AT-derived primary cell lines were exposed to an adipogenic cocktail for 14 days (**Fig. 2.1A**, see **Materials and Methods**). Subsequent staining for lipid droplets revealed that only SVF-adherent cells that were isolated from white AT (WAT) situated outside the peritoneal cavity (i.e., SC and PR) are able to form mature adipocytes that are characterized by the effective accumulation of lipid droplets *in vitro* (**Fig. 2.1B-C**, **Supp. Fig. 2.1.1A**). Conversely, cells that were isolated from intraperitoneal depots (i.e., OM and MC) barely formed any lipid

droplets under adipogenic differentiation conditions, or at most, tiny droplets that were difficult to distinguish from a background stain (**Fig. 2.1B-C**, **Supp. Fig. 2.1.1B-C**, see **Materials and Methods**). Interestingly, while both SC and PR hASPCs differentiated to a higher extent than intraperitoneal cells, PR lines showed the highest adipogenic potential *in vitro*, particularly when cells were differentiated straight after isolation (**Fig. 2.1B-C**, **Supp. Fig. 2.1.1A**). However, at longer times/passages, PR lines tended to become as adipogenic as SC ones (**Supp. Fig. 2.1.2** and **2.1.3A-B**). Furthermore, SC and PR lines showed high inter-individual variation in their ability to differentiate, which is observable as an adipogenic potential gradient for SC lines and a dichotomy for PR lines, as illustrated by very high *versus* very low adipogenic potential (**Supp. Fig. 2.1.3A**). In contrast, OM and MC lines were systematically resistant to adipogenic differentiation (**Supp. Fig. 2.1.2**), while also being the slowest growing lines (**Supp. Fig. 2.1.1D**).

We explored possible correlations between our experimental adiposcore (**Supp. Fig. 2.1.2B**) and physiological parameters such as BMI, age, and gender of the donors but found no correlations except for a tendency for PR cells to become less adipogenic in women and elderly people (**Supp. Fig. 2.1.3C-F**). However, we acknowledge that our cohort's demographic characteristics can bias these observations (**Table 2.1** and **Table 2.2**), i.e., included patients are mainly young and obese, while we also analyzed only a relatively small proportion of PR samples (n=8).

2.3.2 Human SVF-adherent cells exhibit transcriptomic differences that reflect their anatomical origin and adipogenic potential

To explore if the striking phenotypic difference between intra-peritoneal and extra-peritoneal cell lines is reflected in their respective transcriptomes, we set out to perform bulk RNA barcoding and sequencing (BRB-seq)¹⁵⁰ of SVF-adherent primary cell lines from different individuals and depots both at the undifferentiated/expanding state (t0) and after 14 days of adipogenic differentiation (t14) (SC n=22, OM n=16, PR n=8, MC n=4, **Supp. Fig. 2.1.4A**). We found that the major source of variation is explained by the exposure to the adipogenic cocktail, followed by the anatomic origin of the cell lines (**Fig. 2.1D**, **Supp. Fig. 2.1.4B-F**). We observed that all samples at t0 highly express *THY1*, a well-known mesenchymal marker¹⁵¹, at similar levels, except OM samples in which it is slightly but significantly lower expressed (**Supp. Fig. 2.1.4G**). Upon exposure to a differentiation cocktail, cells from all depots induced genes related to extracellular remodeling, insulin response, and positive regulation of fat cell differentiation compared to their undifferentiated state. However, most of these adipogenic-related terms were more enriched in SC and PR compared to OM and MC (**Fig. 2.1E-F**, **Supp. Fig. 2.1.4H-I**). In addition, golden standard markers of adipogenesis and mature adipocytes such as *FABP4*, *PPARG*, *CEBPA*, *ADIPOQ*, *PLIN1-2-4*, *LPL*, and others (see **Methods**) were solely upregulated in PR and SC samples post-differentiation (**Supp. Fig. 2.1.4J**). The expression of the latter correlated with the lipid droplet accumulation of the corresponding lines as quantified by the image-based adiposcore ($\rho=0.81$,

Fig. 2.1G, Supp. Fig. 2.1.2, see Materials and Methods), showing that inter-individual variability in terms of adipogenicity is also reflected at the transcriptomic level. Overall, even if the differentiation medium induced an adipogenic response in OM and MC hASPCs, it did not activate key regulators leading to overt lipid accumulation under the form of lipid droplets as, for example, supported by the enrichment of the “lipid storage” term solely in PR and SC-derived cells (**Fig. 2.1E**).

Next to their clear molecular and phenotypic dissimilarities in adipogenic response, we further investigated potential transcriptomic differences between SVF-adherent cells from different depots, which could underlie their distinct adipogenic potential. As previously reported, developmental genes such as *HOXC8-10*, *HOXA9*, and *HOXD8* were highly expressed in SC samples (**Fig. 2.1H**)^{78,152}, as further illustrated by the enrichment of numerous terms linked to morphogenesis and development compared to the other depots both at t0 and t14 (**Fig. 2.1H, Supp. 1.5**). Interestingly, at t14, SC samples also showed enrichment of cell differentiation-related terms compared to the other depots, even considering the highly adipogenic PR samples (**Fig. 2.1I**). In contrast, PR-enriched genes in differentiated hASPCs were related to thermogenesis, suggesting that these cells have brown-like or beige-like adipocyte characteristics (**Fig. 2.1I**)^{153,154}. In OM samples, we observed a non-adipogenic gene expression signature with positive and negative enrichment of the terms “negative regulation of differentiation” and “white fat cell differentiation” respectively, compared to differentiation medium-exposed SVF-adherent cells from the other adipose depots (**Fig. 2.1I**). Undifferentiated OM SVF-adherent cells also exhibited significantly higher expression of genes linked to an inflammatory response, which remained after exposure to an adipogenic cocktail (**Fig. 2.1I, Supp. Fig. 2.1.5A, Supp. Fig. 2.1.6A**). This is not entirely unexpected given that the OM samples that were analyzed using BRB-seq mainly originated from obese patients undergoing bariatric surgery (**Supp. Fig. 2.1.4A, Table 2.1**), whose OM fat has previously been reported to show signs of inflammation^{79,155–157}. Interestingly, in both t0 and t14 time points, OM cells showed an enrichment of expressed genes linked to the vasculature and epithelium/endothelium development (**Fig. 2.1I, Supp. Fig. 2.1.6B**). This is consistent with our observation that many Keratin-related genes such as *KRT8*, *KRT9*, *KRT18*, and also *LRRN4* or *UPK1B* (**Fig. 2.1H, Supp. Fig. 2.1.5B**) were among the top differentially expressed genes in OM cells *versus* those from other depots. The latter may be reflective of a mesothelial cell signature¹⁵⁸, suggesting that the SVF-adherent cell pool of OM is composed of various cell types, other than hASPCs. Finally, genes that were specifically expressed in MC compared to other depots were linked to protein metabolism and trafficking (**Fig. 2.1I**).

Taken together, we found that each depot features specific gene signatures that can be linked to functional implications, highlighting the regional specialization of AT based on its anatomical location. In addition, the observed experimental adipogenic potential is mirrored by the up- or down-regulation of pro-adipogenic markers in extraperitoneal and intraperitoneal adipose depot-derived cells, respectively. Finally, mesenchymal markers are highly expressed in SVF-adherent cells from all depots, validating the high enrichment of

hASPCs in the SV-adherent fraction. However, OM-derived samples also express an epithelial/mesothelial gene signature, suggesting the presence of mesothelial cells within the Lin[−] SVF of OM.

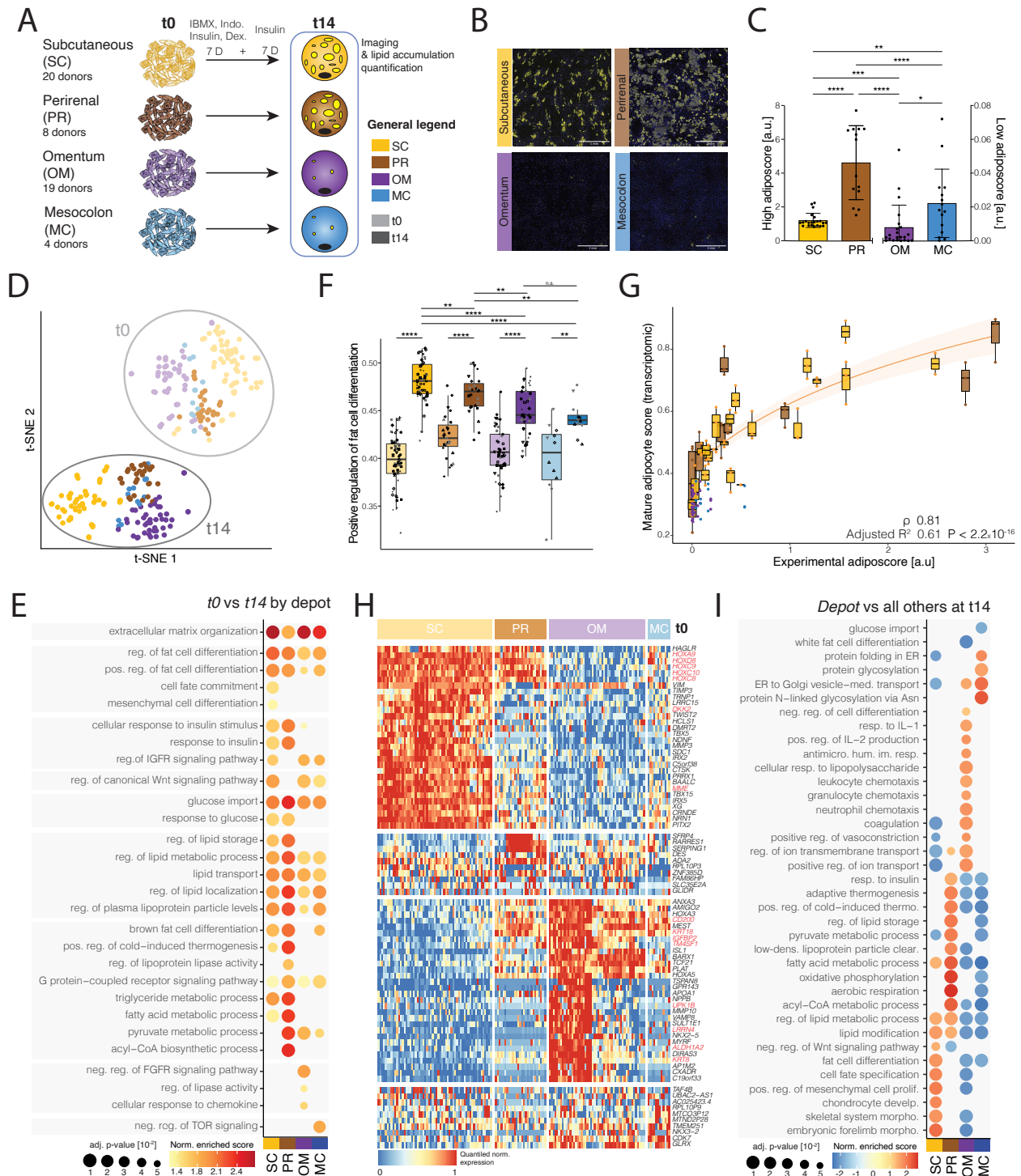


Figure 2.1 – Ex vivo cultures of SVF-adherent cells feature an anatomic footprint in their phenotype and transcriptome.

(A) Schematic of the experimental setup; primary SVF-adherent cell lines from human subcutaneous (SC), perirenal (PR), omental (OM), and mesocolic (MC) adipose tissues were cultured in parallel and harvested at the undifferentiated (t0) and

differentiated (t14) states for transcriptomic (BRB-seq) analysis; the same lines were seeded in a separate assay plate to quantify their adipogenic potential using the adiposcore (see **Materials and Methods**).

- (B) Representative fluorescence microscopy images of SVF-adherent cells directly after isolation expansion to confluence and adipogenic induction (t14); Yellow - Bodipy stains for lipids, blue - Hoechst stains for DNA, scale bar = 1 mm.
- (C) Barplot showing the log (adiposcore + 1) quantification of SVF-adherent cells in B; n = 14-22, 4-5 donors, 3-5 independent wells.
- (D) t-SNE map based on the transcriptomic (BRB-seq) data of SVF-adherent cells from the indicated adipose depots (SC - yellow, PR - brown, OM - purple, MC - blue) and time points (t0 - light, t14 - dark); n = 12-61, 4-20 biological replicates, 1-4 independent replicates for each.
- (E) Dot plot showing enriched, representative terms found by GSEA performed on the differential gene expression analysis results of t0 *versus* t14 samples for each depot of the data shown in D.
- (F) Boxplot displaying the “Positive regulation of fat cell differentiation score”, based on the scaled expression of the corresponding GO term (GO:0045600) of the data shown in D.
- (G) Scatter plot showing the relationship between the image quantification-based experimental adiposcore (shown in **Supp. Fig. 2.1.1**) *versus* the “mature adipocyte score” based on the scaled expression of well-known adipogenic markers (see **Methods**) of the transcriptomic samples from the same donor. Samples are grouped by depots and donors. Spearman correlation and adjusted R^2 of $y \sim \log(x+1)$ (plotted orange line with 95% confidence interval) values are indicated.
- (H) Heatmap of top differentially expressed genes when comparing the indicated depot *versus* the three others at t0 of the data shown in D.
- (I) Dot plot showing representative, enriched terms found by GSEA performed on the differential gene analysis results of each indicated depot *versus* the others at t14 of the data shown in D.

* $p \leq 0.05$, ** $p \leq 0.01$, *** $p \leq 0.001$, **** $p \leq 0.0001$, One-Way ANOVA and Tukey HSD *post hoc* test (C), unpaired two-sided *t*-test (F).

2.3.3 scRNA-seq of SVF Lin[−] fraction reveals both common and unique subpopulations across the subcutaneous, visceral, mesocolic, and perirenal adipose depots

Next, we explored whether the afore-observed transcriptomic and phenotypic differences across SVF-adherent cells derived from distinct adipose depots could in fact be driven by cellular heterogeneity. To do so, and to be as representative as possible of the SVF-adherent cells of the bulk RNA-seq analysis, we performed scRNA-seq of SVF Lin[−] (i.e., CD45[−]/CD31[−]) cells that were isolated from SC (n=3), OM (n=3), MC (n=2, from the same donor), and PR (n=3) adipose samples (**Table 2.2**), analyzing a total of 34'126 cells (on average, ~8'500 cells per depot). We first analyzed each resulting dataset independently, i.e., per depot and per donor (**Supp. Fig. 2.2.1A-B**). In all datasets, we identified hASPCs, defined by the expression of *THY1* and *PDGFRA*, well-known mesenchymal markers¹⁵¹, as well as a population expressing muscle-related markers such as *MYH11* but also *ACTA2* and *TAGLN* (**Supp. Fig. 2.2.1C**), resembling a transcriptomic signature of vascular smooth muscle progenitor cells (VSMPs)¹⁵⁹. Consistent with our bulk transcriptomic analysis, we also identified mesothelial cells, defined by the expression of *MSLN*, *UP3KB*, *LRRN4*, and Keratin-related genes, exclusively among SVF Lin[−] cells that were derived from OM AT (**Supp. Fig. 2.2.1C**, **Supp. Fig. 2.2.1A**). Finally, we identified a small number of immune (high *CD45*) and endothelial (high *PECAM1*) cells in the datasets from donor D07 that likely escaped the magnetic-based (MACS) Lin[−] enrichment that was performed for the corresponding SVF Lin[−] cells, as opposed to FACS used for the remaining datasets, where no CD45⁺ nor CD31⁺ cells are detected (**Supp. Fig. 2.2.1A-C**, for the type of enrichment method used prior to scRNA-seq, see **Table 2.2**).

Consistent with recent reports^{61,96,145}, hASPCs (*THY1* and *PDGFRA* high) displayed high heterogeneity and could be further stratified into at least two main clusters (**Supp. Fig. 2.2.1A**). To explore if and to what extent the identified hASPC subpopulations share molecular features across adipose depots, we performed three independent analyses. First, we calculated the overlap of the top cluster markers between datasets (**Supp. Fig. 2.2.1D**). We found that, while the percentage of shared markers tends to be the highest within samples isolated from the same depot and donor (**Supp. Fig. 2.2.1E-F**), the overlap across depots and donors is, on average, over 50% for most of the identified subpopulations (**Supp. Fig. 2.2.1D**). This result was confirmed when projecting each dataset onto each other using scmap¹⁶⁰, revealing that on average more than 75% of cells from one specific population projected onto the corresponding population in other datasets, regardless of the depot of origin (**Supp. Fig. 2.2.1G**). Finally, we integrated the data by considering each dataset as a different batch and correcting accordingly. Once again, we observed an excellent overlap of the depot-counterpart populations in the tSNE space (**Fig. 2.2A**, **Supp. Fig. 2.2.1H-I**), which was further confirmed by clustering analysis (**Fig. 2.2B**). Taken together, we can confidently stipulate that human adipose SVF contains at least two main hASPC (*THY1* and *PDGFRA* high) subpopulations/states, a feature common to all studied

depots: SC, PR, OM, and MC (**Fig. 2.2C-D**, **Supp. Fig. 2.2.2A-B**). To explore the universality of this finding, we assessed yet another unexplored adipose tissue, the AT which accumulates surrounding the gallbladder in a subset of morbidly obese patients, and even if relatively few hASPCs were ultimately captured, we still retrieved the two main hASPCs subpopulations (n=1, **Supp. Fig. 2.2.1B**).

Based on their respective gene expression signatures, we labeled those two hASPC subpopulations as adipose stem cells (ASCs) and pre-adipocytes (PreAs) (**Fig. 2.2B**). Indeed, ASCs from all depots shared a gene signature enriched for *DPP4*, *CD55*, and *PI16*, and showed enrichment in genes involved in proliferation, collagen synthesis and stemness (**Fig. 2.2C**, **Supp. Fig. 2.2.2C-D**), consistent with the corresponding ASC subpopulation from mouse epigonadal (visceral AT) and SC adipose depots^{96,100,102,146,161} (**Supp. Fig. 2.2.3**). On the other hand, PreAs differentially expressed known markers of committed adipogenic cells such as *PPARG*, *FABP4*, *PDGFRA*, *APOC*, and *APOE* and showed enrichment of terms linked to differentiation, commitment, and lipid transport (**Fig. 2.2C**, **Supp. Fig. 2.2.2C-D**), again aligning with the corresponding mouse PreA population^{96,100,102,146,161} (**Supp. Fig. 2.2.3**). Furthermore, our annotations are consistent with the two ASPC states observed in human SC AT^{96,145} and predicted for OM AT^{61,145} (**Fig. 2.2E**, **Supp. Fig. 2.2.4**). To our knowledge, these hASPC states have never been described for other human anatomical locations.

Upon integration, we identified five smaller populations of hASPCs defined by specific transcriptomic signatures that are most likely subpopulations of PreAs (**Fig. 2.2B-C**). One of them was defined by a high expression of *HHIP* (**Supp. Fig. 2.2.5A-B**). Among the top differentially expressed genes of this population, we recognized several key ortholog markers, such as *F3*, *CLEC11A*, *GDF10*, *MGP*, and *INMT* (**Supp. Fig. 2.2.5A**), of a mouse ASPC subpopulation that we have previously characterized as having non- and anti-adipogenic properties, and accordingly named Adipogenesis Regulators (Aregs)^{102,148}. To compare the transcriptomic signature of this population across species in a more unbiased way, we computed a score based on the orthologs of the top *HHIP*+ hASPC markers, or of Aregs (reported in Ferrero et al.¹⁴⁶ and Zachara et al.¹⁴⁸, see **Methods**) and showed that in both species, the score was significantly enriched in the corresponding population (**Supp. Fig. 2.2.3**). Recently, Emont and colleagues identified a cluster of hASPCs that is characterized by enriched expression of *EPHA3* in their human AT scRNA-seq atlas, which has substantial similarities to murine Aregs¹⁴⁵. Notably, *EPHA3* is specifically expressed by the *HHIP*+ hASPCs that we identified in our analyses, further supporting its alignment with mouse Aregs (**Supp. Fig. 2.2.5A**). To solidify the point that the previously described *EPHA3*+ hASPCs are indeed similar to our *HHIP*+ hASPCs, we transferred our cell annotation onto the Emont et al. dataset¹⁴⁵ and found that the *EPHA3*+ population has a significantly higher prediction score for our *HHIP*+ population than the rest of the hASPCs (**Fig. 2.2F**). Finally, given that *HHIP* is coding for a surface marker, we could confirm the existence of a human SVF Lin⁻/HHIP⁺ cell population in the SC adipose depot using flow cytometry (**Supp. Fig. 2.2.5C-D**).

Another small population of hASPCs, present in every depot and donor, which we refer to as *IFIT+* hASPCs, is defined by an extremely specific expression of interferon-related genes such as *IFIT3*, *IFI6*, and *IFI27*, a gene signature that is reflective of a viral immune response (**Supp. Fig. 2.2.6A-B**). A mesothelial *Ifit+* population has already been reported in mouse OM¹⁴³; yet, our *IFIT+* population does not express mesothelial markers (**Fig. 2.2C**) but mesenchymal ones (**Supp. Fig. 2.2.6C**). However, we found that, based on the expression of ortholog genes between mice and humans, this population shared a very similar signature with *Ifit+* cells that we have previously reported and that emerged when we integrated multiple mouse ASPC scRNA-seq datasets¹⁴⁶ (**Fig. 2.2G, Supp. Fig. 2.2.3**).

Another small hASPC subpopulation that we detected was characterized by high expression of Secreted frizzled-related proteins 2 and 4 (*SFRP2* and *SFRP4*) (**Supp. Fig. 2.2.7A**), and its gene expression patterns were similar to those of a mouse ASPC subpopulation identified using scRNA-seq¹⁴⁶ (**Supp. Fig. 2.2.3**), and a hASPC subpopulation identified by Emont and colleagues¹⁴⁵ (**Supp. Fig. 2.2.7B**). SFRPs are known to inhibit the Wnt signaling pathway, a key regulator of adipocyte differentiation¹⁶², and *SFRP2-4*, in particular, were shown to be upregulated in obesity, especially in visceral WAT¹⁶³. While we identified this population as present in all depots, we observed a general higher expression of *SFRP2*, but not *SFRP4*, in hASPCs from OM adipose depots (**Supp. Fig. 2.2.7C-D**).

While most hASPC subpopulations seem to exist in all analyzed adipose depots, albeit at different proportions, we found two depot-specific cell clusters: *FMO2+* cells were specific to PR and MC, while *IGFBP2+* cells to OM adipose tissue (**Fig. 2.2D, Supp. Fig. 2.2.2A-B**). An enrichment of *IGFBP2+* cell markers was also observed in our bulk transcriptomic datasets of OM samples compared to other depots, both at the undifferentiated and post-adipogenic induction states (**Supp. Fig. 2.2.8A-B**), thus confirming their specificity to OM. Moreover, when projecting our annotation onto the dataset by Emont and colleagues¹⁴⁵, our *IGFBP2+* cluster seems to align with one of their clusters (hASPC6)(**Fig. 2.2E, Supp. Fig. 2.2.4**).

In conclusion, we found hASPCs to be constituted of two main subpopulations/states: the ASCs and PreAs, which are conserved across all depots. However, the heterogeneity of hASPCs is obviously more complex, with more (sub)cellular states. Among them, we identified an OM-specific subpopulation defined by high expression of *IGFBP2*. Finally, in line with the established definition of peritoneum covering visceral AT, we found mesothelial cells almost exclusively in the OM AT (**Fig. 2.2D, Supp. Fig. 2.2.2A, Supp. Fig. 2.2.8C-E**). Only (very few) cells originating from MC samples were also expressing mesothelial markers (**Supp. Fig. 2.2.8E**), in line with the MC being itself covered by the peritoneum.

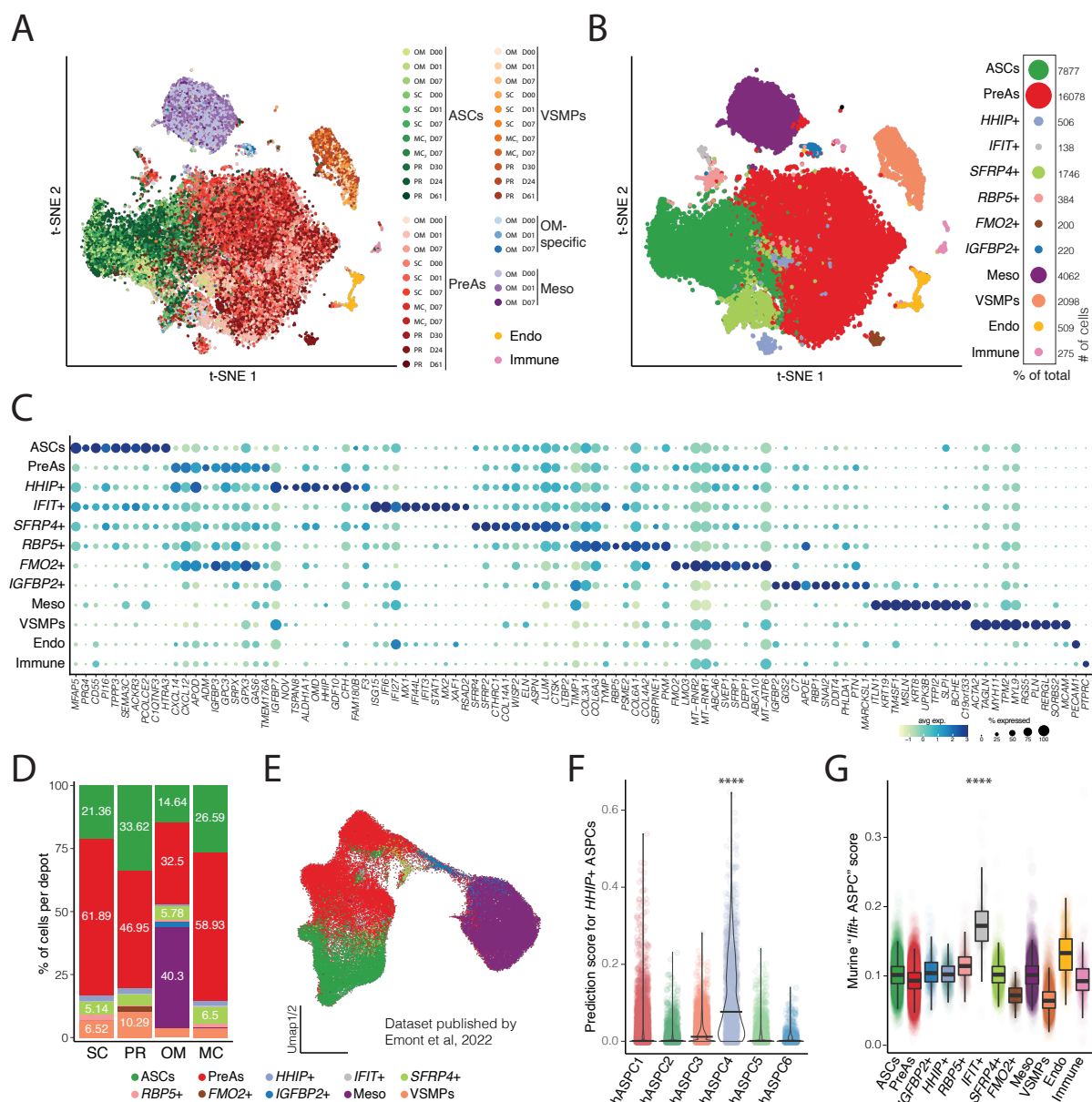


Figure 2.2 – scRNA-seq reveals common and specific cell populations across adipose depots.

- t-SNE cell map of integrated scRNA-seq datasets across four depots and 6 donors (D) (Table 2.2): OM, n=3, SC, n=3, and MC, n=2 (same donor) from matched donors, and PR, n=3 colored by the clustering of each dataset analyzed individually (as shown in Supp. Fig. 2.2.1A).
- t-SNE cell map of the data introduced in A colored by the identified clustering: Adipose Stem Cells (ASCs) - green, Pre-adipocytes (PreAs) - red, HHIP+ ASCs - light blue, IFIT+ ASCs - gray, SFRP4+ ASCs - light green, RBP5+ ASCs - light-red, FMO2+ ASCs - brown, mesothelial cells (Meso) - purple, vascular smooth muscle progenitor cells (VSMCs) - orange, endothelial cells (Endo) - yellow, and immune cells (Immune) - pink. The percentage of cells belonging to each cluster is shown by a dot plot, with the exact number of cells on the right.
- Dot plot of 10 of the main specific markers of each identified cluster shown in B.
- Barplot displaying the percentage of cells of each depot shown in B coming from each cluster, excluding immune and endothelial cells, see color legend below.
- UMAP computed on the integrated data of SC- and OM-derived hASPCs and mesothelial cells published in Emont et al. (2022)¹⁴⁵, colored by the predicted cell type/state when transferring our cell cluster annotation, see color legend for the predicted cell types below.

- (F) Violin plot showing the distribution of the prediction score of the *HHIP*+ hASPC population when transferred onto the scRNA-seq atlas of hASPCs of Emont et al.¹⁴⁵, where they identified hASPC4 as being transcriptomically similar to murine *Aregs*^{102,148}.
- (G) Boxplot showing the distribution of the murine “*Ifit*+ ASPC” scores across the detected, distinct human SVF cell populations. The scores were based on the human orthologs of the murine top markers of the *Ifit*+ ASPCs based on the integration of scRNA-seq datasets of subcutaneous and visceral murine adipose tissues described in Ferrero et al.¹⁴⁶

2.3.4 The Lin[−] fraction of SVF harbors three main subpopulations with specific functions that are ubiquitous across depots

After having characterized the heterogeneity of the cellular SVF Lin[−] landscape across depots, we aimed at refining our functional characterization between depots, now at the subpopulation level. We thereby first focused on the main cell populations that are ubiquitous across depots: the ASCs, the PreAs and the VSMPs (**Fig. 2.2A**). Based on our scRNA-seq analyses expression profiles, we developed a specific sorting strategy that would allow downstream stratification and characterization of each of the aforementioned main SVF Lin[−] populations that are shared across depots. This sorting strategy involves three layers: 1) the first layer involves CD26, encoded by the gene *DPP4* and specifically expressed by ASCs (**Supp. Fig. 2.3.1A**). Consistent with previous studies^{61,96,102}, *Dpp4* expression is specific to the murine ASC cluster¹⁴⁶. 2) The second layer involves Vascular-adhesion protein 1 (VAP1), encoded by the gene *AOC3* and highly expressed in VSMPs (**Supp. Fig. 2.3.1A**). In mouse, *Aoc3* expression has mainly been described as being enriched in the PreA population^{96,102,146}. However, based on our scRNA-seq integration of murine data, *Aoc3* is in fact also highly expressed by murine VSMPs (**Supp. Fig. 2.3.1B**). 3) The third layer aims to enrich for PreAs. Several candidate surface markers appear specific to the PreA population (i.e., *GPC3* or *ICAM1*). However, we reasoned that a simpler PreA enrichment approach would be to select for low expression of CD26 and VAP1. This approach would hold true in every depot except for the OM adipose depot, where two additional OM-specific cell populations would first need to be excluded: the mesothelial and the *IGFBP2*⁺ cells. Based on our transcriptional analyses, we selected the transmembrane 4 L6 family member 1 (*TM4SF1*) as a marker to first exclude OM-specific populations from our analysis (**Supp. Fig. 2.3.1A, C**). In sum, our sorting strategy involves antibodies directed against CD26, VAP1, and TM4SF1 (see **Materials and Methods**) to enrich for human ASCs (SVF Lin[−]/TM4SF1[−]/CD26⁺ (later referred to as CD26⁺)) and VSMPs (Lin[−]/TM4SF1[−]/VAP1⁺ (later referred to as VAP1⁺)), which leaves SVF Lin[−]/TM4SF1[−]/VAP1[−]/CD26[−] cells (later referred to as DN for “double negative”) enriched for PreAs (**Fig. 2.3A-B**).

As expected, and in line with the transcriptomic findings, only OM-derived SVF showed a clearly positive population when stained with anti-TM4SF1 antibody, confirming its high enrichment in OM depot (**Fig. 2.3B, Supp. Fig. 2.3.1D**). However, as in the scRNA-seq datasets, we did find a few TM4SF1⁺ cells among MC SVF Lin[−] cells as well (**Supp. Fig. 2.3.1D**). Analysis of the flow cytometry profiles gathered from up to 37 human donors (**Table 2.1**) allowed us to quantify the relative abundance of the targeted populations in each of the three adipose depots (**Fig. 2.3C**). We found that the ASC pool is less abundant in OM AT compared to that of PR and SC, while SC AT is dominated by PreAs and the OM and PR ones by VSMPs (**Fig. 3D**). In line with our scRNA-seq findings, we found the same three populations in MC AT with relative ratios that resemble those of OM AT (**Supp. Fig. 2.3.1E-F**).

Having confirmed the existence of these shared SVF Lin[−] subpopulations in each depot, we aimed to interrogate their phenotypic behavior *in vitro*. When sorted separately, the CD26⁺ population outpaced all other populations in terms of cell growth regardless of the depot of origin (**Supp. Fig. 2.3.1G**), a feature that confirms their stem-like nature and is consistent with previous observations in mouse and human^{96,164}. While highly proliferative, CD26⁺ scored the lowest in terms of adipogenic potential (**Fig. 2.3E-F**), further supporting the hypothesis that they are located at the very root of the adipogenic lineage. The VAP1⁺ cells had the highest adipogenic potential, followed by DN cells (**Fig. 2.3E-F**). The latter populations also exhibited a lower proliferative capacity compared to the ASC population (**Supp. Fig. 2.3.1G**).

Taking advantage of the relatively large cohort of human donors (n=37, **Table 2.1**) from which the adipose tissue was sampled, we investigated potential correlations between the relative abundance of each of the hASPC subpopulations and corresponding metadata such as BMI, age, and gender of the donors. Interestingly, we found that while the proportion of CD26⁺ cells (enriching for ASCs) is not affected by BMI changes, the latter appears to be correlated with DN depletion (enriching for PreAs). This correlation is particularly high in the SC, but also in the OM AT and is accompanied by a slight increase in the proportion of VAP1⁺ cells (enriching for the VSMPs) (**Fig. 2.3G**). In contrast, the age or sex of the donor did not seem to affect the equilibrium of cell populations within the SVF Lin[−] pool of any of the three analyzed adipose depots (**Supp. Fig. 2.3.2**).

Despite high similarities in the transcriptomes of ASCs and PreAs across depots in the scRNA-seq data, we observed that OM CD26⁺ and DN cells are consistently and significantly less adipogenic than equivalent SC and PR cells. To determine if cell-intrinsic features could explain the low adipogenic capacities of the OM cells, we explored the depot-specific transcriptomic signatures of these subpopulations in our scRNA-seq dataset. We noticed that across depots, the transcriptomes of ASC cells are more related than PreA ones (**Supp. Fig. 2.2.2D**, **Supp. Fig. 2.3.3A**), supporting the hypothesis that depot-specific features accumulate along commitment. We then identified genes of ASCs or PreAs that were enriched in a depot-specific manner (**Fig. 2.3H**, **Supp. Fig. 2.3.3B**). In line with their high adipogenic potential, hASPCs from SC, and especially PreAs, showed significantly higher expression of well-known adipogenic genes and transcription factors such *KLF4*, *KLF6*, *WISP2*, *APOE*, *APOC1*, and *CD36*. The pro-adipogenic character of PR adipose depot-isolated cells was also reflected in their transcriptome (**Supp. Fig. 2.3.3B-C**). For example, *PIK3R1* is the most up-regulated gene in PR compared to other adipose depots, with PI3K/Akt signaling playing a crucial role in adipogenesis of human mesenchymal stem cells¹⁶⁵. In mice, PI3K/Akt signaling has also been linked to browning by regulating GDF5-induced *Smad5* phosphorylation¹⁶⁶. While *GDF5* expression was virtually absent in our scRNA-seq data, *SMAD5* expression was specific to PR PreAs and ASCs. Similarly, *ZBTB16* is a PR-specific marker known to induce browning¹⁶⁷. With respect to populations that showed limited adipogenic potential, MC cells overexpressed genes linked to unfolded protein or protein folding (**Supp. Fig. 2.3.3C**) such as Heat-shock-

proteins (HSPs) (**Fig. 2.3H, Supp. Fig. 2.3.3B**), a large family of molecular chaperones. HSPs have been reported to interact with PPAR γ to either stabilize it and enhance adipogenesis (Hsp90)¹⁶⁸ or to destabilize it and inhibit adipogenesis (Hsp20)¹⁶⁹. OM cells once again showed an expression enrichment of genes linked to the inflammatory response (**Supp. Fig. 2.3.3C**). Among the candidates that were specific to OM were also a number of markers that were previously described in the literature as having a negative impact on adipogenesis (**Fig. 2.3H, Supp. Fig. 2.3.3B, RARRES2, RSPO3, RPL7, PTN, GAL, ALDH1A1, IGFBP3^{152,170–172}). Taken together, we were not only able to validate the findings that we inferred from bulk transcriptomic data at the scRNA-seq level, we also provided evidence that the PreA subpopulations are likely the ones that contribute the most to the depot-specific transcriptomic signatures that we captured at the bulk level.**

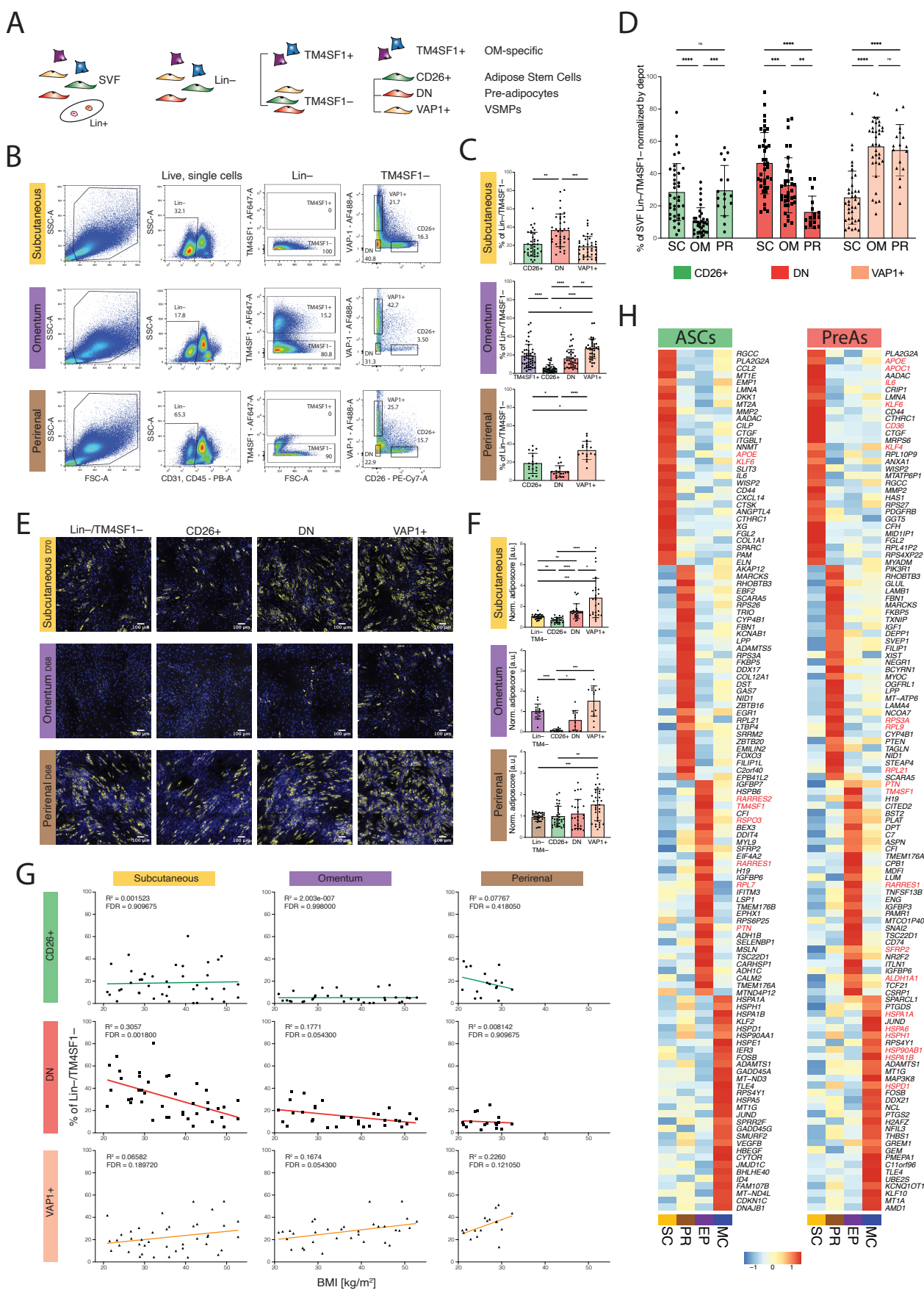


Figure 2.3 – The SVF Lin[−] composition differs between subcutaneous, omental, and perirenal adipose tissues, and shared sub-populations from different anatomical locations exhibit consistent but also intrinsic molecular and cellular phenotypes.

- (A) Sorting strategy scheme to enrich for Adipose stem cells (ASCs), pre-adipocytes (PreAs), Vascular smooth muscle progenitors (VSMPs), and OM-specific cells.
- (B) Flow cytometry-based representative profiles and gating strategy for SC, OM, and PR SVF from the same donor (D23) to isolate SVF Lin[−]/TM4SF1[−] cells.
- (C) Flow cytometry-based analysis of the abundance of each cell subpopulation gated from the Lin[−]/TM4SF1[−] fraction of SVF cells; SC n = 37, OM n = 35, PR n = 17 donors.
- (D) Bar plot to compare the flow cytometry-based abundance of the indicated SVF populations across depots. The three populations accumulate to 100% of Lin[−]/TM4SF1[−] gated cells by depot; SC n = 37, OM n = 35, PR n = 17 donors.
- (E) Representative fluorescence microscopy images of SVF Lin[−]/TM4SF1[−], CD26⁺, DN, and VAP1⁺ SVF populations from each depot after *in vitro* adipogenic differentiation (see **Methods**); Yellow - Bodipy stains for lipids, blue - Hoechst stains for DNA, scale bar = 100 μ m.
- (F) Quantification of the adipogenic potential of the SVF Lin[−]/TM4SF1[−] populations shown in **D**; Values are normalized to average adiposcore of the reference Lin[−]/TM4SF1[−] population; n = 12-21, 3-7 donors, 1-4 independent wells each.
- (G) Scatter plot showing the correlation between the % Lin[−]/TM4SF1[−] cells from each indicated SVF population and BMI across donors.
- (H) Heatmap of the top 30 genes detected as significantly higher expressed in the indicated depot *versus* all other depots (only genes detected as differentially expressed in each pairwise comparison were retained) when focusing on ASCs (left) or PreAs (right); Average log normalized expression scaled by row.

* $p \leq 0.05$, ** $p \leq 0.01$, *** $p \leq 0.001$, **** $p \leq 0.0001$, One-Way ANOVA and Tukey HSD *post hoc* test (**C**, **D**, **F**), and linear regression analysis with its relative goodness of fit, and the FDR-adjusted p -values of the Pearson correlations (**G**).

2.3.5 Mesothelial cells inhibit adipogenesis of omental hASPCs

We next questioned whether the presence of OM-specific cell populations (**Fig. 2.4A**) might influence the adipogenic capacity of the precursor cells themselves, as triggered by two key observations: 1) OM VAP1+ and DN cells, which are depleted of TM4SF1+ cells via the utilized sorting strategy, did show a discrete ability to differentiate (**Fig. 2.3E-F**); 2) several genes that were previously linked to the non-adipogenic phenotype of OM SVF-adherent cells were specific to mesothelial and/or *IGFBP2*+ cells (e.g., *CD200*¹⁷³, *WT1*, and *ALDH1A2*¹⁵², **Supp. Fig. 2.4.1A**).

Using TM4SF1 as a surface marker for OM-specific populations (mesothelial and *IGFBP2*+ cells, **Supp. Fig. 2.3.1C**), we separated TM4SF1+ cells from the total OM SVF Lin[−] fraction to study the adipogenic behavior of “pure” OM hASPCs (**Fig. 2.4B**). In line with our previous observation on the adipogenic potential of OM DN and VAP1+ subpopulations (**Fig. 2.3E-F**), we found that OM SVF Lin[−]/TM4SF1[−] cells, enriching for OM hASPCs and later referred to as TM4SF1[−] cells, are significantly more adipogenic than the total OM SVF Lin[−] fraction, which does contain the OM-specific mesothelial and *IGFBP2*+ cells. Not surprisingly, since mesothelial cells have previously been shown to be non-adipogenic¹⁷⁴, the OM SVF/Lin[−]/TM4SF1+ cells, here referred to as TM4SF1+ cells, did not accumulate any lipid droplets (**Fig. 2.4C-D**). Importantly, however, the increase in differentiation observed for TM4SF1[−] cells compared to the Lin[−] fraction was greater than expected by the simple, proportional removal of the non-adipogenic TM4SF1+ cells (accounting for roughly 20% of the total SVF Lin[−] fraction, **Fig. 2.3C**). Taken together, *in vitro* cultured OM hASPCs seem to be subjected to inhibitory cues that may stem from the OM-specific TM4SF1+ populations. Interestingly, the relative fraction of OM TM4SF1+ cells within the total SVF Lin[−] cell pool positively correlated with the BMI of donors, suggesting a possible functional role of TM4SF1+ cells in AT expansion (**Supp. Fig. 2.4.1B**). Morphologically, TM4SF1+ cells stood out from regular round and cobblestone-like OM hASPCs (OM SVF/Lin[−]/TM4SF1[−])^{175,176} (**Supp. Fig. 2.4.1C**), as they had spindle-like shape characteristic of mesothelial cells.

To test whether the observed inhibitory cues within the OM SVF Lin[−] cell pool has a negative influence not only on the adipogenic potential of OM hASPCs but also on those of SC or PR, we set up a mixing experiment where SC Lin[−] or PR Lin[−] cells were co-cultured with increasing ratios of OM Lin[−] cells (**Fig. 2.4E-F**, and **Supp. Fig. 2.4.2**). We observed that despite a linear increase in the relative proportion of OM SVF Lin[−] cells among SC SVF Lin[−] ones, the resulting decrease in adipogenic potential was non-linear (**Fig. 2.4F**). In other words, the decrease in differentiation was greater than expected by the simple relative “dilution” of SC SVF Lin[−] cells. To control for the fact that SC cells were not overgrown by OM cells, we quantified the relative number of nuclei across conditions which was stable (**Supp. Fig. 2.4.2A**) and controlled that the expression of an SC-specific marker *DKK2* was linearly increasing with the proportion of SC cells (**Supp. Fig. 2.4.2B-C**). Using a similar approach but this time mixing OM SVF Lin[−] cells with PR SVF Lin[−] cells did not reveal any regulatory effect, as we observed a relatively linear relationship between the increase in differentiation and the

proportion of PR cells per well (**Supp. Fig. 2.4.2D-F**). Thus, our findings suggest that the presence of OM TM4SF1+ cells results in lowered adipogenic potential, although this effect is not universal among hASPCs, hinting at depot-specific sensitivities to potential inhibitory cues stemming from OM SVF Lin[−] cells.

2.3.6 IGFBP2+ OM SVF Lin[−] cells can be found in situ and appear to transition between mesothelial and mesenchymal cell types

To better understand the cellular nature of the observed inhibitory effect, we set out to determine which TM4SF1+ population may be responsible for this adipogenic inhibition: the previously described mesothelial cells, and/or a small cluster of cells that highly express *IGFBP2* (**Fig. 2.4A** and **Supp. Fig. 2.3.1C**). The latter appears a plausible candidate since IGFBP2 has previously been shown to exert an anti-adipogenic effect both in mice and humans^{177,178}, which is why we first aimed to better define this population. At the single-cell level, the *IGFBP2*+ population appeared to have an intriguing dual gene expression signature, sharing markers with both hASPCs and mesothelial cells (**Supp. Fig. 2.4.3**). Such expression signature may at first glance suggest a technical artifact known as doublets, when two cells are mistakenly co-captured and considered as a single one. However, *IGFBP2*+ cells did not display a larger library size or number of captured features (**Supp. Fig. 2.2.11**), which would be expected for doublets due to a larger initial RNA content compared to singlets. More importantly, we found that these cells express, on the one hand, specific markers such as *IGFBP2*, *RBP1*, *WNT4*, or *WNT6* and, on the other, markers to a higher level than in ASPCs or mesothelial cells alone (**Supp. Fig. 2.4.3**), which is technically impossible for randomly co-encapsulated cells. To validate the existence of this population in another independent dataset, we transferred our cell annotation onto the recently published scRNA-seq atlas of human SC and OM ATs¹⁴⁵. We found that, first, only cells from OM harbor a positive prediction score for *IGFBP2*+ cells (**Supp. Fig. 2.4.4A**), validating once more their specificity to the OM. Second, the cells predicted as *IGFBP2*+ aligned with a cluster that was independently identified by Emont et al.¹⁴⁵ (**Supp. Fig. 2.4.4B-D**, **Fig. 2.2F**) and showed enrichment for *IGFBP2*+ cell markers, as illustrated by the marker-based expression score (**Supp. Fig. 2.4.4E**). Interestingly, the frequency of this population (relative to ASPCs and mesothelial cells) highly correlated with the BMI of the donors ($\rho=0.95$, **Supp. Fig. 2.4.4F**). Furthermore, and once again, aside from expressing their own specific markers (**Supp. Fig. 2.4.4G-H**), the predicted cells co-expressed mesothelial and ASPC markers (**Supp. Fig. 2.4.4I**) and aligned along a “bridge” between the two cell types. This duality in gene expression could reflect cells that are transitioning from one cell type to another. To computationally test this hypothesis, we performed trajectory inference on OM hASPCs (ASCs, PreAs), *IGFBP2*+ cells, mesothelial cells as well as VSMPs as a negative control. The trajectory was computed using PAGA as it can identify continuous and disconnected structures in the data¹⁷⁹. The inferred graph predicted branches connecting ASPCs to mesothelial cells through *IGFBP2*+ cells (**Fig. 2.4G**). As positive and negative controls of the validity of the graph structure, ASCs and PreAs were

also connected by a robust branch, as previously reported in mouse^{96,146}, and VSMPs were, as expected, not connected to the main trajectory. When ordering the cells by their pseudotime along the trajectory starting from ASCs (**Supp. Fig. 2.4.5A**), we observed a gradual decrease and increase of hASPC and mesothelial cell markers, respectively, along the connecting branch (**Fig. 2.4H-I**), as well as an up-regulation of *IGFBP2*+ cell markers during the transition (**Fig. 2.4H, J, Supp. Fig. 2.4.5B**). Altogether, these results indicate that *IGFBP2*+ cells might represent cells that transition between mesothelial and mesenchymal cell types. Accordingly, we found the GO term “epithelial-to-mesenchymal transition” (EMT) to be enriched among the *IGFBP2*+ cells’ differentially expressed genes (**Supp. Fig. 2.4.5C-D**). In addition to the genes enriched in the GO term, such as Slug (*SNAI2*), we also found several genes that are expressed by the transitioning cells that were previously linked with EMT, such as genes from the Wnt family, Matrix Metalloproteinase (MMPs), ZEB transcription factors, and others^{180–182} (**Supp. Fig. 2.4.5D**). TGF- β signaling, and especially TGF- β 1, has also been described as a master regulator of EMT linked to wound healing and fibrosis^{183,184}. In line, we found that *IGFBP2*+ cells have an enriched expression linked to “response to TGF- β ”, but not significantly to TGF- β 1 in particular. These cells also express genes in relation to epithelial migration and proliferation. Finally, EMT in the peritoneum of mice has been shown to induce the following gene programs: angiogenesis, hypoxia, inflammatory responses, cell cycle markers, and downregulation of adhesion molecules¹⁸⁵. The corresponding GO terms were all significantly enriched among the *IGFBP2*+ cell markers (**Supp. Fig. 2.4.5C**). Thus, our findings point to the existence of cells that likely transition between mesothelial and mesenchymal cells, even under “steady-state-like” conditions.

Having identified *IGFBP2*-expressing and transitioning cells computationally, we next defined a sorting strategy to separate these cells and the mesothelial cells from the total human OM SVF. To do so, we retained TM4SF1 as a valuable marker to segregate OM-specific cells from OM hASPCs and added MSLN as a marker that is solely expressed by mesothelial cells (**Supp. Fig. 2.3.1C**). Hence, we defined *IGFBP2*+ cells as OM SVF Lin[−]/TM4SF1⁺/MSLN[−] and mesothelial cells as OM SVF Lin[−]/TM4SF1⁺/MSLN⁺ (**Supp. Fig. 2.4.6A**), each fraction accounting for 5 to 10% of the total OM SVF/Lin[−] fraction (**Supp. Fig. 2.4.6B**). While we were able to highlight a significant, positive correlation between the abundance of TM4SF1⁺ cells and the BMI of donors based on flow cytometry analysis (**Supp. Fig. 2.4.1B**), that between the abundance of TM4SF1⁺/MSLN[−] cells, enriching for *IGFBP2*+ cells specifically, and BMI was not significant (**Supp. Fig. 2.4.6C**). Using the same panel of markers, we then set out to localize *IGFBP2*+ cells *in situ*. Interestingly, both MSLN and TM4SF1 highly stained the boundaries of the AT lobules (**Supp. Fig. 2.4.7A**), likely revealing a mesothelial mono-layer peritoneum-like structure that pads the OM itself. Accordingly, the majority of cells looked equally intense for both markers; we therefore defined the majority of cells as mesothelial cells (**Fig. 2.4K, red arrows, Supp. Fig. 2.4.7B**). However, intermingled among these mesothelial cells, we identified cells that were much more intense in the TM4SF1 channel than the MSLN one (**Fig. 2.4K, and Supp. Fig. 2.4.7B, white arrows**), reminiscent

of our *IGFBP2*⁺ cell gene expression signature. The absence of background staining was assessed by both unstained control and secondary-only staining (**Supp. Fig. 2.4.7**). Finally, and emphasizing their transitioning cell nature, we found that confluent Lin[−]/TM4SF1⁺/MSLN[−] cells harbor the specific mesothelial-cobblestone-like morphology, but when expanding, they tend to be spindle-like in shape, resembling mesenchymal cells (**Fig. 2.4L, Supp. Fig. 2.4.8**).

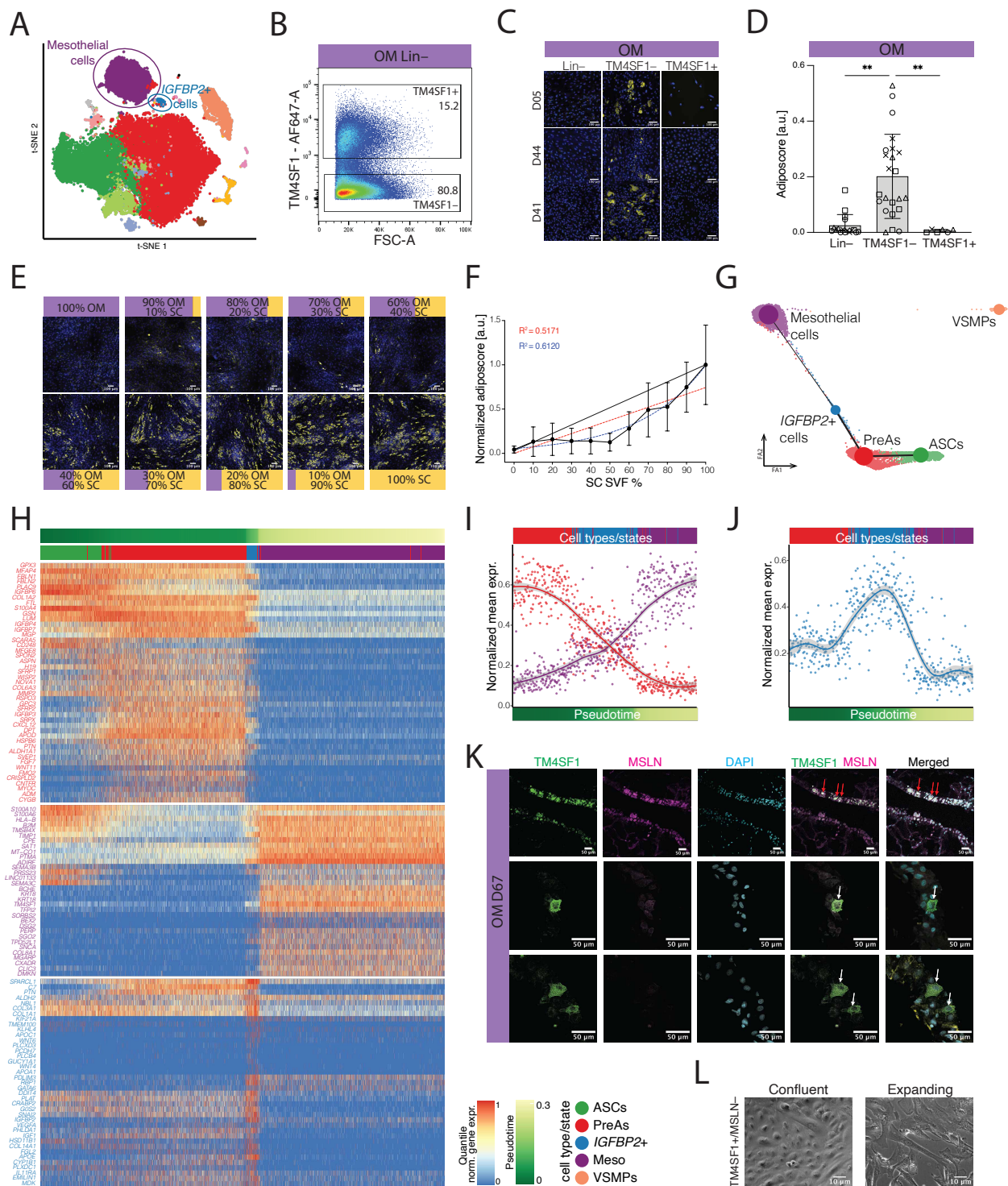


Figure 2.4 – OM SVF harbors cells and signals that mediate adipogenic inhibition, while IGFBP2⁺ cells appear in transition between mesothelial cells and ASCs.

- t-SNE cell map of integrated scRNA-seq datasets highlighting the two OM-specific populations: Mesothelial cells in purple and *IGFBP2*⁺ cells in blue.
- Representative flow cytometry scatter plot of OM SVF Lin⁻ cells (D05) stained with TM4SF1 antibody showing the gating strategy for sorting OM SVF Lin⁻-specific subpopulations as Lin⁻/TM4SF1⁺ and Lin⁻/TM4SF1⁻ cells.

- (C) Representative fluorescence microscopy images of OM SVF Lin⁻, Lin⁻/TM4SF1⁻ and Lin⁻/TM4SF1⁺ cell populations after adipogenic differentiation (see **Methods**); Yellow - Bodipy stains for lipids, blue - Hoechst stains for DNA; Scale bars = 100 μ m.
- (D) Barplot showing the adiposcore of the cell populations that are indicated in C; n = 6-23, 4 donors, 1-6 independent wells for each.
- (E) Representative fluorescence microscopy images of SVF Lin⁻ cells in mixing experiments after 14 days of adipogenic differentiation, where SVF Lin⁻ cells from OM and SC adipose tissues of donor 68 (D68) were mixed directly after cell isolation at the indicated proportions. Yellow - Bodipy stains for lipids, blue - Hoechst stains for DNA, scale bar = 100 μ m.
- (F) Quantification of the extent of adipogenic differentiation of the distinct, mixed OM and SC SVF Lin⁻ cell populations, as presented in E. Values across biological replicates are normalized to the average adiposcore of the reference 100% SC Lin⁻ condition. The relative proportion (0-100%) of SC SVF Lin⁻ cells in each well is plotted on the x-axis. Error bars represent standard deviation from the average, the linear and exponential regression with corresponding R² coefficients are shown in red and blue, respectively. The black line represents the expected increase of adipogenesis for a linear dilution between 0 and 100% of SC SVF Lin⁻ cells; n = 16, 4 biological replicates, 4 independent wells for each.
- (G) PAGA-inferred trajectory superimposed on the PAGA-initialized ForceAtlas2 layout. The size of the dots is proportional to the number of cells in the cluster, and the thickness of the lines indicates the confidence of the obtained trajectory relationship (the thicker, the more confident).
- (H) Heatmap showing the gene expression changes along pseudotime calculated on the trajectory shown in G. Genes decreasing from hASPCs (ASCs and PreAs) to Mesothelial cells are highlighted in red, genes increasing from hASPCs to Mesothelial cells are highlighted in purple, and genes specific to IGFBP2⁺ cells are highlighted in blue; log normalized gene expression scaled by row (quantile normalization).
- (I) Scatter plot showing the average of quantile-normalized gene expression highlighted in red or purple on the heatmap shown in H for each cell along the pseudotime calculated on the trajectory shown in G. The plot focuses on the transition between PreAs (red) and Mesothelial cells (purple), passing by IGFBP2⁺ cells (blue). A locally estimated scatterplot smoothing (LOESS) smoothing with 95% confidence interval is shown.
- (J) Scatter plot showing the average of quantile-normalized gene expression highlighted in blue on the heatmap shown in H for each cell along the pseudotime calculated on the trajectory shown in G. The plot focuses on the transition between PreAs (red) and Mesothelial cells, passing by IGFBP2⁺ cells (blue). A generalized additive model (GAM) fit with 95% confidence interval is shown.
- (K) Confocal microscopy fluorescent images of the *in situ* immunohistochemistry-based localization of TM4SF1⁺ (green) and MSLN⁺ (pink) cells in OM adipose tissue in donor 67. Nuclei are stained with DAPI (blue). The arrows indicate TM4SF1⁺/MSLN⁻ cells (white) and TM4SF1⁺/MSLN⁺ cells (red) in the periphery of the adipose tissue lobules. Scale bars, 50 μ m. Experiments were repeated at least three times, yielding similar results.
- (L) Brightfield microscopy images of OM SVF Lin⁻/TM4SF1⁺/MSLN⁻ (i.e., IGFBP2⁺) cells from donor 67 reveal a mesothelial cobblestone-like morphology when confluent and fibroblast spindle-like morphology upon expansion; Scale bars, 10 μ m.

* $p \leq 0.05$, ** $p \leq 0.01$, *** $p \leq 0.001$, **** $p \leq 0.0001$, REML analysis with matched values for the same donor and Tukey HSD *post hoc* test (D).

2.3.7 IGFBP2+ SVF Lin[−] OM cells inhibit adipogenesis through IGFBP2

Having identified cells with low MSLN but high TM4SF1 expression both *in situ* by immunohistochemistry and *ex vivo* by FACS, we wanted first to validate that cells that we isolated as Lin[−]/TM4SF1⁺/MSLN[−] (**Fig. 2.5A**) correspond to the *IGFBP2*+ cells that we identified in the scRNA-seq data. We first confirmed enriched *IGFBP2* expression in the sorted cells compared to total OM SVF Lin[−] or OM TM4SF1[−]/MSLN[−] ASCs and SC SVF Lin[−] cells by qPCR (**Fig. 2.5B**). To assess whether IGFBP2 is secreted or intracellular¹⁸⁶, we looked for the presence of the IGFBP2 protein in the supernatant of the OM-specific subpopulations as well as in SC and PR SVF Lin[−] cells as negative controls. Using ELISA, we measured the highest concentration of IGFBP2 in the supernatant of OM Lin[−]/TM4SF1⁺/MSLN[−] cells, quantified at approximately 35 ng/ml after 48h, followed by the mesothelial cells which secrete less than 20 ng/ml of IGFBP2. In contrast, we only detected low IGFBP2 levels in the supernatant of OM SVF Lin[−] cells, OM hASCs (OM Lin[−]/TM4SF1[−]/MSLN[−]), or PR Lin[−] and no secretion by the SC SVF Lin[−] cells (**Fig. 2.5C**). To translate these IGFBP2 ELISA values to a more physiological model of IGFBP2 secretion by the OM AT, we incubated total OM AT in PBS and measured the secreted IGFBP2 amount after 24, 48, and 72 hours. The concentration of IGFBP2 increased linearly over time, leading to a secretion of ~5ng/mL for 100mg of tissue every 24h (**Fig. 2.5D**).

Having identified a sorting strategy to stratify the IGFBP2-secreting and mesothelial cells, we now aimed at identifying which cell fraction is responsible for the anti-adipogenic effect exerted by the OM-specific TM4SF1⁺ cells described above (**Fig. 2.4C**). More specifically, given that IGFBP2 is a well-known OM-specific adipokine that has been shown to have anti-adipogenic properties^{177,187,188}, we wondered if the SVF Lin[−]/TM4SF1⁺/MSLN[−] cells could exert this effect in a paracrine fashion. To test this hypothesis, we used a transwell setup to expose receiving cells at the bottom to the secretome of either IGFBP2-secreting, mesothelial, or control cells, preventing cell-to-cell contact. At the bottom, we seeded the highly adipogenic SC SVF Lin[−] cells, since we already showed their sensitivity to the OM SVF Lin[−]-mediated anti-adipogenic effect (**Fig. 2.4E-F**). By doing so, we observed the highest and most significant adipogenic inhibition on SC cells when they were exposed to OM SVF Lin[−]/TM4SF1⁺/MSLN[−] cells, while the adipogenic inhibition was milder and more variable when SC cells were exposed to the OM Lin[−]/TM4SF1⁺/MSLN⁺ fraction (**Fig. 2.5E-F, Supp. Fig. 2.5.1A**). To validate that the PR cells are less responsive to this inhibitory signal, as shown in direct co-culture experiments (**Supp. Fig. 2.4.2D-F**), we performed the same transwell experiment, but this time with PR SVF Lin[−] cells at the bottom. Consistent with our first results, PR hASCs were rather insensitive to the inhibitory action of OM SVF Lin[−] cell subpopulations on adipogenesis (**Supp. Fig. 2.5.1B-D**).

To test whether IGFBP2 is at least partly regulating the high anti-adipogenic effect of IGFBP2-secreting cells, we knocked down (KD) IGFBP2 in the OM SVF Lin[−]/TM4SF1⁺/MSLN[−] cell population using siRNA probes. After validating the KD both at the mRNA and secreted protein levels (**Fig. 2.5G-H**), we used again a transwell set-up to expose SC SVF Lin[−] cells to their secretome as well as to that of OM SVF Lin[−]/TM4SF1⁺/MSLN[−] cells

treated with non-targeting siRNA control (NC1). We found that the SC cells exposed to the *IGFBP2* KD cells are significantly more adipogenic than those exposed to the control (**Fig. 2.5I-J**, **Supp. Fig. 2.5.1E**), further supporting the notion that Lin[−]/TM4SF1⁺/MSLN[−] cells exert an anti-adipogenic action via IGFBP2.

2.3.8 IGFBP2-mediated adipogenic inhibition occurs in an IGF-independent manner

Prompted by the evidence that IGFBP2 at least partially orchestrates the anti-adipogenic environment observed within OM SVF, we set out to better understand the mechanism underlying IGFBP2's anti-adipogenic effect. First, we tested if exogenous recombinant IGFBP2 is itself inhibitory by treating SVF-adherent cells from SC or PR depots with increasing IGFBP2 concentrations ranging from 0.5 to 4nM (**Supp. Fig. 2.5.2A-F**). We observed a linear decrease of differentiation of SC cells with increasing IGFBP2 concentrations, while only a milder effect was observed on PR cells. Notably, we observed significant inhibition of SC cells starting from as low as 1nM IGFBP2 (**Fig. 2.5K-L**). This is a value close to that measured in the supernatant of IGFBP2 (Lin[−]/TM4SF1⁺/MSLN[−])-secreting cells (**Fig. 2.5C**), which is why we used it for all further experiments.

IGFBP2 is known to act through two main mechanisms involving either IGF-dependent or IGF-independent signaling¹⁸⁹. Under the first scenario, the presence of IGFBP2 in the extracellular environment of hASPCs would sequester IGF-I and/or IGF-II and interfere with their pro-adipogenic signaling^{190–193}. Under the second scenario, IGFBP2 would activate a signaling cascade by binding to the $\alpha 5 \beta 1$ integrin receptor, inducing cells to stay in their pre-adipocyte state¹⁹⁴. Hence, we aimed to narrow down through which of these mechanisms IGFBP2 might influence adipogenesis of hASPCs from adipose depots to which we had recurrent access (i.e., SC, PR, and OM).

To test the first hypothesis of IGFBP2 sequestering IGFs, we co-treated SVF-adherent cells with both IGFBP2 and IGF-I or IGF-II, as well as with the three recombinant proteins alone. Based on the literature^{191,193}, we decided to use a concentration of 10nM for both IGF-I and IGF-II, given that, rather surprisingly, we were unable to observe a significant effect on the adipogenic potential of hASPCs treated with IGFs at any concentration ranging from 2.5 to 40nM, neither on SC or PR SVF Lin[−] cells (**Supp. Fig. 2.5.2A, G-J, D, K-N**). For SC cells, the drop in adipogenic potential was comparable when cells were treated with IGFBP2 both in the presence or in the absence of IGFs (**Fig. 2.5K-L**, **Supp. Fig. 2.5.3A**), suggesting an IGF-independent action of IGFBP2. Once again, PR lines appeared to be less sensitive to the action of IGFBP2 and IGF treatments. In fact, even though we observed a similar trend to that observed for SC cell behavior when treating PR cells with IGFBP2 both in the presence or in the absence of IGFs, none of the observed decreases in adipogenic potential was significant when compared to the non-treated cells (**Supp. Fig. 2.5.3B-D**). Overall, this is consistent with our previous observations suggesting that PR SVF-adherent cells are less sensitive to the inhibitory effect of OM SVF Lin[−] cells in the cell mixing setup (**Supp. Fig. 2.4.2D-F**) and of OM SVF Lin[−]/TM4SF1⁺/MSLN[−] cells in the transwell setup (**Supp. Fig. 2.5.1B-D**).

Next, we explored to what extent OM TM4SF1– cells, enriching for OM hASPCs, can respond to IGFBP2 and IGF treatments, since these cells anatomically co-exist with the IGFBP2-secreting cells. Even if OM TM4SF1– cells are intrinsically lowly adipogenic, we observed a significant differentiation decrease when these cells were treated with IGFBP2 (**Fig. 2.5M-N, Supp. Fig. 2.5.3F**), which further supports the anti-adipogenic potential of IGFBP2-secreting cells in their depot of origin. Contrary to PR and SC cells, OM cells were more sensitive to the IGF-I and IGF-II treatments but with a high degree of variability between batches (**Fig. 2.5M-N**). However, when co-treated with IGFs and IGFBP2, the differentiation of OM TM4SF1– cells was again significantly lower than in non-treated cells (**Fig. 2.5M-N, Supp. Fig. 2.5.3E**). The fact that IGF treatment could not maintain the increased adipogenic potential when cells were treated with IGFs only, even if given in excess (10nM of IGFs versus 1nM of IGFBP2 for a stoichiometry of 1:1), further suggests an IGF-independent mode of action by IGFBP2.

We then tested the second hypothesis, namely that IGFBP2 may act in an IGF-independent fashion by activating the $\alpha 5 \beta 1$ integrin receptor¹⁹⁴. To do so, we used echistatin, a known antagonist of the integrin receptor¹⁹⁵, at a concentration of 100 nM for the first 48h of adipogenic induction¹⁷⁷, as longer treatment resulted in cell detachment. We therefore coupled echistatin to IGFBP2 treatment only during the first 48h of differentiation. Interestingly, we found that echistatin alone is able to significantly enhance the differentiation of SC SVF-adherent cells, while, when cells were co-treated with IGFBP2 and echistatin, the adipogenic potential of the treated cells was similar to that of non-treated control cells (**Fig. 2.5K, O, Supp. Fig. 2.5.3A**). Interfering with integrin receptor function in PR SVF-adherent cells yielded a similar trend in overall adipogenic potential as observed for SC cells (**Supp. Fig. 2.5.3B-C, F**). This result highlights the important role played by integrin receptor signaling in mediating the adipogenic potential of cells, as echistatin had a significant effect even on the highly adipogenic PR cells.

Finally, when treating OM TM4SF1– cells with echistatin, we observed a significant increase in the ability of these intrinsically non-adipogenic cells to accumulate lipid droplets (**Fig. 2.5M, P, and Supp. Fig. 2.5.3E**), in line with findings by Yau and colleagues¹⁷⁷. Furthermore, co-treatment with echistatin and IGFBP2, both competing for binding to the $\alpha 5 \beta 1$ integrin receptor, led to a significant increase in differentiation compared to non-treated cells, but less than echistatin-only treatments (**Fig. 2.5M, P, and Supp. Fig. 2.5.3E**).

Taken together, our observations point to the existence of an OM-specific and transitioning cell population that highly expresses and secretes IGFBP2, which negatively impacts the adipogenic potential of OM and SC hASPCs, by signaling through an IGF-independent mechanism involving the integrin receptor $\alpha 5 \beta 1$. However, we cannot completely exclude that the restored adipogenic potential of the analyzed cells (as compared to non-treated control cells) may be driven by two independent and opposite effects, i.e., inhibition by IGFBP2 and enhancement by echistatin. Indeed, the observed significant increase in adipogenesis for example of PR

cells upon echistatin treatment (**Supp. Fig. 2.5.3B-C, F**) suggests that the integrin receptor can also negatively regulate adipogenic potential in a manner that may be independent of IGFBP2 activation.

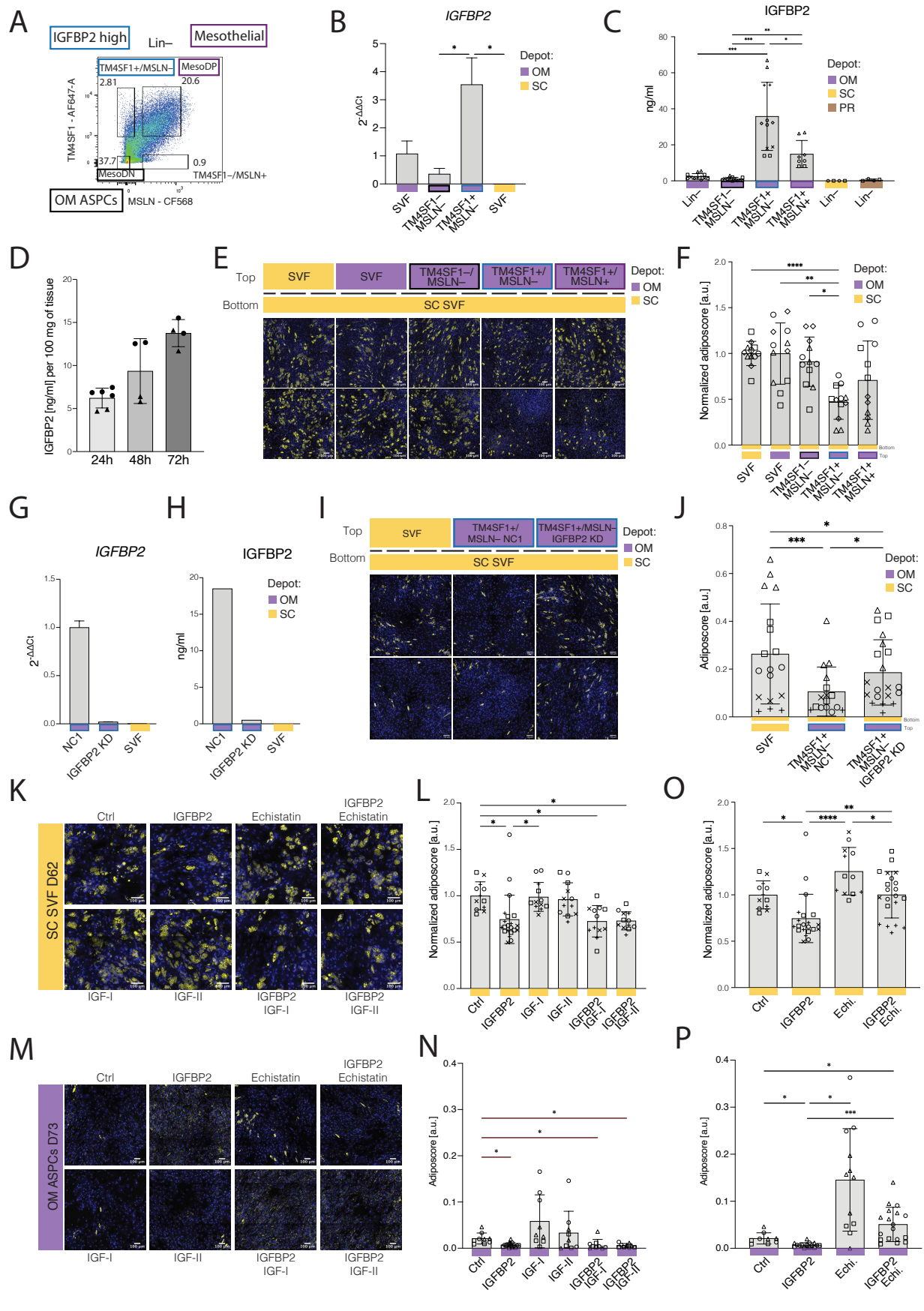


Figure 2.5 – IGFBP2+ cells secrete IGFBP2 to inhibit adipogenesis of neighboring cells through an IGF-independent, paracrine mechanism.

- (A) Representative flow cytometry scatter plot of OM SVF Lin[−] cells (D53) stained with TM4SF1 and MSLN showing the gating strategy to enrich for specific SVF Lin[−] subpopulations: Lin[−]/TM4SF1[−]/MSLN[−] (OM ASCs - Black border), Lin[−]/TM4SF1⁺/MSLN[−] (IGFBP2⁺ cells, Blue border), or Lin[−]/TM4SF1⁺/MSLN⁺ (mesothelial cells, Purple border); DP: Double Positive; DN: Double Negative.
- (B) qPCR-based quantification of *IGFBP2* expression. Ct values are normalized first to *HPRT1* expression, then to the Δ Ct of OM SVF cells; n=4, 2 donors, 2 technical replicates.
- (C) ELISA-based quantification of secreted IGFBP2 (ng/mL) in the supernatant of the indicated cellular populations after 48h of secretion in a serum-free medium; n=8, 4 donors, 2 technical replicates.
- (D) ELISA-based quantification of IGFBP2 levels (ng/mL), as secreted by 100mg of OM adipose tissue over the indicated time window in PBS; n=4, 2 donors, 2 technical replicates.
- (E) Representative fluorescence microscopy images of “receiver” SC SVF adherent cells, at the bottom of a transwell set-up, after adipogenic differentiation when co-cultured with the indicated SVF populations on top of the transwell: paired SC SVF adherent cells, OM SVF adherent cells, OM SVF/Lin[−]/TM4SF1[−] (OM ASCs), OM SVF/Lin[−]/TM4SF1⁺/MSLN[−] (IGFBP2⁺) cells, or OM SVF/Lin[−]/TM4SF1⁺/MSLN⁺ (mesothelial) cells. Top row: SC cells from D25, OM cells from D54; bottom row: SC and OM cells from D65.
- (F) Barplot showing the adiposcore quantification of “receiver” cells in E. Values are normalized to the average adiposcore of the reference top SC SVF adherent condition; n=12, 4 donors, 3 independent wells.
- (G) qPCR-based quantification of *IGFBP2* expression in SVF/Lin[−]/TM4SF1⁺/MSLN[−] cells subjected to either *IGFBP2* siRNA or non-targeting siRNA control (NC1), as retrieved from the transwell set-up. SC SVF adherent cells are also used as negative control. Ct values are normalized first to *HPRT1* expression, then to the Δ Ct of NC1 control; n = 2, 1 donor, two technical replicates.
- (H) ELISA-based quantification of IGFBP2 levels in the supernatant of OM SVF Lin[−]/TM4SF1⁺/MSLN[−] cells subjected to either *IGFBP2* siRNA or non-targeting siRNA control (NC1). SC SVF/Lin[−] cells are used as negative control; n = 2, 1 donor, two technical replicates.
- (I) Representative fluorescence microscopy images of “receiver” SC SVF adherent cells, at the bottom of the transwell set-up, after adipogenic differentiation when co-cultured, with the indicated cells on top of the transwell: paired SC SVF adherent control cells, OM SVF/Lin[−]/TM4SF1⁺/MSLN[−] cells treated with non-targeting siRNA control (NC1), OM SVF/Lin[−]/TM4SF1⁺/MSLN[−] cells treated with *IGFBP2* siRNA. Top row: SC and OM cells from D74, bottom row: SC cells from D63, and OM cells from D75.
- (J) Barplot showing the adiposcore quantification of “receiver” cells in I; n=16-20, 4 donors, 2-4 independent wells.
- (K) Representative fluorescence microscopy images of SC SVF-adherent cells after adipogenic differentiation when treated with the indicated interfering compounds: IGFBP2 1nM, IGF-I 10nM, IGF-II 10nM, Echistatin 100nM.
- (L) Barplot showing the adiposcore quantification of cells in K with a focus on the IGF-dependent signaling pathway of IGFBP2. Values are normalized to the average adiposcore of the untreated control cells (Ctrl); n=12, 4 donors, three independent wells.
- (M) Representative fluorescence microscopy images of OM SVF/Lin[−]/TM4SF1[−]/MSLN[−] cells after adipogenic differentiation when treated with the indicated, interfering compounds: IGFBP2 1nM, IGF-I 10nM, IGF-II 10nM, Echistatin 100nM.
- (N) Barplot showing the adiposcore quantification of cells in M with a focus on the IGF-dependent signaling pathway of IGFBP2. Values are normalized to the average adiposcore of the untreated control cells (Ctrl); n=9, 3 donors, three independent wells.
- (O) Barplot showing the adiposcore quantification of cells in K with a focus on the IGF-independent signaling pathway of IGFBP2. Values are normalized to the average adiposcore of the untreated control cells (Ctrl); n=12, 4 donors, three independent wells.
- (P) Barplot showing the adiposcore quantification of cells in M with a focus on the IGF-independent signaling pathway of IGFBP2. Values are normalized to the average adiposcore of the untreated control cells (Ctrl); n=9, 3 donors, three independent wells.

For images in E, I, K, and M: Yellow - Bodipy stains for lipids, blue - Hoechst stains for DNA, scale bar=100 μ m. * $p \leq 0.05$, ** $p \leq 0.01$, *** $p \leq 0.001$, **** $p \leq 0.0001$, One-Way ANOVA and Tukey HSD *post hoc* test (B, C, F, L, O), REML analysis with matched values for the same donor and Tukey HSD *post hoc* test (J, N, P).

2.4 Conclusion

Despite significant efforts, our understanding of hASPC heterogeneity and function across human adipose depots is still limited, which has been further hampered by the lack of hASPC consensus markers. Consequently, hASPCs tend to be studied in form of total SVF Lin[−], which blurs their cellular and functional characterization. To address this, we performed a comprehensive exploration of human SC, PR, OM, and MC AT SVF Lin[−] population structure and function. Our bulk analyses revealed extensive molecular and phenotypic variation among these depots (**Fig. 2.1**). On a global level, we confirmed earlier observations that only SVF-adherent cells from extraperitoneal ATs (SC and PR) displayed high adipogenic potential *ex vivo*, while their intraperitoneal counterparts (OM and MC) were refractory to adipogenesis^{196–198}. This is also reflected by the fact that SC and PR SVF-adherent cells featured a highly adipogenic transcriptomic signature compared to OM and MC ones (**Supp. Fig. 2.1.4H, J**), which in contrast featured a more inflammatory and epithelial/mesothelial gene expression profile (OM) (Alvehus et al. 2010), or a protein trafficking (heat shock protein) signature (MC) (**Fig. 2.1I**). However, despite being highly adipogenic, we also found important molecular differences among extraperitoneal ATs, revealing that, contrary to SC, the gene expression profile of PR SVF-adherent cells was enriched for terms associated with the oxidative respiratory chain, thermogenic response, and mitochondrial activity (**Fig. 2.1I**). This suggests that PR hASPCs may be prone to beiging, potentially reflecting an influence of the nearby adrenal gland¹⁹⁸.

To better explore potential cellular mechanisms underlying the distinct adipogenic properties of the four analyzed depots, we resolved SVF Lin[−] heterogeneity by performing scRNA-seq on about 34'000 cells (an average of 8'500 cells per depot) and comparing the resulting data with publicly available datasets from both human and mouse ATs^{145,146}. These analyses allowed us to identify at least six hASPC populations that are shared across the ATs (**Fig. 2.2B**), including four relatively small ones, such as *HHIP*+ or *IFIT*+ hASPCs, as well as two main ones: i) the hASCs, which mapped to the mouse *Dpp4*+ population^{96,100,102} and the human *DPP4*+ cells⁹⁶, and ii) the hPreAs, which mapped to the mouse *Icam1*+/*Aoc3*+ population^{96,102} and human *ICAM1*+ clusters⁹⁶. Subsequent population sorting thereby revealed that the ASC pool is proportionally the smallest in OM AT (**Fig. 2.3D**), supporting the hypothesis that SC and PR ATs have a greater capacity to expand through hyperplasia compared to OM AT^{11,203}. A third cluster that was ubiquitous in all analyzed human depots is the VSMP cluster which highly expresses *AOC3* (VAP1) (**Fig. 2.2B, Supp. Fig. 2.3.1A**). Although *Aoc3* has mainly been described as being expressed by murine PreAs^{96,102}, murine VSMPs do exist and also highly express *Aoc3* (**Supp. Fig. 2.2.3, Supp. Fig. 2.3.1B**). As hPreAs also exhibit basal *AOC3* expression, we cannot completely rule out that VAP1 also enriches for a fraction of human *AOC3*-expressing PreAs. In our study, VAP1+ cells were the most adipogenic, but at the transcriptomic level, *AOC3*-high cells also expressed muscle-related markers (**Fig. 2.2C**), which seems contradictory. However, beige/brown AT progenitors have been described to upregulate muscle-related markers to become thermogenic^{69,204–207}. Thus, we cannot exclude that VSMP and/or

VAP1-enriched PreAs are in fact beige progenitors, although the fact that VAP1+ cell abundance was lower in SC compared to OM and PR ATs would in this regard be counterintuitive since SC is the preferential site for beige adipogenesis²⁰⁸. Nevertheless, it seems worthy to elucidate the function of these VSMP cells given their greater abundance in high versus normal weight individuals across all analyzed adipose depots (**Fig. 2.3G**). This may reflect an attempt to either induce a thermogenic response to balance excessive energy take or to create new vasculature to support (excessive) adipose tissue expansion (or both). Overall, when comparing the human and mouse ASPC landscapes, there are clear similarities but also differences. For example, while *F3*+ ASPCs form a clearly distinct cluster in mouse^{96,102,146,148,149}, they appear to be rarer in humans, as they only emerged after aggregating all of our datasets (**Fig. 2.2A-B**). Moreover, while *F3* is a specific marker for anti-adipogenic ASPC populations in mice, it is much less specific in humans, where *HHIP* appears to be a more specific marker for this cell population (**Supp. Fig. 2.2.5A**).

Next to AT-ubiquitous cell populations, we also found some that are exclusive to one adipose depot. A striking example is the mesothelial cells that we almost exclusively detected in OM AT (**Fig. 2.2D**). While the presence of such cells within the OM SVF fraction is well-established^{91,100,143,145}, our functional characterization revealed that the mesothelial cells, even if variable across replicates, can in fact mildly inhibit the differentiation of OM hASPCs (**Fig. 2.5E-F**), suggesting that the mesothelium surrounding the OM AT could have a regulatory impact on its plasticity. But more strikingly, we identified a mesothelial-like subpopulation that is also specific to the OM and that exhibits a robust anti-adipogenic capacity. We found that the latter OM SVF/Lin[−]/TM4SF1+/MSLN[−] cells highly secrete IGFBP2 (**Fig. 2.5C**) and can as such negatively regulate the adipogenic capacity of both SC and OM hASPCs (**Fig. 2.5I-J**), consistent with IGFBP2's previously reported anti-adipogenic properties^{177,209}. Our findings thereby indicate that these cells' anti-adipogenic properties are mediated through an IGF-independent mechanism, most likely through the activation of integrin receptor signaling in a paracrine fashion. Stromal populations that negatively regulate the adipogenic capacity of ASPCs have recently been discovered in mouse ATs by our^{102,148} and other labs^{91,149}. The discovery of the OM SVF/Lin[−]/TM4SF1+/MSLN[−] cells now suggests that also in humans, AT (here, OM) plasticity may be orchestrated by distinct regulatory features including not only (more systemic) endocrine signals but also specialized niche cells that are not necessarily mesenchymal in nature.

The identification of a TM4SF1+/MSLN[−]-IGFBP2-secreting cell population also provides new insights into the mechanisms underlying the well-established limited adipogenic capacity of OM hASPCs, even though IGFBP2 signaling could only partially explain the reduced capacity of OM hASPCs compared to other depots (**Fig. 2.3E-F**). This indicates that OM hASPCs still feature cell-intrinsic and transcriptomically independent mechanisms that render them refractory to differentiation and more specialized to mediating inflammation and vascular remodeling (**Supp. Fig. 2.3.3C**). Nevertheless, the identification of these IGFBP2-secreting cells raises questions as to their cellular origin and physiological relevance. We found that *IGFBP2*+ cells co-expressed

mesenchymal and mesothelial markers and showed enrichment of mesothelial to mesenchymal transition (MMT) markers (**Fig. 2.4H-I**, **Supp. Fig. 2.4.5C**). Moreover, when sorted as TM4SF1+/MSLN– cells, they exhibited a cobblestone-mesothelial morphology while, upon expansion, a spindle-mesenchymal one (**Fig. 2.4L**), suggesting that these cells are likely able to undergo MMT, a still poorly characterized process that has been described to also be driven by IGFBP2 itself^{210–213}. While this cellular process is known, it has mainly been described in development, wound healing and cancer. Our results suggest however that MMT can also occur in adulthood at steady-like state. Interestingly, by projecting our annotation onto the recently published single-cell atlas of human AT¹⁴⁵, we found not only that *IGFBP2*+ cells can be detected in the OM adipose depots of both lean and obese donors, which we confirmed through flow cytometry (**Supp. Fig. 2.4.6**), we also observed a highly positive correlation between inferred *IGFBP2*+ cell abundance and BMI (**Supp. Fig. 2.4.4F**). The latter observation appears to contrast with results from previous studies though, which found in fact an anti-correlation between BMI^{214–216}, onset of metabolic syndrome²¹⁷ including type 2 diabetes and NAFLD²¹⁸ on the one hand and circulating IGFBP2 serum levels on the other. Since IGFBP2 is also secreted by other organs such as the liver^{187,218}, additional research will therefore be required to reconcile IGFBP2's role in seemingly controlling local OM adipose tissue plasticity versus acting as a systemic metabolic regulator.

While an important proportion of human visceral fat is contained in the OM, this depot is rather minimal in mouse²¹⁹. It may therefore prove difficult to find an equivalent population in mouse. However, a very recent study by Zhang et al.⁹¹ of mouse epididymal AT did identify “mesothelial-like cells” that shared markers with both mesothelial and mesenchymal cells and that were also defined by high *Igfbp2* expression. This suggests that OM *IGFBP2*+ cells may be cellularly and functionally conserved between mouse and human, which in turn may open new experimental avenues to study their relevance in mediating OM AT plasticity in distinct metabolic contexts. Longer-term, such studies may then lead to new therapeutic strategies to render OM hASPCs more adipogenic and less inflammatory, which could be a valuable novel approach to treat metabolic disorders linked to obesity, especially given the protective and anti-diabetic effect that has been attributed to IGFBP2²¹⁶.

2.5 Materials and methods

Bioethics

All materials used in this study have been obtained from AT donors from two independent cohorts: the Cohort of Obese Patients of Lausanne with ethically approved license by the commission of the Vaud Canton (CER-VD Project PB_2018-00119) and a control healthy cohort from renal transplantation donors with ethically approved license by the commission of the Vaud Canton (CER-VD 2020-02021). The coded samples were collected undersigned informed consent conforming to the guidelines of the 2000 Helsinki declaration. **Table 2.3** illustrates cohorts demographics.

Human ASPCs isolation and culture

2-3 cm³ biopsies from SC, OM, PR and MC ATs were washed in PBS to remove excess blood, weighted and finely minced using scissors. Minced adipose tissue was incubated with 0.28 U/ml of liberase TM (Roche #05401119001) in DPBS with calcium and magnesium (Gibco #14040091) for 60 min at 37 °C under agitation. Vigorous shaking was performed after 45 min of incubation to increase the yield of recovered SVF cells. The digested tissue was mixed with an equal volume of 1% human albumin (CSL Behring) in DPBS –/– (Gibco #14190094) to stop the lysis. Following a 5-min centrifugation at 400 g at room temperature, floating lipids and mature adipocytes were discarded by aspiration and the resuspended SVF pellet was sequentially filtered through 100-µm and 40-µm cell strainers to ensure a single cell preparation. To lyse red blood cells, pelleted SVF was resuspended in VersaLyse solution (Beckman Coulter #A09777) according to the manufacturer's recommendations and washed once with 1% albumin solution. Obtained red blood cell-free SVF suspension was then either plated for experiments, expanded and cryoprotected or stained for sorting (see below). The SVF used for expansion or experiments was plated at a density of at least 100'000 cells per square centimeter in high glucose MEMalpha GlutaMax medium (Gibco #32561037) supplemented with 5% human platelet lysate (Sigma #SCM152) and 50 µg/ml Primocin (InvivoGen #ant-pm-2). For culturing human ASPCs, TrypLE Select reagent (Gibco #12563011) was used to collect the cells from the cell culture plates.

Bulk RNA barcoding and sequencing (BRB-seq)

All cells for BRB-seq were seeded in parallel in six 24-well plates. Cells from three wells were harvested undifferentiated (t0 time point) upon cell expansion in the 24-well plate. Cells from the three remaining wells were expanded until confluence and harvested in TRIzol (Sigma, #T3934) after 14 days of adipogenic differentiation (t14 time point). RNA was extracted from all samples in parallel using the Direct-ZOL 96 well plate format (Zymo, #R2054), and BRB-seq libraries were prepared as previously described²²⁰ and further detailed by the Mercurius™ Protocol (Alithea Genomics). In brief, 7-200 ng of total RNA from each sample was reverse transcribed in a 96-well plate using SuperScript™ II Reverse Transcriptase (Lifetech 18064014) with

individual barcoded oligo-dT primers, featuring a 12-nt-long sample barcode (IDT). Double-stranded cDNA was generated by second-strand synthesis via the nick translation method using a mix containing 2 µl of RNase H (NEB, #M0297S), 1 µl of *E. coli* DNA ligase (NEB, #M0205 L), 5 µl of *E. coli* DNA Polymerase (NEB, #M0209 L), 1 µl of dNTP (10 mM), 10 µl of 5x Second Strand Buffer (100 mM Tris, pH 6.9, (AppliChem, #A3452); 25 mM MgCl₂ (Sigma, #M2670); 450 mM KCl (AppliChem, #A2939); 0.8 mM β-NAD (Sigma, N1511); 60 mM (NH₄)₂SO₄ (Fisher Scientific Acros, #AC20587); and 11 µl of water was added to 20 µl of Exol-treated first-strand reaction on ice. The reaction was incubated at 16 °C for 2.5 h. Full-length double-stranded cDNA was purified with 30 µl (0.6x) of AMPure XP magnetic beads (Beckman Coulter, #A63881) and eluted in 20 µl of water.

The Illumina-compatible libraries were prepared by tagmentation of 10-40 ng of full-length double-stranded cDNA with 1 µl of in-house produced Tn5 enzyme (11 µM). After tagmentation, the libraries were purified with DNA Clean and Concentrator kit (Zymo Research #D4014) eluted in 20 µl of water and PCR amplified using 25 µl NEB Next High-Fidelity 2x PCR Master Mix (NEB, #M0541 L), 2.5 µl of each i5 and i7 Illumina index adapter (IDT) using the following program: incubation 72 °C—3 min, denaturation 98 °C—30 s; 15 cycles: 98 °C—10 s, 63 °C—30 s, 72 °C—30 s; final elongation at 72 °C—5 min. The libraries were purified twice with AMPure beads (Beckman Coulter, #A63881) at a 0.6x ratio to remove the fragments < 300 nt. The resulting libraries were profiled using a High Sensitivity NGS Fragment Analysis Kit (Advanced Analytical, #DNF-474) and measured using a Qubit dsDNA HS Assay Kit (Invitrogen, #Q32851) prior to pooling and sequencing using the Illumina NextSeq 500 platform using a custom primer and the High Output v2 kit (75 cycles) (Illumina, #FC-404-2005). The library loading concentration was 2.4 pM, and the sequencing configuration was as follows: R1 21c / index i7 8c / index i5 8 c/ R2 55c.

In parallel, the same cells were seeded in four independent 96well plates and imaged after 14 days of differentiation to quantify their adipogenic potential (see “*In vitro* adipogenic differentiation of hASPCs”).

Analysis of BRB-seq data

Preprocessing

After sequencing and standard Illumina library demultiplexing, the *fastq* files were aligned to the human reference genome GRCh38 using STAR (Version 2.7.3a), excluding multiple mapped reads. Resulting BAM files were sample-demultiplexed using BRB-seqTools v.1.4 (<https://github.com/DeplanckeLab/BRB-seqTools>) and the “gene expression x samples” read, and UMI count matrices were generated using HTSeq v0.12.4.

General methods

Samples with a too low number of reads or UMIs were filtered out. Genes with a count per million greater than 1 in at least 3 samples were retained. Raw counts were then normalized as log counts per million with a pseudo count of 1, using the function *cpm* from *EdgeR*²²¹ version 3.30.3. If the samples were from different

batches, the raw counts were first normalized using quantile normalization as implemented in voom from the package *limma*²²² version 3.44.3 and then corrected for batch effects using combat from *sva* version 3.36.0. PCAs were computed using prcomp with the parameters center and scale set to TRUE. Differential expression analyses were performed using *DESeq2*²²³ version 1.28.1 and adding batch as a cofactor when necessary.

Scores:

Scores were calculated as the sum of the integrated gene expression scaled between 0 and 1 per gene of the mentioned gene lists. For **Supp. Fig. 2.2.3A** the top differentially expressed genes of murine fat depots populations identified based on the integration of 3 scRNA-seq datasets and published in Ferrero et al.¹⁴⁶ were used to compute the cell type scores.

Gene expression heatmaps:

Heatmaps display row-normalized expression and were generated using pheatmap version 1.0.12. The columns and rows were clustered using the method “ward.2D” of hclust of the package *stats*.

Gene set enrichment analysis:

Gene set enrichment analysis was performed using the package *clusterprofiler*²²⁴ version 3.16.1.

scRNA-seq of SVF Lin[−] cells

SVF Lin[−] cells from different depots and donors were enriched with either FACS or MACS (**Table 2.2**) and resuspended in 1% human albumin in DPBS solution prior to be loaded into the Chromium Single Cell Gene Expression Solution (10x Genomics), following the manufacturer’s recommendations targeting a recovery of 4000 to 5000 cells per run. scRNA-seq libraries were obtained following the 10x Genomics recommended protocol, using the reagents included in the Chromium Single Cell 3’ v3 Reagent Kit. Libraries were sequenced on the NextSeq 500 v2 (Illumina) instrument using 150 cycles (18 bp barcode + UMI, and 132-bp transcript 3’ end), obtaining ~5 × 10⁸ raw reads.

Analysis of scRNA-seq data

Analysis of the datasets individually

Raw fastqs were processed using the default CellRanger pipeline (v 2.1.0, 10X Genomics, Pleasanton, CA). The same transcriptome version was used to align all the datasets (GRCh38.92). All the data were then loaded on R (R version 3.6.1). Cells were filtered for the number of Unique Molecular Identifiers (UMIs) and genes using isOutlier from the package *scater*, which determines which values in a numeric vector are outliers based on the median absolute deviation (MAD) (nmads set between 3 and 4), and filters for too high a percentage

of UMIs mapping to mitochondrial RNA (~10%) or ribosomal RNA (~20%) or too low a percentage of UMIs mapping to protein-coding genes (~80%).

The datasets were first analyzed one by one using the Seurat pipeline¹⁰³. After cell filtering, only genes expressed in at least 3 cells were kept. The data were scaled for the number of UMIs and features using the function `ScaleData` and the remaining default parameters. The first 50 principal components of the PCA were computed using `RunPCA`, and then evaluated for significance using the `JackStraw` function of Seurat. Only the first PCs successively having a p-value < 0.05 among the top 50 PCs were selected for downstream analysis. Clustering was performed using `FindNeighbors`. The robustness of the clustering was assessed using `clustree` displaying the relationship between the clusters with increasing resolution. Differential expression analysis was computed using the `FindAllMarkers` function of Seurat for the selected clustering. Only genes detected as differentially expressed ($\log_2FC > \log_2(1.2)$, $p_{adj} < 0.05$) for both the Likelihood-ratio test (`test.use = "bimod"`) and Wilcoxon Rank Sum test (`test.use = "wilcox"`) were selected.

Each sample was processed and sequenced individually, with the exception of the samples PR - D30 and PR - D61. The isolated cells of these two samples and donors were mixed. The cells were identified as belonging to each donor post-processing based on two criteria: the results of the clustering of the dataset, which clearly separated the cells from the two individuals, and the expression of *XIST* as the two donors were of the opposite sex. Cells ambiguously assigned to a donor (i.e, having a positive expression of *XIST* while clustering with the cells of the donor patient or the opposite) were filtered out.

Comparison of top markers of individual datasets

For each pair of subpopulations and dataset, the percentage of shared markers between their top 100 differentially expressed genes with the highest FC were calculated and displayed on **Supp. Fig. 2.2.1D-F**.

Scmap

The *Scmap* package²²⁵ was used to project the cells of a dataset X onto the identified subpopulations of a dataset Y. Each pair of dataset X, Y and its inverse Y, X were computed. More precisely, the datasets were normalized using the "Single-cell Analysis Toolkit for Gene Expression Data in R" (*scater* package). The data were log normalized using the `logNormCounts` functions using the size factor estimated with `computeSumFactors`. The 1000 most informative features of each dataset were selected using the `selectFeatures` function of *scmap*, which is based on a modified version of the *M3Drop* method. The centroids of each cluster for each dataset were calculated with the function `indexCluster`, and finally, the datasets were projected onto one another using the function `scmapCluster`.

Data integration

The datasets from each individual patient and depot, at the exception of GB-D07 (due to a very low number of captured ASPCs), were integrated following the standard workflow of Seurat pipeline. The datasets were

normalized in log scale with a scale factor of 10000. The top 2000 highly variable genes were selected using the `FindVariableFeatures` function with the parameter `selection.methods` set to “vst”. The anchors were identified using `FindIntegrationAnchors`. The top 2000 variable features identified by `SelectIntegrationFeatures` and the first 60 principal components of the PCA were used as input to perform canonical correlation analysis. The integrated data computed by `IntegrateData` were then used for dimensionality reduction and clustering based on the first 60 principal components of the PCA. Clustering was computed for different clustering resolutions. The final clustering result was based on the clustering results at different resolutions depending on the robustness of the clusters and the specificity of their differentially expressed markers. Top differentially expressed genes were identified using the `FindConservedMarkers` function of Seurat after setting the default assay to RNA, the adjusted p-values were combined using Tippet’s method as implemented by the function `minimump` from *metap* R package (`meta.method = metap::minimump`)²²⁶. Only groups of cells with at least 10 cells were tested (`min.cells.group = 10`). Specifically, for the *IGFBP2*+ cell cluster, as we found only a few cells per batch and we focused on that cell type in part of the manuscript, DEGs were further computed using *EdgeR* and correcting for batch. More precisely, genes not expressed in at least 2% of the cells were filtered out using the function `filterByExpr`. After converting the count matrix into a `DGEList` using `DGEList`, the data were normalized with `calcNormFactors`. The design matrix was defined following the formula $\sim 0 + \text{clust} + \text{batch}$, where `clust` corresponds to the cluster of every cell and `batch` to its dataset (as individually shown on **Supp. Fig. 2.2.1A**). The dispersion was estimated using `estimateDisp`. The quasi-likelihood negative binomial generalized log-linear model was fitted using `glmQLFit`, followed by the quasi-likelihood *F*-test `glmQLFtest` contrasting the *IGFBP2*+ cluster *versus* the other clusters (pondered by the number of clusters).

Identification of depot-specific markers for ASCs and PreAs

DEG analysis was performed on the integrated data, by selecting the cells of the population of interest (ASCs or PreAs) and contrasting between all possible pairs of depots using the function `FindMarkers` of Seurat. This is possible as we have 3 replicates for SC, OM, PR, and 2 for MC, however, for the latter, those were coming from two biological samples from the same donor. A set of markers was considered depot-specific when significantly differentially expressed in a depot *versus* any other depot. A gene was defined as differentially expressed when its average log Fold Change (defined as the average of the log Fold Change in each replicate) was positive and an adjusted p-value smaller than 0.05.

Comparison with murine ASPCs

a. Murine data integration

The integration of five datasets of adult mouse SC and OM ATs provided by Schwalie et al.¹⁰², Burl et al.¹⁰⁰, Hepler et al.¹⁴⁷ and Merrick et al.⁹⁶ was performed as described in Ferrero et al.¹⁴⁶. The clustering originally published in Ferrero et al.¹⁴⁶, focusing on ASPCs, merged the cells close to endothelial cells into one main cluster. The clustering was here revised to include vascular smooth muscle progenitor cells. For consistency

with the human data, the top markers of the subpopulation were computed as defined above. The top markers were ordered by the average of the \log_2 Fold Change of each dataset.

b. Score

Scores of the mouse ASPC subpopulations, mesothelial cells, and vascular smooth muscle progenitor cells were based on their human orthologs and calculated as the sum of the gene expression scaled between 0 and 1 per gene of the top markers (average \log_2 Fold Change across batches > 0 and adjusted p-value < 0.05) of each murine ASPC subpopulation (ASCs, PreAs, Aregs, *Ifit+*, and *Cilp+* ASCs), mesothelial cells and vascular smooth muscle progenitor cells. The scores were then scaled by the number of genes on each list.

Comparison with the dataset from Emont et al.¹⁴⁵

The whole human single-nucleus/cell dataset (here reported as “scRNA-seq”) provided by Emont *et al.*¹⁴⁵ was downloaded on the single cell portal (study no. [SCP1376](#), All cells). The dataset was then subsetted for the cells defined as ASPC or mesothelium by the authors (as defined in the metadata “cell_type2”), and the PCA was recomputed as well as clustering, tSNE and UMAP with the first 50 PCs as input. First, an *IGFBP2* expression score was computed using the AddModuleScore function. The dataset containing only ASPCs, and mesothelial cells was then split by samples, and the symbol gene IDs were converted to Ensembl ID using the GRCh38 release 92 from the Ensembl gene annotation as reference. The few genes with no corresponding Ensembl IDs were filtered out, and, in the rare case of two corresponding Ensembl IDs, only one was kept. Each sample was log normalized with the default normalization of the *Seurat* package and then scaled for the features selected using SelectIntegrationFeatures with each of the samples of Emont et al.¹⁴⁵ and our generated single-cell SC and OM datasets as input. The first 50 PCs were computed based on the scaled data. Clustering was performed following the default Seurat clustering pipeline for resolutions spanning from 0.1 to 3. Each sample of the Emont et al.¹⁴⁵ dataset was then projected on our integration (see *Analysis of single-cell RNA-seq, Data integration*), using the FindTransferAnchors and TransferData functions of the *Seurat* package with the default parameters.

Trajectory analysis

Trajectory analysis was performed on the integrated normalized data subsetting for Epiploic samples. Potential doublets were excluded from the analysis using DoubletFinder²²⁷ on each epiploic scRNA-seq dataset individually. Cells labeled as ASCs, PreAs, *IGFBP2+* cells, Mesothelial cells, and VSMPs were selected. The first 50 PCs were computed using the *pca* function of *scanpy*²²⁸ and the neighborhood graph was computed with the default parameters (pp.neighbors). The connectivity between our defined cell classifications was computed using the *paga* function¹⁷⁹, and low-connectivity edges were thresholded at 0.03. We computed the ForceAtlas2 (FA2) graph²²⁹ using PAGA-initialization (draw_graph). The *Dynverse* package²³⁰ was used to compute the most variable genes along the branch connecting PreAs and Mesothelial cells through *IGFBP2+* cells (calculate_branch_feature_importance).

FACS sorting of human SVF subpopulations

SVF cells were resuspended in 1% albumin solution to the concentration of 10^5 cells/ml, and the staining antibody panels (**Table 2.4**) were added in titration-determined quantities. The cells were incubated with the cocktail of antibodies on ice for 30 min protected from light, after which they were washed and stained with propidium iodide (Molecular Probes #P3566) for assessing viability, and subjected to FACS using a Becton Dickinson FACS Aria II sorter or a MoFlo Astrios EQ, Cell Sorter - Beckman Coulter. Compensation measurements were performed for single stains using compensation beads (eBiosciences #01-2222-42).

The following gating strategy was applied while sorting the cells: first, the cells were selected based on their size and granularity or complexity (side and forward scatter), and then any event that could represent more than one cell was eliminated. Next, the live cells were selected based on propidium iodide negativity, and from those, the Lin[−](CD31[−]/CD45[−]) population was selected. At first, all SC, OM, and PR cells were stained with the OM-specific panel, including mesothelial markers, but since SC and PR SVF cells were consistently negative for the TM4SF1 and MSLN markers over three consecutive experiments, SC and PR cells were only stained with the SC and PR panels, respectively (**Table 2.4**). For the SC samples, from the Lin[−] fraction of cells, Lin[−]/CD26⁺, Lin[−]/VAP1⁺, Lin[−]/DN, and Lin[−]/HHIP⁺ cells were defined against unstained controls and FMO controls. For the PR samples, from the Lin[−] fraction of cells, Lin[−]/CD26⁺, Lin[−]/VAP1⁺, and Lin[−]/DN cells were defined against unstained controls and FMO controls. For the OM samples, OM-specific subpopulations were first isolated from the Lin[−] gate as Lin[−]/TM4SF1⁺/MSLN[−] and Lin[−]/TM4SF1⁺/MSLN⁺ populations. From the remaining Lin[−]/TM4SF1[−] gate, we then isolated Lin[−]/TM4SF1[−]/CD26⁺, Lin[−]/TM4SF1[−]/VAP1⁺, and Lin[−]/TM4SF1[−]/DN cells. Acquired FCS files were analyzed using FlowJo software to infer population abundances that were plotted using GraphPad Prism.

In vitro adipogenic differentiation and chemical treatments of hASPCs

Cells were seeded for adipogenic differentiation at high density (65k cells /cm²) in 3-5 replicate wells of a 96-well black plate (Corning #353219). After 48h or when cells were confluent for at least 24h, cells were treated with induction cocktail (high glucose DMEM (#61965), 10% FBS, 50 µg/ml Primocin, 0.5 mM IBMX (Sigma #15879), 1 µM dexamethasone (Sigma #D2915), 1.7 µM insulin (Sigma #19278), 0.2 mM indomethacin (Sigma #I7378) for 7 days, followed by a maintenance cocktail (high glucose DMEM, 10% FBS, 50 µg/ml Primocin, 1.7 µM insulin) for another 7 days. No medium refreshment was performed between these two timepoints. For the chemical treatments, the above-mentioned differentiation and maintenance cocktails were supplemented with the recombinant IGFBP2 protein at 1nM (R&D, #674-B2-025), recombinant IGF-I protein at 10nM (Sigma, #I3769), recombinant IGF-II protein at 10nM (R&D, #292-G2-050), Blocking anti-human IGFBP2 antibody (scavenging) 1 mg/ml (R&D, #AF674) and Echistatin 100 nM (R&D, #3202). Chemicals were added to both induction and maintenance cocktails except for Echistatin which was added to the

induction cocktail only and withdrawn 48h after induction since inhibiting the integrin receptor resulted in cell detachment when Echistatin was kept in culture for longer periods than 48h. In the Echistatin mixed with IGFBP2 condition, only IGFBP2 was kept after 48h. IGFBP2, IGF-I and IGF-II were first titrated at the concentrations shown in **Supp. Fig. 2.5.2**.

Cell proliferation assay

Sorted cells were split into four and seeded in 4 different wells of a 12well plate and allowed to attach and start to proliferate for 7 to 10 days. One well of each cell population was trypsinized after this period. Cells were resuspended in 1 ml of medium, counted twice using a hemacytometer, and the mean count was used as the baseline number of cells from which cell increase was calculated. The same counting was performed on the remaining wells every two days. The expansion medium was refreshed every two days.

Mixing and transwell experiments

For the mixing experiments, unexpanded Lin[−] SVF cells were isolated with MACS using Miltenyi LD columns (Miltenyi, #130-042-901) on manual mono-MACS separators after staining with magnetic anti-human CD45 and CD31 microbeads (Miltenyi, #130-045-801 and #130-091-935) according to the manufacturer's protocol. MACS-isolated Lin[−] cells from SC, OM, and PR samples were counted in duplicates and mixed at high density (65k cells /cm²) in 11 ratios from 0 to 100%. After 24h, the cells were induced to differentiate following the adipogenic differentiation protocol. For the transwell experiments, we used 96well plate format transwell inserts with 0.4 mm (Corning #CLS3391) pores to allow protein and small molecule diffusion through the membrane, but not cell migration. 96well transwell-receiving plates (Corning #3382) were first coated with type I collagen (Corning #354249) 1:500 in DPBS before use to facilitate cell adhesion. Sorted donor OM subpopulations and expanded receiver SC and PR SVF-adherent cells were plated and expanded separately onto the top transwell insert and the bottom receiving plate, respectively. When confluent, the transwell insert was put in contact with the receiver plate, and all cells were induced to differentiate following the listed differentiation protocol.

Enzyme-linked immunosorbent assay (ELISA)

For the supernatant measure, cells were expanded for two passages and seeded into a 6well plate. Once confluent, the expansion medium was aspirated, and wells were washed twice with PBS to ensure residual serum, dead cell and protein removal. 2ml of OPTI-Pro serum-free medium (Thermo, #12309050) was added to each well and incubated with the cells at 37°C for 48h. After incubation, SFM medium was harvested, spun for 10 min at 4°C max speed to clear potential cell debris. Cleared supernatant was aliquoted and stored at -80°C until further usage. For the whole AT IGFBP2 secretion assays, three times 200-400 mg of OM AT were put in 500ml of DPBS (Gibco #14190169) and incubated at 37°C for 24, 48 and 72 hours. After incubation,

DPBS was harvested, spun for 10 min at 4°C max speed to clear potential cell debris and stored at -80°C until further usage. The Anti-human IGFBP2 ELISA kit (Sigma, #RAB0233-1KT) was used to quantify IGFBP2 protein in the supernatants according to the manufacturer's recommendations. Before loading samples on the ELISA membranes, the total protein concentration was quantified using the Qubit™ Protein Broad Range assay kit (Thermo, #A50669) and 300 ng of total protein was added per reaction. Incubation of samples with primary antibodies was performed O/N at 4°C. At the end of the assay, absorbance was read at 450 nm using a SPARK® Microplate reader.

Immunohistochemistry

Human AT biopsies were washed twice in PBS to remove excess blood and divided in 50 to 100 mg for fixation in 4% PFA (paraformaldehyde, electron microscopy grade (VWR #100504-858)) for 2 hours at 4°C with gentle shaking. Next, the tissue was washed with PBS and incubated with 30% sucrose O/N at 4°C with gentle shaking. Cryoblocks were prepared using Cryomatrix (Thermo Fisher Scientific #6769006), and 25-µm sections were generated using a Leica CM3050S cryostat at -30°C. The tissue was air-dried for 30 min at -20°C in the cryostat itself, then 1h at RT. Slides were additionally fixed 10 min in 4% PFA at RT, washed two times 5 minutes with PBS, permeabilized at RT with 0.25% TritonX100 (Sigma #T9284) for 10 minutes, washed twice with PBS again and antigen blocking was performed at RT for 30 min with 1% BSA in PBS. Primary antibodies (anti-TM4SF1, anti-MSLN, anti-PLIN1) in 1% BSA were applied O/N at 4°C with gentle shaking following the titrations indicated in **Table 2.4**. The following day, after two PBS washes, and quick 1% BSA dip, the secondary antibody (anti-rabbit AF-647) in 1% BSA was applied for 40 min at RT following the titrations in **Table 2.4**. Nuclei were stained with 1mg/ml DAPI (Sigma #D9564) for 10 min and washed twice in PBS prior to mounting with Fluoromount G (Southern Biotech #0100-01). The slides were then imaged with a Leica SP8 Inverted confocal microscope (objectives: HC PL Fluotar 10x/0.30 air, HC PL APO 20x/0.75 air, HC PL APO 40x/1.25 glyc, HC PL APO 63x/1.40 oil). The results presented in **Fig. 2.4K** and **Supp. Fig. 2.4.7** were replicated in at least three independent experiments. We note that we also verified that the signal we detected is not the result of autofluorescence of the AT or from unspecific binding of secondary antibodies (**Supp. Fig. 2.4.7**).

Imaging and quantification of *in vitro* adipogenesis

On the 14th day of differentiation, cells were either fixed with 4% PFA (EMS, #15710) and stained at a later timepoint or live-stained with fluorescence dyes: Bodipy 10 mg/ml (boron-dipyrromethene, Invitrogen #D3922) for lipids and Hoechst 1 mg/ml (Sigma, #B2883) for nuclei. Cells were incubated with the dyes in PBS, for 30 min in the dark, washed twice with PBS, and imaged. If the imaging was performed on live cells, we used FluoroBrite DMEM (Gibco # A1896701) supplemented with 10% FBS as acquisition medium. Given substantial variation in the extent of lipid accumulation by the tested cell fractions (within the same well but also across technical replicates), the imaging was optimized to cover the largest surface possible of the 96

well. Moreover, a z-stack acquisition in a spinning-disc mode and Z-projection were performed in order to capture the extent of *in vitro* adipogenesis with the highest possible accuracy. Specifically, the automated platform Operetta (Perkin Elmer) was used for imaging. First, 3–6 z-stacks were acquired for every field of view in a confocal mode of the microscope in order to produce high-quality images for downstream z-projection and accurate thresholding. Next, 25 images per well were acquired using a Plan Neofluar 10× Air, NA 0.35 objective for the transwell-receiving plates or 20× air objective NA 0.8 for normal 96w plates (Falcon, #353219), with no overlap for further tiling and with the aim of covering the majority of the well for an accurate representation of lipid accumulation (see **Methods** in ^{148,231}). The lasers were set in time exposure and power to assure that in both the Hoechst and the Bodipy channels, the pixel intensity was between 500 and 4000, and in all cases at least two times higher than the surrounding background. The images, supported by Harmony software, were exported as TIFF files. They were subsequently tiled, and Z-projected with the maximum intensity method. To accurately estimate and represent differences in adipocyte differentiation, a quantification algorithm for image treatment was developed in collaboration with the EPFL BIOP imaging facility. In brief, image analysis was performed in ImageJ/Fiji, lipid droplets (yellow) and nuclei (blue) images were filtered using a Gaussian blur (sigma equal to 2 and 3, respectively) before automatic thresholding. The automatic thresholding algorithm selections were chosen based on visual inspection of output images. The area corresponding to the thresholded lipid signal was then divided by the area corresponding to the thresholded nuclei area and used to calculate the Adiposcore ($\text{totalLipidArea}/\text{totalNucleiArea}$). In the figures, representative blown-up cropped images of each sample are shown. To reduce technical variation across the biological replicates (different donors), adiposcores were normalized to the average adiposcore of the indicated control when we compared conditions within highly differentiating lines like SC and PR. Adiposcores were compared without normalization when we wanted to directly compare adiposcores across depots (i.e., **Fig. 2.1C**) or among poorly-differentiating samples like OM when the absolute values of adiposcores were < 0.01 (**Fig. 2.4D**, **Fig. 2.5J**, **N** and **P**, and **Supp. Fig. 2.1.2B**, and **Supp. Fig. 2.1.3**).

siRNA-mediated knockdown

To achieve knockdown of IGFBP2, direct transfection was performed on OM SVF Lin[−]/TM4SF1⁺/MSLN[−] cells using the IGFBP2 IDT, TriFECTA DsiRNAs kit using 3 pooled siRNAs: hs.Ri.IGFBP2.13.1, hs.Ri.IGFBP2.13.2, hs.Ri.IGFBP2.13.3. In brief, after sorting, cells were expanded for one or two rounds, then harvested and plated at mid-low density (45k cells/cm²) and allowed to adhere. The following day, transfection mix was prepared as Opti-MEM medium (Invitrogen #31985062), 1.5% Lipofectamine RNAiMAX (Invitrogen #13778150) and 20 nM of the pooled siRNAs. In the transfection mix, lipofectamine-siRNA transfection particles were allowed to form for 15 min at RT with gentle shaking. After incubation, the transfection mix was diluted 10 times (to a final concentration of siRNA of 2 nM) in MEMalpha GlutaMax medium (Gibco #32561037) supplemented with 2.5% human platelet lysate (Sigma #SCM152), w/o antibiotics and

exchanged to the plated cell medium. After 48h, medium was changed to differentiation medium (for the transwell assay), with serum free medium (for ELISA validation) or directly taken in TRIzol (for qPCR validation).

RNA isolation and qPCR

Expanded OM and SC SVF-adherent, OM SVF Lin⁻/TM4SF1⁻/MSLN⁻, OM SVF Lin⁻/TM4SF1⁺/MSLN⁻ cells as well as cells subjected to siRNA-mediated knockdowns 48h post-transfection were collected into TRIzol (Sigma, #T3934). The direct-zol RNA kit (Zymo Research #R2062) was used to extract RNA, followed by reverse transcription using the SuperScript II VILO cDNA Synthesis Kit (Invitrogen # 11754050). Expression levels of mRNA were assessed by real-time PCR using the PowerUp SYBR Green Master Mix (Thermo Fisher Scientific #A25743). mRNA expression was normalized to the *Hprt1* gene. Primer sequences used: *IGFBP2* – Fw CGAGGGCACTTGTGAGAAGCG, Rv TGTTTCATGGTGCTGTCCACGTG; *HPRT* – Fw CAGCCCTGGCGTCGTGATTA, Rv GTGATGGCCTCCCATCTCCTT.

Statistical methods

The experiments were not randomized, and the investigators were not blinded in experiments. The paired Student's *t*-test was used to determine statistical differences between two groups, with the null hypothesis being that the two groups are equal. Multiple comparisons were corrected using false discovery rate (FDR) correction. When specified, one-way ANOVA or RELM test followed by Tukey honest significant difference (HSD) post hoc correction was applied, the null hypothesis being defined so that the difference of means was zero. (Adjusted) **p*-value < 0.05, ***p*-value < 0.01, ****p*-value < 0.001 were considered statistically significant. All boxplots display the mean as a dark band, the box shows the 25th and 75th percentiles, while the whiskers indicate the minimum and maximum data points in the considered dataset excluding outliers. All bar plots display the mean value and the standard deviation from the mean as error bar.

2.6 Miscellaneous

Acknowledgment

The authors thank the EPFL and UNIL Core Facilities: FCCF (Flow Cytometry Core Facility EPFL, especially Miguel Garcia), FCF (Flow Cytometry Facility, especially Danny Labes), BIOP (BioImaging and Optics Platform, especially Olivier Buri, Romain Guiet and José Artacho), GECF (Gene Expression Core Facility, especially Bastien Mangeat and Elisa Cora), HCF (Histology Core Facility, especially Jessica Dessimoz). Open access funding provided by EPFL, a Leenaards Foundation MD-PhD Fellowship to R.F. (#531466) and a Leenaards Prize for Biomedical Translational Research to B.D. (Project #5154.5), a Personalized Health and Related Technologies (PHRT) PhD student fellowship (#2017/307) to P.R. and PHRT Grants (#2017/502 & #2019/719) to B.D., as well as a Swiss National Science Foundation Project grant (#310030_182655) to B.D.

Authors contributions

R.F., P.R. and B.D. designed the study and wrote the manuscript. R.F. conducted all experimental procedures and analyzed acquired images, flow cytometric measures, qPCRs, ELISAs and immunohistochemistry. P.R. conducted all analyses related to transcriptomics both at the single-cell and bulk levels. J.R. and M.Z. assisted with sample processing, cell culture and preparation of sequencing libraries. J.R. performed histological assays. J.P. provided assistance with flow cytometry-related procedures. D.A. and V.G. assisted with bulk transcriptomic-associated procedures and data processing. V.G. and W.S. assisted with the transcriptomic analyses. L.F., S.M., T. Z., N.P., M.S. and M.M. provided access to human samples. V.G., W.S. and C.C. provided extensive comments to the manuscript.

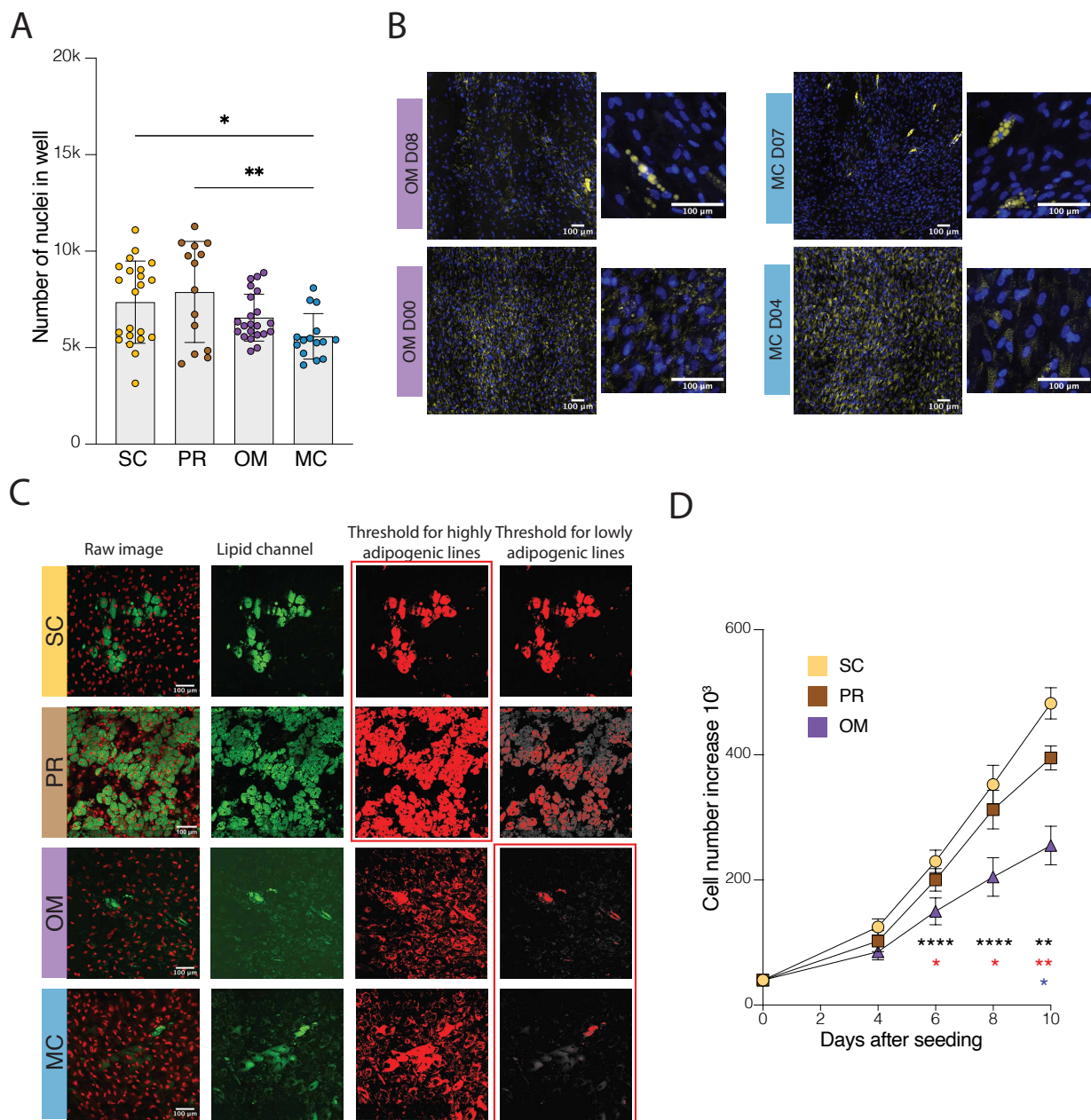
Corresponding author

Bart Deplancke

Competing interest declaration

The authors declare to have no conflict of interest.

2.7 Supplementary Figures and Tables



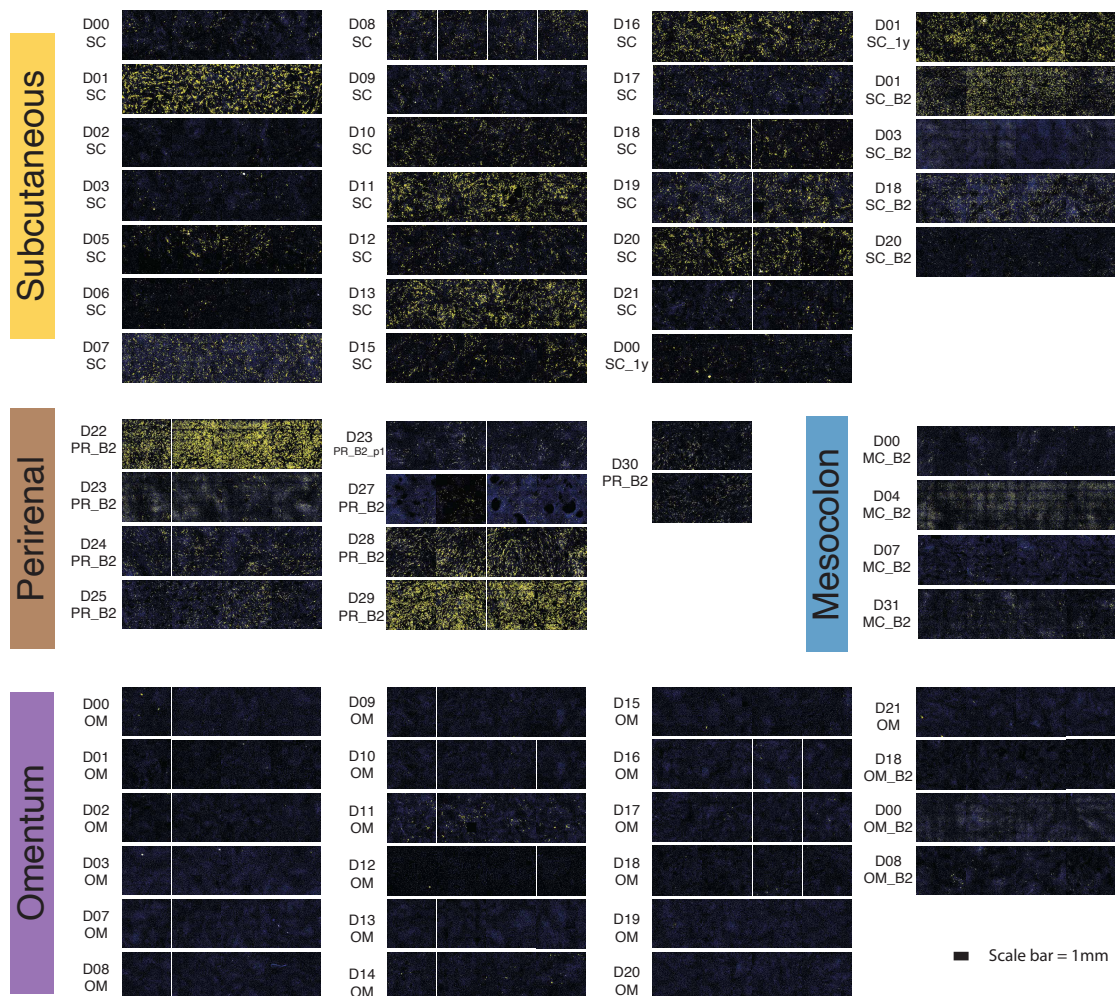
Supplementary Figure 2.1.1 – Across depot comparisons of SVF-adherent cells at low passage.

- (A) Total number of nuclei in each well (see **Methods** for more details) of images in **Fig. 2.1B**; $n=14-22$, 4-5 donors, 3-5 independent wells.
- (B) Representative confocal images of intraperitoneal OM- and MC-derived SVF-adherent cells after 14 days of differentiation; Top: lines that form very few mature lipid droplets, Bottom: lines that form small lipid droplets that are barely distinguishable from background; Yellow - Bodipy stains for lipids, blue - Hoechst stains for DNA.
- (C) Image-processing steps to define what signal from the lipid channel is considered as fully formed lipid droplets and which is not. Red squares indicate the thresholding parameters chosen for the final analysis to exclude background from the low adipogenic lines and to not underestimate the lipid area of the highly differentiating lines (PR). In the first two columns, green denotes lipids, red nuclei, and in the last two columns, red is the signal measured above the defined threshold (see **Methods**).

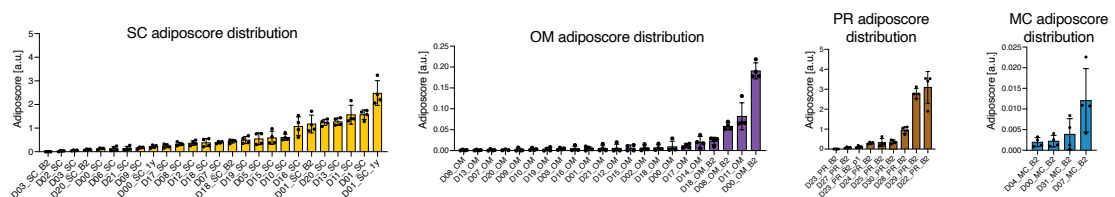
(D) Relative cell number increase over time of culture for SC, OM, and PR SVF-adherent cells; n=12, 4 donors per depot; Black stars compare SC versus OM, Red: PR versus OM, Blue: SC versus PR.

* $p \leq 0.05$, ** $p \leq 0.01$, *** $p \leq 0.001$, **** $p \leq 0.0001$, One-Way ANOVA and Tukey HSD *post hoc* test (A), and RELM analysis and Tukey HSD *post hoc* test (D).

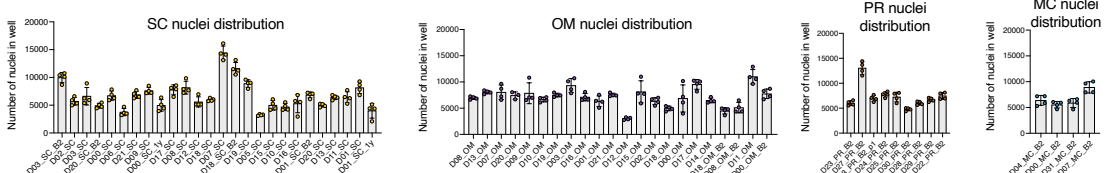
A



B



C

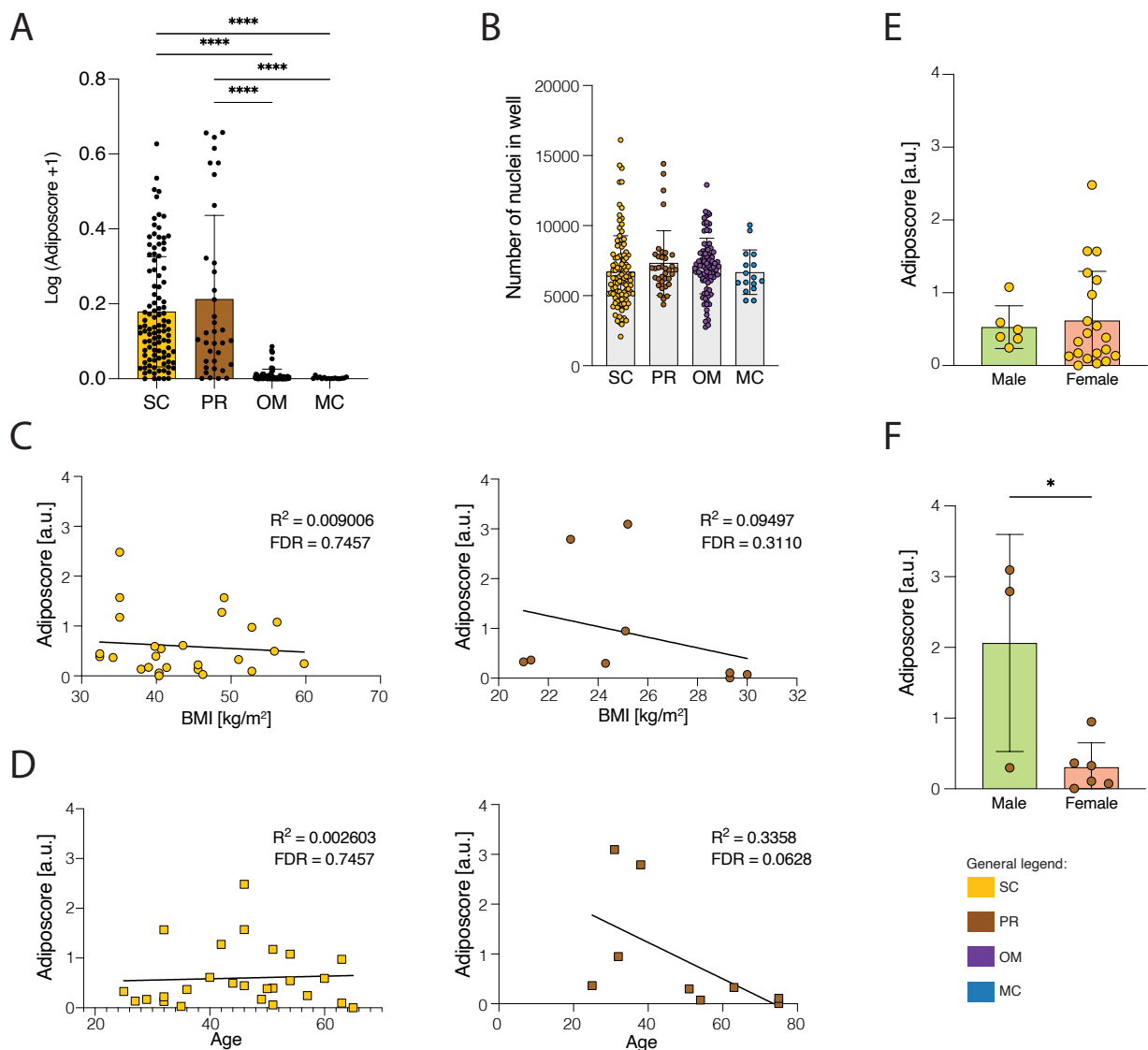


Supplementary Figure 2.1.2 – Adipogenic differentiation potential of cell lines is highly variable across individual donors.

- (A) Full well images of four independent wells after image processing (25 merged Z-projected tiles taken with a 20x objective, see **Materials and Methods**) enabling us to quantify the adipogenic potential of each cell line that was analyzed by BRB-seq18 after 14 days of adipogenic differentiation. The cells were differentiated after 2 to 6 passages. The blue color represents the signal above threshold for the DNA stain, and the yellow color represents the signal above threshold for the lipid stain. Subcutaneous, yellow (SC): n=104, 4 independent wells, 26 cell lines, 20 donors (D); Perirenal, brown (PR): n=36, 4 independent wells, 9 cell lines, 8 donors; Omentum, purple (OM): n=88, 4 independent wells, 22 cell lines, 18 donors;

Mesocolon, blue (MC): n=16, 4 independent wells, 4 cell lines, 4 donors; Scale bar=1 mm. B2 indicates the second biological replicate of a certain line, and 1y indicates the few samples from patient 1 year post bariatric surgery.

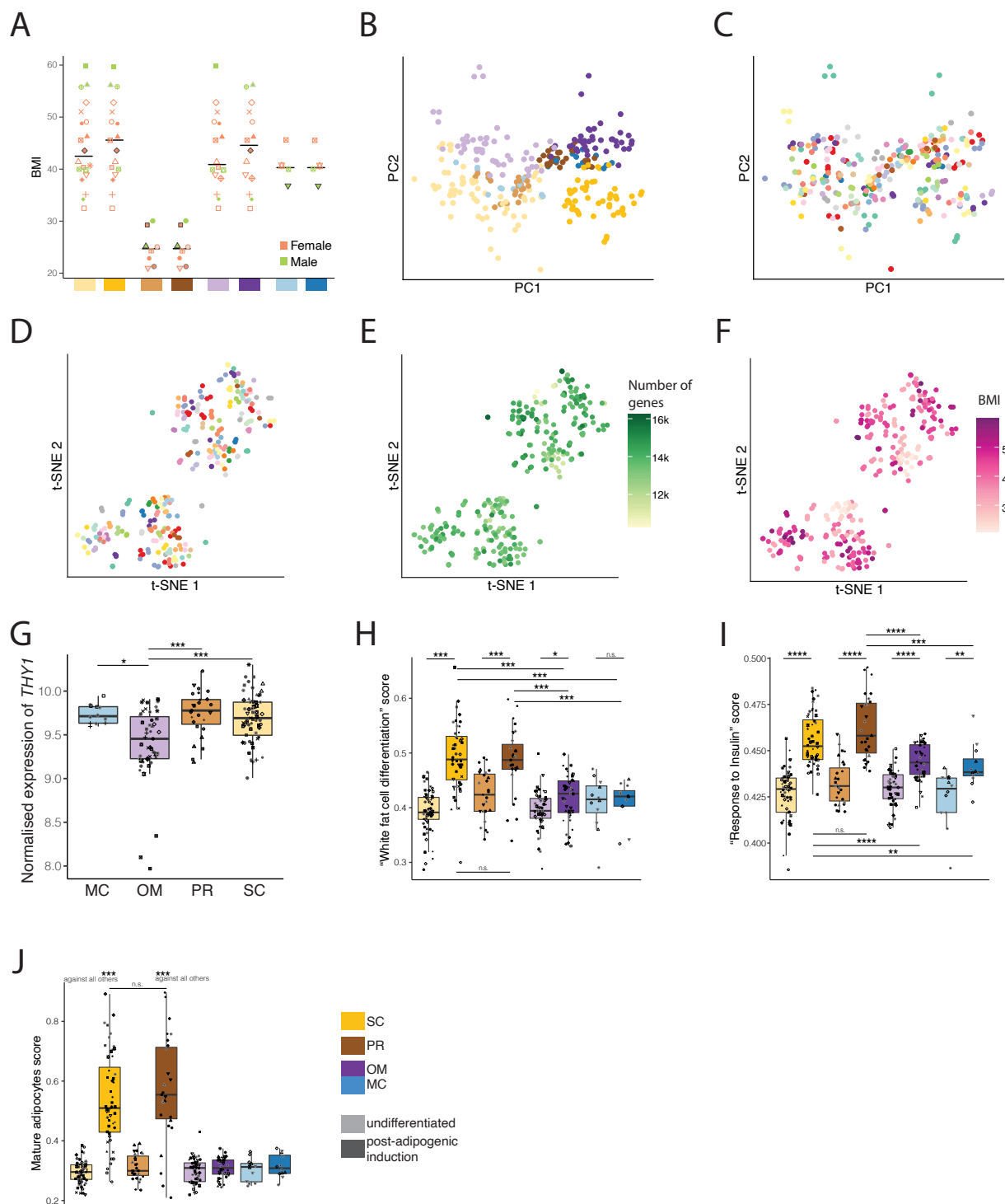
- (B)** Distribution of the ratios between the total lipid area and the total DNA area measured in the images shown in A, i.e., adiposcore (see **Methods** for more details), ordered by increasing values across all cell lines shown in A.
- (C)** Total number of nuclei in each well quantified by segmenting the DNA area above threshold of images in A and plotted in the same order as in B.



Supplementary Figure 2.1.3 – The adipogenic potential of SVF-adherent lines from different depots and their correlation with metadata.

- (A) Quantification of the adipogenic potential derived from images in **Supp. Fig. 2.1.2A** representing differentiated SVF-adherent cells after expansion (passaged 2 to 6 times). On the y axes, the log(adiposcore+1) is plotted. SC: n=104, 4 independent wells, 26 cell lines, 20 donors; PR: n=36, 4 independent wells, 9 cell lines, 8 donors; OM: n=88, 4 independent wells, 22 cell lines, 18 donors; MC: n=16, 4 independent wells, 4 cell lines, 4 donors.
- (B) Total number of nuclei in each well (see **Methods**) of images shown in **Supp. Fig. 2.1.2A**.
- (C) Scatter plot showing the correlation between the adiposcore of highly adipogenic lines (SC - left and PR - right) and the BMI of respective donors. The line represents the linear regression analysis.
- (D) Scatter plot showing the correlation between the adiposcore of highly adipogenic lines (SC - left and PR - right) and the age of respective donors. The line represents a linear regression analysis.
- (E) Barplot showing the distribution of the adiposcore of SC lines between men and women.
- (F) Barplot showing the distribution of the adiposcore of PR lines between men and women.

* $p \leq 0.05$, ** $p \leq 0.01$, *** $p \leq 0.001$, **** $p \leq 0.0001$, and linear regression analysis with its relative goodness of fit, and the FDR-adjusted p-values of the Pearson correlations (C, D), One-Way ANOVA and Tukey HSD post hoc test (E, F).

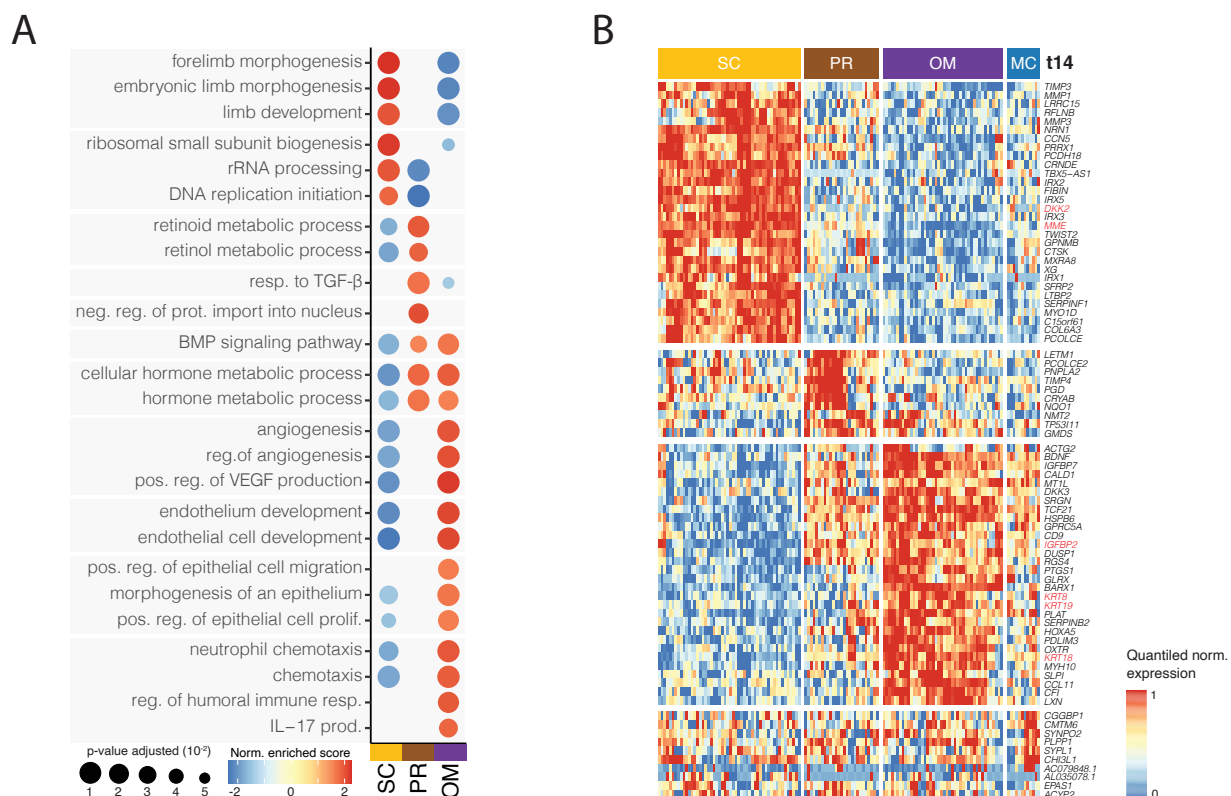


Supplementary Figure 2.1.4 – Human SVF-adherent cells from different depots differentially upregulate the adipogenesis response upon exposure to an adipogenic cocktail.

- (A) Plot showing the number of donors and distribution of their BMI and sex included in the BRB-seq¹⁵⁰ analysis across the different depots and time points.
- (B) PCA based on the BRB-seq¹⁵⁰ data of SVF-adherent cells from the indicated adipose depots (SC - subcutaneous, PR - perirenal, OM - omentum, MC - mesocolic) and indicated time points (t0 - undifferentiated, t14 - 14 days post-adipogenic induction).
- (C) PCA, as described in B, colored by donors.

- (D) t-SNE map shown in **Fig. 2.1D** computed on the 10 first PCs of the PCA displayed in **B**, colored by donors.
- (E) t-SNE map shown in **Fig. 2.1D** colored by the number of detected genes.
- (F) t-SNE map shown in **Fig. 2.1D** colored by the BMI of the donors.
- (G) Boxplot displaying the expression distribution of THY1, a known mesenchymal cell marker, across samples from the indicated depots at t0.
- (H) Boxplots displaying the “white fat cell differentiation score” based on the scaled expression of the genes from the GO term “white fat cell differentiation” (GO:0050872) for the indicated depots and time points (see **Methods**).
- (I) Boxplots displaying the “response to insulin score” based on the scaled expression of the genes from the GO term “response to insulin” (GO:0032868) for the indicated depots and time points (see **Methods**).
- (J) Boxplots displaying the “mature adipocyte score” based on the scaled expression of the following markers: FABP4, PPARG, ADIPOQ, LIPE, LPL, PLIN1, PLIN2, PLIN4, CEBPA, CEBPB, CIDEC, CIDEA, for the indicated depots and time points (see **Methods**).

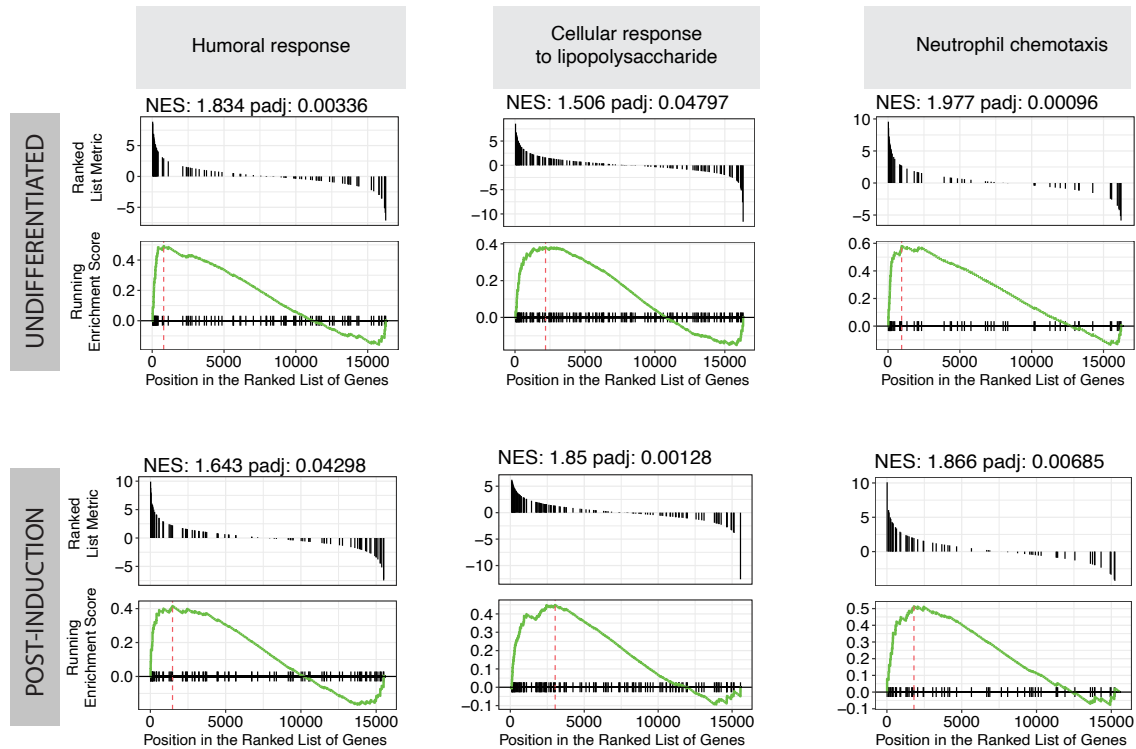
* $p \leq 0.05$, ** $p \leq 0.01$, *** $p \leq 0.001$, **** $p \leq 0.0001$, unpaired two-sided t-test (G-J).



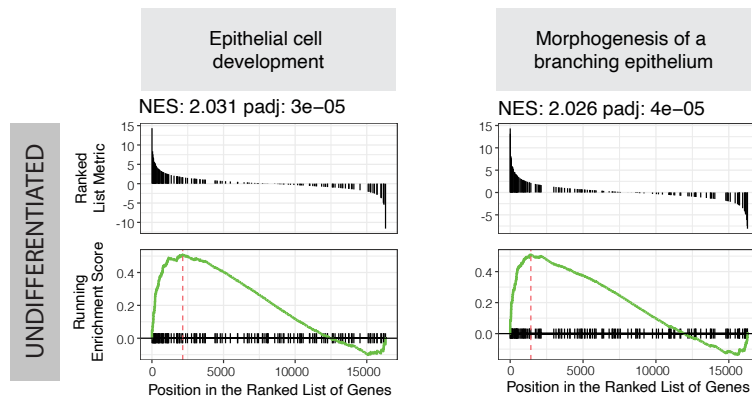
Supplementary Figure 2.1.5 – SVF-adherent cells from different depots have distinct transcriptomic signatures both when undifferentiated and when differentiated.

- (A) Dotplot showing enriched, representative terms that were found by GSEA performed on the differential gene expression analysis results of each indicated depot versus all others at t0 (i.e., undifferentiated state) of the transcriptomic data shown in **Fig. 2.1D**.
- (B) Heatmap of top differentially expressed genes when comparing the indicated adipose depot versus the three others at t14.

A

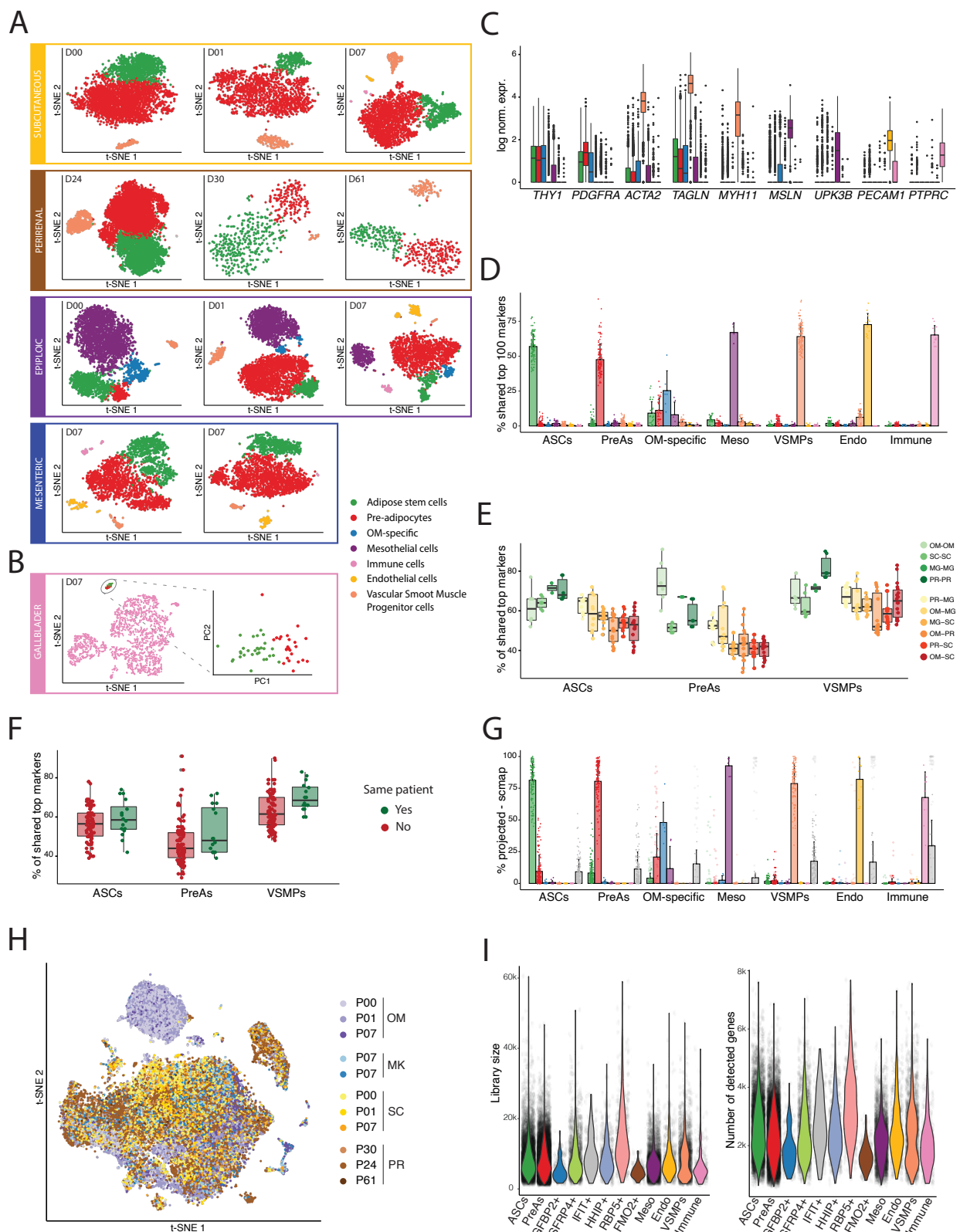


B



Supplementary Figure 2.1.6 – The expression of genes related to “inflammatory response” and “vasculature and epithelium development” is enriched in OM adipose depot-derived cells compared to those from other depots.

- (A) GSEA plot of selected inflammatory response GO terms (“humoral response” GO:0006959, “cellular response to lipopolysaccharides” GO:0071222, “neutrophil chemotaxis” GO:0030593), based on the differential expression analysis of SVF-adherent cells derived from OM adipose depots versus those from other depots (SC, PR, MC) at t0 (i.e., undifferentiated state) or t14 (i.e., post-adipogenic induction).
- (B) GSEA plot of the GO terms “epithelial cell development” (GO:0060429) and “morphogenesis of a branching epithelium” (GO:0048754), based on the differential expression analysis of SVF-adherent cells derived from OM adipose depots versus those from other depots (SC, PR, MC) at t0 (i.e., undifferentiated state).

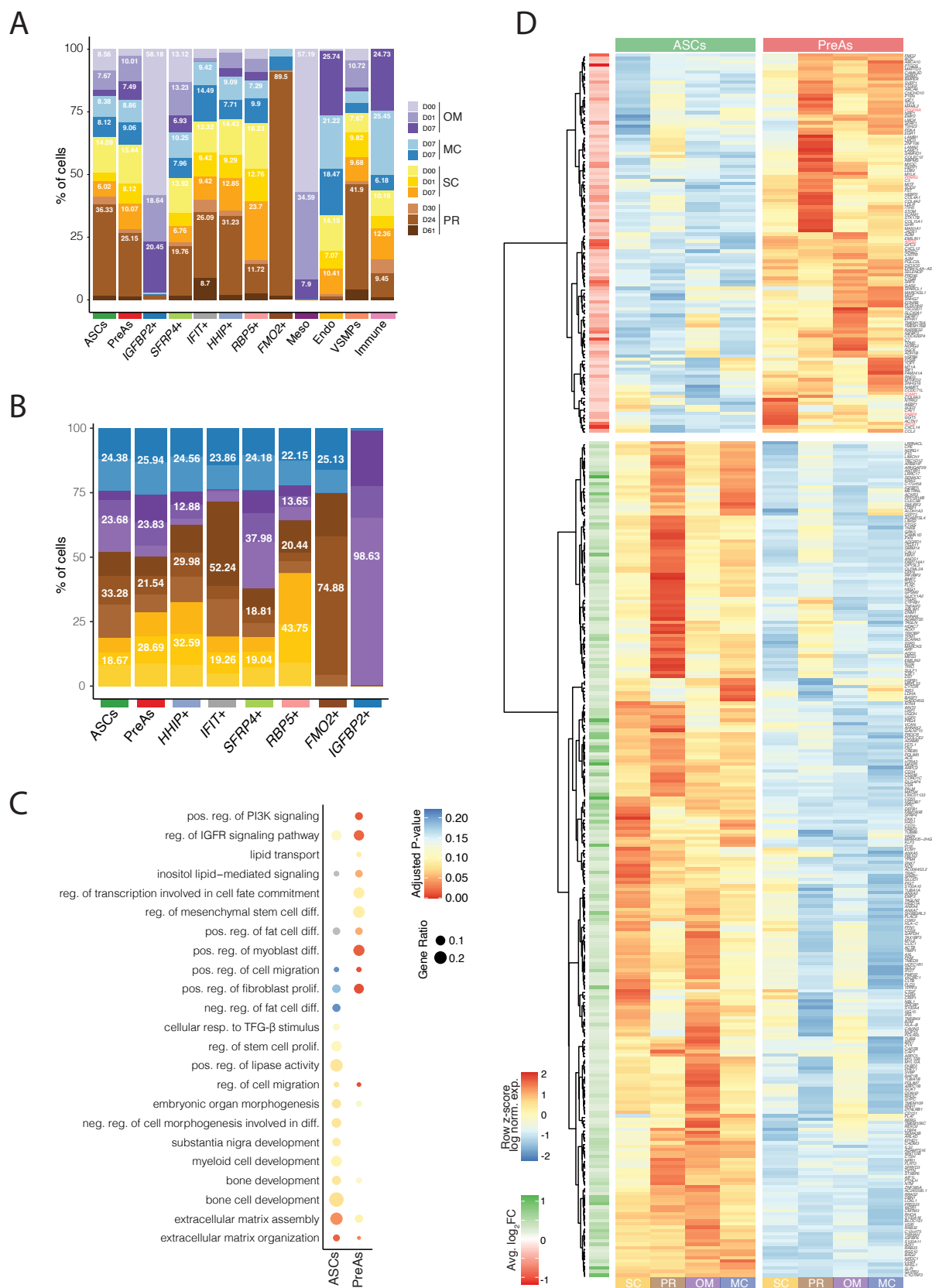


Supplementary Figure 2.2.1 – scRNA-seq reveals common cell populations across adipose depots and donors.

(A) t-SNE cell maps of individual scRNA-seq datasets of SVF Lin⁻ cells isolated from four adipose depots (SC, OM, MC, and PR) and six different donors (D, as indicated in the corner of each t-SNE, see **Table 2.2**), visualizing the identified subpopulations of hASPCs: adipose stem cells (ASCs; green), pre-adipocytes (PreAs; red), OM-specific cells (blue), as well as mesothelial

cells (purple), vascular smooth muscle progenitor cells (VSMPs; dark orange), endothelial (light orange) and immune cells (pink). The number of cells per dataset from top to bottom and by row: 3929, 4169, 2162, 4262, 2042, 2670, 8583, 600, 509, 2650, 2550.

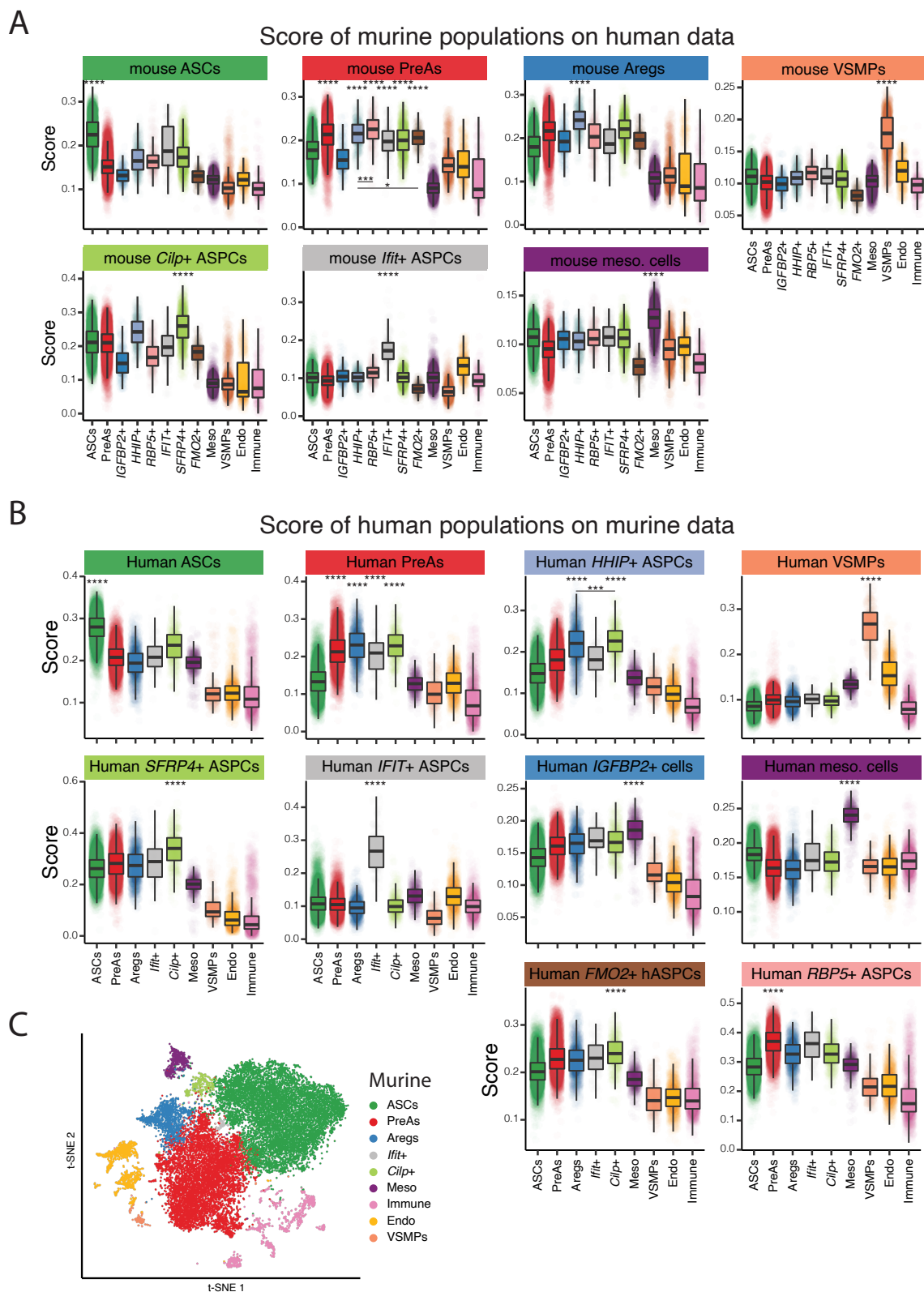
- (B) left - t-SNE cell map of a scRNA-seq dataset of SVF Lin[−] cells isolated from gallbladder-associated adipose tissue from one donor, visualizing the identified populations: immune cells (pink) and hASPCs (ASCs in green and preAs in red). The high proportion of immune cells in the dataset likely reflects a technical artefact where SVF cells may have been under-stained prior to MACS separation; right - PCA of the highlighted hASPCs of the left panel visualizing the two hASPC subpopulations: adipose stem cells (ASCs; green) and pre-adipocytes (PreAs; red), a total of 54 cells.
- (C) Boxplot showing the log normalized gene expression distribution of selected markers in the different hASPC subpopulations depicted in panels A and B.
- (D) The percentage of shared top 100 differentially expressed genes between each subpopulation and sample shown in panels A and B; each point represents the number of shared markers between the indicated subpopulations (x-axis) of an individual dataset X and a subpopulation (coloring) in another individual dataset Y.
- (E) The percentage of shared top 100 differentially expressed genes as shown in panel D but limited to the comparison of the same populations (ASCs with ASCs, PreAs with PreAs, and VSMPs with VSMPs) across depots and donors, split by the type of depot of the comparison pairs; comparisons between samples originating from the same depots are highlighted in shades of green, and comparison of samples originating from different depots are in shades from yellow to red.
- (F) The percentage of shared top 100 differentially expressed genes as shown in panel D but limited to the comparison of the same populations (ASCs with ASCs, PreAs with PreAs, and VSMPs with VSMPs) across depots and donors, stratified according to whether the pairs of compared samples are originating from the same donor (green) or not (red).
- (G) The percentage of cells of a subpopulation projected onto each subpopulation and sample based on scmap²²⁵ results (see **Methods**). Each point represents the percentage of a subpopulation (x-axis) of an individual dataset X projected onto a subpopulation (coloring) of another dataset Y. Projections of subpopulations (x-axis) non-existing in the reference data are highlighted as shaded circles.
- (H) t-SNE cell map of the integration of all scRNA-seq datasets described in **Fig. 2.2A** and **B** colored by sample.
- (I) Violin plot showing the distribution of library size (left) or the number of detected genes (right) across the different clusters shown in **Fig. 2.2B**.



Supplementary Figure 2.2.2 – Human ASCs and PreAs feature different signaling pathways.

(A) Barplot displaying the percentage of cells of each cluster shown in Fig. 2.2B coming from each batch.

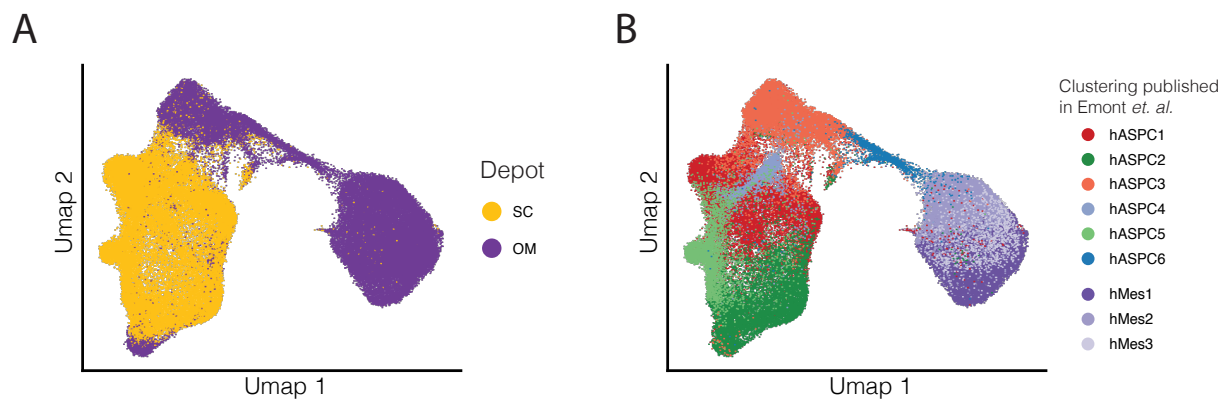
- (B) Barplot displaying the percentage of cells of each cluster shown in **Fig. 2.2B** coming from each depot (shades of colors indicate the different batches). The values were corrected for the number of cells per batch and the number of replicates per depot (n=3 for SC, PR, and OM, versus n=2 for MC).
- (C) Dot plot showing enriched biological process GO terms based on differentially expressed genes of ASCs or PreAs of the integrated scRNA-seq data shown in **Fig. 2.2A** and **B**.
- (D) Heatmap of the differentially expressed genes between the Adipose Stem Cell (ASC) population and the Pre-adipocyte (PreA) one across depots.



Supplementary Figure 2.2.3 – Several cell populations that were identified in the human SVF Lin[−] fraction across adipose depots correspond to cell populations identified in mice.

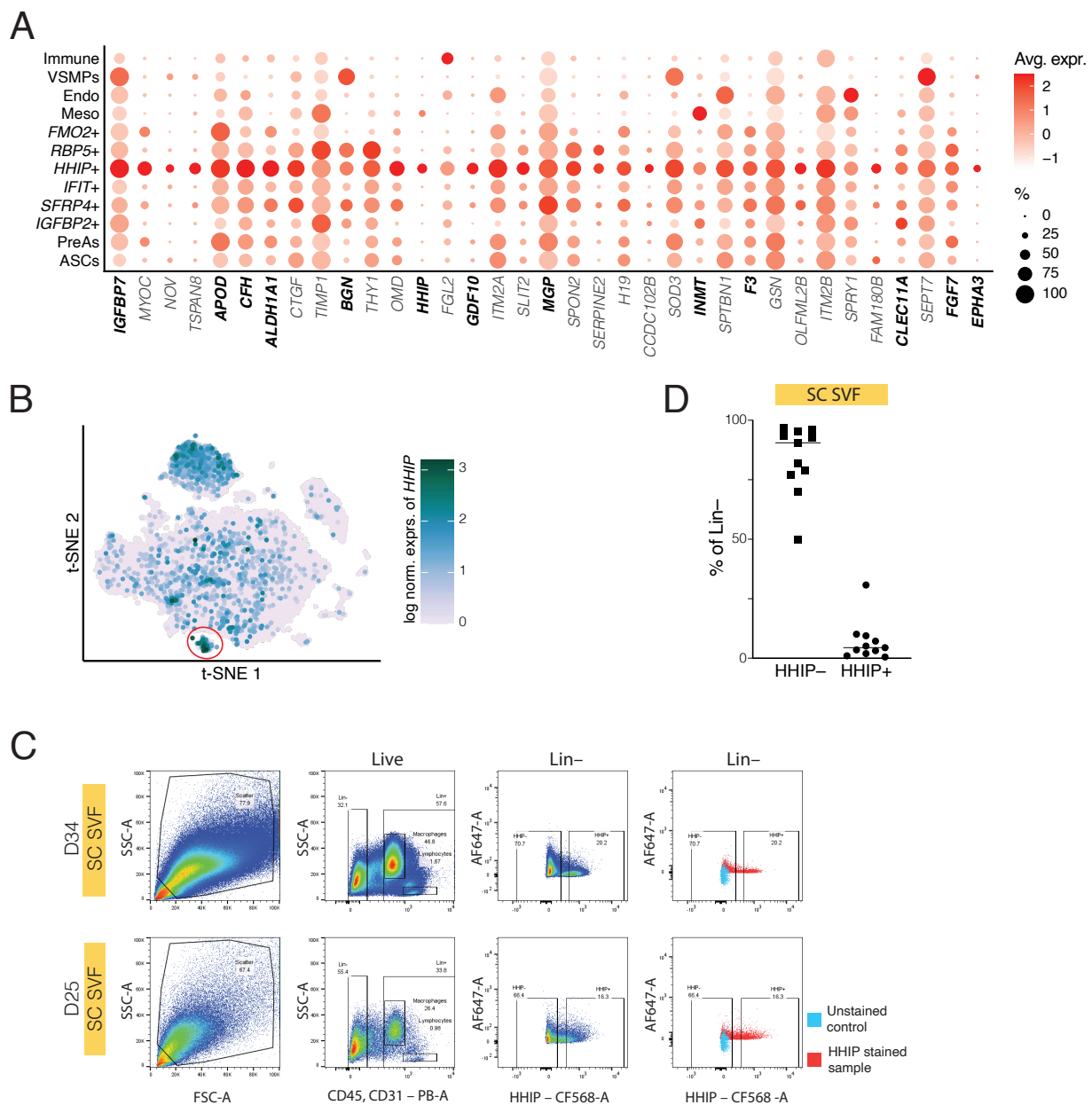
- (A) Boxplot showing the distribution of the indicated murine WAT cell population scores across the detected, distinct human SVF cell populations. The scores were based on the human orthologs of the murine top markers, which were computed in the analysis presented in Ferrero et al.¹⁴⁶ integrating scRNA-seq datasets of subcutaneous and visceral adipose tissue.
- (B) Boxplot showing the distribution of the indicated human cell populations across the different mouse cell populations defined in Ferrero et al.¹⁴⁶. The scores were based on the mouse orthologs of the human top markers of the clusters shown in **Fig. 2.2B**.
- (C) t-SNE cell map of integrated scRNA-seq datasets^{60,87,88} from OM and SC fat depots visualizing the identified subpopulations of mouse subcutaneous cells: adipose stem cells (ASCs), pre-adipocytes (PreAs), Aregs, Ifit+ ASPCs, Cilp+ ASPCs, mesothelial, endothelial, and immune cells.

* $p \leq 0.05$, ** $p \leq 0.01$, *** $p \leq 0.001$, **** $p \leq 0.0001$, unpaired two-sided t-test (**A, B**), only the statistics for the highest mean(s) are shown. The indicated adjusted p-value categories hold for all comparisons with the corresponding category, except if stated otherwise.



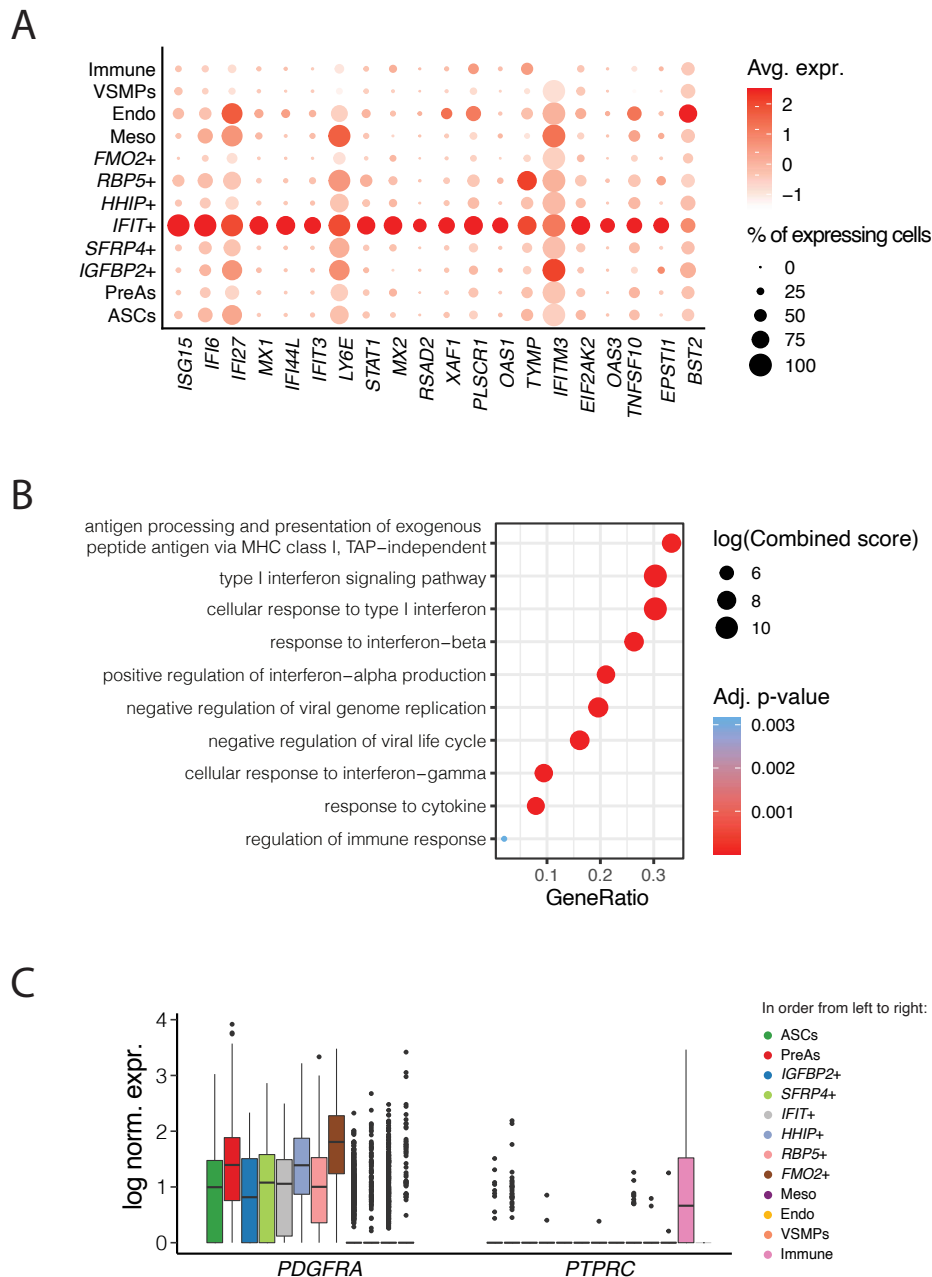
Supplementary Figure 2.2.4 – Metadata of the scRNA-seq atlas of hASPCs and mesothelial cells published by Emont *et al.*⁵⁹.

- (A) UMAP of hASPCs and human mesothelial cells from scRNA-seq data provided by Emont *et al.*⁵⁹ colored by the depot of origin.
- (B) UMAP of hASPCs and human mesothelial cells from scRNA-seq data provided by Emont *et al.*⁵⁹ colored by the clustering published in the latter study.



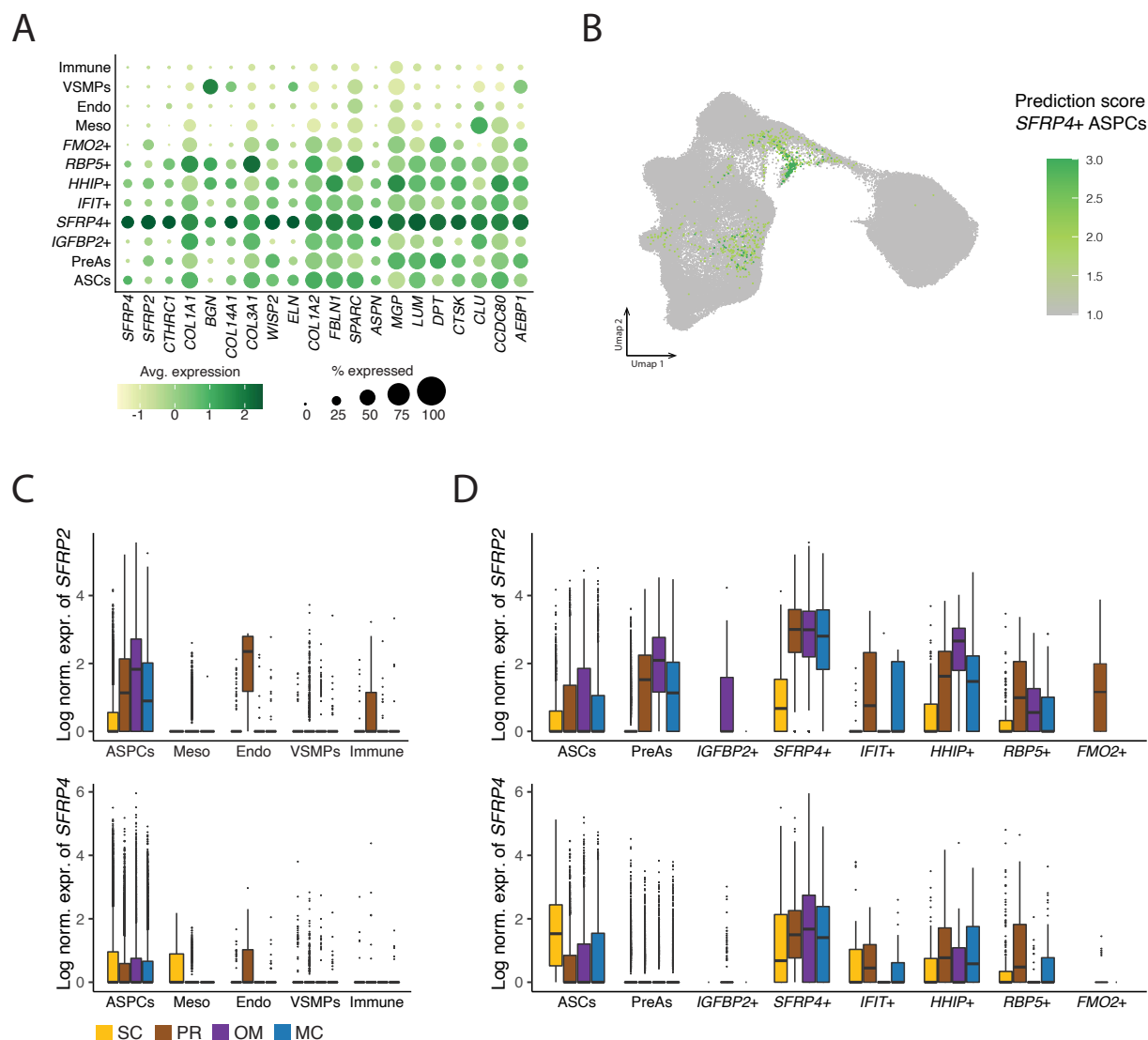
Supplementary Figure 2.2.5 – A HHIP+ hASPC population shares key marker genes with the murine Adipogenesis regulators (Aregs).

- Dot plot displaying the average expression and percentage of expressing cells of the top 20 markers of HHIP+ hASPCs across the clusters shown in **Fig. 2.2B**. The orthologs of the murine top Areg markers (as defined in Zachara et al., 2022¹¹³) are highlighted in bold.
- t-SNE cell map of the integrated data of human SVF cells shown in **Fig. 2.2A** and **B** colored by the log normalized expression of HHIP. The HHIP+ hASPC cluster is highlighted with a red circle.
- Representative flow cytometry-based gating of HHIP+ events on SC adipose depot-derived SVF Lin⁻ cells. The HHIP+ staining is highly variable across donors: donor D34 harbors a more distinct population, D25 more a continuum of positive events.
- Flow cytometry-based quantification of Lin⁻/HHIP+ events in SC SVF Lin⁻, n=11.



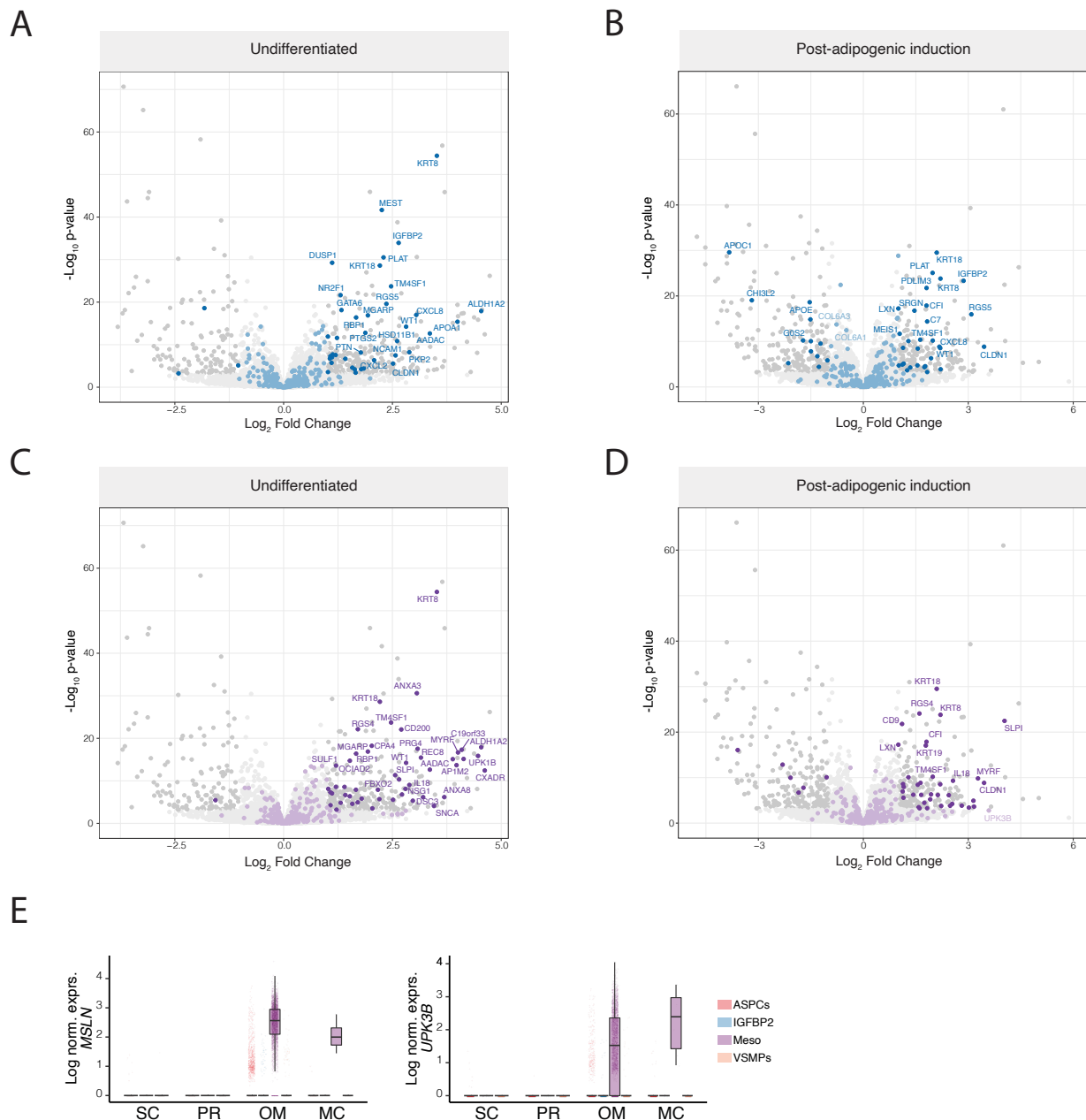
Supplementary Figure 2.2.6 – A population of IFIT+ hASPCs features enriched viral immune response gene expression.

- (A) Dot plot showing the average expression and percentage of expressing cells of the top 20 markers of *IFIT+* hASPCs across the clusters shown in Fig. 2.2B.
- (B) Dot plot showing representative GO terms that are enriched based on the differentially expressed genes of *IFIT+* hASPCs.
- (C) Boxplot showing the distribution of the log normalized expression of *PDGFRA* and *PTPRC* (CD45) across the cluster shown in Fig. 2.2B.



Supplementary Figure 2.2.7 – A hASPC population shared across depots is defined by high SFRP2 and SFRP4 expression.

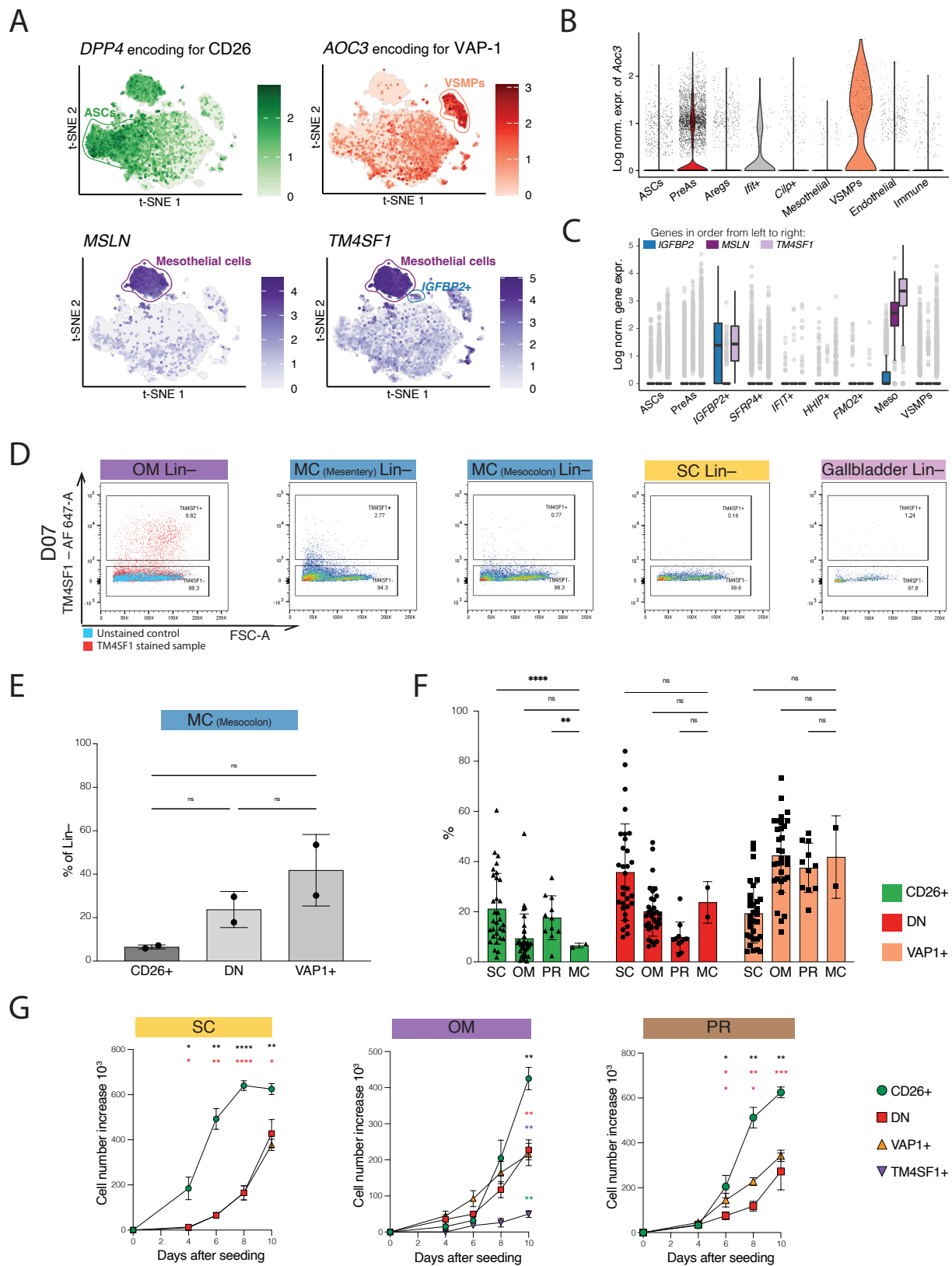
- (A) Dot plot displaying the average expression and percentage of expressing cells of the top markers of SFRP4+ hASPCs across the clusters shown in Fig. 2.2B.
- (B) UMAP of hASPCs and human mesothelial cells from scRNA-seq data provided by Emont et al.⁵⁹ colored by the prediction score of SFRP4+ cells when transferring our cell cluster annotation.
- (C) Box plot showing the distribution of SFRP2 (top) and SFRP4 (bottom) expression in the different cell types from the integrated scRNA-seq data, colored by depot of origin.
- (D) Box plot showing the distribution of SFRP2 (top) and SFRP4 (bottom) expression in the different hASPC subpopulations from the integrated scRNA-seq data, colored by depots of origin.



Supplementary Figure 2.2.8 – Mesothelial and IGFBP2+ cell markers are enriched in SVF cells from the OM adipose depot compared to other depots, both pre- and post-adipogenic induction.

- (A) Volcano plot displaying differential gene expression results based on the BRB-seq¹⁵⁰ data of expanded SVF-adherent cells from the OM adipose depot versus SVF-adherent cells from other depots (SC, PR, and MC fat depots). Top IGFBP2 markers identified using scRNA-seq datasets are highlighted in blue, while significantly differentially expressed genes ($\log_2\text{FC} > 1$, adjusted $p\text{-value} < 0.01$) are highlighted in darker colors.
- (B) Volcano plot displaying differential gene expression results based on the BRB-seq¹⁵⁰ data of SVF-adherent cells from the OM adipose depot versus SVF-adherent cells from other depots (SC, PR, and MC fat depots) post-adipogenic induction. Top IGFBP2+ cells markers identified using scRNA-seq datasets are highlighted in blue, significantly differentially expressed genes ($\log_2\text{FC} > 1$, adjusted $p\text{-value} < 0.01$) are highlighted in darker colors.
- (C) Volcano plot displaying differential gene expression results based on the BRB-seq¹⁵⁰ data of SVF-adherent cells from the OM adipose depot versus SVF-adherent cells from other depots (SC, PR, and MC). Top mesothelial markers identified using scRNA-seq datasets are highlighted in purple, while significantly differentially expressed genes ($\log_2\text{FC} > 1$, adjusted $p\text{-value} < 0.01$) are highlighted in darker colors.

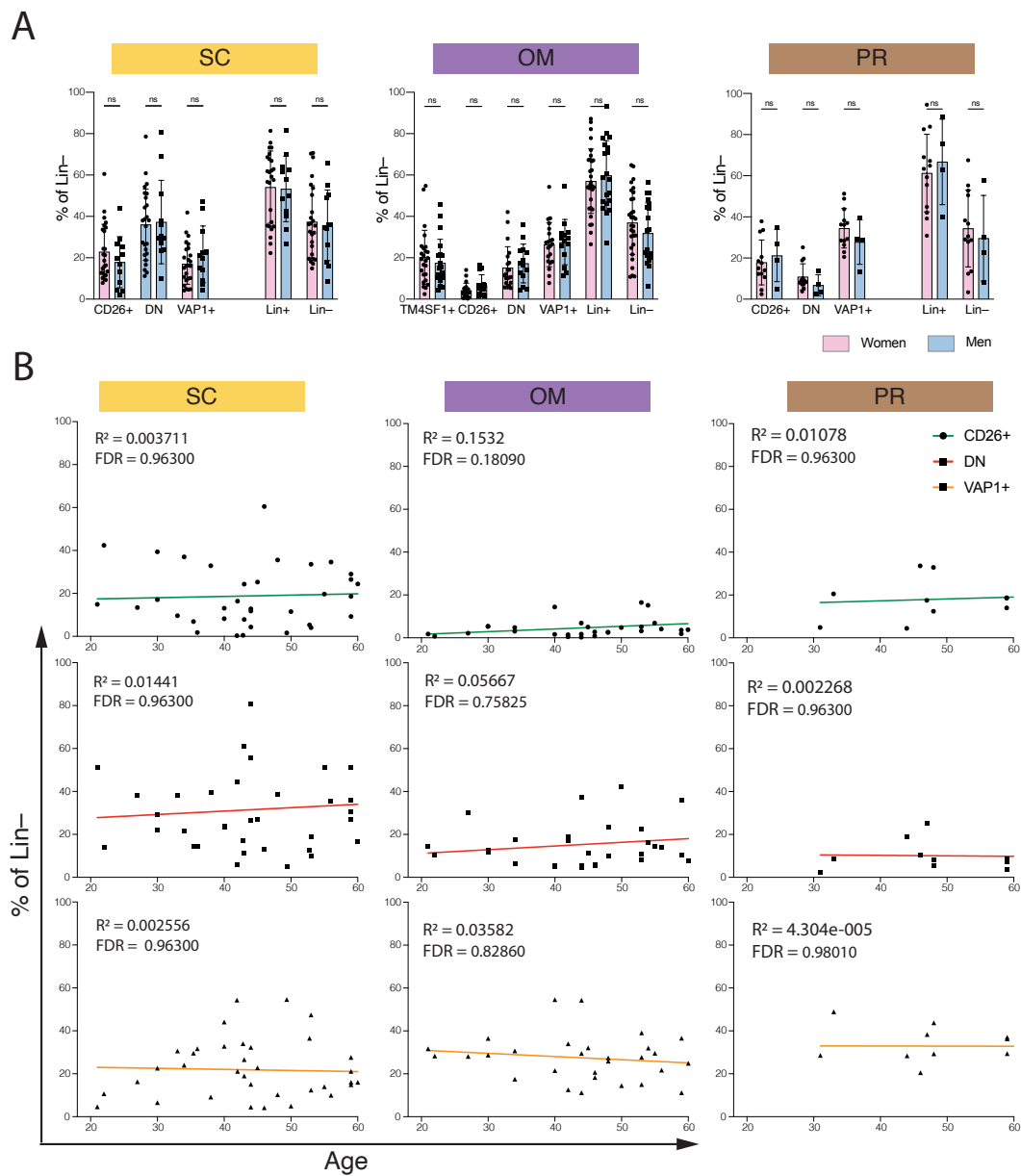
- (D) Volcano plot displaying differential gene expression results based on the BRB-seq¹⁵⁰ data of SVF-adherent cells from the OM adipose depot versus SVF-adherent cells from other depots (SC, PR, and MC) post-adipogenic induction. Top mesothelial markers identified using scRNA-seq datasets are highlighted in purple, while significantly differentially expressed genes ($\log_2FC > 1$, adjusted p-value < 0.01) are highlighted in darker colors.
- (E) Volcano plot displaying differential gene expression results based on the BRB-seq¹⁵⁰ data of SVF-adherent cells from the OM adipose depot versus SVF-adherent cells from other depots (SC, PR, and MC) post-adipogenic induction. Top mesothelial markers identified using scRNA-seq datasets are highlighted in purple, while significantly differentially expressed genes ($\log_2FC > 1$, adjusted p-value < 0.01) are highlighted in darker colors.
- (F) Box plot displaying the log normalized expression of MSLN (top) and UPK3B (bottom) across hASPCs (ASCs, PreAs, HHIP+, IFIT+, SFRP4+, RBP5+ ASCs), IGFBP2+ cells, Mesothelial cells (Meso) and Vascular Smooth Muscle progenitors (VSMPs), grouped by the depot of origin indicated on the x-axis.



Supplementary Figure 2.3.1 – The selection of scRNA-seq-inferred surface markers enables the enrichment of main SVF cell populations across all analyzed adipose depots.

- (A) t-SNE cell map of integrated scRNA-seq datasets described in **Fig. 2.2A** and **B** colored by the expression of genes corresponding to the surface markers that were used to isolate each subpopulation experimentally.
- (B) Violin plot showing the distribution of the log normalized expression of Aoc3 based on the scRNA-seq integration of murine datasets (see **Methods**).
- (C) Boxplot showing the distribution of the log normalized scRNA-seq-based expression for IGFBP2, MSLN, and TM4SF1 (color) across the different human cell populations (x-axis).
- (D) Flow cytometry profiles of Lin[−]/TM4SF1⁺ populations after TM4SF1 staining from five different adipose depot-derived SVF cells from the same donor.
- (E) Flow cytometry-based analysis of the abundance of each indicated cell population gated from the Lin[−] fraction of MC SVF cells. Bar plots indicate mean, error bars standard deviation; n=2 donors.
- (F) Bar plot to compare flow cytometry-based abundances of the indicated cell populations across SC, PR, OM, and MC adipose depots within the SVF Lin[−] fraction. The three populations accumulate to 100% by depot. For OM, each cell population is also TM4SF1[−] to deplete for OM-specific populations; SC n=37, OM n=35, PR n=17; MC n=2 donors.
- (G) Relative cell number increase over time of culture for CD26⁺, DN, and VAP1⁺ cells in each depot. For OM, the three cell populations were gated from the Lin[−]/TM4SF1[−] population and the growth speed of Lin[−]/TM4SF1⁺ OM-specific cells were also recorded; n=12, 3 donors, 3-4 populations per depot.

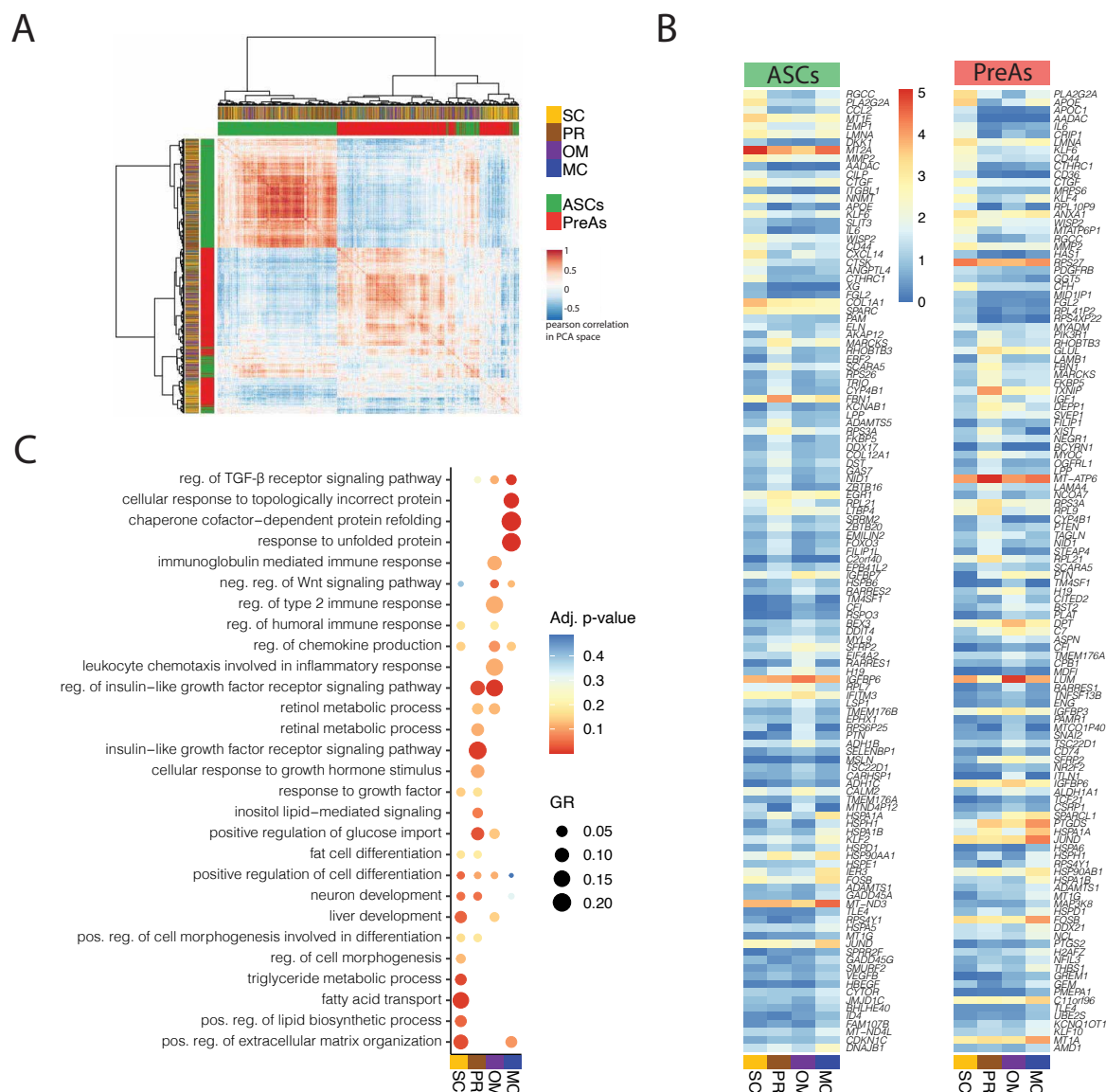
SC - Subcutaneous, PR - Perirenal, OM - Omentum, MC - mesocolic/mesenteric; * $p \leq 0.05$, ** $p \leq 0.01$, *** $p \leq 0.001$, **** $p \leq 0.0001$, One-Way ANOVA and Tukey HSD post hoc test (E) and RELM analysis and Tukey HSD post hoc test (F). Black compares CD26⁺ versus DN, Red CD26⁺ versus VAP1⁺, Blue DN versus TM4SF1⁺, Green VAP1⁺ versus TM4SF1⁺, Pink DN versus VAP1⁺.



Supplementary Figure 2.3.2 – Correlation between the FACS-based abundance of the indicated SVF Lin⁻ subpopulations shared across depots and physiological data of the donors.

- (A) Grouped bar plots showing subpopulation abundance in male versus female donors (SC n=37, OM n=35, PR n=17 donors).
 (B) Scatter plot showing the correlation between FACS-based subpopulation abundance and donor age. The line represents a linear regression analysis.

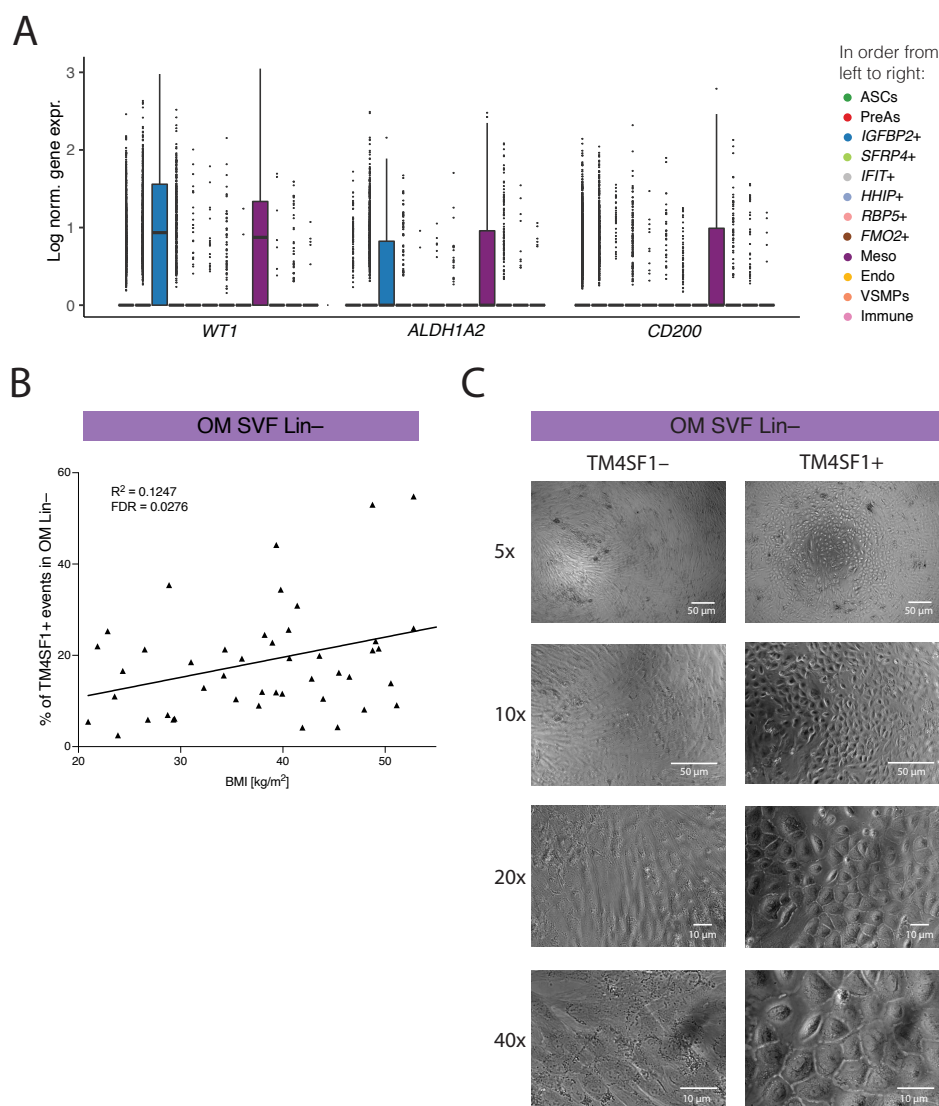
SC - Subcutaneous, PR - Perirenal, OM - Omentum; * $p \leq 0.05$, ** $p \leq 0.01$, *** $p \leq 0.001$, **** $p \leq 0.0001$, Unpaired Two-Way ANOVA (mixed model) multiple comparisons and Tukey HSD *post hoc* test (A) and linear regression analysis with its relative goodness of fit, and the FDR-adjusted p -values of the Pearson correlations (B).



Supplementary Figure 2.3.3 – ASCs and PreAs, even if detected across depots, exhibit distinct gene expression profiles.

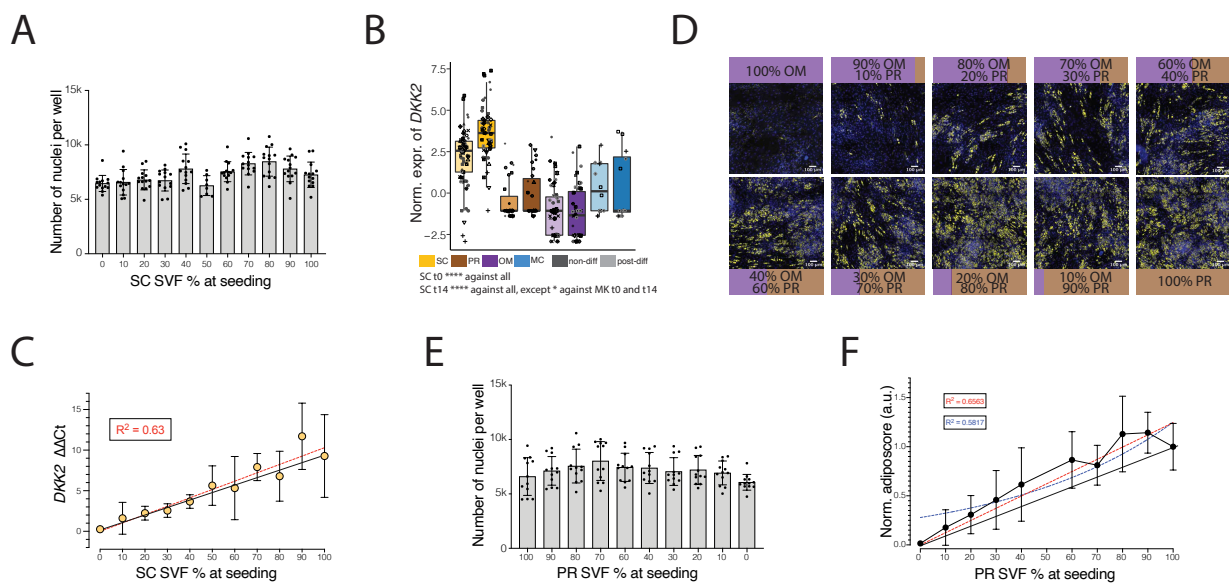
- (A) Heatmap of the correlation between 2000 randomly selected ASCs and PreAs based on the first 30 principal components of the PCA space of integrated scRNA-seq data shown in **Fig. 2.2A**; a similar number of cells was selected for each depot and population.
- (B) Heatmap of the top 30 genes detected as significantly higher expressed in the indicated depot versus all other depots (only genes detected as differentially expressed in each pairwise comparison were retained) when focusing on ASCs (left) or PreAs (right); log normalized expression.
- (C) Dot plot of enriched, representative GO terms based on the differentially expressed genes specific to the indicated depot, as explained in **A**.

SC - Subcutaneous, PR - Perirenal, OM - Omentum, MC - Mesocolic.



Supplementary Figure 2.4.1 – Known anti-adipogenic markers are overrepresented in OM-specific cell populations that express TM4SF1, and the proportion of TM4SF1+ cells positively correlates with BMI. Mesothelial and IGFBP2+ cells also display different mor-phologies.

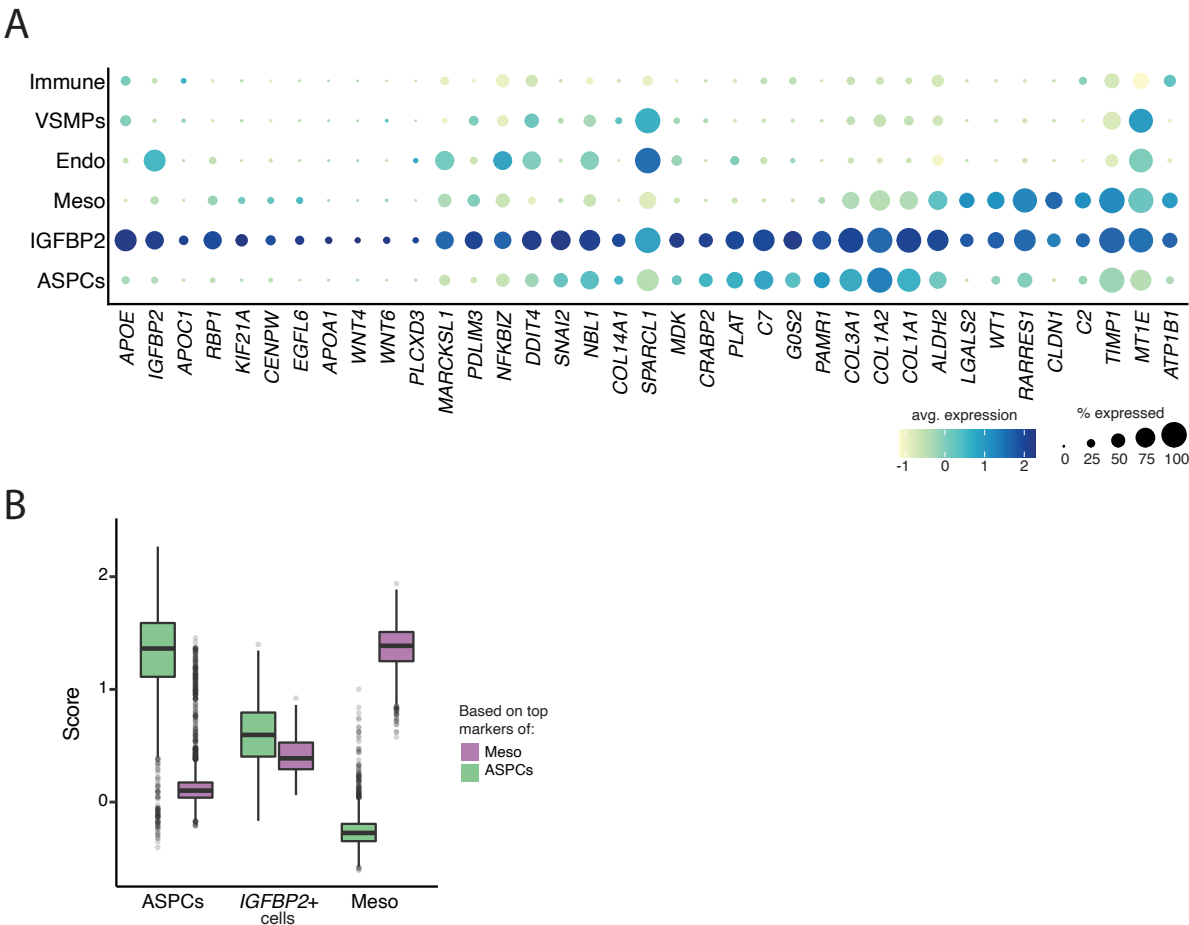
- (A) Boxplot showing the distribution of log normalized expression of the scRNA-seq data of WT1, ALDH1A2, and CD200 (x-axis) across the indicated cell populations (defined by the colors).
- (B) Scatter plot showing the correlation between the OM SVF Lin-/TM4SF1+ fraction based on flow cytometry analysis and the BMI of donors; the line represents a linear regression analysis with its relative goodness of fit; the p-value was computed performing a Pearson correlation.
- (C) Bright-field transmission light microscopy images of spindle-like OM (Omentum) ASCs (OM SVF/Lin-/TM4SF1-) and cobblestone-like OM-specific TM4SF1+ populations.



Supplementary Figure 2.4.2 – Mixing OM SVF with PR SVF does not affect the adipogenic potential of PR cells.

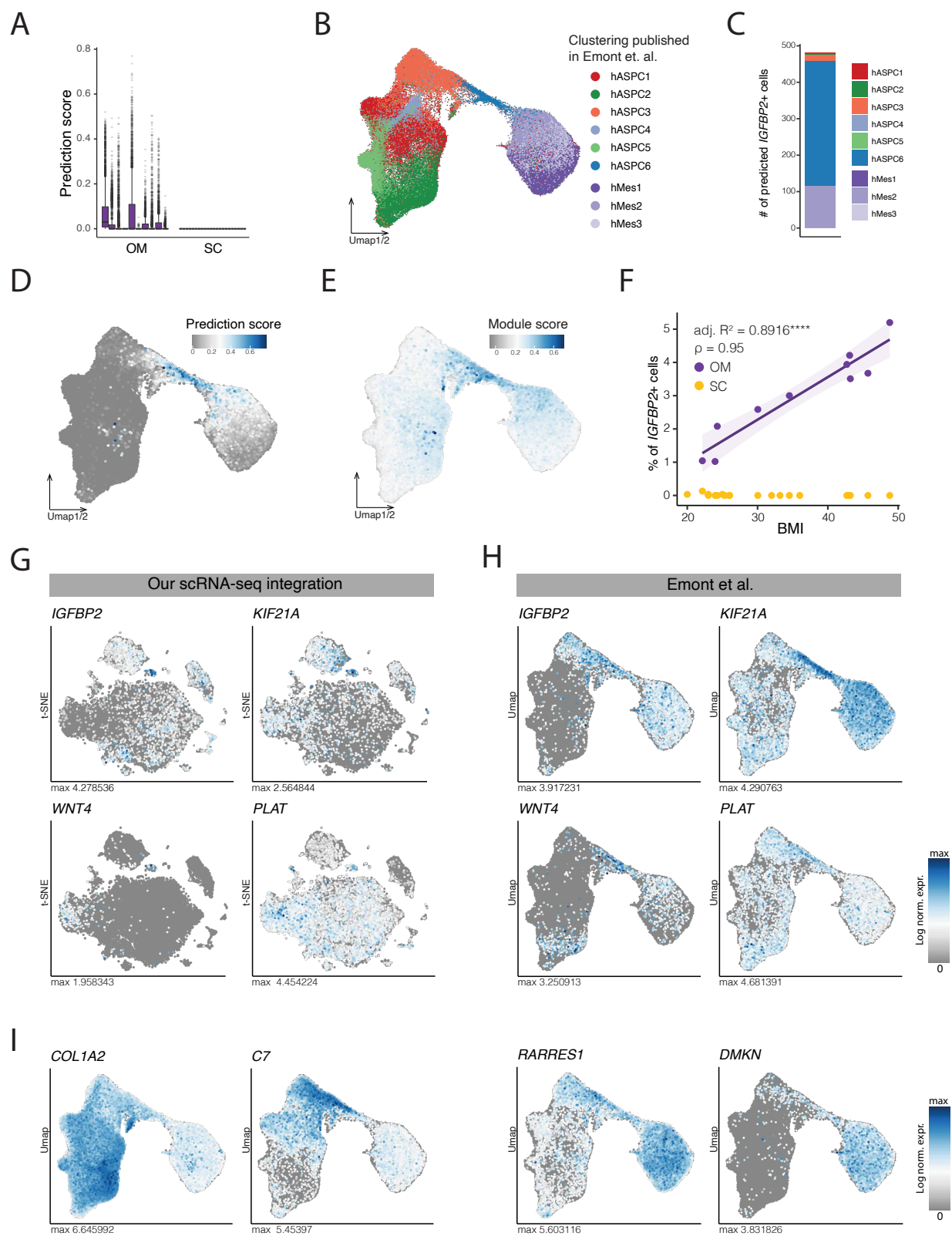
- (A) Total number of nuclei in each well (see **Methods** for more details) of images in **Fig. 2.4E**, $n=16$, 4 biological replicates, 4 independent wells for each.
- (B) Boxplot showing the distribution of batch normalized expression of DKK2 of BRB-seq¹⁵⁰ data of SVF-isolated cells from the indicated depots and treatment conditions, $n=12-61$, 4-20 biological replicates, 1-4 independent wells for each.
- (C) qPCR-based gene expression levels of DKK2 (a subcutaneous depot-specific gene), normalized by HPRT1 expression and 0% subcutaneous (SC) to control for correct mixing ratios in the experiment shown in **Fig. 2.4E**. The linear regression and corresponding R^2 coefficient values are shown in red; a black line links the lowest value to the highest value; $n=4$, 2 biological replicates, 2 independent wells for each.
- (D) Representative fluorescence microscopy images of SVF Lin⁻ cells in mixing experiments after 14 days of adipogenic differentiation, where SVF Lin⁻ cells from OM and PR of Donor 68 were mixed directly after cell isolation at the indicated proportions. Yellow - Bodipy stains for lipids, blue - Hoechst stains for DNA, scale bar=100 mm.
- (E) Total number of nuclei in each well (see **Methods** for more details) of images in **C**; $n=12$, 4 biological replicates, 3 independent wells for each.
- (F) Quantification of the extent of adipogenic differentiation of the distinct, mixed OM and PR SVF Lin⁻ cell populations, as presented in **E**. Values across biological replicates are normalized to the average adiposcore of the reference 100% PR Lin⁻ condition. The relative proportion (0-100%) of PR SVF Lin⁻ cells in each well is plotted on the x-axis. Error bars represent standard deviation from the average, linear and exponential regression with corresponding R^2 coefficients shown in red and blue, respectively. The black line represents the expected increase of adipogenesis for a linear dilution between 0 and 100% of PR SVF Lin⁻ cells; $n=16$, 4 biological replicates, 4 independent wells for each.

SC - Subcutaneous, PR - Perirenal, OM - Omentum, MC - Mesocolic.



Supplementary Figure 2.4.3 – IGFBP2+ cells exhibit a specific gene expression profile that also shares signatures with both ASCs and mesothelial cells.

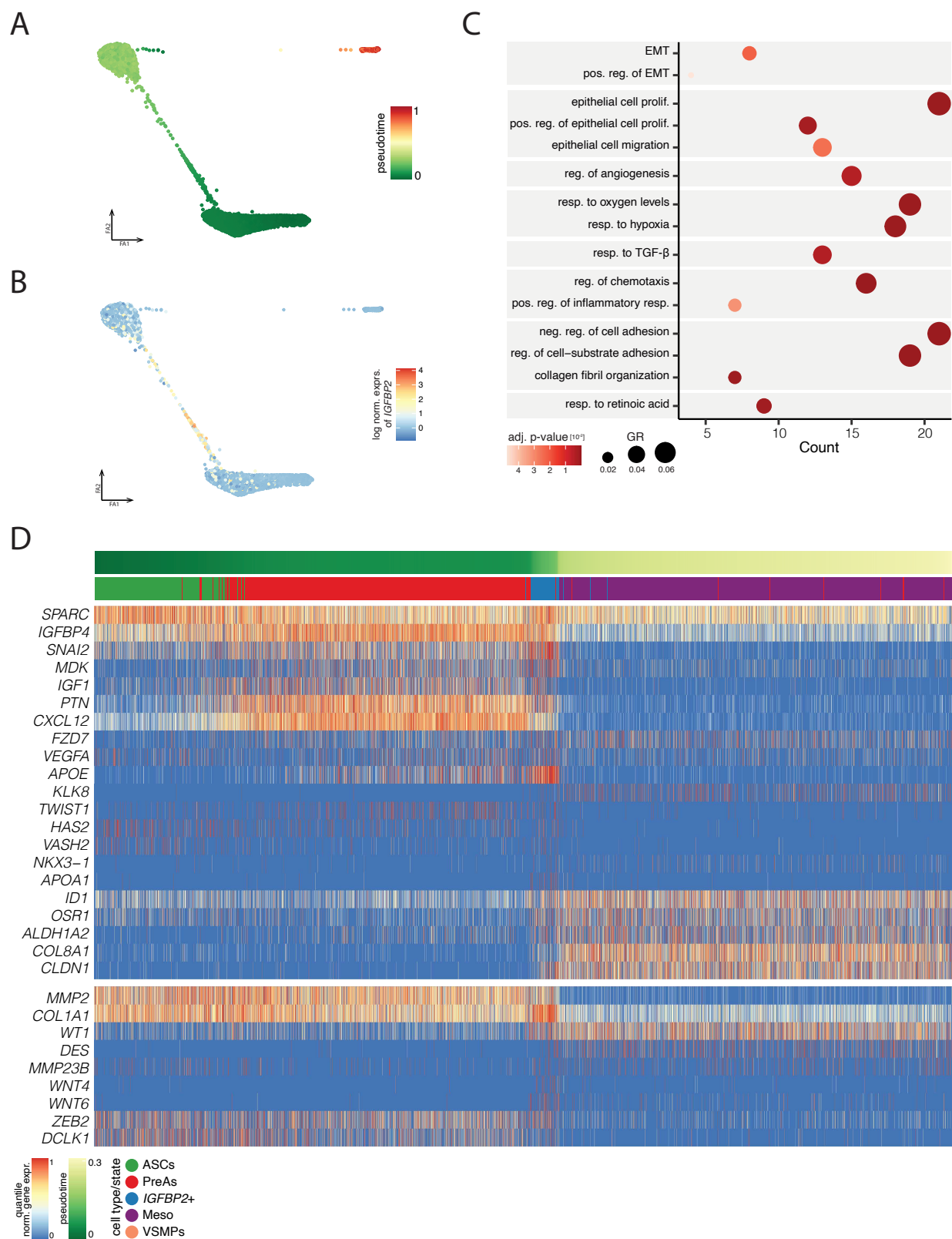
- (A) Dot plot displaying the average expression and percentage of expressing cells of the top IGFBP2+ cell markers across the clusters shown in **Fig. 2.2B**.
- (B) Boxplot showing the distribution of the score based on the top mesothelial cell markers (purple) or the top ASC and preA markers (green) in OM hASPCs (ASCs and PreAs), IGFBP2+ cells, and mesothelial cells.



Supplementary Figure 2.4.4 – Cells from the sc and snRNAseq atlas of WAT published by Emont and colleagues are predicted as IGFBP2+ cells.

(A) Boxplot showing the distribution of the prediction score of IGFBP2+ cells when transferring our cell cluster annotation on the data published by Emont et al.⁵⁹ for the indicated adipose depots (x-axis); SC - Subcutaneous, OM - Omentum.

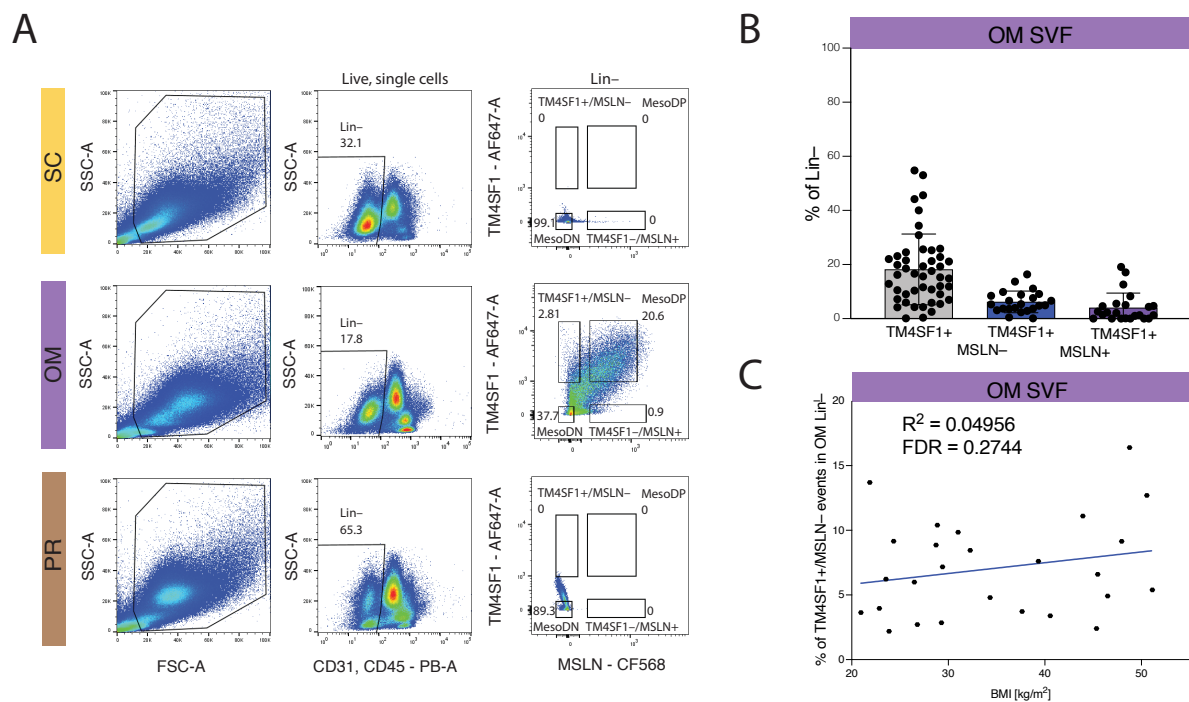
- (B) UMAP computed on the integrated data of hASPCs and human mesothelial cells reported by Emont et al.⁵⁹ colored by the clustering provided in the same study.
- (C) Bar plot displaying the number of cells predicted as IGFBP2+ cells into each of the clusters of mesothelial cells and ASPCs originally reported by Emont et al.⁵⁹, shown in **B**.
- (D) UMAP described in **B** colored by the prediction score of IGFBP2+ cells when transferring our cell cluster annotation on the data reported by Emont et al.⁵⁹.
- (E) UMAP described in **B** colored by the score based on the top IGFBP2+ cell markers.
- (F) Correlation between every donor's BMI and the percentage of hASPC6 cells (IGFBP2+-like) for each donor based on the scRNA-seq dataset provided by Emont et al.⁵⁹; the percentage was calculated for each donor as the fraction of mesothelial cells and ASPCs combined.
- (G) tSNE cell map of our integrated scRNA-seq data colored by the log-normalized expression of the indicated IGFBP2+ cell markers.
- (H) UMAP described in **B** colored by the log-normalized expression of some IGFBP2+ cell markers as in **G**.
- (I) UMAP described in **B** colored by the log-normalized expression of the indicated markers shared by predicted IGFBP2+ cells and ASPCs or Mesothelial cells.



Supplementary Figure 2.4.5 – IGFBP2+ cells are cells that transition between mesothelial and mesenchymal cell states.

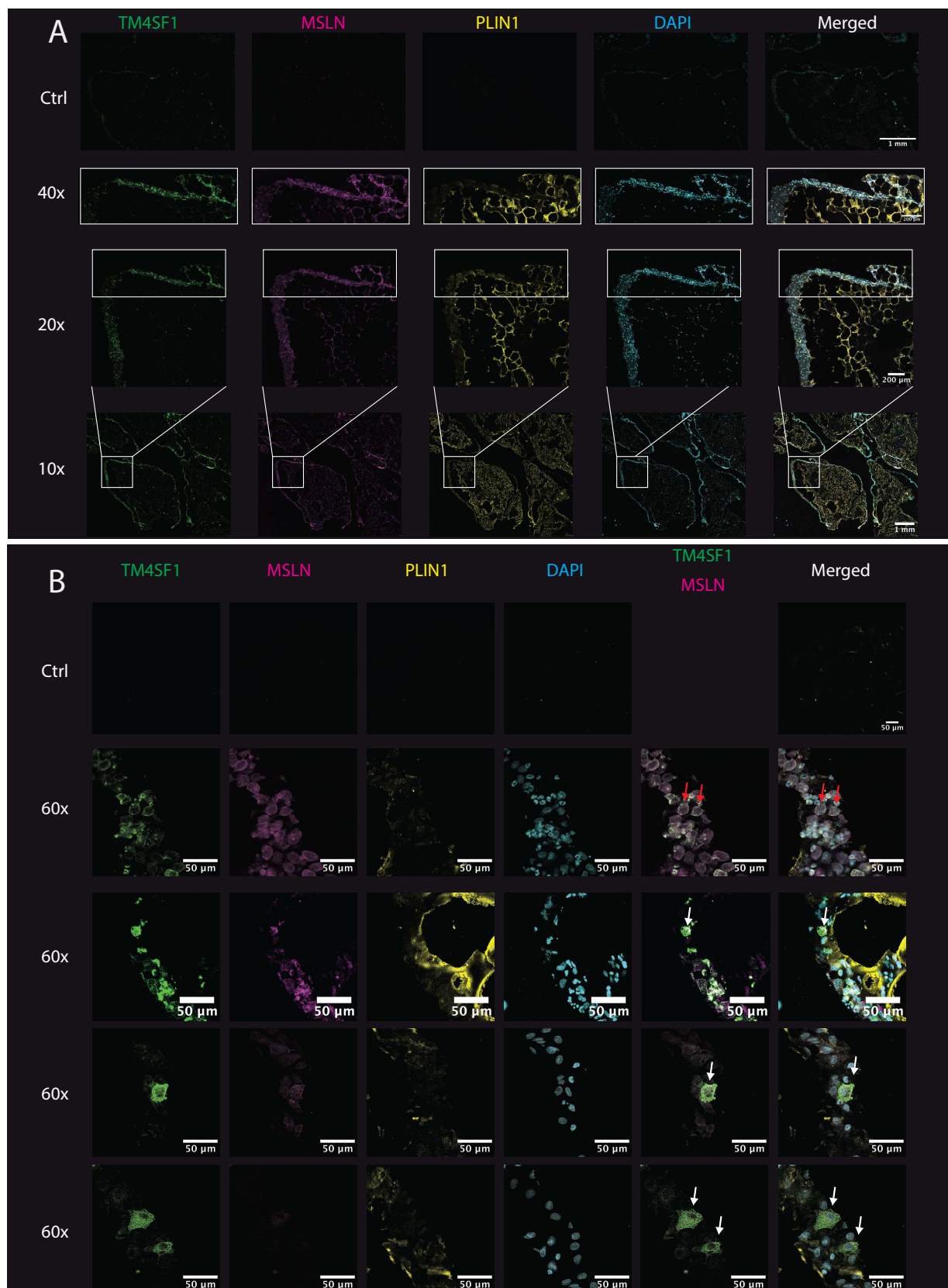
(A) PAGA-inferred trajectory¹⁷⁹ superimposed on the PAGA-initialized ForceAtlas2 layout between ASCs, PreAs, IGFBP2+ cells, mesothelial cells, and VSMPs as shown in **Fig. 2.4G**, colored by the inferred pseudotime (starting from ASCs).

- (B) PAGA-inferred trajectory¹⁷⁹ as shown in **A** colored by the log normalized expression of IGFBP2.
- (C) Dot plot of key GO terms enriched based on IGFBP2+ cell markers.
- (D) Heatmap showing the change of gene expression along the trajectory pseudotime shown in **A** for EMT-related genes (top: genes found as enriched when performing GO enrichment analysis, bottom: other EMT-related genes found in the literature). For visualization purposes, the number of cells was downsampled proportionally along pseudotime (see **Methods**).



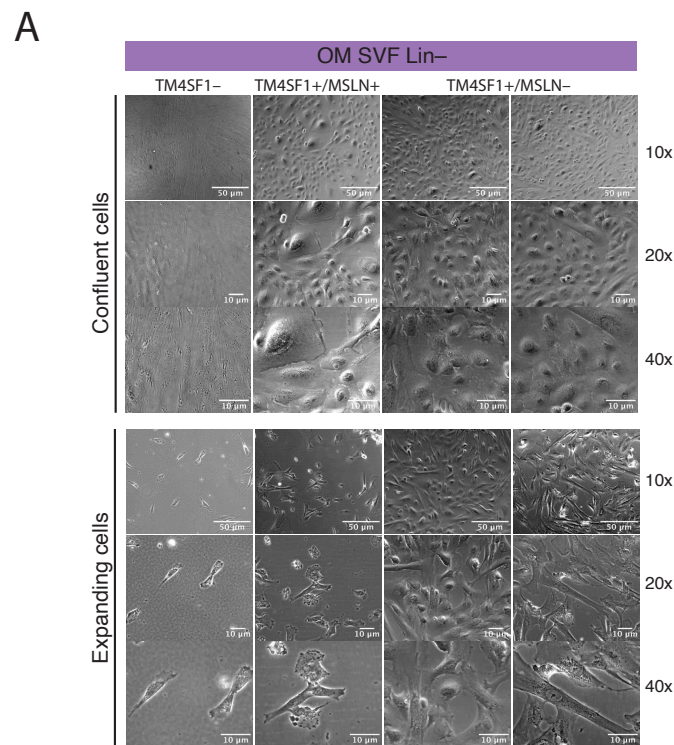
Supplementary Figure 2.4.6 – TM4SF1 and MSLN markers allow distinguishing between the two OM-specific subpopulations.

- (A) Representative flow cytometry plots of SC (Subcutaneous), OM (Omentum), and PR (Perirenal) SVF/Lin- from donor 53 stained with TM4SF1 and MSLN and gating strategy to enrich for ASCs (Lin-/TM4SF1-/MSLN-), IGFBP2+ cells (Lin-/TM4SF1+/MSLN-) or mesothelial cells (Lin-/TM4SF1+/MSLN+) exclusively in OM SVF. Similar profiles were obtained from at least three donors.
- (B) Quantification of the relative abundance of indicated cell populations based on Flow cytometry profiles; n=23-47 donors.
- (C) Scatter plot showing the correlation between the OM SVF Lin-/TM4SF1+/MSLN- fraction based on flow cytometry analysis and the BMI of donors; the line represents a linear regression analysis with its relative goodness of fit; the p-value was computed performing a Pearson correlation.



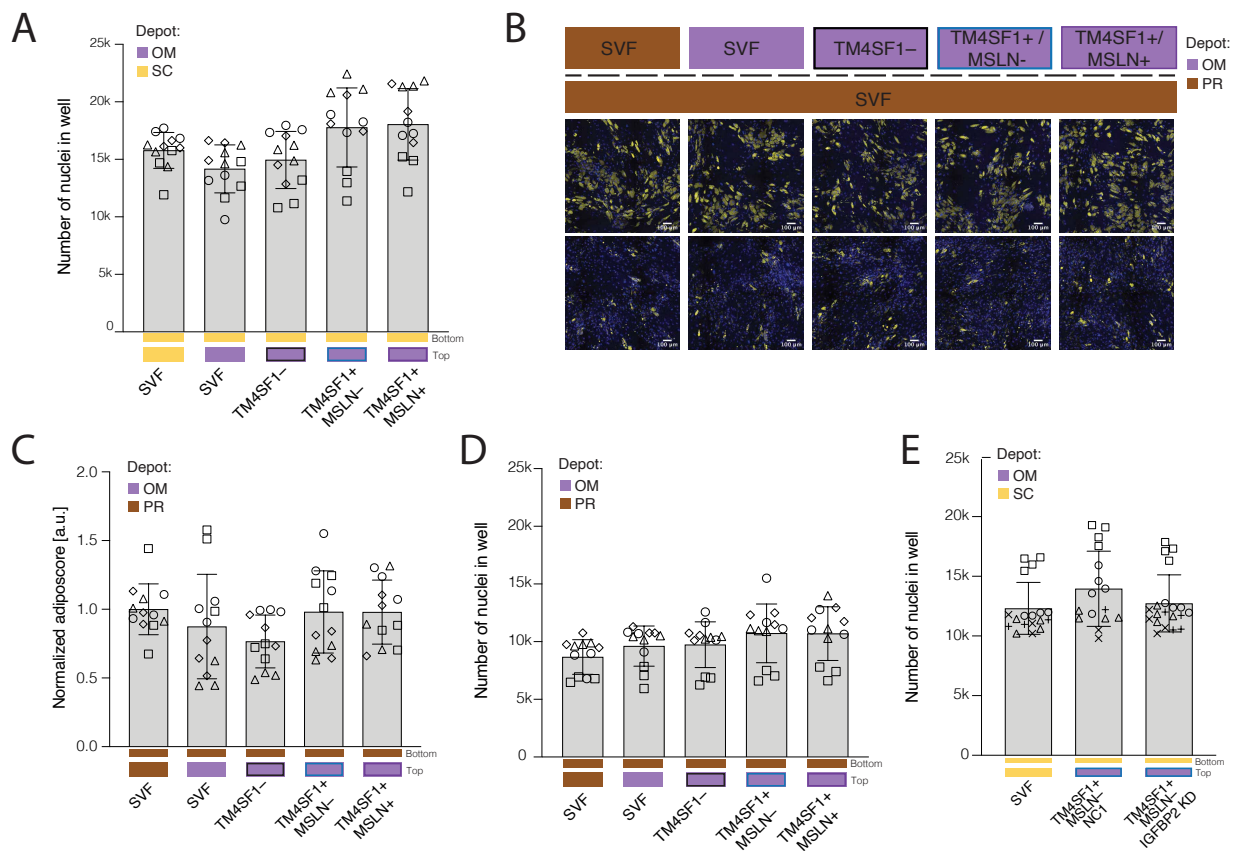
Supplementary Figure 2.4.7 – Detection of TM4SF1+/MSLN+ and TM4SF1+/MSLN– cells by in situ immunohistochemistry.

- (A)** Confocal microscopy fluorescent images after TM4SF1 (Green), Perilipin (PLIN1) (Yellow), and MSLN (Pink) immunohistochemistry staining of whole OM AT cryo-cuts. The top row is the unstained control. DAPI staining for nuclei is colored in Cyan. The experiment was repeated three times, yielding similar results.
- (B)** Confocal microscopy fluorescent images after TM4SF1 (Green), Perilipin (PLIN1) (Yellow) and MSLN (Pink) immunohistochemistry staining of whole OM AT cryocuts. The top row is the unstained control. DAPI staining for nuclei is colored in Cyan. The experiment was repeated three times, yielding similar results. The white arrows point to TM4SF1+ cells, the red arrows point to TM4SF1+/MSLN+ cells.



Supplementary Figure 2.4.8 – TM4SF1+/MSLN- cells change morphology upon expansion *in vitro*.

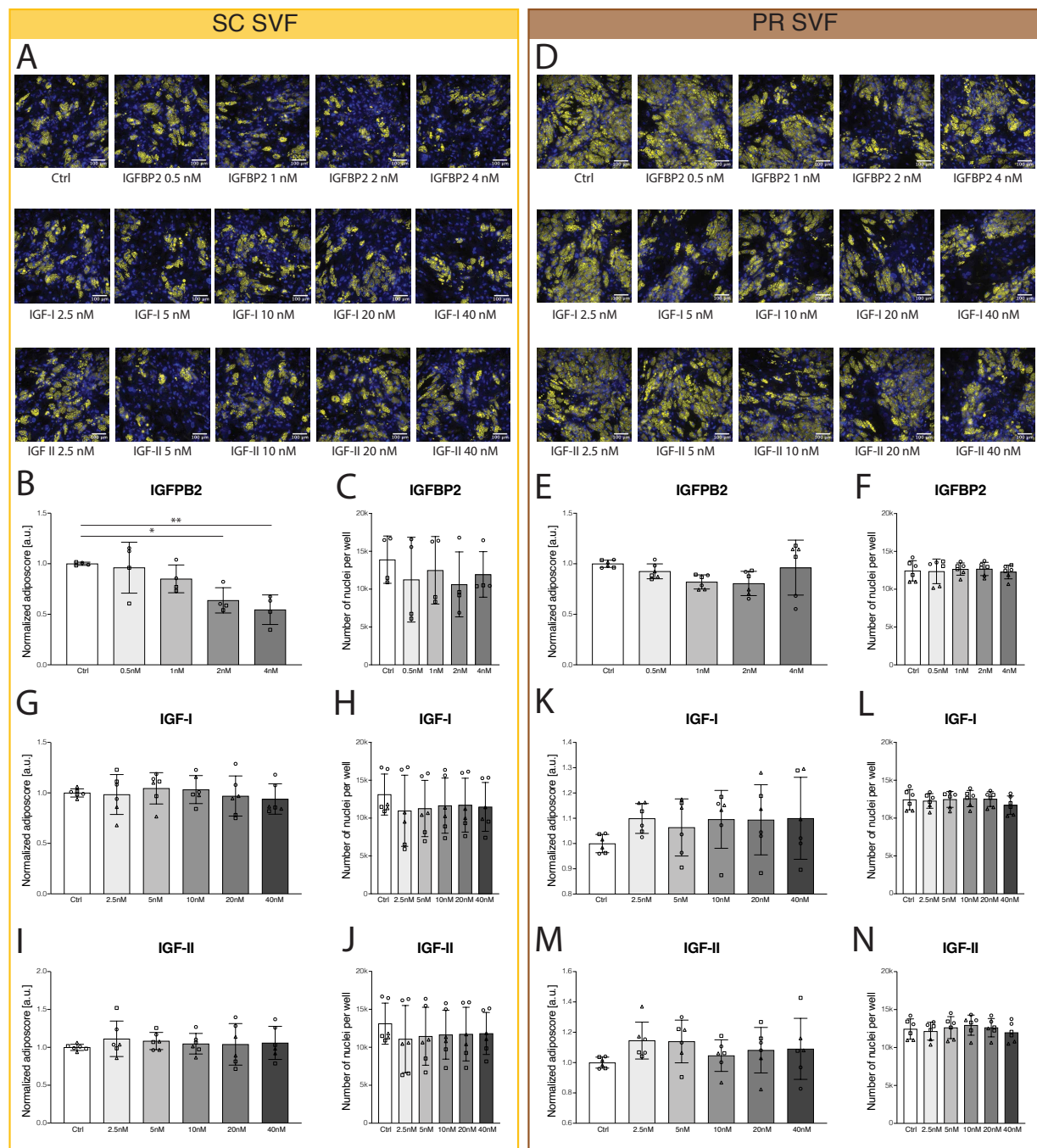
- (A) Bright-field transmission light microscopy images of confluent or expanding spindle-like OM (Omentum) ASCs (OM SVF/Lin-/TM4SF1-) and cobblestone-like Mesothelial cell (OM SVF/Lin-/TM4SF1+/MSLN+) and IGFBP2+ (defined as OM SVF/Lin-/TM4SF1+/MSLN-) cell populations.



Supplementary Figure 2.5.1 – PR SVF-adherent cells are insensitive to the inhibition exerted by IGFBP2-secreting cells in a transwell setting.

- (A) Total number of nuclei in each well (see **Methods** for more details) of images in **Fig. 2.5E**; n=12, 4 donors, 3 independent wells.
- (B) Representative fluorescence microscopy images of “receiver” PR SVF-adherent cells, at the bottom of the transwell set-up, after adipogenic differentiation when co-cultured with the indicated SVF fractions at the top: paired PR SVF-adherent cells, OM SVF-adherent cells, OM SVF/Lin⁻/TM4SF1⁻ (OM ASCs), OM SVF/Lin⁻/TM4SF1⁺/MSLN⁻ (IGFBP2-secreting cells), or OM SVF/Lin⁻/TM4SF1⁺/MSLN⁺ cells (mesothelial cells). First row: PR and OM cells from D54, Second row: SC and OM cells from D65.
- (C) Barplot showing the adiposcore quantification of bottom cells in **B**. Values are normalized to the average adiposcore of the reference top PR SVF-adherent condition; n=12, 4 donors, 3 independent wells.
- (D) Total number of nuclei in each well (see **Methods** for more details) of images in **B**; n=12, 4 donors, 3 independent wells.
- (E) Total number of nuclei in each well (see **Methods** for more details) of images in **Fig. 2.5I**; n=16-20, 4 donors, 2-4 independent wells.

SC Subcutaneous - Yellow, OM Omentum - Purple, PR Perirenal - Brown.

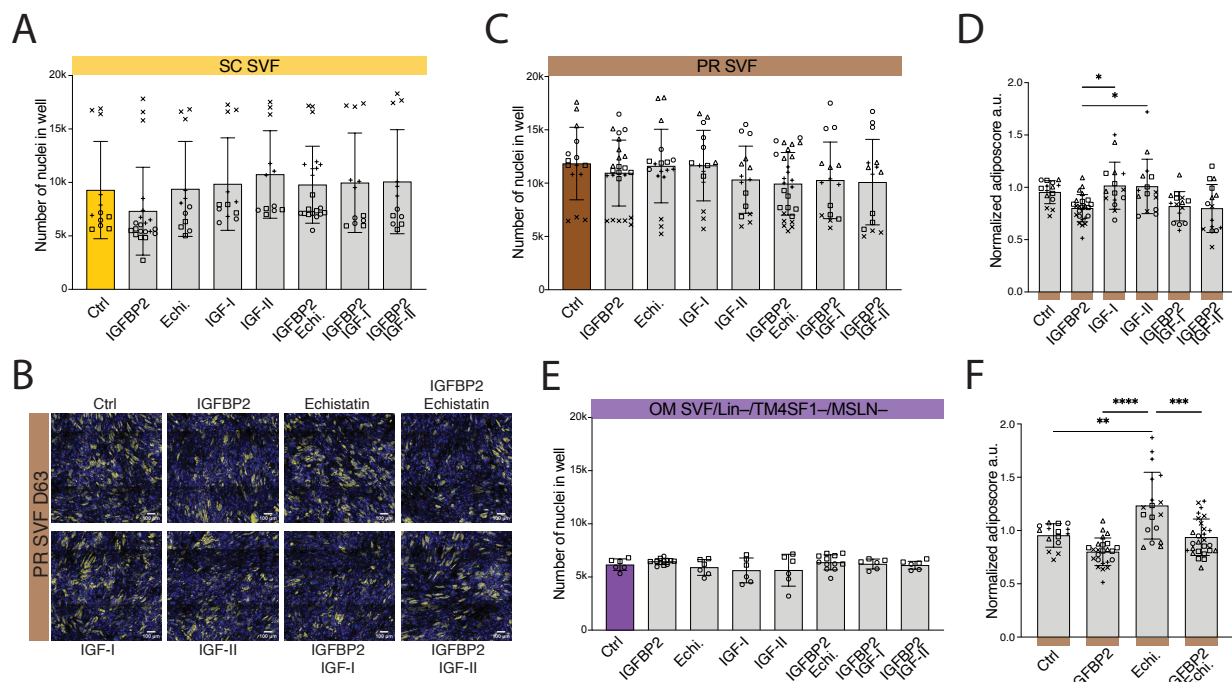


Supplementary Figure 2.5.2 – Experimental titration of IGFBP2, IGF-I, and IGF-II recombinant proteins to test their effect on adipogenic differentiation.

- (A) Representative fluorescent microscopy images of SC SVF-adherent cells treated with the indicated concentrations of interfering compounds. Scale bar=100 mm.
- (B) Barplot showing the adiposcore quantification of IGFBP2-treated cells in **A**. The adiposcores are normalized to the non-treated cells (Ctrl); n=4, 2 donors, 2 independent wells.
- (C) Total number of nuclei in each well (see **Methods** for more details) for IGFBP2-treated cells in **A**; n=6, 3 donors, 2 independent wells.
- (D) Representative fluorescent microscopy images of PR SVF cells treated with the indicated concentrations of interfering compounds. Scale bar=100 mm.

- (E) Barplot showing the adiposcore quantification of IGFBP2-treated cells in **D**. The adiposcores are normalized to the non-treated cells (Ctrl); n=4, 2 donors, 2 independent wells.
- (F) Total number of nuclei in each well (see **Methods** for more details) for IGFBP2-treated cells in **D**; n=6, 3 donors, 2 independent wells.
- (G) Barplot showing the adiposcore quantification of IGF-I-treated cells in **A**. The adiposcores are normalized to the non-treated cells (Ctrl); n=4, 2 donors, 2 independent wells.
- (H) Total number of nuclei in each well (see **Methods** for more details) for IGF-I-treated cells of panel **A**; n=6, 3 donors, 2 independent wells.
- (I) Barplot showing the adiposcore quantification of IGF-II-treated cells in **A**. The adiposcores are normalized to the non-treated cells (Ctrl); n=4, 2 donors, 2 independent wells.
- (J) Total number of nuclei in each well (see **Methods** for more details) for IGF-II treated cells of panel **A**; n=6, 3 donors, 2 independent wells.
- (K) Barplot showing the adiposcore quantification of IGF-I-treated cells in **D**. The adiposcores are normalized to the non-treated cells (Ctrl); n=4, 2 donors, 2 independent wells.
- (L) Total number of nuclei in each well (see **Methods** for more details) for IGF-I-treated cells of panel **D**; n=6, 3 donors, 2 independent wells.
- (M) Barplot showing the adiposcore quantification of IGF-II-treated cells in **D**. The adiposcores are normalized to the non-treated cells (Ctrl); n=4, 2 donors, 2 independent wells.
- (N) Total number of nuclei in each well (see **Methods** for more details) for IGF-II treated cells of panel **D**; n=6, 3 donors, 2 independent wells.

For each image: Yellow - Bodipy stains for lipids, blue - Hoechst stains for DNA. * $p \leq 0.05$, ** $p \leq 0.01$, *** $p \leq 0.001$, **** $p \leq 0.0001$ One-Way ANOVA and Tukey HSD *post hoc* test.



Supplementary Figure 2.5.3 – Treatment with IGFBP2 did not significantly affect the adipogenic differentiation of PR SVF-adherent cells, while treatment with Echistatin increased the accumulation of lipid droplets.

- (A) Total number of nuclei in each well (see **Methods** for more details) for cells in **Fig. 2.5K**. n=12, 4 donors, 3 independent wells per replicate.
- (B) Representative fluorescence microscopy images of PR SVF cells after adipogenic differentiation when treated with the indicated interfering compounds. IGFBP2 1nM, IGF-I 10nM, IGF-II 10nM, Echistatin 100nM.
- (C) Total number of nuclei in each well (see **Methods** for more details) for cells in **A**. n=12, 4 donors, 3 independent wells per replicate.
- (D) Barplot showing the adiposcore quantification of cells in **A** focusing on the IGF-independent signaling pathway of IGFBP2. The adiposcores are normalized to the non-treated cells (Ctrl); n=12, 4 donors, three independent wells.
- (E) Total number of nuclei in each well (see **Methods** for more details) for cells in **Fig. 2.5N**. n=12, 4 donors, 3 independent wells per replicate.
- (F) Barplot showing the adiposcore quantification of cells in **A** focusing on the IGF-dependent signaling pathway of IGFBP2. The adiposcores are normalized to the non-treated cells (Ctrl). n=12, 4 donors, three independent wells.

SC Subcutaneous - Yellow, OM Omentum - Purple, PR Perirenal - Brown; For each images: Yellow - Bodipy stains for lipids, blue - Hoechst stains for DNA *p ≤ 0.05, **p ≤ 0.01, ***p ≤ 0.001, ****p ≤ 0.0001 One-Way ANOVA and Tukey HSD post hoc test.

Table 2.1 – Donors' information

Donor code	Fig1 & supp	Fig2 & supp	Fig3 & supp	Fig4 & supp	Fig 5 & supp	Height	Weight	BMI	Age	Gender	Type of surgery
D00	Ci, AS, BRB	scRNAseq				1.74	138	45.58	32	Female	Gastric bypass
D01	Ci, AS, BRB	scRNAseq				1.77	110	35.11	46	Female	Gastric bypass
D02	Ci, AS, BRB					1.78	146.5	46.23	35	Female	Gastric bypass
D03	Ci, AS, BRB					1.64	108.6	40.37	51	Female	Gastric bypass
D04	Ci, AS, BRB					1.66	112	40.64	54	Female	Gastric bypass
D05	Ci, AS, BRB		FC	Ci, AS		1.66	112	40.64	54	Female	Gastric bypass
D06	Ci, AS, BRB		FC			1.71	111	37.96	27	Female	Gastric bypass
D07	Ci, AS, BRB	scRNAseq				1.79	128	39.94	51	Male	Gastric bypass
D08	Ci, AS, BRB					1.59	129	51.02	25	Female	Gastric bypass
D09	Ci, AS, BRB		FC			1.6	106	41.4	29	Female	Gastric bypass
D10	Ci, AS, BRB		FC			1.53	102	43.57	40	Female	Gastric bypass
D11	Ci, AS, BRB		FC			1.64	132	49.07	32	Female	Gastric bypass
D12	Ci, AS, BRB		FC			1.76	106	34.22	36	Male	Gastric bypass
D13	Ci, AS, BRB		FC			1.67	136	48.76	42	Female	Gastric bypass
D14	Ci, AS, BRB		FC	Mix AS		1.56	93	38.21	26	Female	Gastric bypass
D15	Ci, AS, BRB		FC	Mix AS		1.7	115	39.79	60	Male	Gastric bypass
D16	Ci, AS, BRB		FC			1.79	180	56.17	54	Male	Gastric bypass
D17	Ci, AS, BRB		FC			1.74	181	59.78	57	Male	Gastric bypass
D18	Ci, AS, BRB					1.72	96	32.44	50	Female	Gastric bypass
D19	Ci, AS, BRB		FC			1.74	169	55.81	44	Male	Gastric bypass
D20	Ci, AS, BRB		FC			1.68	149	52.79	63	Female	Gastric bypass
D21	Ci, AS, BRB		FC			1.68	110	38.97	49	Female	Gastric bypass
D22	Ci, AS, BRB		FC			1.89	90	25.19	31	Male	Nephrectomy
D23	Ci, AS, BRB		FC, Profiles			1.6	75	29.29	75	Female	Nephrectomy
D24	Ci, AS, BRB	scRNAseq			TW AS	1.53	57	24.34	63	Female	Nephrectomy
D25	Ci, AS, BRB		FC			1.62	55	20.95	65	Female	Nephrectomy
D26			FC			1.61	102	39.35	60	Female	Gastric bypass
D27	Ci, AS, BRB		FC			1.75	92	30.04	59	Male	Nephrectomy
D28	Ci, AS, BRB					1.61	65	25.07	45	Female	Nephrectomy
D29	Ci, AS, BRB	scRNAseq	FC, AS			1.62	60	22.86	46	Female	Nephrectomy
D30	Ci, AS, BRB					1.68	60	21.25	63	Female	Nephrectomy
D31	Ci, AS, BRB					1.76	114	36.8	38	Male	Gastric bypass
D32	Ci, AS, BRB		FC			1.57	114	36.8	38	Female	Gastric bypass
D33	Ci, AS, BRB		FC			1.6	100	40.56	46	Female	Nephrectomy
D34	Ci, AS, BRB		FC			1.75	56	21.87	48	Female	Nephrectomy
D35	Ci, AS, BRB		FC		TW AS	1.58	95	31.02	72	Female	Nephrectomy
D36			FC						50	Female	Gastric bypass
D37			FC			1.59	114	45.09	27	Female	Gastric bypass
D38			FC			1.85	169	49.37	40	Male	Gastric bypass
D39			FC			1.56	102	41.91	44	Female	Gastric bypass
D40			FC			1.83	176.8	52.79	30	Male	Gastric bypass
D41			FC	Ci, AS		1.66	118	42.82	42	Female	Gastric bypass
D42			FC			1.73	106	35.41	55	Male	Gastric bypass
D43			FC, AS			1.65	98	35.99	21	Female	Gastric bypass
D44			FC, AS	Ci, AS					48	Male	Gastric bypass
D45			FC			1.79	110	34.33	40	Male	Gastric bypass
D46			FC			1.67	90	32.27	44	Male	Gastric bypass
D47			FC			1.64	122	45.35	45	Male	Gastric bypass
D48			FC			1.71	133	45.48	34	Female	Gastric bypass
D49			FC			1.47	85	39.33	53	Female	Gastric bypass
D50			FC			1.67	105	37.64	56	Female	Gastric bypass
D51			FC			1.85	175	51.13	34	Male	Gastric bypass
D52			FC			1.7	141	48.78	22	Female	Gastric bypass
D53			FC		TW AS, Ci	1.71	136	46.51	53	Male	Gastric bypass
D54			FC		TW AS	1.64	86	31.97	43	Female	Gastric bypass
D55			FC			1.64	136	50.56	53	Female	Gastric bypass
D56			FC			1.64	129	47.96	30	Female	Gastric bypass
D57			FC			1.7	127	43.94	54	Male	Gastric bypass
D61		scRNAseq				1.76	81	26.14	75	Male	Nephrectomy
D62			FC		Chem AS, Ci	1.72	85	28.73	59	Female	Nephrectomy
D63			FC		Chem AS, Ci	1.61	84	32.4	48	Female	Nephrectomy
D64			FC			1.65	78	28.65	33	Female	Nephrectomy
D65			FC, AS		TW AS, Ci, ELISA	1.73	88	29.4	66	Male	Nephrectomy
D66			FC, AS		TW AS, ELISA	1.65	65	23.87	44	Female	Nephrectomy
D67			FC, AS	Mix AS, IHC, BF		1.59	73	28.87	67	Female	Nephrectomy
D68			FC, AS, Ci	Mix Ci, AS		1.82	78	23.54	27	Male	Nephrectomy
D69			FC, AS			1.62	70	26.67	59	Female	Nephrectomy
D70			FC, AS, Ci			1.76	83	26.79	59	Male	Nephrectomy
D71			FC			1.77	83	26.49	42	Male	Nephrectomy
D72				AS		1.77	129	41.17	70	Male	Gastric bypass
D73					Chem AS, Ci	1.7	80	27.68	61	Female	Nephrectomy
D74					KD, Chem AS	1.5	71	31.55	55	Female	Nephrectomy
D75					Chem AS, KD, ELISA	1.86	76	21.99	55	Male	Nephrectomy
D76					Chem AS, ELISA	1.72	91	30.75	38	Male	Nephrectomy

Legend

- AS Adiposcore
- BF brightfield images
- BRB Barcoded bulkRNA sequencing
- Chem chemical experiments
- Ci Confocal imaging
- ELISA enzyme-linked immunosorbent assay
- FC flow cytometry
- IHC Immunohistochemistry
- KD siRNA knockdown experiments
- Mix mixing experiments
- Profiles flow cytometry scatter plot profiles
- scRNAseq single-cell RNA sequencing
- TW transwell

Table 2.2 – Donors' specifications for scRNA-seq

Red: Obese, Yellow: Overweight, Green: Normoweight

Donor code	Age	Gender	Weight [kg]	Height [m]	BMI [kg/m ²]	Type of surgery	Enrichment for SVF Lin- before scRNAseq	Analysed depots
D00	32	Female	138	1.74	45.58	Gastric bypass	FACS	SC, OM
D01	46	Female	110	1.77	35.11	Gastric bypass	FACS	SC, OM
D07	51	Male	128	1.79	39.94	Gastric bypass	MACS	SC, OM, MC1 and MC2
D24	63	Female	57	1.53	24.34	Live donor nephrectomy	FACS	PR
D30	63	Female	60	1.68	21.25	Live donor nephrectomy	FACS	PR
D61	75	Male	81	1.76	26.14	Live donor nephrectomy	FACS	PR

Table 2.3 – Cohorts specifications

	Cohort of obese patients	Control cohort of kidney donors
Number	55	26
Gender (M:F)	21:34	8:17
Age Mean \pm SD	42.4 \pm 11.7	53.9 \pm 13.6
BMI Mean \pm SD [kg/m ²]	43.4 \pm 6.6	26.8 \pm 3.3
Weight Mean \pm SD [kg]	124.1 \pm 25.1	75.3 \pm 12.2
Height Mean \pm SD [cm]	168 \pm 9	167.3 \pm 9.3
Type of surgery	Gastric bypass	Live donor nephrectomy
Accessible biopsies	SC, OM, MC	SC, OM, PR

Table 2.4 – Antibody specifications for FACS

Target	Provider	Catalog number	Host specie	Fluorophore conjugate	Biotium Mix n Stain fluorore conjugate	Biotium Mix n Stain reference	Working titration	SC SVF Panel	OM SVF Panel	PR SVF Panel
Human HHIP	Sigma Aldrich	WH0064399M1	Mouse	uncoupled	CF568	92235	1:20			
Human MSLN	Biologend	530101	Mouse	uncoupled	CF568	92255	1:25			
Human VAP-1	R&D	IC39571G	Mouse	AF488	-	-	1:80			
Human CD26	Biologend	302714	Mouse	PE/Cy7	-	-	1:80			
Human CD45	Biologend	304022	Mouse	Pacific Blue	-	-	1:400			
Human CD31	Biologend	303114	Mouse	Pacific Blue	-	-	1:100			
Human TM4SF1/L6	R&D	FAB8164R	Mouse	AF647	-	-	1:20			

Table 2.5 – Antibody specifications for IHC

Grey indicates secondary antibodies

Target	Provider	Catalog number	Host specie	Fluorophore conjugate	Biotium Mix n Stain fluorore conjugate	Biotium Mix n Stain reference	Working titration	Primary (I) or Secondary (II)
Human MSLN	Biologend	530101	Mouse	uncoupled	CF568	92255	1:50	I
Human TM4SF1/L6	R&D	FAB8164R	Mouse	AF488	-	-	1:50	I
Human PLIN1	Abcam	ab172907	Rabbit	uncoupled			1:200	I
anti-Rabbit IgG (H+L)	Thermo	A-31573	Donkey	AF647			1:200	II

Chapter 3 | Conclusion and future perspectives

3.1 The adipose-tissue SVF and its heterogeneity across species

3.1.1 The ASPC heterogeneity in mouse

The advent of scRNA-seq techniques allowed for unprecedented and unbiased revelation of new cell sub-populations within heterogeneous cell populations²³². If the scientific community has been able to produce whole body atlases of simple research models such as *C. elegans*²³³ and *D. melanogaster*²³⁴, when it comes to higher mammals accounting for billions of cells, we have no other ways than exploring organ by organ, tissue by tissue the underlying cell heterogeneity. The Deplancke lab undertook the scRNA-seq-based exploration of adipose stem and progenitor cells (ASPCs) in 2015 and since then contributed to a number of groundbreaking discoveries, among which was resolving the heterogeneity of mouse subcutaneous (SC) ASPCs¹⁰². Shortly after, several other labs corroborated our findings^{96,100} and added depth to general knowledge by resolving epigonadal^{100,101} or omental¹⁴³ mouse ASPCs heterogeneity, all concluding on the fact that the ASPC pool is heterogenous regardless of the anatomic depot of origin^{145,146,235}. Specifically, the mouse ASPC landscape across depots is populated by two canonical mesenchymal cell types/states, the adipose stem cells (ASC) and the pre-adipocytes (PreA). Downstream functionalization of these cell sub-populations corroborated the choice of nomenclature, given that ASCs (*Dpp4+*, *Cd55+*) as opposed to PreAs (*Icam1+*, *Aoc3+*) showed greater proliferation abilities, while the latter the highest adipogenic potential^{96,146}. Transcriptomically close to ASCs and PreAs stood an enigmatic cell type characterized by a high and specific expression of *F3* and which robustly clustered apart from the two main populations^{96,102,146}. Technically, this mouse *F3+* population should not be considered as an ASPC as it is unable itself to form mature adipocytes, instead, exerts a negative regulation on neighboring adipogenic cells like ASC or PreAs, hence the proposed nomenclature of Aregs (for Adipogenesis regulators)¹⁰². Lineage tracing analysis further validated the newly established niche landscape, in fact it was shown that ASCs stand at the very root of adipogenesis, and can give rise to both PreAs and Aregs *in vivo*⁹⁶. By integrating all publicly available datasets in 2020¹⁴⁶, a fourth, final mesenchymal population showed consistent clustering. This is the *Clip+* population. Although no functional characterization was performed on the *Clip+* population itself, their transcriptome is somewhat close to both ASCs and Aregs and an interesting hypothesis would be that they could be specialized Aregs precursor cells. Trajectory inference analysis and targeted lineage tracing experiments would help lift the veil on this aspect. Interestingly, a few cells from the integrated dataset (*Ifit+* cluster) are characterized by high expression of interferon-related markers. The gene expression signature of these cells is reminiscent of fibroblast-inflammatory cells that are highly specialized in innate immune response directed against viruses that locate preferentially in the red pulp of the spleen²³⁶. Therefore, these cells may act as specialized sensors for viral infection of the adipose tissue, and it would be interesting to interrogate their role in the tropism of specific viruses, such as SARS-CoV2, towards adipose tissue. Besides the two canonical ASPC clusters, the Areg and its potential progenitor

Clip+ and the specialized anti-viral cluster *Ifit+*, which are identifiable in both subcutaneous and epigonadal mouse AT¹⁴⁶, is a cell cluster that is not mesenchymal in nature, but rather epithelial, and that exclusively stems from epigonadal- and omental-derived datasets: the mesothelial cells^{100,101,145,146}. Considering the newly established subpopulation landscape of the ASPCs in the adult mouse, further work should focus on interrogating how the equilibrium of the niche changes upon physiological conditions in health and disease. As such, it would be useful to develop reporter mouse models for each of the uncovered cell subpopulation. This could be achieved, for example, by fluorescently labeling one of the top differentially expressed markers of each subpopulation. Once these tools ready, we would be able to interrogate changes in the relative abundance of each cell subpopulation in different biological scenarios (i.e. early development and pre-pubertal time, upon aging and post-menopausal time, across genders, as well as under high-fat diet or high-glucose pulse conditions) and test the biological limits of adipose tissue plasticity.

The anti-adipogenic effect of Aregs is one of the most intriguing aspects that arose from studying the mouse ASPC niche. Despite that the non- and anti-adipogenic character of these cells have been challenged by other labs⁹⁶, we¹⁴⁸ and others¹⁴⁹ proved the phenotype consistency of Aregs (CD142+ (= F3+)) cells across a number of different conditions (i.e. mouse strains, FACS gating strategy, differentiation cues) in recent studies. Out of all tested conditions, two appeared to be crucial to ensure the correct sorting and characterization of non- and anti-adipogenic Aregs. On the one hand, in adult mice, it is important to exclude contamination of Aregs by Vap1+ ASPCs. Hence Dong and colleagues proposed a refined sorting strategy, where Aregs are defined as SC SVF Lin⁻/Sca1+/VAP1-/CD55-/CD142+ ASPCs¹⁴⁹. On the other hand, the animal age from which cells were isolated turned out to be critical to ensure Aregs phenotype. In fact, Aregs isolated from SC adipose tissue of pup mice, specifically from the pre-weaning age, appeared to be highly adipogenic – to at least the same extent as the other ASPCs (CD142- (=F3-) ASPCs) – and were incapable of negatively influencing the adipogenic potential of neighboring cells¹⁴⁸. Weaning is a critical event in the metabolism of mammals including humans, where the gut of the offspring has to learn to digest complex sugars and nutrients that were absent in the mother's milk. As such, weaning is accompanied by a drastic change in the gut microbiota^{237–240}. It is by now well established that some nutrients in the gut can only be absorbed following pre-metabolization by the microbiome, and a number of vitamins and essential nutrients for the organism, including retinoic acid, are subjected to this bacterial pre-processing step before being at the host organism disposal²⁴¹. We showed that retinoic acid, together with secreted proteins CD142 and MGP play a key role through an auto-paracrine axis to ensure the non-adipogenic character of the Aregs on one side, and on the other side in the inhibitory mechanism of Aregs toward neighboring ASPCs¹⁴⁸. Hence, it would be tempting to hypothesize that changes in the gut microbiome upon weaning might be influencing the phenotype of Aregs. This could be tested by exploring Aregs behavior in germ-free mice, mice subjected to selected depletion of microbiota through antibiotic treatment, or by altering the timings of the diet-transition enforced by weaning.

3.1.2 The ASPC heterogeneity in human

Mice are certainly a great resource when it comes to expanding our general knowledge of how fundamental biology mechanisms operate at the whole-body scale in a mammalian organism. However, findings in mice might not be always translated in humans^{242,243}. A relevant example is the discovery of the leptin hypothalamic-pituitary endocrine axis in the mid '90s²⁴⁴. The leptin axis is one of the major food intake regulation axes in mice. Knocking out the *Lep* gene in the wild-type mouse is responsible by itself for the onset of severe obesity as a consequence of excessive food intake by the animal (*Ob/Ob* mouse model)²⁴⁵. However, when it comes to humans, perturbations in the leptin signaling axis were described in only sporadic cases of severe obesity, as a consequence of homozygotic mutation in the leptin-coding region of *Lep*²⁴⁶. In addition, except for the patients with a non-sense mutation in the leptin gene itself, where the leptin analog therapy rescued a normal body weight²⁴⁷, no drug-discovery-related attempt to enhance the leptin axis was effective for weight management therapy, and to date, the only drug-development attempts concerning the leptin axes are carried out in the field of cancer biology²⁴⁸. Several other important differences exist between the mouse and human adipose tissue. For example, the brown adipose tissue is a fully functional and important organ in mice, both in early life and adulthood, responsible for maintaining body temperature homeostasis throughout the entire lifespan of the animal²⁴⁹. In humans, brown adipose tissue is mainly present in newborns, while during adulthood, only vestigial depots are found in the supraclavicular, mediastinal, cervical, axillary, paraspinal and perirenal regions²⁵⁰ and might only marginally contribute to the regulation of body temperature. Another striking difference in the AT distribution in mice versus humans is the anatomy of the main visceral AT. The omentum, the main human visceral adipose tissue is nothing more than a tiny line of tissue above the stomach of the mouse, barely distinguishable from the pancreas, inversely, the mouse epigonadal AT occupies the vast majority of the animal abdominal space, while is barely distinguishable from the human gonad itself²⁵¹. Given these differences in adipose tissue biology and the possibility that findings in mouse AT might not extrapolate to humans, there was a need to understand the heterogeneity and functionality of human ASPCs.

Throughout my Ph.D., I got access to adipose tissue biopsies from three anatomic locations (Subcutaneous = SC, Perirenal = PR, Omentum = OM) and sporadic from two of them (Mesocolon = MC and the Gallbladder-associated AT = GB) and was able to collect samples from up to 85 donors (**Table 2.1**). This allowed to depict a comprehensive snapshot of similarities and differences in the hASPC composition in function of the anatomic depot of origin both at the single-cell (~34'000 SVF/Lin[−] cells analyzed) resolution (**Fig. 2.2**) and at the bulk transcriptomic one (20 SC, 8 PR, 19 OM, and 4 MC primary cell lines analyzed) (**Fig. 2.1**). Like in mice and in other publicly available work^{96,145}, two main hASPC populations, the hASCs (*DPP4+*, *CD55+*) and the hPreAs (*ICAM1+*, *APOD+*) appeared to be present in all four canonical adipose tissues (SC, PR, OM. And MC) as well as in the GB AT, which is at times present around the gallbladder of morbidly obese donors exclusively. We

experimentally proved that hASC-enriched SVF cells (Lin⁻/TM4SF1⁻/CD26⁺) are more proliferative and less adipogenic than hPreA-enriched SVF cells (Lin⁻/TM4SF1⁻/DN) regardless of the anatomic depot of origin (**Fig. 2.3E-F** and **Supp. Fig. 2.3.1G**). *In silico* trajectory analysis that we performed, also hints at the lineage dependency of these two cell populations (**Fig. 2.4G**) as was previously described⁹⁶. Aside hASCs and PreAs stand another transcriptomically well-distinct cell subpopulation common to all anatomic locations. These cells that resemble Vascular Smooth Muscle Progenitors (VSMP)¹⁵⁹ highly express muscle-related markers such as actin and myosin (**Fig. 2.2.1C**) and represent between 2 to 10% of the SVF Lin⁻ cells depending on the depot (**Fig. 2.2D**). Using *AOC3* marker encoding for VAP-1 surface protein, we were able to sort VSMP-enriched SVF cells (Lin⁻/TM4SF1⁻/VAP1⁺) (**Fig. 2.3E-F**) which surprisingly showed the highest adipogenic potential *in vitro* (even higher than the PreAs defined as Lin⁻/TM4SF1⁻/DN) (**Fig. 2.3E-F**) coupled to the slowest growing pace (**Supp. Fig. 2.3.1G**). If at the first glance is contradictory that muscle-primed cells can be so adipogenic, this could be explained by the fact that VSMPs are in fact beige adipocytes progenitors^{69,204–207}. Another more technical explanation for the observed high-adipogenic phenotype of VSMPs would be that despite the fact that they significantly express to the highest extent *AOC3*, a number of PreAs also express *AOC3*. It would thus be advisable to investigate if the high adipogenicity of VAP1⁺ cells come from in fact a “contamination” by highly adipogenic PreAs.

Like in mouse, we identified a number of other minor clusters including one expressing *HHIP* that resemble mouse Aregs (**Supp. Fig. 2.2.5**), one expressing *SFRP4* that resembles *Clip+* cells in mouse (**Supp. Fig. 2.2.7**) and even one that expresses *IFIT* like mouse *Ifit+* cells that may be involved in innate immunity response (**Supp. Fig. 2.2.6**)²³⁶. While the overall transcriptomic signatures are close to the ones of the mouse populations, the top expressing markers of human cells are slightly different and this difference should be taken into account for further investigations. Interestingly, one of the minor clusters from the human merged dataset was specific to the PR and MC AT (**Fig. 2.2D**, **Supp. Fig. 2.2.1H**, **Supp. Fig. 2.2.2A-B**), however, >80% of the cells from this cluster come also from one single donor (**Supp. Fig. 2.2.2A**), it is thus difficult to draw conclusions on if this cluster is truly PR-MC-specific or patient-specific. Aside from the above-mentioned pan-anatomic clusters, stand out two depot-specific ones: the mesothelial and the *IGFBP2*⁺ cells, which are exclusively retrieved in the OM AT (**Fig. 2D**, **Supp. Fig. 2.2.2A-B**) and whose new functional properties are discussed in the paragraph below. Overall, mounting evidence point to the fact that we should no longer ignore the underlying human nor mouse ASPCs heterogeneity for future work aiming at understanding the neo-adipogenesis process. For future perspectives, it would be interesting to include even more adipose tissue types (for example the pericardial, epicardial, mediastinal or orbital) to study not only their ASPC composition but also the heterogeneity of two important cellular players of the adipose tissue that were missed by the current study: the mature adipocytes themselves and the resident immune cells.

3.2 Mesothelial cells are key effectors of the stromal vascular fraction

Mesothelial cells build up the peritoneum, a monolayer of mesothelial cells upholstering the abdominal cavity²⁵². However, the functional role of mesothelial cells in the abdominal cavity has not been extensively studied so far. In this work, we identified mesothelial cells (OM SVF Lin[−]/TM4SF1⁺/MSLN⁺) and mesothelial-like *IGFBP2*⁺ cells (OM SVF Lin[−]/TM4SF1⁺/MSLN[−]) (**Fig. 2.5A, Supp. Fig. 2.3.1C**) exclusively in the human SVF of the OM AT (**Supp. Fig. 2.4.6A**). In mice, mesothelial cells can be found in the murine epigonadal^{91,100,101,145} and omental¹⁴³ ATs. Therefore, future works studying visceral AT ASCs should make sure to exclude mesothelial cells from the “true” ASCs for any transcriptomic and functional analyses. To do so, we used TM4SF1 as a pan-mesothelial marker, and we observed that the OM SVF/Lin[−] fraction depleted of TM4SF1⁺ cells (OM SVF/Lin[−]/TM4SF1[−] cells), was significantly more adipogenic than the total fraction of OM SVF Lin[−] cells (**Fig 2.4C-D**), hinting to the fact that mesothelial cells and mesothelial-like cells might play a negative role in regulating the OM hASC adipogenesis. Moreover, we demonstrated, that TM4SF1⁺ cells can further be segregated into two functional subpopulations, one that is MSLN⁺ (OM SVF Lin[−]/TM4SF1⁺/MSLN⁺) and another that is MSLN[−] (OM SVF Lin[−]/TM4SF1⁺/MSLN[−]) (**Fig. 2.5A, Supp. Fig. 2.3.1C**). While both populations were able to inhibit the adipogenesis of hASCs to some extent, only the MSLN[−] fraction did so in a consistent and robust way (**Fig. 2.5E-F**). We were further able to prove that the inhibition stems from the fact that TM4SF1⁺/MSLN[−] highly secrete and express IGFBP2 (**Fig. 2.5B-C**), which inhibited adipogenesis through the activation of the integrin receptor $\alpha 5\beta 1$ (**Fig. 2.5K-P**)¹⁸⁶. During the length of this thesis, we demonstrated this point by chemical and recombinant protein interference assays in primary cultures (**Fig. 2.5K-P**). Future works could further complement this line of research by better understanding the intracellular downstream effects of the integrin receptor activation. This could be done also in primary human cultures, by knocking down the integrin receptor and comparing the phosphorylation status of intracellular proteins in the presence or absence of the IGFBP2 protein treatment. Similarly, to further understand the transcriptional reprogramming occurring in OM SVF cells upon IGFBP2 treatment, ChIP-seq or ATAC-seq assays could be performed.

In our samples, the percentage of OM-specific TM4SF1⁺ cells (mesothelial and *IGFBP2*⁺ together) measured by flow cytometry positively correlated with the donor's BMI (**Supp. Fig. 2.4.1B**). Taking advantage of the Emont et al. atlas¹⁴⁵, we were able to corroborate *in silico* a positive correlation between *IGFBP2*⁺ cells specifically and the donors' BMIs (**Supp. Fig. 2.4.4F**). While such findings hint at a functional role of the *IGFBP2*⁺ cells *in vivo*, IGFBP2 serum levels in humans negatively correlated with BMI^{214–216}, and characteristic features of the onset of the metabolic syndrome²¹⁷, including type 2 diabetes and NAFLD²¹⁸. Circulating levels of IGFBP2, however, are highly determined by hepatic IGFBP2 secretion^{218,253}, and, therefore, might not reflect its regulation in OM AT. To further characterize the role of IGFBP2 in human physiology it would also be

interesting to interrogate whole genome sequencing biobanks to look for SNP in the *IGFBP2* locus and study what is the phenotypic trait associated to it, with a specific focus on metabolic traits.

IGFBP2-secreting cells are rare among the OM SVF (2-5% of Lin⁻ cells) (**Fig. 2.4.6B**) and once in culture are slow-growing cells, difficult to expand to reach useful cell numbers. This could constitute a critical limitation for studies aiming to unravel their biological function. The inner limitations of human biopsy collections might also limit our ability to better understand the effects of IGFBP2 signaling *in vivo*. In this sense, it would be useful to investigate whether IGFBP2-secreting cells exist in the epigonadal AT of the mouse. A possible avenue to do so is to validate antibodies directed against the mouse TM4SF1 and MSLN antigens, and to use the same sorting strategy described in humans, however, given the described fundamental differences that we systematically observed across human and mouse AT biology, it would be more appropriate to favor an unbiased approach and first look for *Igfbp2*⁺ cells in publicly available scRNAseq datasets obtained from mouse epigonadal SVFs directly^{91,100,101,145}. This could allow us to identify new mouse-specific surface markers to eventually validate through flow cytometry. In that direction, Zhang and colleagues⁹¹ recently identified through single-cell transcriptomics a mesothelial cell population that highly expresses *Igfbp2* in the adult mouse epWAT. In contrast, at a younger age (P3) *Igfbp2* was differentially expressed by the smooth muscle cell cluster (likely resembling the human VSMPs). Ultimately, genetically modified animal tools would greatly help to explore the role of *Igfbp2* *in vivo*. Transgenic human *Igfbp2*-expressing mice, as well as *Igfbp2*-KO and eGFP-tagged mice, are commercially available and could provide new avenues to evaluate the role of IGFBP2 in adipose tissue biology upon metabolic challenges. Similarly, the eGFP-tagged-IGFBP2 transgenic mouse would allow to easily sort *Igfbp2*⁺ cells as well as to visualize them *in situ*.

In this work we highlighted a new functional role of mesothelial cells with regard to adipogenesis regulation, however they might also be functionally relevant with regard to the cross-talk with the immune system^{143,201,254}. We showed that SVF-adherent cells from the OM AT highly express pro-inflammatory markers and upregulate pathways related to immune response (**Fig. 2.1I, Supp. Fig. 2.1.5A**). Interestingly, the mesothelial cluster in the scRNA-seq specifically expresses chemokines and cytokines like IL-33, IL-1b and IL-18 as well as WT1 that all have been shown to contribute to the low-grade inflammation often linked to visceral obesity^{252,254–256}. Further effort should be put into understanding if the inflammatory signals we captured among OM SVF-adherent cells are secreted by mesothelial cells, the ASPCs or if it is a crosstalk between the two cell types that induces an overall inflammatory response. The cross-talk between mesothelial cells and ASPCs could be studied using co-culture transwell systems, where non-inflammatory cells like SC or PR ASPCs would be harvested for transcriptomic analysis after being exposed to paracrine signaling cues of mesothelial or IGFBP2-secreting cells, or vice-versa. Similar experiments could be designed to evaluate the interaction of IGFBP2-expressing cells with immune cells. Another valuable and interesting approach would be to use

spatial transcriptomics and histochemistry techniques to study the physical interaction between immune and mesothelial cells.

3.3 The emerging concept of negative regulation of adipogenesis

3.3.1 Do Aregs exist in human?

Aregs is a new functional cell population that was first described by our lab in 2018¹⁰². In mice, they are defined as subcutaneous SVF Lin[−]/Sca1⁺/CD142⁺ cells, which appear to inhibit adipogenesis both *in vitro* and *in vivo*. Their relative abundance among SVF cells increases upon HFD feeding^{102,148,149}, which may seem counterintuitive at a first glance, but in fact could reflect either (1) a compensatory mechanism to counteract the adipose tissue expansion, or (2) the development of intrinsic resistance to the regulatory mechanism of Aregs upon weight gain. Finding an equivalent population in humans was among the fundamental endeavors of the present work. Interestingly, while a clear and consistent cluster of *F3*-expressing cells was identified in both subcutaneous and visceral SVFs of the mouse^{145,257}, it looks like they are an extremely rare cell type in humans. In fact, we were able to detect an Areg-like cluster only after aggregating all our datasets together. In addition to their rareness, *F3*, the highly specific mouse marker is much less specific to human Aregs and is expressed instead at low levels by all the hASPCs. Based on our analysis *in silico*, *HHIP* should be considered a more valuable marker in the context of human Aregs biology given its specific enrichment in what we identified as the Areg-like cluster (**Supp. Fig. 2.2.5**). Validating a sorting strategy based on HHIP staining would therefore be an appropriate approach to better characterize human Aregs.

Despite human Areg-like cells are yet to be fully defined and characterized, understanding the mechanism of action of mouse Aregs is highly relevant since it is likely conserved across species. In fact, recent work from our lab showed that when SC hASPCs (SC SVF-adherent cells) are exposed to mouse Aregs (SC SVF Lin[−]/Sca1⁺/CD142⁺) in a transwell system, this resulted in significant impairment in their adipogenic potential, similar to the observed inhibitory action of Aregs on mouse adipogenic CD142[−] ASPCs (SC SVF Lin[−]/Sca1⁺/CD142[−])¹⁴⁸. Using the same rationale, it would be interesting to interrogate the effect of the inhibitory power of mouse Aregs on hASPCs derived from OM and PR AT as well, aiming at understanding if Aregs' inhibitory power is universal. The human-mouse hybrid setup could also be a useful tool to better understand the mechanism of action of Aregs taking advantage of the genetic differences between species.

In an interesting twist, our lab recently reported that when mouse adipogenic CD142[−] ASPCs are exposed to the Aregs secretome in the transwell setup, not only they ceased to be adipogenic, but their transcriptome became close to the one of Aregs. This is suggestive of a snowball effect where Aregs presence would induce an Areg-like state in their surrounding cells¹⁴⁸. This could stem from a canonical protein-receptor cell-signaling mechanism^{148,149} but also through signaling based on extracellular vesicles/exosomes "transmission".

Mesenchymal cells are known heavy producers of extracellular vesicles that carry anti-inflammatory and therapeutic properties^{258,259}. The hypothesis that Aregs would therefore signal through exocytosis of cytoplasmic vectors that would fuse to the cytoplasm of receiving cells and carry Aregs' mRNA with them could be interesting to pursue. Our findings showing that hASPCs can be influenced by Aregs could be helpful for this purpose, as one could look for contaminating mouse mRNA into the receiving hASPCs transcriptome as a way to elegantly test if Aregs signal through an extracellular vesicle flow. This approach, however, would not detect peptides, lipids or other metabolites that could mediate actions through extracellular vesicle communication, which cannot be ruled out.

In the present work we show for the first time that negative regulators of adipogenesis exist not only in mice but also in humans. Mesothelial cells and specifically *IGFBP2*⁺ cells, residing within the OM AT are able to negatively regulate the neoadipogenesis of OM ASPCs but also SC ASPCs. This finding opens a number of research avenues to understand how these cells modulate the plasticity of OM AT *in vivo*. This could have important therapeutic consequences, as OM AT expansion is linked to metabolically unhealthy obesity. In order to advance in a more unbiased way toward this understanding, it would be great to undertake a multi-omics approach, where we would perform combined proteomics, lipidomics and metabolomics on IGFBP2-secreting cell supernatant to identify in a more direct way what are the cues that are effectively secreted by the cells. Another interesting approach in both Aregs and IGFBP2⁺ cell biology would be to test the universality of their regulatory mechanism on whole new systems such as the muscle and the bone marrow as well as on bone or cartilage morphogenesis. In all these systems to have a precise means to control tissue renewal would allow precious advances in tissue engineering and transplantation.

3.3.2 Adipogenesis is differentially regulated across anatomic locations

Despite high similarity across hASPCs derived from different anatomic regions, we and others⁷⁹ were able to demonstrate, that cells from different depots carry over a transcriptomic footprint from their anatomic origin (**Fig. 2.1H-I**). As such, SC SVF-adherent cells highly express several developmental related HOX genes, PR cells have several pathways linked to oxidative respiratory chain and thermogenesis upregulated while OM cells are extremely inflammatory and carry an epithelial signature compared to MC which are characterized by heat-shock-protein (HSP) expression. It is therefore reasonable to think that different regulatory processes reign in different anatomic depots. Interestingly IGFBP2 signaling seems to act differentially across depots. While OM and SC hASPCs adipogenesis is effectively blunted by IGFBP2 at the concentration of around 30 ng/ml (1nM) (**Fig. 2.5K-P**), PR cells seem to be overall less sensitive to IGFBP2 (**Supp. Fig. 2.5.1B-C, Supp. Fig. 2.5.3B, D-F**). Interestingly, OM SVF-adherent cells compared to all other depots differentially express IGFBP2 both at the undifferentiated state and the differentiated one. In contrast, PR ASPCs upregulate IGFBP2 exclusively upon differentiation (low IGFBP2 expression at PR t0, high IGFBP2 expression at PR t14) (**Fig. 3.1**).

Taken together, not only does the concentration of the inhibitory cue seem to play a key role in determining selectively which adipose depots to regulate, but determinant could also be the timing of secretion and the signaling mode. In this sense, it is important to note that IGFBP2 might not only act as a secreted protein, but it can also have intracellular actions, for example, by interacting with tumor-suppressing genes such as *PTEN*. It would therefore be interesting in the case of PR to identify if the IGFBP2 upregulation results in its secretion or not.

IGFBP2 certainly contributes to the refractoriness of OM ASCs to form lipid droplets *in vitro* but it still cannot be fully explained why intraperitoneal-derived ASCs are so strongly refractory to adipogenesis upon cell culture. Even the most highly adipogenic OM ASC population (OM SVF Lin[−]/TM4SF1[−]/VAP1⁺) is by far not as adipogenic as the SC or PR corresponding populations (**Fig. 2.3E**). This observation hints at the fact that there must be some cell-intrinsic mechanism that prevents OM ASCs to become adipocytes. Several OM-specific markers aside from IGFBP2 could potentially be involved in the cell-intrinsic non-adipogenic character of OM ASCs. For instance, retinoic acid^{148,152}, GAL¹⁷⁰, PTN¹⁷¹, SLPI²⁶⁰, BCHE²⁶¹ and CD200¹⁷³ are all differentially expressed by OM ASCs and have previously been described as being anti-adipogenic factors. Interfering with these markers, by knocking them down or overexpressing them as well as dissecting their signaling pathways may lead to new discoveries in the field of adipogenesis regulation. Rspo2 has been reported to play a key role in the inhibitory mechanism used by Aregs to inhibit¹⁴⁹. To test how hASCs from different depots respond to RSPO2 treatment would be interesting to evaluate its relevance in human adipose tissue biology.

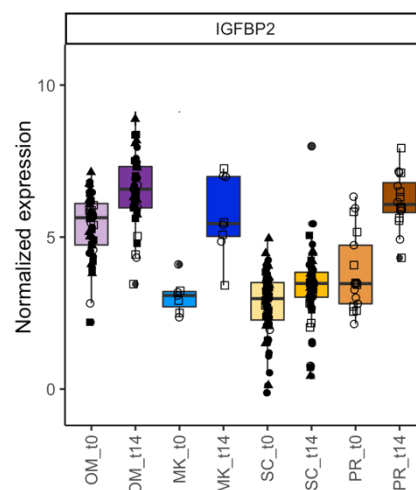


Figure 3.1 – IGFBP2 expression at t0 and t14 across depots.

Boxplot showing the distribution of batch normalized expression of *IGFBP2* of BRB-seq¹⁵⁰ data of SVF-isolated cells from the indicated depots and treatment conditions, n=12-61, 4-20 biological replicates, 1-4 independent wells for each.

3.4 Understanding the adipogenic lineage

3.4.1 The mesothelium as a possible origin for OM adipocytes

Aside from being able to negatively regulate adipogenesis, we showed the *IGFBP2*⁺ cells are susceptible to transition between mesothelial and mesenchymal cell states. Based on scRNA-seq data and pseudotime analysis, we showed that these cells order along a trajectory connecting ASCs to mesothelial cells (**Fig. 2.4G**). Along the connecting branch, mesothelial and ASCs markers increase and decrease, respectively, while some genes including *IGFBP2* and others previously linked to mesothelial to mesenchymal transition (MMT) peak at the center of the trajectory (**Fig. 2.4J**). While MMT acts similarly to the Epithelial to Mesenchymal Transition (EMT), its role in physiopathology is still unclear and has mainly been described in lung, liver and kidney fibrosis as well as in the context of peritoneal fibrosis during dialysis²⁵². MMT is however not necessarily a detrimental event. Due to these transitional properties, the omentum is routinely used in visceral surgery as a living patch to reconstruct perforated intestines. MMT is uttermost important during organogenesis, where mesothelial cells - expressing *Msln* - give rise to various cell types, such as fibroblast, or smooth muscle, of the visceral organs²⁵². Our work put forward the hypothesis that MMT would not only occur during early developmental stages but would happen in adulthood in a steady-like state.

Whether the MMT in adulthood would be the root of adipocyte formation in the omentum is a controverted subject that, if proven valid, would revolutionize our vision of OM AT plasticity. A lineage tracing study performed on murine epididymal fat originally, showed that eWAT but not scWAT nor BAT adipocytes express *Wt1*, likely reflecting an origin from *Wt1*⁺ mesothelial cells⁶², while mesothelial cells were also described to be adipogenic *in vitro*²⁶². A very recent study confirmed that mature eWAT adipocytes do express *Wt1*, but also demonstrated that only *Wt1* *Pdgfra*⁺ cells were able to give rise to mature adipocytes, while canonical *Krt19*⁺ *Wt1*⁺ mesothelial cells were unable to do so both at the developmental level and under forced adipose tissue expansion via high-fat diet¹⁷⁴. Interestingly, our *IGFBP2*⁺ cells express *PDGFRa* but not *KRT19*. We never directly tested the adipogenic abilities of our *IGFBP2*-secreting cells but this would be certainly an interesting experiment to perform. Similarly, it would be interesting to see if overexpression of known MMT transcription factors in mesothelial cells isolated from human omentum, would trigger a gene expression profile similar to the *IGFBP2*⁺ cells.

3.4.2 Redirecting the adipogenic lineage towards beiging

In the present work, we were able for the first time to determine the relative abundance of different cell subpopulations in the SVF Lin[−] niche of human SC, OM and PR AT of over 30 donors (**Fig. 2.3B-C**). This analysis showed that the ASC population is the least abundant in the OM AT, compared to SC and PR (**Fig. 2.3D, Supp. Fig. 2.3.1F**). This likely reflects exhaustion of the OM ASC pool in adulthood, which could explain the

preferential hypertrophic mode of expansion of OM AT. Conversely, PreAs predominate the ASC landscape of SC ASCs, while VSMP (or VAP1+-expressing PreAs) predominate the visceral ones (i.e. OM, PR and MC) (**Fig. 2.3D**, **Supp. Fig. 2.3.1F**). With increased BMI, and regardless of the anatomic depot, we highlighted an overall shift of the niche equilibrium from the PreAs (whose abundance negatively correlates to BMIs) to the VSMP pool (whose abundance positively does) (**Fig. 2.3G**). If we couple this hypothesis with the cell hierarchy model proposed by Merrick and colleagues⁹⁶, where mouse ASC would give rise to ICAM1+ cells and CD142+ cells, it would be interesting to explore if human ASC could give rise to both DN PreAs and VAP1+ VSMPs/PreAs as an early commitment to white or beige adipogenesis respectively. If this was the case, the observed increase in the relative proportion of VAP1+ cells in all ATs may reflect a desperate attempt to induce a thermogenic response to balance the excessive energy intake or to create new vasculature with the AT expansion.

Sprouting literature highlights how beige/brown adipogenesis is often coupled to the upregulation of myogenic-like markers necessary to dissipate energy under the form of heat^{69,204–207}. In this regard, it would be interesting to test the ability of VAP1+ cells specifically to upregulate *UCP1* under adrenergic stimulation or to perform respirometry or mitochondrial activity tests on these cells and compare their behavior with the other cell subpopulations as this would mount evidence supporting the hypothesis that VAP1+ cells could be thermogenic.

3.5 The Omentum AT as a hotspot for abdominal cancer metastasis

More than a bare energy reservoir, the omentum is a fascinating crossroad between connective and lymphatic tissue able to secrete endocrine signals, combat infections and store lipids. Clinically many visceral malignancies, including ovarian, gastric and colorectal cancers preferentially metastasize to the omentum^{263,263}. The exact signals that mediate this process are still subject to research and future efforts will be needed to dissect if the pro-metastatic signals come from a particular stromal cell population. In mice, metastatic cells are found in so-called “milky spots”, of the epigonadal WAT²⁶⁴, which are specialized niches of immune and mesothelial cells reminiscent of small lymph nodes^{143,265,266}. Milky spots do not exist in the human omentum, but, in line with them, mesothelial cells rather locate on the periphery of the tissue²⁶⁷. Nevertheless, with the whole new resolution we brought to the cell composition of the stromal vascular fraction of the omentum, it would be relevant to question the role that mesothelial as well as *IGFBP2*+ cells play in the nesting of tumoral cells in the omentum. Mesothelial cells notably secrete IL-6 and IL-8 involved in gastric cancer metastasis²⁶⁸. TM4SF1, our validated pan-mesothelial surface marker, has been described as a bad prognosis marker in pancreatic ductal cancer, as it might facilitate metastasization of the tumor²⁶⁹. Consequently, current efforts focus on TM4SF1 as a potential new therapeutic target to prevent the invasion and metastasization of ovarian cancer²⁷⁰. Finally, *IGFBP2* itself has been described as “the dark horse” in

metabolism²⁰⁹ and constitutes a marker for tumor progression in gliomas, prostatic cancer and breast cancer. Among the proposed mechanisms by which IGFBP2 could influence tumor prognosis are the interaction with extracellular matrix (ECM) components, such as surface proteoglycan receptors and integrin receptors. By affecting ECM components, IGFBP2 would allow tumor cells to detach from their native matrix and migrate. In addition, IGFBP2 could also influence tumor progression by downregulating the expression of *PTEN* or *CDKN2A*, which are known tumor-suppressing genes²⁷¹ as well as preventing the translocation of p21 or PAPA1 to the²⁷².

It would be extremely insightful to study if the metastatic process would be altered in genetically modified mice that have their mesothelial cell function impaired either by KO of IGFBP2 or TM4SF1. It would also be interesting to use *in situ* techniques such as immunohistochemistry or spatial transcriptomics in human metastasis resections. Macrophages also seem to play a key role in facilitating tumor metastasis to the omentum²⁷³, which could be influenced by the crosstalk with mesothelial cells, creating the perfect microenvironment for cancer proliferation. Therefore, mesothelial cells in adipose tissue open a whole new field for the identification of therapeutic approaches to improve the prognosis of such aggressive diseases.

Altogether we provided the first systematic and cross-anatomical functionalization of hASPC subpopulations proposed a new mechanism explaining why visceral ASPCs are reluctant to adipogenesis *in vitro* and discussed universal and unique characteristics of the adipose tissue in the function of its anatomic location and species of origin. Interfering locally with the IGFBP2 signaling in the visceral adipose tissue may contribute to promoting a healthy neoadipogenesis axed on hyperplasia instead of hyper-trophy and ease the inflammatory status linked to visceral obesity.

References

1. Smith, K. B. & Smith, M. S. Obesity Statistics. *Primary Care: Clinics in Office Practice* **43**, 121–135 (2016).
2. Nguyen, D. M. & El-Serag, H. B. The Epidemiology of Obesity. *Gastroenterol Clin North Am* **39**, 1–7 (2010).
3. Huang, P. L. A comprehensive definition for metabolic syndrome. *Dis Model Mech* **2**, 231–237 (2009).
4. The top 10 causes of death. <https://www.who.int/news-room/fact-sheets/detail/the-top-10-causes-of-death>.
5. Bhattacharya, J. & Bundorf, M. K. The incidence of the healthcare costs of obesity. *Journal of Health Economics* **28**, 649–658 (2009).
6. Yanovski, S. Z. & Yanovski, J. A. Long-term Drug Treatment for Obesity: A Systematic and Clinical Review. *JAMA* **311**, 74–86 (2014).
7. Fiorenza, C. G., Chou, S. H. & Mantzoros, C. S. Lipodystrophy: pathophysiology and advances in treatment. *Nat Rev Endocrinol* **7**, 137–150 (2011).
8. *Evaluation of Total and Regional Adiposity. Handbook of Obesity* 49–96 (CRC Press, 2003). doi:10.3109/9780203913376-6.
9. Gallagher, D. *et al.* Healthy percentage body fat ranges: an approach for developing guidelines based on body mass index. *Am J Clin Nutr* **72**, 694–701 (2000).
10. Nevill, A. M., Stewart, A. D., Olds, T. & Holder, R. Relationship between adiposity and body size reveals limitations of BMI. *American Journal of Physical Anthropology* **129**, 151–156 (2006).
11. Sakers, A., De Siqueira, M. K., Seale, P. & Villanueva, C. J. Adipose-tissue plasticity in health and disease. *Cell* **185**, 419–446 (2022).
12. Chan, D. C., Watts, G. F., Barrett, P. H. R. & Burke, V. Waist circumference, waist-to-hip ratio and body mass index as predictors of adipose tissue compartments in men. *QJM: An International Journal of Medicine* **96**, 441–447 (2003).
13. Gibson, S. & Ashwell, M. A simple cut-off for waist-to-height ratio (0.5) can act as an indicator for cardiometabolic risk: recent data from adults in the Health Survey for England. *British Journal of Nutrition* **123**, 681–690 (2020).
14. Heymsfield, S. B., Wang, Z., Visser, M., Gallagher, D. & Pierson, R. N. Techniques used in the measurement of body composition: an overview with emphasis on bioelectrical impedance analysis. *Am J Clin Nutr* **64**, 478S–484S (1996).
15. Macias, N., Alemán-Mateo, H., Esparza-Romero, J. & Valencia, M. E. Body fat measurement by bioelectrical impedance and air displacement plethysmography: a cross-validation study to design bioelectrical impedance equations in Mexican adults. *Nutrition Journal* **6**, 18 (2007).
16. Shepherd, J., Ng, B., Sommer, M. & Heymsfield, S. B. Body Composition by DXA. *Bone* **104**, 101–105 (2017).
17. Kamel, E. G. *et al.* Measurement of abdominal fat by magnetic resonance imaging, dual-energy X-ray absorptiometry and anthropometry in non-obese men and women. *Int J Obes* **23**, 686–692 (1999).

18. Bi, X. *et al.* DEXA MEASURED VISCERAL ADIPOSE TISSUE PREDICTS IMPAIRED GLUCOSE TOLERANCE AND METABOLIC SYNDROME IN OBESE CAUCASIAN AND AFRICAN AMERICAN WOMEN. *Eur J Clin Nutr* **69**, 329–336 (2015).
19. Kaul, S. *et al.* Dual-energy X-ray absorptiometry for quantification of visceral fat. *Obesity (Silver Spring, Md.)* **20**, (2012).
20. Pescatori, L. C. *et al.* Quantification of visceral adipose tissue by computed tomography and magnetic resonance imaging: reproducibility and accuracy. *Radiol Bras* **52**, 1–6 (2019).
21. Al Jawaldeh, A. *Food and nutrition surveillance systems: a manual for policy-makers and programme managers.* (2018).
22. Fairbrother, U., Kidd, E., Malagamuwa, T. & Walley, A. Genetics of Severe Obesity. *Curr Diab Rep* **18**, 85 (2018).
23. Karam, J. G. & McFarlane, S. I. Secondary causes of obesity. *Therapy* **4**, 641–651 (2007).
24. Mahmoud, A. M. An Overview of Epigenetics in Obesity: The Role of Lifestyle and Therapeutic Interventions. *Int J Mol Sci* **23**, 1341 (2022).
25. Domecq, J. P. *et al.* Drugs Commonly Associated With Weight Change: A Systematic Review and Meta-analysis. *J Clin Endocrinol Metab* **100**, 363–370 (2015).
26. Farooqi, I. S. & O’Rahilly, S. Genetics of Obesity in Humans. *Endocrine Reviews* **27**, 710–718 (2006).
27. Grundy, S. M. Obesity, Metabolic Syndrome, and Cardiovascular Disease. *The Journal of Clinical Endocrinology & Metabolism* **89**, 2595–2600 (2004).
28. Drager, L. F., Togeiro, S. M., Polotsky, V. Y. & Lorenzi, -Filho Geraldo. Obstructive Sleep Apnea. *Journal of the American College of Cardiology* **62**, 569–576 (2013).
29. Ix, J. H. & Sharma, K. Mechanisms Linking Obesity, Chronic Kidney Disease, and Fatty Liver Disease: The Roles of Fetuin-A, Adiponectin, and AMPK. *J Am Soc Nephrol* **21**, 406–412 (2010).
30. Van Raemdonck, K., Umar, S., Szekanecz, Z., Zomorodi, R. K. & Shahrara, S. Impact of obesity on autoimmune arthritis and its cardiovascular complications. *Autoimmunity Reviews* **17**, 821–835 (2018).
31. Shiri, R., Lallukka, T., Karppinen, J. & Viikari-Juntura, E. Obesity as a Risk Factor for Sciatica: A Meta-Analysis. *American Journal of Epidemiology* **179**, 929–937 (2014).
32. Lauby-Secretan, B. *et al.* Body Fatness and Cancer--Viewpoint of the IARC Working Group. *N Engl J Med* **375**, 794–798 (2016).
33. Argyrakopoulou, G., Dalamaga, M., Spyrou, N. & Kokkinos, A. Gender Differences in Obesity-Related Cancers. *Curr Obes Rep* **10**, 100–115 (2021).
34. Pham, D.-V. & Park, P.-H. Tumor Metabolic Reprogramming by Adipokines as a Critical Driver of Obesity-Associated Cancer Progression. *International Journal of Molecular Sciences* **22**, 1444 (2021).
35. Lavalley, K. L., Zhang, X. C., Schneider, S. & Margraf, J. Obesity and Mental Health: A Longitudinal, Cross-Cultural Examination in Germany and China. *Front Psychol* **12**, 712567 (2021).
36. de Noronha, S. R. *et al.* High fat diet induced-obesity facilitates anxiety-like behaviors due to GABAergic impairment within the dorsomedial hypothalamus in rats. *Behav Brain Res* **316**, 38–46 (2017).

37. Baker, K. D., Loughman, A., Spencer, S. J. & Reichelt, A. C. The impact of obesity and hypercaloric diet consumption on anxiety and emotional behavior across the lifespan. *Neurosci Biobehav Rev* **83**, 173–182 (2017).
38. Goldstein, D. J. Beneficial health effects of modest weight loss. *Int J Obes Relat Metab Disord* **16**, 397–415 (1992).
39. Hall, K. D. & Kahan, S. Maintenance of lost weight and long-term management of obesity. *Med Clin North Am* **102**, 183–197 (2018).
40. Ruban, A., Stoenchev, K., Ashrafian, H. & Teare, J. Current treatments for obesity. *Clin Med (Lond)* **19**, 205–212 (2019).
41. Nest, S. *et al.* [Liraglutide in the treatment of obesity : a multidisciplinary approach]. *Rev Med Suisse* **18**, 516–521 (2022).
42. Sahebkar, A. *et al.* Effect of orlistat on plasma lipids and body weight: A systematic review and meta-analysis of 33 randomized controlled trials. *Pharmacol Res* **122**, 53–65 (2017).
43. Torgerson, J. S., Hauptman, J., Boldrin, M. N. & Sjöström, L. XENical in the prevention of diabetes in obese subjects (XENDOS) study: a randomized study of orlistat as an adjunct to lifestyle changes for the prevention of type 2 diabetes in obese patients. *Diabetes Care* **27**, 155–161 (2004).
44. Vilsbøll, T., Christensen, M., Junker, A. E., Knop, F. K. & Gluud, L. L. Effects of glucagon-like peptide-1 receptor agonists on weight loss: systematic review and meta-analyses of randomised controlled trials. *BMJ* **344**, d7771 (2012).
45. Greenway, F. L. *et al.* Effect of naltrexone plus bupropion on weight loss in overweight and obese adults (COR-I): a multicentre, randomised, double-blind, placebo-controlled, phase 3 trial. *Lancet* **376**, 595–605 (2010).
46. Tchang, B. G., Aras, M., Kumar, R. B. & Aronne, L. J. Pharmacologic Treatment of Overweight and Obesity in Adults. in *Endotext* (eds. Feingold, K. R. *et al.*) (MDText.com, Inc., 2000).
47. Angrisani, L. *et al.* Roux-en-Y Gastric Bypass Versus Sleeve Gastrectomy as Revisional Procedures after Adjustable Gastric Band: 5-Year Outcomes. *Obes Surg* **27**, 1430–1437 (2017).
48. Mantziari, S., Duvoisin, C., Demartines, N., Favre, L. & Suter, M. [Long-term results (≥ 10 years) after bariatric surgery : review of the literature.]. *Rev Med Suisse* **14**, 636–640 (2018).
49. Adams, T. D. *et al.* Weight and Metabolic Outcomes 12 Years after Gastric Bypass. *N Engl J Med* **377**, 1143–1155 (2017).
50. Busetto, L. *et al.* Long-term cardiovascular risk and coronary events in morbidly obese patients treated with laparoscopic gastric banding. *Surgery for Obesity and Related Diseases* **10**, 112–120 (2014).
51. Sjöström, L. *et al.* Bariatric surgery and long-term cardiovascular events. *JAMA* **307**, 56–65 (2012).
52. Garg, A. Lipodystrophies: Genetic and Acquired Body Fat Disorders. *The Journal of Clinical Endocrinology & Metabolism* **96**, 3313–3325 (2011).
53. Guzman, N. & Vijayan, V. HIV-associated Lipodystrophy. *StatPearls* (2022).
54. Chiquette, E., Oral, E. A., Garg, A., Araújo-Vilar, D. & Dhankhar, P. Estimating the prevalence of generalized and partial lipodystrophy: findings and challenges. *Diabetes Metab Syndr Obes* **10**, 375–383 (2017).

-
55. Araújo-Vilar, D. & Santini, F. Diagnosis and treatment of lipodystrophy: a step-by-step approach. *J Endocrinol Invest* **42**, 61–73 (2019).
 56. Lima, J. G. *et al.* Causes of death in patients with Berardinelli-Seip congenital generalized lipodystrophy. *PLoS One* **13**, e0199052 (2018).
 57. Chan, J. L. *et al.* Clinical effects of long-term metreleptin treatment in patients with lipodystrophy. *Endocr Pract* **17**, 922–932 (2011).
 58. Chong, A. Y., Lupsa, B. C., Cochran, E. K. & Gorden, P. Efficacy of leptin therapy in the different forms of human lipodystrophy. *Diabetologia* **53**, 27–35 (2010).
 59. Emont, M. P. *et al.* A single-cell atlas of human and mouse white adipose tissue. *Nature* **603**, 926–933 (2022).
 60. Merrick, D. *et al.* Identification of a mesenchymal progenitor cell hierarchy in adipose tissue. *Science* **364**, eaav2501 (2019).
 61. Vijay, J. *et al.* Single-cell analysis of human adipose tissue identifies depot and disease specific cell types. *Nat Metab* **2**, 97–109 (2020).
 62. Chau, Y.-Y. *et al.* Visceral and subcutaneous fat have different origins and evidence supports a mesothelial source. *Nat Cell Biol* **16**, 367–375 (2014).
 63. Stenkula, K. G. & Erlanson-Albertsson, C. Adipose cell size: importance in health and disease. *American Journal of Physiology-Regulatory, Integrative and Comparative Physiology* **315**, R284–R295 (2018).
 64. Eto, H. *et al.* Characterization of structure and cellular components of aspirated and excised adipose tissue. *Plast Reconstr Surg* **124**, 1087–1097 (2009).
 65. Suga, H. *et al.* Numerical measurement of viable and nonviable adipocytes and other cellular components in aspirated fat tissue. *Plast Reconstr Surg* **122**, 103–114 (2008).
 66. Berry, R. & Rodeheffer, M. S. Characterization of the adipocyte cellular lineage in vivo. *Nat. Cell Biol.* **15**, 302–308 (2013).
 67. Berry, D. C., Stenesen, D., Zeve, D. & Graff, J. M. The developmental origins of adipose tissue. *Development* **140**, 3939–3949 (2013).
 68. Cleal, L., Aldea, T. & Chau, Y.-Y. Fifty shades of white: Understanding heterogeneity in white adipose stem cells. *Adipocyte* **6**, 205–216 (2017).
 69. Wang, W. & Seale, P. Control of brown and beige fat development. *Nat Rev Mol Cell Biol* **17**, 691–702 (2016).
 70. Pradhan, R. N., Zachara, M. & Deplancke, B. A systems perspective on brown adipogenesis and metabolic activation. *Obes Rev* **18 Suppl 1**, 65–81 (2017).
 71. Huang, N. *et al.* Novel insight into perirenal adipose tissue: A neglected adipose depot linking cardiovascular and chronic kidney disease. *World J Diabetes* **11**, 115–125 (2020).
 72. Grigoraş, A. *et al.* Perirenal Adipose Tissue—Current Knowledge and Future Opportunities. *J Clin Med* **10**, 1291 (2021).

-
73. Efremova, A. *et al.* A large proportion of mediastinal and perirenal visceral fat of Siberian adult people is formed by UCP1 immunoreactive multilocular and paucilocular adipocytes. *J Physiol Biochem* **76**, 185–192 (2020).
 74. Siciliano, C. *et al.* The adipose tissue of origin influences the biological potential of human adipose stromal cells isolated from mediastinal and subcutaneous fat depots. *Stem Cell Research* **17**, 342–351 (2016).
 75. Christensen, R. H., von Scholten, B. J., Lehrskov, L. L., Rossing, P. & Jørgensen, P. G. Epicardial adipose tissue: an emerging biomarker of cardiovascular complications in type 2 diabetes? *Ther Adv Endocrinol Metab* **11**, 2042018820928824 (2020).
 76. Wu, Z. *et al.* Mesenteric adipose tissue contributes to intestinal barrier integrity and protects against nonalcoholic fatty liver disease in mice. *Am J Physiol Gastrointest Liver Physiol* **315**, G659–G670 (2018).
 77. Meza-Perez, S. & Randall, T. D. Immunological functions of the omentum. *Trends Immunol* **38**, 526–536 (2017).
 78. Passaro, A. *et al.* Gene expression regional differences in human subcutaneous adipose tissue. *BMC Genomics* **18**, 202 (2017).
 79. Schleinitz, D. *et al.* Identification of distinct transcriptome signatures of human adipose tissue from fifteen depots. *Eur J Hum Genet* **28**, 1714–1725 (2020).
 80. Jackson-Jones, L. H. *et al.* Stromal Cells Covering Omental Fat-Associated Lymphoid Clusters Trigger Formation of Neutrophil Aggregates to Capture Peritoneal Contaminants. *Immunity* **52**, 700-715.e6 (2020).
 81. Rodeheffer, M. S., Birsoy, K. & Friedman, J. M. Identification of White Adipocyte Progenitor Cells In Vivo. *Cell* **135**, 240–249 (2008).
 82. Cawthorn, W. P., Scheller, E. L. & MacDougald, O. A. Adipose tissue stem cells meet preadipocyte commitment: going back to the future[S]. *Journal of Lipid Research* **53**, 227–246 (2012).
 83. Berry, R. & Rodeheffer, M. S. Characterization of the adipocyte cellular lineage in vivo. *Nat Cell Biol* **15**, 302–308 (2013).
 84. Vishvanath, L. *et al.* Pdgfr β + Mural Preadipocytes Contribute to Adipocyte Hyperplasia Induced by High-Fat-Diet Feeding and Prolonged Cold Exposure in Adult Mice. *Cell Metabolism* **23**, 350–359 (2016).
 85. Ong, W. K. *et al.* Identification of Specific Cell-Surface Markers of Adipose-Derived Stem Cells from Subcutaneous and Visceral Fat Depots. *Stem Cell Reports* **2**, 171–179 (2014).
 86. García-Rubio, J. *et al.* Cytometric analysis of adipose tissue reveals increments of adipocyte progenitor cells after weight loss induced by bariatric surgery. *Scientific Reports* **8**, (2018).
 87. Schwalie, P. C. *et al.* A stromal cell population that inhibits adipogenesis in mammalian fat depots. *Nature* **559**, 103–108 (2018).
 88. Burl, R. B. *et al.* Deconstructing Adipogenesis Induced by β 3-Adrenergic Receptor Activation with Single-Cell Expression Profiling. *Cell Metab* **28**, 300-309.e4 (2018).
 89. Hepler, C. & Gupta, R. K. The expanding problem of adipose depot remodeling and postnatal adipocyte progenitor recruitment. *Mol Cell Endocrinol* **445**, 95–108 (2017).
 90. Cho, D. S., Lee, B. & Doles, J. D. Refining the adipose progenitor cell landscape in healthy and obese visceral adipose tissue using single-cell gene expression profiling. *Life Sci Alliance* **2**, e201900561 (2019).

91. Zhang, Q. *et al.* Distinct functional properties of murine perinatal and adult adipose progenitor subpopulations. *Nat Metab* **4**, 1055–1070 (2022).
92. Stuart, T. *et al.* Comprehensive Integration of Single-Cell Data. *Cell* **177**, 1888–1902.e21 (2019).
93. Butler, A., Hoffman, P., Smibert, P., Papalexi, E. & Satija, R. Integrating single-cell transcriptomic data across different conditions, technologies, and species. *Nat Biotechnol* **36**, 411–420 (2018).
94. Vijay, J. *et al.* Single-cell analysis of human adipose tissue identifies depot- and disease-specific cell types. *Nat Metab* **2**, 97–109 (2020).
95. Sárvári, A. K. *et al.* Plasticity of Epididymal Adipose Tissue in Response to Diet-Induced Obesity at Single-Nucleus Resolution. *Cell Metab* **33**, 437–453.e5 (2021).
96. Merrick, D. *et al.* Identification of a mesenchymal progenitor cell hierarchy in adipose tissue. *Science* **364**, eaav2501 (2019).
97. Acosta, J. R. *et al.* Single cell transcriptomics suggest that human adipocyte progenitor cells constitute a homogeneous cell population. *Stem Cell Research & Therapy* **8**, 250 (2017).
98. Hepler, C. *et al.* Identification of functionally distinct fibro-inflammatory and adipogenic stromal subpopulations in visceral adipose tissue of adult mice. *Elife* **7**, e39636 (2018).
99. Spallanzani, R. G. *et al.* Distinct immunocyte-promoting and adipocyte-generating stromal components coordinate adipose-tissue immune and metabolic tenors. *Sci Immunol* **4**, eaaw3658 (2019).
100. Burl, R. B. *et al.* Deconstructing Adipogenesis Induced by β 3-Adrenergic Receptor Activation with Single-Cell Expression Profiling. *Cell Metabolism* **28**, 300–309.e4 (2018).
101. Hepler, C. *et al.* Identification of functionally distinct fibro-inflammatory and adipogenic stromal subpopulations in visceral adipose tissue of adult mice. *eLife* **7**, e39636 (2018).
102. Schwalie, P. C. *et al.* A stromal cell population that inhibits adipogenesis in mammalian fat depots. *Nature* **559**, 103 (2018).
103. Butler, A., Hoffman, P., Smibert, P., Papalexi, E. & Satija, R. Integrating single-cell transcriptomic data across different conditions, technologies, and species. *Nat. Biotechnol.* **36**, 411–420 (2018).
104. Stuart, T. *et al.* Comprehensive Integration of Single-Cell Data. *Cell* **177**, 1888–1902.e21 (2019).
105. Holmes, C. & Stanford, W. L. Concise review: stem cell antigen-1: expression, function, and enigma. *Stem Cells* **25**, 1339–1347 (2007).
106. O’Leary, H., Ou, X. & Broxmeyer, H. E. The role of dipeptidyl peptidase 4 in hematopoiesis and transplantation. *Curr Opin Hematol* **20**, 314–319 (2013).
107. Kim, M., Bae, Y. K., Kwon, J., Jeon, H. B. & Jin, H. J. Dipeptidyl peptidase-4 (DPP4) induce Cellular Senescence in Human Umbilical Cord Blood-Derived Mesenchymal Stem Cells. *The FASEB Journal* **30**, 1b40–1b40 (2016).
108. Stefkovich, M., Traynor, S., Cheng, L., Merrick, D. & Seale, P. Dpp4+ interstitial progenitor cells contribute to basal and high fat diet-induced adipogenesis. *Mol Metab* **54**, 101357 (2021).

109. Saygin, C. *et al.* CD55 regulates self-renewal and cisplatin resistance in endometrioid tumors. *J Exp Med* **214**, 2715–2732 (2017).
110. Soland, M. A. *et al.* Mesenchymal Stem Cells Engineered to Inhibit Complement-Mediated Damage. *PLOS ONE* **8**, e60461 (2013).
111. Simsek Kiper, P. O. *et al.* Cortical-Bone Fragility — Insights from sFRP4 Deficiency in Pyle’s Disease. *New England Journal of Medicine* **374**, 2553–2562 (2016).
112. Dong, H. *et al.* Identification of a regulatory pathway inhibiting adipogenesis via RSPO2. *Nat Metab* **4**, 90–105 (2022).
113. Zachara, M. *et al.* Mammalian adipogenesis regulator (Areg) cells use retinoic acid signalling to be non- and anti-adipogenic in age-dependent manner. *The EMBO Journal* **41**, e108206 (2022).
114. Leménager, H. *et al.* Cell immaturity and white/beige adipocyte potential of primary human adipose-derived stromal cells are restrained by culture-medium TGFβ1. *Stem Cells* **38**, 782–796 (2020).
115. Chen, Y. *et al.* Thermal stress induces glycolytic beige fat formation via a myogenic state. *Nature* **565**, 180–185 (2019).
116. Farup, J. *et al.* Human skeletal muscle CD90+ fibro-adipogenic progenitors are associated with muscle degeneration in type 2 diabetic patients. *bioRxiv* 2020.08.25.243907 (2020) doi:10.1101/2020.08.25.243907.
117. Rivera-Gonzalez, G. C. *et al.* Skin Adipocyte Stem Cell Self-Renewal Is Regulated by a PDGFA/AKT-Signaling Axis. *Cell Stem Cell* **19**, 738–751 (2016).
118. Sun, C. *et al.* Mosaic Mutant Analysis Identifies PDGFRα/PDGFRβ as Negative Regulators of Adipogenesis. *Cell Stem Cell* **26**, 707–721.e5 (2020).
119. Gao, Z., Daquinag, A. C., Su, F., Snyder, B. & Kolonin, M. G. PDGFRα/PDGFRβ signaling balance modulates progenitor cell differentiation into white and beige adipocytes. *Development* **145**, dev155861 (2018).
120. Camps, J. *et al.* Interstitial Cell Remodeling Promotes Aberrant Adipogenesis in Dystrophic Muscles. *Cell Reports* **31**, 107597 (2020).
121. Baglioni, S. *et al.* Functional differences in visceral and subcutaneous fat pads originate from differences in the adipose stem cell. *PLoS One* **7**, e36569 (2012).
122. Takeda, K. *et al.* Retinoic Acid Mediates Visceral-Specific Adipogenic Defects of Human Adipose-Derived Stem Cells. *Diabetes* **65**, 1164–1178 (2016).
123. Berry, R. & Rodeheffer, M. S. Characterization of the adipocyte cellular lineage in vivo. *Nat. Cell Biol.* **15**, 302–308 (2013).
124. Trapnell, C. *et al.* The dynamics and regulators of cell fate decisions are revealed by pseudotemporal ordering of single cells. *Nat. Biotechnol.* **32**, 381–386 (2014).
125. Michailova, K. N. & Usunoff, K. G. The milky spots of the peritoneum and pleura: structure, development and pathology. *Bio-medical Reviews* **15**, 47–66 (2004).

126. Liu, J., Geng, X. & Li, Y. Milky spots: omental functional units and hotbeds for peritoneal cancer metastasis. *Tumour Biol* **37**, 5715–5726 (2016).
127. Lee, K. Y. *et al.* Developmental and functional heterogeneity of white adipocytes within a single fat depot. *EMBO J* **38**, e99291 (2019).
128. Kanamori-Katayama, M. *et al.* LRRN4 and UPK3B Are Markers of Primary Mesothelial Cells. *PLoS One* **6**, e25391 (2011).
129. Buechler, M. B. *et al.* A Stromal Niche Defined by Expression of the Transcription Factor WT1 Mediates Programming and Homeostasis of Cavity-Resident Macrophages. *Immunity* **51**, 119–130.e5 (2019).
130. Koga, S. *et al.* Peripheral PDGFR α +gp38+ mesenchymal cells support the differentiation of fetal liver-derived ILC2. *J Exp Med* **215**, 1609–1626 (2018).
131. John, B. *et al.* Regulation of the bi-directional cross-talk between ovarian cancer cells and adipocytes by SPARC. *Oncogene* **38**, 4366–4383 (2019).
132. Freese, K. E. *et al.* Adipose-derived stems cells and their role in human cancer development, growth, progression, and metastasis: a systematic review. *Cancer Res* **75**, 1161–1168 (2015).
133. Mahlaköiv, T. *et al.* Stromal cells maintain immune cell homeostasis in adipose tissue via production of interleukin-33. *Sci Immunol* **4**, eaax0416 (2019).
134. Kolodin, D. *et al.* ANTIGEN- AND CYTOKINE-DRIVEN ACCUMULATION OF REGULATORY T CELLS IN VISCERAL ADIPOSE TISSUE OF LEAN MICE. *Cell Metab* **21**, 543–557 (2015).
135. Soleymaninejadian, E., Pramanik, K. & Samadian, E. Immunomodulatory properties of mesenchymal stem cells: cytokines and factors. *Am J Reprod Immunol* **67**, 1–8 (2012).
136. Kuefner, M. S. *et al.* Secretory phospholipase A2 group IIA modulates insulin sensitivity and metabolism. *J Lipid Res* **58**, 1822–1833 (2017).
137. Perdikari, A. *et al.* BATLAS: Deconvoluting Brown Adipose Tissue. *Cell Rep* **25**, 784–797.e4 (2018).
138. Silva, K. R. & Baptista, L. S. Adipose-derived stromal/stem cells from different adipose depots in obesity development. *World Journal of Stem Cells* **11**, 147–166 (2019).
139. Cho, D. S., Lee, B. & Doles, J. D. Refining the adipose progenitor cell landscape in healthy and obese visceral adipose tissue using single-cell gene expression profiling. *Life Science Alliance* **2**, e201900561 (2019).
140. Louwen, F., Ritter, A., Kreis, N. N. & Yuan, J. Insight into the development of obesity: functional alterations of adipose-derived mesenchymal stem cells. *Obes Rev* **19**, 888–904 (2018).
141. Kim, S. M. *et al.* Loss of white adipose hyperplastic potential is associated with enhanced susceptibility to insulin resistance. *Cell Metab.* **20**, 1049–1058 (2014).
142. Ghaben, A. L. & Scherer, P. E. Adipogenesis and metabolic health. *Nat. Rev. Mol. Cell Biol.* **20**, 242–258 (2019).

143. Jackson-Jones, L. H. *et al.* Stromal Cells Covering Omental Fat-Associated Lymphoid Clusters Trigger Formation of Neutrophil Aggregates to Capture Peritoneal Contaminants. *Immunity* **52**, 700–715.e6 (2020).
144. Marcelin, G. *et al.* A PDGFR α -Mediated Switch toward CD9high Adipocyte Progenitors Controls Obesity-Induced Adipose Tissue Fibrosis. *Cell Metabolism* **25**, 673–685 (2017).
145. Emont, M. P. *et al.* A single-cell atlas of human and mouse white adipose tissue. *Nature* **603**, 926–933 (2022).
146. Ferrero, R., Rainer, P. & Deplancke, B. Toward a Consensus View of Mammalian Adipocyte Stem and Progenitor Cell Heterogeneity. *Trends Cell Biol* **30**, 937–950 (2020).
147. Hepler, C. *et al.* Directing visceral white adipocyte precursors to a thermogenic adipocyte fate improves insulin sensitivity in obese mice. *eLife* **6**, (2017).
148. Zachara, M. *et al.* Mammalian adipogenesis regulator (Areg) cells use retinoic acid signalling to be non- and anti-adipogenic in age-dependent manner. *The EMBO Journal* **41**, e108206 (2022).
149. Dong, H. *et al.* Identification of a regulatory pathway inhibiting adipogenesis via RSPO2. *Nat Metab* **4**, 90–105 (2022).
150. Alpern, D. *et al.* BRB-seq: ultra-affordable high-throughput transcriptomics enabled by bulk RNA barcoding and sequencing. *Genome Biology* **20**, 71 (2019).
151. Saalbach, A. & Anderegg, U. Thy-1: more than a marker for mesenchymal stromal cells. *FASEB J* **33**, 6689–6696 (2019).
152. Takeda, K. *et al.* Retinoic Acid Mediates Visceral-Specific Adipogenic Defects of Human Adipose-Derived Stem Cells. *Diabetes* **65**, 1164–1178 (2016).
153. Brunmeir, R. *et al.* Comparative Transcriptomic and Epigenomic Analyses Reveal New Regulators of Murine Brown Adipogenesis. *PLOS Genetics* **12**, e1006474 (2016).
154. Bai, N. *et al.* Bola3 Regulates Beige Adipocyte Thermogenesis via Maintaining Mitochondrial Homeostasis and Lipolysis. *Frontiers in Endocrinology* **11**, (2021).
155. Wellen, K. E. & Hotamisligil, G. S. Inflammation, stress, and diabetes. *J Clin Invest* **115**, 1111–1119 (2005).
156. Trayhurn, P. & Wood, I. S. Adipokines: inflammation and the pleiotropic role of white adipose tissue. *Br J Nutr* **92**, 347–355 (2004).
157. Arner, P. Introduction: the inflammation orchestra in adipose tissue. *J Intern Med* **262**, 404–407 (2007).
158. Kanamori-Katayama, M. *et al.* LRRN4 and UPK3B Are Markers of Primary Mesothelial Cells. *PLOS ONE* **6**, e25391 (2011).
159. Majesky Mark W., Dong Xiu Rong, Regan Jenna N., Hoglund Virginia J., & Schneider Michael. Vascular Smooth Muscle Progenitor Cells. *Circulation Research* **108**, 365–377 (2011).
160. Kiselev, V. Y. *et al.* SC3: consensus clustering of single-cell RNA-seq data. *Nature Methods* **14**, 483–486 (2017).
161. Sárvári, A. K. *et al.* Plasticity of Epididymal Adipose Tissue in Response to Diet-Induced Obesity at Single-Nucleus Resolution. *Cell Metabolism* **33**, 437–453.e5 (2021).

162. Ehrlund, A. *et al.* Characterization of the Wnt inhibitors secreted frizzled-related proteins (SFRPs) in human adipose tissue. *J Clin Endocrinol Metab* **98**, E503–508 (2013).
163. Zhang, Y. *et al.* Effects of SFRP4 overexpression on the production of adipokines in transgenic mice. *Adipocyte* **9**, 374–383 (2020).
164. Hatzmann, F. M. *et al.* Dipeptidyl peptidase-4 cell surface expression marks an abundant adipose stem/progenitor cell population with high stemness in human white adipose tissue. *Adipocyte* **11**, 601–615 (2022).
165. Yu, W. *et al.* Critical role of phosphoinositide 3-kinase cascade in adipogenesis of human mesenchymal stem cells. *Mol Cell Biochem* **310**, 11–18 (2008).
166. Hinoi, E. *et al.* PI3K/Akt is involved in brown adipogenesis mediated by growth differentiation factor-5 in association with activation of the Smad pathway. *Biochemical and Biophysical Research Communications* **450**, 255–260 (2014).
167. Plaisier, C. L. *et al.* Zbtb16 has a role in brown adipocyte bioenergetics. *Nutr Diabetes* **2**, e46 (2012).
168. Desarzens, S., Liao, W.-H., Mammi, C., Caprio, M. & Faresse, N. Hsp90 blockers inhibit adipocyte differentiation and fat mass accumulation. *PLoS One* **9**, e94127 (2014).
169. Peng, J. *et al.* An Hsp20-FBXO4 Axis Regulates Adipocyte Function through Modulating PPAR γ Ubiquitination. *Cell Reports* **23**, 3607–3620 (2018).
170. Li, R.-Y. *et al.* Galanin inhibits leptin expression and secretion in rat adipose tissue and 3T3-L1 adipocytes. *J Mol Endocrinol* **33**, 11–19 (2004).
171. Gu, D. *et al.* The effect of pleiotrophin signaling on adipogenesis. *FEBS Lett* **581**, 382–388 (2007).
172. de Silva, H. C., Firth, S. M., Twigg, S. M. & Baxter, R. C. Interaction between IGF binding protein-3 and TGF β in the regulation of adipocyte differentiation. *Endocrinology* **153**, 4799–4807 (2012).
173. Ong, W. K. *et al.* Identification of specific cell-surface markers of adipose-derived stem cells from subcutaneous and visceral fat depots. *Stem Cell Reports* **2**, 171–179 (2014).
174. Westcott, G. P. *et al.* Mesothelial cells are not a source of adipocytes in mice. *Cell Reports* **36**, 109388 (2021).
175. Dauleh, S. *et al.* Characterisation of Cultured Mesothelial Cells Derived from the Murine Adult Omentum. *PLoS One* **11**, (2016).
176. Hewett, P. W. & Murray, J. C. Human omental mesothelial cells: A simple method for isolation and discrimination from endothelial cells. *In Vitro Cell Dev Biol - Animal* **30**, 145–147 (1994).
177. Yau, S. W. *et al.* IGFBP-2 inhibits adipogenesis and lipogenesis in human visceral, but not subcutaneous, adipocytes. *International Journal of Obesity* **39**, 770–781 (2015).
178. Xi, G. *et al.* The Heparin-Binding Domains of IGFBP-2 Mediate Its Inhibitory Effect on Preadipocyte Differentiation and Fat Development in Male Mice. *Endocrinology* **154**, 4146–4157 (2013).
179. Wolf, F. A. *et al.* PAGA: graph abstraction reconciles clustering with trajectory inference through a topology preserving map of single cells. *Genome Biology* **20**, 59 (2019).

180. Yang, J. *et al.* Guidelines and definitions for research on epithelial–mesenchymal transition. *Nat Rev Mol Cell Biol* **21**, 341–352 (2020).
181. Nisticò, P., Bissell, M. J. & Radisky, D. C. Epithelial-Mesenchymal Transition: General Principles and Pathological Relevance with Special Emphasis on the Role of Matrix Metalloproteinases. *Cold Spring Harb Perspect Biol* **4**, a011908 (2012).
182. Sureban, S. M. *et al.* DCLK1 regulates pluripotency and angiogenic factors via microRNA-dependent mechanisms in pancreatic cancer. *PLoS One* **8**, e73940 (2013).
183. Weber, C. E., Li, N. Y., Wai, P. Y. & Kuo, P. C. Epithelial-Mesenchymal Transition, TGF- β , and Osteopontin in Wound Healing and Tissue Remodeling After Injury. *Journal of Burn Care & Research* **33**, 311–318 (2012).
184. Marconi, G. D. *et al.* Epithelial-Mesenchymal Transition (EMT): The Type-2 EMT in Wound Healing, Tissue Regeneration and Organ Fibrosis. *Cells* **10**, 1587 (2021).
185. Tsai, J. M. *et al.* Surgical adhesions in mice are derived from mesothelial cells and can be targeted by antibodies against mesothelial markers. *Sci Transl Med* **10**, ean6735 (2018).
186. Li, T. *et al.* IGFBP2: integrative hub of developmental and oncogenic signaling network. *Oncogene* **39**, 2243–2257 (2020).
187. Yang, R.-Z. *et al.* Identification of omentin as a novel depot-specific adipokine in human adipose tissue: possible role in modulating insulin action. *American Journal of Physiology-Endocrinology and Metabolism* **290**, E1253–E1261 (2006).
188. Schäffler, A. *et al.* Genomic structure of human omentin, a new adipocytokine expressed in omental adipose tissue. *Biochimica et Biophysica Acta (BBA) - Gene Structure and Expression* **1732**, 96–102 (2005).
189. Boughanem, H., Yubero-Serrano, E. M., López-Miranda, J., Tinahones, F. J. & Macias-Gonzalez, M. Potential Role of Insulin Growth-Factor-Binding Protein 2 as Therapeutic Target for Obesity-Related Insulin Resistance. *International Journal of Molecular Sciences* **22**, 1133 (2021).
190. Hesse, D. *et al.* Effect of adipocyte-derived IGF-I on adipose tissue mass and glucose metabolism in the Berlin Fat Mouse. *Growth Factors* **36**, 78–88 (2018).
191. Wang, F. *et al.* Insulin-like growth factor I promotes adipogenesis in hemangioma stem cells from infantile hemangiomas. *Molecular Medicine Reports* **19**, 2825–2830 (2019).
192. Zhang, K. *et al.* Insulin-like growth factor 2 promotes the adipogenesis of hemangioma-derived stem cells. *Exp Ther Med* **17**, 1663–1669 (2019).
193. Alfares, M. N., Perks, C. M., Hamilton-Shield, J. P. & Holly, J. M. P. Insulin-like growth factor-II in adipocyte regulation: depot-specific actions suggest a potential role limiting excess visceral adiposity. *American Journal of Physiology-Endocrinology and Metabolism* **315**, E1098–E1107 (2018).
194. Uetaki, M. *et al.* Regulatory roles of fibronectin and integrin $\alpha 5$ in reorganization of the actin cytoskeleton and completion of adipogenesis. *Mol Biol Cell* **33**, ar78 (2022).

195. Kumar, C. C. *et al.* Biochemical characterization of the binding of echistatin to integrin alphavbeta3 receptor. *J Pharmacol Exp Ther* **283**, 843–853 (1997).
196. Baglioni, S. *et al.* Functional Differences in Visceral and Subcutaneous Fat Pads Originate from Differences in the Adipose Stem Cell. *PLoS One* **7**, (2012).
197. Baer, P. C. Adipose-derived mesenchymal stromal/stem cells: An update on their phenotype in vivo and in vitro. *World J Stem Cells* **6**, 256–265 (2014).
198. Jespersen, N. Z. *et al.* Heterogeneity in the perirenal region of humans suggests presence of dormant brown adipose tissue that contains brown fat precursor cells. *Molecular Metabolism* **24**, 30–43 (2019).
199. Alvehus, M., Burén, J., Sjöström, M., Goedecke, J. & Olsson, T. The Human Visceral Fat Depot Has a Unique Inflammatory Profile. *Obesity* **18**, 879–883 (2010).
200. Ritter, A. *et al.* Characterization of adipose-derived stem cells from subcutaneous and visceral adipose tissues and their function in breast cancer cells. *Oncotarget* **6**, 34475–34493 (2015).
201. Darimont, C. *et al.* Contribution of mesothelial cells in the expression of inflammatory-related factors in omental adipose tissue of obese subjects. *Int J Obes* **32**, 112–120 (2008).
202. Pötsch, B., Grulich-Henn, J., Rössing, R., Wille, D. & Müller-Berghaus, G. Identification of endothelial and mesothelial cells in human omental tissue and in omentum-derived cultured cells by specific cell markers. *Lab Invest* **63**, 841–852 (1990).
203. Kim, S. M. *et al.* Loss of white adipose hyperplastic potential is associated with enhanced susceptibility to insulin resistance. *Cell Metab.* **20**, 1049–1058 (2014).
204. Long, J. Z. *et al.* A smooth muscle-like origin for beige adipocytes. *Cell Metab.* **19**, 810–820 (2014).
205. Chen, Y. *et al.* Thermal stress induces glycolytic beige fat formation via a myogenic state. *Nature* **565**, 180–185 (2019).
206. Wang, W. *et al.* A PRDM16-Driven Metabolic Signal from Adipocytes Regulates Precursor Cell Fate. *Cell Metabolism* **30**, 174–189.e5 (2019).
207. Sun, W. *et al.* snRNA-seq reveals a subpopulation of adipocytes that regulates thermogenesis. *Nature* **587**, 98–102 (2020).
208. Chan, M. *et al.* Identification of a natural beige adipose depot in mice. *J Biol Chem* **294**, 6751–6761 (2019).
209. Russo, V. C., Azar, W. J., Yau, S. W., Sabin, M. A. & Werther, G. A. IGFBP-2: The dark horse in metabolism and cancer. *Cytokine Growth Factor Rev* **26**, 329–346 (2015).
210. Koopmans, T. & Rinkevich, Y. Mesothelial to mesenchyme transition as a major developmental and pathological player in trunk organs and their cavities. *Commun Biol* **1**, 1–14 (2018).
211. Zhu, H. *et al.* IGFBP2 promotes the EMT of colorectal cancer cells by regulating E-cadherin expression. *Int J Clin Exp Pathol* **12**, 2559–2565 (2019).
212. Haschemi, R. *et al.* Insulin-like Growth Factor Binding Protein-2 (IGFBP2) Is a Key Molecule in the MACC1-Mediated Platelet Communication and Metastasis of Colorectal Cancer Cells. *Int J Mol Sci* **22**, 12195 (2021).

-
213. Chatterjee, S., Park, E. S. & Soloff, M. S. Proliferation of DU145 prostate cancer cells is inhibited by suppressing insulin-like growth factor binding protein-2. *International Journal of Urology* **11**, 876–884 (2004).
214. Beld, A. W. van den *et al.* IGFBP-2 and aging: a 20-year longitudinal study on IGFBP-2, IGF-I, BMI, insulin sensitivity and mortality in an aging population. *European Journal of Endocrinology* **180**, 109–116 (2019).
215. Wheatcroft, S. B. *et al.* IGF-Binding Protein-2 Protects Against the Development of Obesity and Insulin Resistance. *Diabetes* **56**, 285–294 (2007).
216. Hedbacker, K. *et al.* Antidiabetic Effects of IGFBP2, a Leptin-Regulated Gene. *Cell Metabolism* **11**, 11–22 (2010).
217. Heald, A. H. *et al.* Insulin-like growth factor binding protein-2 (IGFBP-2) is a marker for the metabolic syndrome. *Exp Clin Endocrinol Diabetes* **114**, 371–376 (2006).
218. Fahlbusch, P. *et al.* Physiological Disturbance in Fatty Liver Energy Metabolism Converges on IGFBP2 Abundance and Regulation in Mice and Men. *Int J Mol Sci* **21**, 4144 (2020).
219. Rosen, E. D. & Spiegelman, B. M. What We Talk About When We Talk About Fat. *Cell* **156**, 20–44 (2014).
220. Alpern, D. *et al.* BRB-seq: ultra-affordable high-throughput transcriptomics enabled by bulk RNA barcoding and sequencing. *Genome Biology* **20**, 71 (2019).
221. McCarthy, D. J., Chen, Y. & Smyth, G. K. Differential expression analysis of multifactor RNA-Seq experiments with respect to biological variation. *Nucleic Acids Res* **40**, 4288–4297 (2012).
222. Ritchie, M. E. *et al.* limma powers differential expression analyses for RNA-sequencing and microarray studies. *Nucleic Acids Res* **43**, e47 (2015).
223. Love, M. I., Huber, W. & Anders, S. Moderated estimation of fold change and dispersion for RNA-seq data with DESeq2. *Genome Biol* **15**, 550 (2014).
224. Yu, G., Wang, L.-G., Han, Y. & He, Q.-Y. clusterProfiler: an R package for comparing biological themes among gene clusters. *OMICS* **16**, 284–287 (2012).
225. Kiselev, V. Y., Yiu, A. & Hemberg, M. scmap: projection of single-cell RNA-seq data across data sets. *Nat Methods* **15**, 359–362 (2018).
226. Dewey, M. metap: meta-analysis of significance values. *R package version 1.8* (2022).
227. McGinnis, C. S. *et al.* MULTI-seq: sample multiplexing for single-cell RNA sequencing using lipid-tagged indices. *Nat Methods* **16**, 619–626 (2019).
228. Wolf, F. A., Angerer, P. & Theis, F. J. SCANPY: large-scale single-cell gene expression data analysis. *Genome Biology* **19**, 15 (2018).
229. Jacomy, M., Venturini, T., Heymann, S. & Bastian, M. ForceAtlas2, a Continuous Graph Layout Algorithm for Handy Network Visualization Designed for the Gephi Software. *PLOS ONE* **9**, e98679 (2014).

-
230. Saelens, W., Cannoodt, R., Todorov, H. & Saeys, Y. A comparison of single-cell trajectory inference methods. *Nat Biotechnol* **37**, 547–554 (2019).
231. Zachara, M. *et al.* Mammalian adipogenesis regulator (Areg) cells use retinoic acid signalling to be non- and anti-adipogenic in age-dependent manner. *The EMBO Journal* **41**, e108206 (2022).
232. Carangelo, G., Magi, A. & Semeraro, R. From multitude to singularity: An up-to-date overview of scRNA-seq data generation and analysis. *Frontiers in Genetics* **13**, (2022).
233. Cao, J. *et al.* Comprehensive single-cell transcriptional profiling of a multicellular organism. *Science* **357**, 661–667 (2017).
234. Li, H. *et al.* Fly Cell Atlas: A single-nucleus transcriptomic atlas of the adult fruit fly. *Science* **375**, eabk2432 (2022).
235. Deutsch, A., Feng, D., Pessin, J. E. & Shinoda, K. The Impact of Single-Cell Genomics on Adipose Tissue Research. *International Journal of Molecular Sciences* **21**, 4773 (2020).
236. Pezoldt, J. *et al.* Single-cell transcriptional profiling of splenic fibroblasts reveals subset-specific innate immune signatures in homeostasis and during viral infection. *Commun Biol* **4**, 1–14 (2021).
237. Subramanian, S. *et al.* Persistent gut microbiota immaturity in malnourished Bangladeshi children. *Nature* **510**, 417–421 (2014).
238. Gomez de Agüero, M. *et al.* The maternal microbiota drives early postnatal innate immune development. *Science* **351**, 1296–1302 (2016).
239. Le Doare, K., Holder, B., Bassett, A. & Pannaraj, P. S. Mother's Milk: A Purposeful Contribution to the Development of the Infant Microbiota and Immunity. *Frontiers in Immunology* **9**, (2018).
240. Al Nabhani, Z. *et al.* A Weaning Reaction to Microbiota Is Required for Resistance to Immunopathologies in the Adult. *Immunity* **50**, 1276–1288.e5 (2019).
241. Grizotte-Lake, M. *et al.* Gut commensals suppress epithelial cell retinoic acid synthesis to regulate intestinal interleukin-22 activity and prevent microbial dysbiosis. *Immunity* **49**, 1103–1115.e6 (2018).
242. Lai, M., Chandrasekera, P. C. & Barnard, N. D. You are what you eat, or are you? The challenges of translating high-fat-fed rodents to human obesity and diabetes. *Nutr Diabetes* **4**, e135 (2014).
243. Fuller, K. N. Z. & Thyfault, J. P. Barriers in translating preclinical rodent exercise metabolism findings to human health. *J Appl Physiol (1985)* **130**, 182–192 (2021).
244. Zhang, Y. *et al.* Positional cloning of the mouse obese gene and its human homologue. *Nature* **372**, 425–432 (1994).
245. Jeet Singh, H. The Unfolding Tale of Leptin. *Malays J Med Sci* **8**, 1–6 (2001).
246. Gibson, W. T. *et al.* Congenital Leptin Deficiency Due to Homozygosity for the $\Delta 133G$ Mutation: Report of Another Case and Evaluation of Response to Four Years of Leptin Therapy. *The Journal of Clinical Endocrinology & Metabolism* **89**, 4821–4826 (2004).

-
247. Farooqi, I. S. *et al.* Effects of Recombinant Leptin Therapy in a Child with Congenital Leptin Deficiency. *New England Journal of Medicine* **341**, 879–884 (1999).
248. Greco, M. *et al.* Leptin-Activity Modulators and Their Potential Pharmaceutical Applications. *Biomolecules* **11**, 1045 (2021).
249. Virtue, S. & Vidal-Puig, A. Assessment of brown adipose tissue function. *Frontiers in Physiology* **4**, (2013).
250. Leitner, B. P. *et al.* Mapping of human brown adipose tissue in lean and obese young men. *Proceedings of the National Academy of Sciences* **114**, 8649–8654 (2017).
251. Chusyd, D. E., Wang, D., Huffman, D. M. & Nagy, T. R. Relationships between Rodent White Adipose Fat Pads and Human White Adipose Fat Depots. *Front Nutr* **3**, 10 (2016).
252. Gupta, O. T. & Gupta, R. K. Visceral Adipose Tissue Mesothelial Cells: Living on the Edge or Just Taking Up Space? *Trends Endocrinol. Metab.* **26**, 515–523 (2015).
253. Yang, J. *et al.* Circulating IGFBP-2 levels are inversely associated with the incidence of nonalcoholic fatty liver disease: A cohort study. *J Int Med Res* **48**, 0300060520935219 (2020).
254. Spallanzani, R. G. *et al.* Distinct immunocyte-promoting and adipocyte-generating stromal components coordinate adipose tissue immune and metabolic tenors. *Science Immunology* **4**, eaaw3658 (2019).
255. Mahlaköiv, T. *et al.* Stromal cells maintain immune cell homeostasis in adipose tissue via production of interleukin-33. *Science Immunology* **4**, eaax0416 (2019).
256. Buechler, M. B. *et al.* A Stromal Niche Defined by Expression of the Transcription Factor WT1 Mediates Programming and Homeostasis of Cavity-Resident Macrophages. *Immunity* **51**, 119-130.e5 (2019).
257. Yang, J. *et al.* Single-cell dissection of the obesity-exercise axis in adipose-muscle tissues implies a critical role for mesenchymal stem cells. *Cell Metabolism* **34**, 1578-1593.e6 (2022).
258. Kou, M. *et al.* Mesenchymal stem cell-derived extracellular vesicles for immunomodulation and regeneration: a next generation therapeutic tool? *Cell Death Dis* **13**, 1–16 (2022).
259. Keshtkar, S., Azarpira, N. & Ghahremani, M. H. Mesenchymal stem cell-derived extracellular vesicles: novel frontiers in regenerative medicine. *Stem Cell Research & Therapy* **9**, 63 (2018).
260. Liu, C. *et al.* Fat-Specific Knockout of Mecp2 Upregulates Slpi to Reduce Obesity by Enhancing Browning. *Diabetes* **69**, 35–47 (2020).
261. Chen, V. P. *et al.* Butyrylcholinesterase Deficiency Promotes Adipose Tissue Growth and Hepatic Lipid Accumulation in Male Mice on High-Fat Diet. *Endocrinology* **157**, 3086–3095 (2016).
262. Lansley, S. M. *et al.* Mesothelial cell differentiation into osteoblast- and adipocyte-like cells. *J Cell Mol Med* **15**, 2095–2105 (2011).
263. Freese, K. E. *et al.* Adipose-Derived Stems Cells and Their Role in Human Cancer Development, Growth, Progression, and Metastasis: A Systematic Review. *Cancer Res* **75**, 1161–1168 (2015).

-
264. Liu, J., Geng, X. & Li, Y. Milky spots: omental functional units and hotbeds for peritoneal cancer metastasis. *Tumour Biol* **37**, 5715–5726 (2016).
265. Cruz-Migoni, S. & Caamaño, J. Fat-Associated Lymphoid Clusters in Inflammation and Immunity. *Front Immunol* **7**, 612 (2016).
266. Michailova, K. N. & Usunoff, K. G. The milky spots of the peritoneum and pleura: structure, development and pathology. *Bio-medical Reviews* **15**, 47 (2004).
267. Strieder-Barboza, C. *et al.* Single-nuclei Transcriptome of Human AT Reveals Metabolically Distinct Depot-Specific Adipose Progenitor Subpopulations. 2022.06.29.496888 Preprint at <https://doi.org/10.1101/2022.06.29.496888> (2022).
268. Kersy, O. *et al.* Omental Tissue-Mediated Tumorigenesis of Gastric Cancer Peritoneal Metastases. *Frontiers in Oncology* **9**, (2019).
269. Zheng, B. *et al.* TM4SF1 as a prognostic marker of pancreatic ductal adenocarcinoma is involved in migration and invasion of cancer cells. *Int. J. Oncol.* **47**, 490–498 (2015).
270. Gao, C., Yao, H., Liu, H., Feng, Y. & Yang, Z. TM4SF1 is a potential target for anti-invasion and metastasis in ovarian cancer. *BMC Cancer* **19**, 237 (2019).
271. Perks, C. M., Vernon, E. G., Rosendahl, A. H., Tonge, D. & Holly, J. M. P. IGF-II and IGFBP-2 differentially regulate PTEN in human breast cancer cells. *Oncogene* **26**, 5966–5972 (2007).
272. Moore, L. M. *et al.* IGFBP2 is a candidate biomarker for Ink4a-Arf status and a therapeutic target for high-grade gliomas. *Proc Natl Acad Sci U S A* **106**, 16675–16679 (2009).
273. Etzerodt, A. *et al.* Tissue-resident macrophages in omentum promote metastatic spread of ovarian cancer. *Journal of Experimental Medicine* **217**, e20191869 (2020).

Radiana Ferrero

MD-PhD student

Laboratory of Systems Biology and Genetics

Life Science – Institute of Bioengineering

École Polytechnique Fédérale de Lausanne (EPFL)

SV 3823 – Station 19 – 1015 Lausanne

Contacts

rferrero@live.com

Citizenship

Italian, Swiss

Spoken languages

English, French, Italian

Education

2018 – 2023 MD-PhD in Bioengineering and Biotechnologies, École Polytechnique Fédérale de Lausanne (EPFL), Switzerland

2015 – 2018 Master in Human Medicine, Université de Lausanne (UNIL), Switzerland

2012 – 2015 Bachelor in Human Medicine, Université de Lausanne (UNIL), Switzerland

Work experience in research

2018 – 2023 MD-PhD student
Institute of Bioengineering, EPFL, Lausanne, Switzerland
Project: “Cross-anatomical single-cell definition and characterization of human adipose progenitor niche”
Supervisor: Professor Bart Deplancke

2017 – 2018 Master student
Institute of pathology, Centre Hospitalier Universitaire Vaudois (CHUV), Lausanne, Switzerland
Project: “V5-tag of SYT-SSX chimeric protein in the context of synovial sarcoma”
Supervisor: Professor Ivan Stamenkovic

Work experience in clinics

2017 – 2018 Medical school clinical internships

1 month	<i>General medicine</i> – Dr. J-P Randin, Lausanne, Switzerland
1 month	<i>Transplantation immunology</i> – HUG, Geneva, Switzerland
1 month	<i>Psychiatry, Accueil Observation Crise</i> – CHUV, Lausanne, Switzerland
1 month	<i>General surgery</i> – Clinica Luganese, Lugano, Switzerland
1 month	<i>Otolaryngology</i> – HFR, Fribourg, Switzerland
2 months	<i>Internal medicine</i> – HJB, St-Imier, Switzerland
1 month	<i>Infectious diseases</i> – Hôpital Tenon, Paris, France
2 months	<i>Emergencies</i> – Hôpital Tenon, Paris, France

Other work experiences

2016 – 2018 Polysomnography technician
Centre Lausannois de Médecine du Sommeil (CLMS), Av. Juste-Olivier 21, 1006 Lausanne, Switzerland
Reference: Dr. Eric Lainey

2014 – 2017	Teaching and logistics Etu Prep Molliqaj Villard, Ch. de la Gravière 2, 1227 Les Acacias, Switzerland Reference: Dr. Nicolas Villard
2014 – 2017	Librarian auxiliary Bibliothèque Universitaire de Médecine (Bium), Ch. des Falaises 2, 1005 Lausanne, Switzerland Reference: Mme Isabelle de Kaenel

Teaching and supervision experience

2021-2022	BIO-310 Immunologie, Prof. Lemaitre – 2h lecture entiteled « Immunology of Covid-19 » Content preparation and ex-cathedra lecture
2018-2020	BIO-378 Travaux pratiques de physiologie, Prof. Pexieder – The electrocardiogram
2018-2020	BIO-377 Physiologie par systèmes, Prof. Roy
2015-2017	Physiscs, physiology and histology support lessons to first year medical school students (EtuPrep) 4h lectures ex-cathedra and content preparation
2019	Supervision of SV-EPFL bachelor project, one day a week for five months
2020	Supervision of SV-EPFL bachelor project, one day a week for five months
2022	Supervision of IMC University of applied sciences, Kermes, Austria bachelor project, 6 full-time months

Talks and posters

2020	Super sandwich seminar, SV faculty seminar, EPFL, Talk
2021	IBI-EDBB Grad Student Mini-Symposia, EPFL, Talk
2019-2020	Joint UNIL-EPFL PhD retreat, Talk and Poster
2019	Summer school “Shaping the future of medicine”, Poster
2019	Stem cell retreat, Münsingen, Switzerland
2018-2022	MD-PhD retreat Unil, Poster and Talk (2022)

Prizes and grants

2021	Prize for the best poster, “An omentum specific mesothelial population inhibits adipogenesis”, MD-PhD retreat, Unil
2018	Prize for the best poster, “V5-tag of SYT-SSX”, Master-Day school of Medicine, Unil
2018	MD-PhD scholarship from Lenaards Foundation

Publications

2020	Ferrero, R. , Rainer, P. & Deplancke, B. Toward a Consensus View of Mammalian Adipocyte Stem and Progenitor Cell Heterogeneity. Trends Cell Biol 30, 937–950.
2022	Zachara, M., Rainer, P. Y., Hashimi, H., Russeil, J. M., Alpern, D., Ferrero, R. , Litovchenko, M., Deplancke, B. Mammalian adipogenesis regulator (Areg) cells use retinoic acid signalling to be non- and anti-adipogenic in age-dependent manner. The EMBO Journal 41, e108206.
2016	Ferrero, R. , Gönczy, L., Meinherz, A., Rossier, G. & Thévoz, F. Le RAI-HC: l’avis des professionnels de santé des CMS vaudois. Primary and Hospital Care, doi:10.4414/phc-f.2016.01252.

Radiana Ferrero

MD-PhD student

Laboratory of Systems Biology and Genetics

Life Science – Institute of Bioengineering

École Polytechnique Fédérale de Lausanne (EPFL)

SV 3823 – Station 19 – 1015 Lausanne

Contacts

rferrero@live.com

Citizenship

Italian, Swiss

Spoken languages

English, French, Italian

Education

2018 – 2023	MD-PhD in Bioengineering and Biotechnologies, École Polytechnique Fédérale de Lausanne (EPFL), Switzerland
2015 – 2018	Master in Human Medicine, Université de Lausanne (UNIL), Switzerland
2012 – 2015	Bachelor in Human Medicine, Université de Lausanne (UNIL), Switzerland

Work experience in research

2018 – 2023	MD-PhD student Institute of Bioengineering, EPFL, Lausanne, Switzerland
Project:	“Cross-anatomical single-cell definition and characterization of human adipose progenitor niche”
Supervisor:	Professor Bart Deplancke
2017 – 2018	Master student Institute of pathology, Centre Hospitalier Universitaire Vaudois (CHUV), Lausanne, Switzerland
Project:	“V5-tag of SYT–SSX chimeric protein in the context of synovial sarcoma”
Supervisor:	Professor Ivan Stamenkovic

Work experience in clinics

2017 – 2018	Medical school clinical internships
1 month	<i>General medicine</i> – Dr. J-P Randin, Lausanne, Switzerland
1 month	<i>Transplantation immunology</i> – HUG, Geneva, Switzerland
1 month	<i>Psychiatry, Accueil Observation Crise</i> – CHUV, Lausanne, Switzerland
1 month	<i>General surgery</i> – Clinica Luganese, Lugano, Switzerland
1 month	<i>Otolaryngology</i> – HFR, Fribourg, Switzerland
2 months	<i>Internal medicine</i> – HJB, St-Imier, Switzerland
1 month	<i>Infectious diseases</i> – Hôpital Tenon, Paris, France
2 months	<i>Emergencies</i> – Hôpital Tenon, Paris, France

Other work experiences

2016 – 2018	Polysomnography technician Centre Lausannois de Médecine du Sommeil (CLMS), Av. Juste-Olivier 21, 1006 Lausanne, Switzerland
Reference:	Dr. Eric Lainey

2014 – 2017	Teaching and logistics Etu Prep Molliqaj Villard, Ch. de la Gravière 2, 1227 Les Acacias, Switzerland Reference: Dr. Nicolas Villard
2014 – 2017	Librarian auxiliary Bibliothèque Universitaire de Médecine (Bium), Ch. des Falaises 2, 1005 Lausanne, Switzerland Reference: Mme Isabelle de Kaenel

Teaching and supervision experience

2021-2022	BIO-310 Immunologie, Prof. Lemaitre – 2h lecture entiteled « Immunology of Covid-19 » Content preparation and ex-cathedra lecture
2018-2020	BIO-378 Travaux pratiques de physiologie, Prof. Pexieder – The electrocardiogram
2018-2020	BIO-377 Physiologie par systèmes, Prof. Roy
2015-2017	Physiscs, physiology and histology support lessons to first year medical school students (EtuPrep) 4h lectures ex-cathedra and content preparation
2019	Supervision of SV-EPFL bachelor project, one day a week for five months
2020	Supervision of SV-EPFL bachelor project, one day a week for five months
2022	Supervision of IMC University of applied sciences, Kermes, Austria bachelor project, 6 full-time months

Talks and posters

2020	Super sandwich seminar, SV faculty seminar, EPFL, Talk
2021	IBI-EDBB Grad Student Mini-Symposia, EPFL, Talk
2019-2020	Joint UNIL-EPFL PhD retreat, Talk and Poster
2019	Summer school “Shaping the future of medicine”, Poster
2019	Stem cell retreat, Münsingen, Switzerland
2018-2022	MD-PhD retreat Unil, Poster and Talk (2022)

Prizes and grants

2021	Prize for the best poster, “An omentum specific mesothelial population inhibits adipogenesis”, MD-PhD retreat, Unil
2018	Prize for the best poster, “V5-tag of SYT-SSX”, Master-Day school of Medicine, Unil
2018	MD-PhD scholarship from Lenaards Foundation

Publications

2020	Ferrero, R. , Rainer, P. & Deplancke, B. Toward a Consensus View of Mammalian Adipocyte Stem and Progenitor Cell Heterogeneity. Trends Cell Biol 30, 937–950.
2022	Zachara, M., Rainer, P. Y., Hashimi, H., Russeil, J. M., Alpern, D., Ferrero, R. , Litovchenko, M., Deplancke, B. Mammalian adipogenesis regulator (Areg) cells use retinoic acid signalling to be non- and anti-adipogenic in age-dependent manner. The EMBO Journal 41, e108206.
2016	Ferrero, R. , Gönczy, L., Meinherz, A., Rossier, G. & Thévoz, F. Le RAI-HC: l’avis des professionnels de santé des CMS vaudois. Primary and Hospital Care, doi:10.4414/phc-f.2016.01252.